CONTENTS

ABSTRACTS

Łukasz Bąk, Stanisław Noga, Feliks Stachowicz
The Experimental Investigation of the Screen Operation in the Parametric Resonance Conditions

In this paper the experimental studies of the screen working in the parametric resonance condition are discussed. The investigations are conducted for laboratory parametric resonance screen. The measuring test is performed for four cases of tension force values. The full sheet metal instead of the sieve is used. For each considered case the natural frequency of the plate and the parameter modulation frequency are determined. The achieved results are presented and discussed. It is shown that the highest sieve plate amplitude is obtained when the parameter modulation frequency is two times larger than natural frequency of the sieve plate. This parametric resonance vibration was observed only for tension force equal to 4000 N because of the rotational speed limits of electrical vibratos.

Václav Tesař
Fluidic Generator of Microbubbles – Oscillator with Gas Flow Reversal for a Part of Period

Paper presents a fluidic device developed for generation of small (less than 1 mm in diameter) microbubbles in a liquid from gas passing gas through small passages. Until now the bubbles are larger than the size of aerator passage exits so that making the passages smaller did not result in obtaining the desirable microbubbles. Analysis of high-speed camera images (obtained with a special lens of large working distance) have shown show that the large bubble size is caused by slow ascent motion of very small bubbles so that they get into mutual contact and grow by conjunction. The solution is to pulsate the supplied gas flow by a no-moving-part fluidic oscillator. The generated small bubble is moved back into the aerator passage where it is for a part of oscillation period protected from the conjunction with other, previously generated microbubbles.

Ernest Czerwiński, Paweł Olejnik, Jan Awrejcewicz
Modeling and Parameter Identification of Vibrations of a Double Torsion Pendulum with Friction

The purpose of this paper is to investigate a double torsion pendulum with planar frictional contact. The single torsion pendulum with one-degree-of-freedom is an angular equivalent of the linear harmonic oscillator. The second degree of freedom has been obtained by adding a free body to the inverted single torsion pendulum. The free body's angular displacement is caused by frictional forces appearing in the interface (contact zone) between the free body and the pendulum column's head kinematically excited at its base by a mechanism with torsion spiral spring. An experimental station has been set up and run to find most unknown parameters of the pendulum from the time series of state variables taken as inputs to the Nelder-Mead method of identification. The obtained results proved significant usability of the identification method in the case of numerical simulation of the pendulum's dynamical model. It has not been satisfactorily proved in the case of time characteristics coming from a real system that exhibits also some unrecognized physical effects.

Sławomir Wudarczyk, Artur Muraszkowski
A Concept and Simulation Studies of a Mechatronic Stair Transporter for the Disabled

A numerical model of existing stair climber with its passenger was built and its operation was analysed through simulations. A modification of the stair climber has been developed on a basis of the simulation studies. The modification depends on equipping the device with additional controllable mechanism the function of which is to change the position of the passenger's centre of gravity. Comparative simulation studies were carried out for the standard version and the modified version of the stair transporter in a system for the dynamic.

Sergiy Lupenko, Nadiia Lutsyk, Yuri Lapusta
Cyclic Linear Random Process as a Mathematical Model of Cyclic Signals

In this study the cyclic linear random process is defined, that combines the properties of linear random process and cyclic random process. This expands the possibility describing cyclic signals and processes within the framework of linear random processes theory and generalizes their known mathematical model as a linear periodic random process. The conditions for the kernel are given and the probabilistic characteristics of generated process of linear random process in order to be a cyclic random process. The advantages of the cyclic linear random process are presented. It can be used as the mathematical model of the cyclic stochastic signals and processes in various fields of science and technology.

Tadeusz Kaczorek
Minimum Energy Control of Positive Time-Varying Linear Systems

The minimum energy control problem for the positive time-varying linear systems is formulated and solved. Sufficient conditions for the existence of solution to the problem are established. A procedure for solving of the problem is proposed and illustrated by a numerical example.

Shiv Manjaree, Bahadur Chand Nakra, Vijyant Agarwal
Comparative Analysis for Kinematics of 5-DOF Industrial Robotic Manipulator

This paper gives the kinematic analysis of a 5-DOF industrial robotic manipulator while considering wrist in motion. Analytical solutions have been obtained for forward kinematics and inverse kinematics to accurately position the end-effector of robotic manipulator in three dimensional spaces. For the first time, a hybrid neuro-fuzzy intelligent technique with two different membership functions has been studied and their performances are comparatively evaluated with analytical solutions. An experiment has been performed for a desired trajectory. It is seen that the results for the intelligent technique are reasonably in agreement with experiment. Also, the results obtained highlight the importance of selection of a particular membership function for robotic manipulators of industrial use.

Ihor Kuz, Olga Kuz, Heorgij Sulym
Stress- Strain State of Elastic Plate with an Arbitrary Smooth Notch

The paper contains comparing calculations of the stress fields in an elastic plate with notch along the arc of a circle, ellipse or parabola obtained by analytic method based on complex Kolosov-Muskhelishvili potentials and by numerical variation-difference method. These fields differ by no more than 2%, which, in particular, indicates the reliability of such numerical implementation. This discrepancy can be explained by the fact that in the analytical solution domain is unbounded, while the numerical calculation was carried out, obviously, for a finite field. The given stresses at the top of the notch along the arc of an ellipse or a parabola significantly increase with increasing of the relative depth of the notch (while increasing its depth or decreasing width).

Viorel Ungureanu, Dan Dubina, Andrei Crisan, Antonio Madeo, Giuseppe Zagari, Giovanni Zucco, Raffaele Zinno
Koiter Asymptotic Analysis of Thin-Walled Cold-Formed Steel Members

An imperfection sensitivity analysis of cold-formed steel members in compression is presented. The analysis is based on Koiter's approach and Monte Carlo simulation. If the modes interaction is correctly accounted, than the limit load and the erosion of critical buckling load can be easily evaluated. Thousands of imperfection can be analysed with very low computational cost and an effective statistical evaluation of limit performance can be carried out. The analysis is done on pallet rack uprights in compression, based on an intensive experimental study carried out at the Politehnica University of Timisoara.

Carlos M.N. Velosa, Kouamana Bousson
Robust Output Regulation of Uncertain Chaotic Systems with Input Magnitude and Rate Constraints

The problem of output regulation deserves a special attention particularly when it comes to the regulation of nonlinear systems. It is well-known that the problem is not always solvable even for linear systems and the fact that some demanding applications require not only magnitude but also rate actuator constraints makes the problem even more challenging. In addition, real physical systems might have parameters whose values can be known only with a specified accuracy and these uncertainties must also be considered to ensure robustness and on the other hand because they can be crucial for the type of behaviour exhibited by the system as it happens with the celebrated chaotic systems. The present paper proposes a robust control method for output regulation of chaotic systems with parameter uncertainties and subjected to magnitude and rate actuator constraints. The method is an extension of a work recently addressed by the same authors and consists in decomposing the nonlinear system into a stabilizable linear part plus a nonlinear part and in finding a control law based on the small-gain principle. Numerical simulations are performed to validate the effectiveness and robustness of the method using an aeronautical application. The output regulation is successfully achieved without exceeding the input constraints and stability is assured when the parameters are within the specified intervals. Furthermore, the proposed method does not require much computational effort because all the control parameters are computed offline.

Alexander Bogdanovich, Oleg Yelovoy, Leonid Sosnovskiy, Victor Komissarov, Sergey Tyurin
Local Damages During Rolling and Mechano-Rolling Fatigue for the Mechanical System Shaft – Roller (0.45 Carbon Steel – 25ХГТ Steel, 20ХН3А Steel – 20ХН3А Steel)

The report provides a description of local damages which are formed in the process of wear-fatigue tests. The analysis of local surface wave-like damages during rolling and mechano-rolling fatigue for the shaft-roller mechanical system under steady-state and multi-stage loading conditions is given. It is shown that the study of local wear-fatigue damage was made possible by new methods of testing and measuring wear-fatigue tests and damages, which are described in the report. New characteristics to estimate the parameters of the local wear-fatigue damage are proposed. The concept of local fatigue curves is introduced. The laws of local wear-fatigue damage for the shaft - roller system are analysed.

Wojciech Cieszyński, Michał Zięba, Jacek Reiner
Real time Trajectory Correction System of Optical Head In Laser Welding

Application of laser welding technology requires that the laser beam is guided through the whole length of the joint with sufficiently high accuracy. This paper describes result of research on development of optomechatronic system that allows for the precise positioning of the laser head's TCP point on the edge of welded elements during laser processing. The developed system allows for compensation of workpiece's fixture inaccuracies, precast distortions and workpiece deformations occurring during the process.

THE EXPERIMENTAL INVESTIGATION OF THE SCREEN OPERATION IN THE PARAMETRIC RESONANCE CONDITIONS

Łukasz BĄK*, Stanisław NOGA*, Feliks STACHOWICZ*

*Faculty of Mechanical Engineering and Aeronautics, Rzeszow University of Technology,
Al. Powstańców Warszawy12, 35-959 Rzeszów, Poland

lbak@prz.edu.pl, noga@prz.edu.pl, stafel@prz.edu.pl

received 15 May 2015, revised 10 December 2015, accepted 11 December 2015

Abstract: In this paper the experimental studies of the screen working in the parametric resonance condition are discussed. The investigations are conducted for laboratory parametric resonance screen. The measuring test is performed for four cases of tension force values. The full sheet metal instead of the sieve is used. For each considered case the natural frequency of the plate and the parameter modulation frequency are determined.The achieved results are presented and discussed. It is shown that the highest sieve plate amplitude is obtained when the parameter modulation frequency is two times larger than natural frequency of the sieve plate. This parametric resonance vibration was observed only for tension force equal to 4000 N because of the rotational speed limits of electrical vibratos.

Keywords: Vibrating Screen, Parametric Resonance, Natural Frequencies

1. INTRODUCTION

Vibro-impact mechanisms, such as screeners and drilling/cutting devices, are usually designed to operate in a resonance regime (RR) (Michalczyk, 1995). Then the most powerful energy flux can be achieved from the exciter to the vibrating component, and high oscillation amplitude of the target structure can be obtained using excitation of a relatively low intensity. Parametric resonance PR is the state of oscillating instability which can arise under periodic disturbance of a parameter of the structure, for example, under periodic variation of the pendulum length or the tensile force in a beam, plate or a flexible screen (Parszewski, 1992; Virgin, 2007).

The problem of the parametric resonance in mechanical systems is studied by numerous researches and development centres (Başar et al., 1987; Bąk et al., 2013; de Silva, 2005; Hagedorn and Koval, 1971; Michalczyk, 1995; Nguyen, 2013; Osiński, 1985; Parszewski, 1982; Slepyan and Slepyan, 2013, 2014). The parametric resonance phenomenon has been known since 19th century. For the first time, this phenomenon is described by Hill and Mathieu and can be found as the fundamental theory related to the vibration of the slender structures and the parametric resonance phenomenon (the so–called Hill or Mathieu equation (de Silva, 2005; Kaliski, 1996; Parszewski, 1982; Virgin, 2007)). The analysis of parametric vibration in the beam system including the Timoshenko theory is discussed by Hagedorn and Koval (1971).While the parametric vibration of a Bernoulli beam with constant transverse loading is analysed by Osiński (1985).In paper of Yang and Chen (2006), the problem of stability in transverse parametric vibration of axially accelerating beam is studied. In the consideration the Newton's second law and Boltzmann's superposition principle are used. The numerical method, based on a finite element discretisation, is proposed to solve the parametric resonance problem of a shell structures by Başar et al. (1987). Work of Nguyen (2013) deals with analysis of the parametric resonance of the simple supported rectangular plate by using the von Karman large-deflection theory. In general parametric resonance is undesirable effect in machines construction (for example in gear wheels cooperation, slender structures, and other) (Virgin, 2007). But in some cases, the parametric resonance phenomenon, allows to achieve higher performance processing.

A good example of confirmation, can be vibratory machines for screening and transport of aggregate (Bąk et al., 2013; Osiński, 1985). Free vibrations of the screen sieve, operation in the parametric resonance conditions, are analyzed in the paper of Bąk et al. (2013) by using analytical and numerical method. The simple dynamic model of the vibrating screen operating in the parametric resonance mode is proposed by Slepyan and Slepyan (2013, 2014). The proposed model includes two mass points connected by the prestressed string. Furthermore, in the above mentioned papers the description of the sample screen system working in the parametric resonance condition is presented. While in papers of Song et al. (2009) and Li (1995), new constructions of the vibrating screen working near resonance zone and chaotically excited are considered. Complex vibration analysis of the new type of large vibrating screen with hyperstatic net-beam structure is conducted in paper of Zhao et al (2009). Another analysis related to the motion of the sieve of the vibrating screen along the variable elliptical trace during screening processes is discussed by He and Liu (2009). This paper continues the recent authors investigations concerning the vibration of screen systems (Bąk et al., 2013). The present paper deals with the experimental investigations of the laboratory screen operating in the parametric resonance condition. The aim of these investigations is to determine the natural frequencies of the sieve and the parameter modulation frequencies (the excitation frequencies) as a function of the sieve tension force. Firstly, the description of the screen is presented. Then the results of the dynamical investigations are presented and discussed.

DOI 10.1515/ama-2015-0031

2. DESCRIPTION OF THE LABORATORY SCREEN

The laboratory parametric resonance screen (Fig.1) is made in accordance to the project based on the GEPARD-2 screen. GEPARD-2 screen was formerly designed by V. Slepyan from Loginov Partnership Mining Company in Kiev. All assemblies of the screen are mounted on the base frame which is composed of square profiles welded together.

The laboratory screen consists of the following assemblies and devices:

- sieve size: 700 x 750 mm x 1 mm,
- two electrical vibrators with eccentric mass control from 0 to 2.97 kN,
- four strain gauge sleeves connected with HBM QUANTUM X840 data acquisition system,
- two PCB model 353B14 accelerometer,
- laser speedometer with resolution 1 rpm,
- NI 9234 IEPE measuring module supported by the Signal Express software.

Fig. 1. Parametric resonance screen

Moreover in the experiment the PHANTOM V710 high speed camera is used. The total estimated weight of the screen system is 200 kg. In the presented investigations, the full sheet metal instead of the sieve is used. For each case the value of the tension force was established with using strain gauges sleeves which are mounted on the suspension bolt (Fig.2).

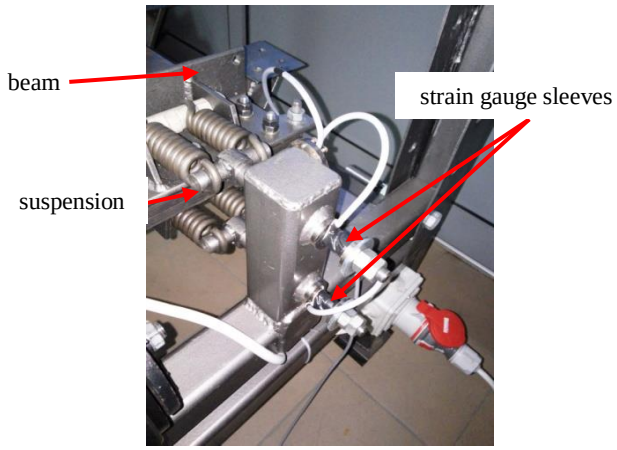

Fig. 2. The strain gauges sleeves assembly for tension force measurement

3. EXPERIMENTAL METHODS

As mentioned earlier, the experiment is performed for the plate without cut outs. The plate is made from 1 mm thickness spring steel sheet grade 1.8159 (Tab. 1).The plate is mounted between two beams of the screen with additional rubber pads for reducing plate bending stresses (Fig. 1).For estimation of tension force rough calculations were performed by using the string tension force equation:

$$F_t = 4f^2 l^2 P\rho \tag{1}$$

where: F_t – tension force, f – frequency, l– string length (plate width), P - string (plate) cross-section area, ρ - material density.

This formula has been proposed by Slepyan and Slepyan (2014) for preliminary adjustment of screen tension to obtain the resonant frequency equal 25 Hz. In this frequency the most efficiency screening is observed. The adjustment parameters which were applied during test are shown in Tab.2. For each adjusted tension force the resonant plate vibrations can be obtained by changing the rotational speed of electrical vibrators in the range of 2300÷3466 rpm. The eccentric masses are adjusted on 50% of nominal centrifugal force equal to 2972 N. By taking into account variable angular velocity of eccentric masses excitation force is calculated. Rotational speed data is measured by laser sensor and then converted to excitation frequency.

Tab. 1. Mechanical properties for spring steel sheet1.8159

Mechanical property	Value
Young modulus, GPa	210
Ulitimate tensile stress, MPa	590
Tensile Yeld stress, MPa	395
Elongation A_{50}, %	24
Denisity, g/cm^3	7.84

Tab. 2. Screen adjustment parameters

Tension force, N	Excitation force, N	Excitation frequency, Hz
4000	1571 / 2151	49.4 and57.8
4800	1818	53.13
5200	1913	54.5
6000	1987	55.55

Two PCB piezoelectric accelerometers with measurement range ±1000gare used to determine the frequency and vibration level. Voltage signal from the sensors is converted and collected as acceleration versus time data. Further signal processing is performed in MATLAB software by using Fast Fourier Transform functions(FFT) and Chebyshev filter.

Plate vibrations are recorded also by using high speed camera with speed rate 400 fps. This rate is sufficient to determine the mode shapes of vibrating plate and to observe the system behaviour.

4. RESULTS

The results of the plate vibration frequency are shown in Tab. 3. The first parametric vibration is observed when the plate

natural frequency to excitation frequency ratio is nearly equal to 0.6 in all respected cases. As the tension force increased the natural frequency for plate also increased what was expected (Fig. 3). Comparing the tension forces from rough calculations and from measurement test huge differences are observed. For this reason the equation of string tension cannot be used even for rough calculation of sieve natural vibrations. A small change of proper excitation frequency (±0.5 Hz) caused amplitude fading. The second parametric resonance is found when the rotational speed of vibrators increases. It is obtained for plate natural frequency to excitation frequency ratio equal to 0.5. This parametric resonance vibration was observed only for tension force equal to 4000 N because of the rotational speed limits of electrical vibratos. This result confirms the theory of parametric resonance that the primary parametric resonance appears when the frequency of parameter change is two times larger than the natural frequency of the system.

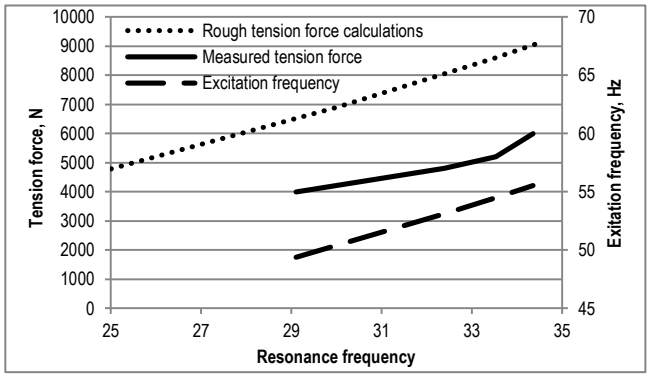

Fig. 3. Dependence among the tension force, resonance frequency and excitation frequency

Resonant frequencies of the plate are determined by analysis of the amplitude spectrum graphs (Fig.4). The highest peak in the graph demonstrates the resonant frequency of plate. In the graph for first parametric resonance there is also one high peak localized near frequency equal to 20 Hz (Fig.4a). This could be the effect of high amplitude screen beams vibrations which are observed during the test. Beams vibrations highly disturbed the plate motion and the screen work as well, which is confirmed by high speed camera record. For second parametric resonance there are no visible peaks close to plate resonant frequency (Fig.4b). The further peaks in high frequency level had no visible effect on plate vibrations. The screen operation is stabile and the beams vibrate with very small amplitude.

Tab. 3. Plate resonant frequencies

Tension force, N	Plate vibration frequency, Hz	Plate resonant frequency /excitation frequency ratio
4000	29.1	0.589 and 0.503
4800	32.4	0.61
5200	33.5	0.615
6000	34.35	0.618

Large differences between the first and the second plate parametric vibrations are clearly visible by taking into account the acceleration versus time graph (Fig. 5). The amplitude of the first resonant vibration (Fig. 5a) is less than 40 g and for second resonant vibration more than 80 g (Fig. 5b). Application of excitation frequency twice as large as the natural plate vibration resulted in more than twice vibration amplitude in comparison with the first parametric vibrations. This is important from the point of view of the screening efficiency. High vibration amplitude causes the vibro-impact occurrence. This phenomenon enable to screen the naturally wet fine granular materials (e.g., sand) by breaking glutted particles of material without additional water supply.

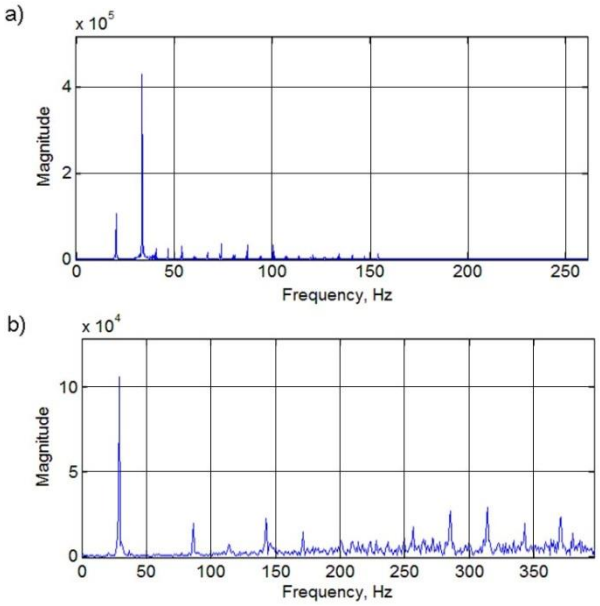

Fig. 4. Amplitude spectrum graphs: a) force tension: 5200 N, excitation frequency: 54.5 Hz; b) force tension: 4000 N, excitation frequency: 57.8 Hz

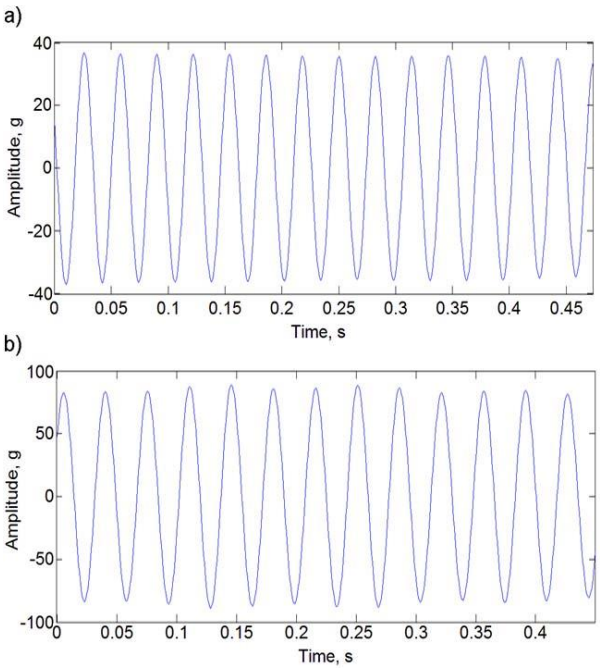

Fig. 5. Filtered acceleration versus time data for force tension 4000 N, a) excitation frequency: 49.4 Hz; b) excitation frequency: 57.8 Hz

Beside the vibrations amplitude level the mode shape of vibration is also very important. The first mode shape of plate vibration is observed in both excitation frequencies 49.4 Hz and 57.8 Hz

DOI 10.1515/ama-2015-0031

(Fig. 6). This confirms that the first natural frequency of a plate with tension equal to 4000 N is 29.1 Hz. For second parametric vibration large plate deformation is visible caused by large vibration amplitude (Fig. 6b).

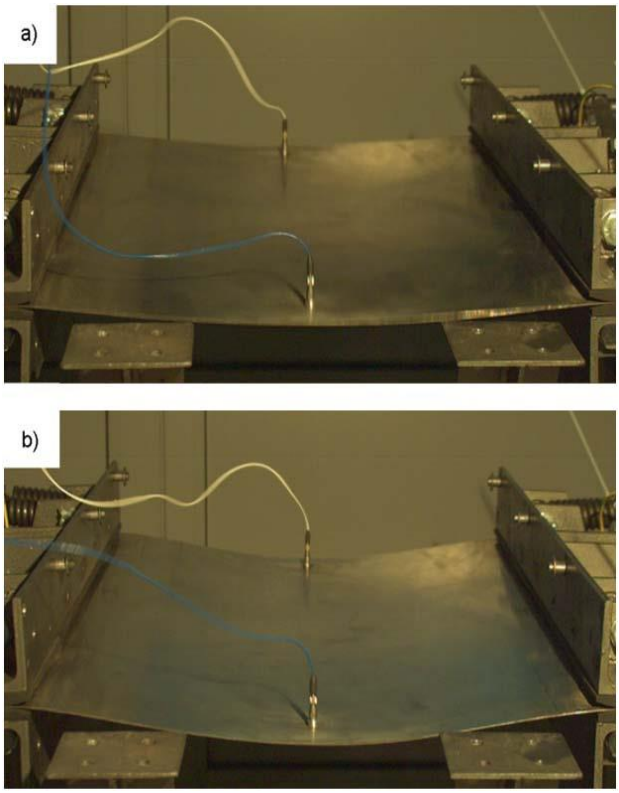

Fig. 6. Plate vibrations shapes (maximum deformation) for tension force 4000 N caught by high speed camera: excitation frequency: 49.4 Hz; b) excitation frequency: 57.8 Hz

5. CONCLUSIONS

This work deals with the experimental investigations of the laboratory screen operating in the parametric resonance condition.

In the experimental investigation, natural frequency of the sieve plate and parameter modulation frequency are determined for four cases of the tension force value. As it was expected the value of the sieve plate natural frequency and parameter modulation frequency grow parallel to the growing tension force.

The plate vibrations in parametric resonance conditions occurred for two resonant frequency to excitation frequency ratios - 0.6 and 0.5.Plate parametric vibrations for frequency ratio 0.6 characterise relatively low amplitude. High amplitude beams vibrations with frequency of 20 Hz were observed which disturbed the plate vibrations. The highest sieve plate amplitude is obtained when the parameter modulation frequency is two times larger than the natural frequency of the sieve plate.

The experimental approach demonstrated in this paper can be used for the case with the real sieve and for further investigation related to the screening process.

REFERENCES

1. **Başar Y., Eller C., Krätzig W.B.** (1987), Finite element procedures for parametric resonance phenomena of arbitrary elastic shell structures, *Computational Mechanics*, 2, 89-98.
2. **Bąk Ł., Noga S., Skrzat A., Stachowicz F.** (2013), Dynamic analysis of vibrating screener system, *Journal of Physics: Conference Series*, 451, 012028.
3. **de Silva C.** (2005*), Vibration and shock handbook*, Taylor & Francis, Boca Raton.
4. **Hagedorn P., Koval L.R.** (1971), On the parametric stability of a Timoshenko beam subjected to a periodic axial load, *Ingenieur - Archiv*, 40, 211-220.
5. **He X.-M., Liu Ch.-S.** (2009), Dynamics and screening characteristics of vibrating screen with variable eliptical trace, *Mining Science and Technology*, 19, 0508-0513.
6. **Kaliski S.** (1996*), Vibrations and waves in solids*, IPPT PAN, Warsaw (in Polish).
7. **Li Z.** (1995), Chaotic vibration sieve, *Mechanism and Maschine Theory*, 30, 613-618.
8. **Michalczyk J.** (1995), *Vibrating machinery, dynamic calculatons, vibration and noise*, WNT, Warsaw (in Polish).
9. **Nguyen H.** (2013), Simultaneous resonances involving two mode shapes of parametrically-excited rectangular plates, *Journal of Sound and Vibration*, 332, 5103–5114.
10. **Osiński J.** (1985), The analysis of parametric vibrations of continuous systems with constant transversal loading by asymptotic method and finite elements, *Journal of Theoretical and Applied Mechanics*, Vol. 2, No. 23, 241-254 (in Polish).
11. **Parszewski Z.** (1982*), Vibration and dynamics of machines*, WNT, Warsaw (in Polish).
12. **Slepyan L.I., Slepyan V.I.** (2013), Modeling of parametrically excited vibrating, *Journal of Physics: Conference Series*, 451, 012026.
13. **Slepyan L.I., Slepyan V.I.** (2014), Coupled mode parametric resonance in a vibrating screen model, *Mechanical Systems and Signal Processing*, 43, 295-304.
14. **Song Y., Jiang X.-H., Song J., Zhang J.-X.** (2009), Dynamic analysis of a chaotic vibrating screen, *Procedia Earth and Planetary Science*, 1, 1525-1531.
15. **Virgin L.N.** (2007), *Vibration of axially loaded structures*, Cambridge University Press, Cambridge.
16. **Yang X.-D., Chen L.-Q.** (2006), Stability in parametric resonance of axially accelerating beams constituted by Boltzmann's superposition principle, Journal of Sound and Vibration, 289, 54–65.
17. **Zhao Y.-M., Liu Ch.-S., He X.-M., Zhang Ch.-Y., Wang Y.-B., Ren Z.-T.** (2009), Dynamic design theory and application of large vibrating screen, *Procedia Earth and Planetary Science*, 1, 776-784.

Acknowledgments: This work was supported by the European Research Agency - 7th FP PEOPLE PROGRAMME Marie Curie Industry-Academia Partnerships and Pathways, grant agreement No. 284544

FLUIDIC GENERATOR OF MICROBUBBLES – OSCILLATOR WITH GAS FLOW REVERSAL FOR A PART OF PERIOD

Václav TESAŘ*

*Institute of Thermomechanics v.v.i., Academy of Sciences of the Czech Republic, Dolejškova 1402/5, 182 00 Praha 8, Czech Republic

tesar@it.cas.cz

received 10 June 2015, revised 11 December 2015, accepted 14 December 2015

Abstract: Paper presents a fluidic device developed for generation of small (less than 1 mm in diameter) microbubbles in a liquid from gas passing gas through small passages. Until now the bubbles are larger than the size of aerator passage exits so that making the passages smaller did not result in obtaining the desirable microbubbles. Analysis of high-speed camera images (obtained with a special lens of large working distance) have shown show that the large bubble size is caused by slow ascent motion of very small bubbles so that they get into mutual contact and grow by conjunction. The solution is to pulsate the supplied gas flow by a no-moving-part fluidic oscillator. The generated small bubble is moved back into the aerator passage where it is for a part of oscillation period protected from the conjunction with other, previously generated microbubbles.

Keywords: Fluidics, Oscillators, Microbubbles, U-Tube Resonator

1. INTRODUCTION

An important development has been recently taking place in areas of engineering working with gas bubbles in liquids. The key factor is introduction of energetically efficient generation of microbubbles, of diameter less than 1 mm (Rodríguez-Rodríguez et al., 2015) – but larger than 1 μm so that they should not be confused with differently behaving smaller nanobubbles (Prevenslik 2011, Zimmerman et al., 2011). Microbubbles can intensify and accelerate several processes.

1.1. Applications and importance of microbubbles

An area in which microbubbles have already demonstrated their intensification capability are processes that depend on diffusion transport of gas into liquid. The large total surface of microbubbles, together with longer diffusion time (due to low microbubble ascent velocity), lead to unprecedented high transfer rates. A typical example of the intensification is the increased transfer of oxygen into the liquid in waste water processing (Terasaka et al., 2011, Rehman et al., 2015, Rawat et al., 2011). The decomposition of organic waste is actually done by aerobic bacteria, the metabolism of which is roughly 90% more intensive than that of anaerobic ones. Aeration to provide the aerobic bacteria with the oxygen they need is the most energy consuming activity in waste water treatment plants. The improvement achieved by microbubbles enhances substantially the overall efficiency of the treatment process.

An increase in effectiveness was also demonstrated in the use of microbubbles for separation of substances by flotation (Coward et al., 2015, Hanotu et al., 2012, 2013). Microbubbles, by their strong clinging to contaminants like oil or grease, make possible efficient and environmentally friendly removal of fats in product cleaning. Microbubbles also exhibit a remarkable washing effect without chemical detergents. For example, Watanabe et al., (2013) describe use of microbubbles for de-contamination of silicon wafers. Microbubbles were also demonstrated by Xi (2012), to be efficient for disinfection by removal of pathogens. Coward et al., (2015) demonstrated efficient flotation harvesting of algae grown in bioreactors for producing biofuels.

In food industry microbubbles can extend shelf life of products of foamy character – whipped cream, ice-cream, sorbets, and mousses – in addition giving them interesting taste properties. Microbubble foam was demonstrated to remain stable for up to a year. Also of interest for food industry is water evaporation ability of microbubbles (Zimmerman et al., 2013) without the heat reaching the dried product.

Hydrodynamic resistance of ships may be reduced by air microbubbles, as demonstrated by McCormick and Bhattacharyya already in 1973 having shown a 30% reduction in friction drag. Their lack of further progress was due to inefficient generation of microbubbles -- by electrolysis, needing more energy than was saved in vessel propulsion. This problem of energetically efficient microbubble generation plagued also other similar attempts, including those able to show reductions by up to 80 % (Bogdevich et al., 1978; Madavan et al., 1984). Recent tests with microbubbles were made with very large models (Watanabe et al., 1998; Moriguchi and Kato, 2002; Yanuar et al., 2012), at Reynolds numbers near to those of practical use. Of interest to process engineers is analogous decrease of friction in tube flows (Pang et al., 2014, Shams et al., 2014)

A wide and increasing spectrum of microbubble uses is currently in medicine. Microbubbles can convert energy of ultrasonic vibration into a local thermal therapeutic effect (Kanagawa, 2013). Streaming effect on microbubbles in ultrasonic field can destroy

DOI 10.1515/ama-2015-0032

cells (Kooiman et al., 2011) and can cause their outer membranes to become permeable for drugs (Oh et al., 2014) particularly anti-cancer ones (Watanabe et al., 2008). Microbubbles are also used in measuring absolute blood pressure (Tremblay-Darveau et al., 2014).

Many currently developed uses of microbubbles aim at use in microfluidics. They are used in gene manipulation (Sun et al., 2014), biosensors (Kuznetsova and Coakley, 2007), mixing of reactants for chemical reaction (Lee et al., 2012) or sorting (Wang, 2012). Important progress is also being done in optofluidics, where ordered arrays of microbubbles can create tuneable optical components (Hashimoto et al., 2006; Allouch et al., 2014).

The most important current problem of geopolitics is the distribution of cheap crude oil sources in individual parts of the world. The sources are in politically unstable regions, e.g., in Near East, but absent in the areas of most consumption (Europe, North America). A solution is envisaged in producing liquid fuels from lipids in algae (Lam and Lee, 2012; Leite et al., 2013; Kargbo 2010). The processes used actually simulate the way by which fossil crude oil was produced 300 million years ago. Decisive factor for success of this idea is increasing the economy of all algae growing and processing steps. One of these steps, seemingly secondary but in fact quite important, is supplying CO2 which algae need for photosynthesis. In photobioreactors. This is done by bubbling the gas through the algae-containing liquid column (Hu et al., 2015), where an improvement of the diffusion transport by CO_2 microbubbles may be an essential enhancement. Another perhaps less obvious effect achieved by the gas bubbles in bioreactors is removal of O_2 produced by the algae. Oxygen is an inhibitor to microalgae growth and at saturation level it is toxic. Zimmerman et al. (2011) demonstrated that O_2 removal leads to much higher algae growth rates.

1.2 New microbubble generation method

In view of the above list of promising microbubble uses (by far not complete), there is no wonder interest in them has been propagating rapidly. Many advantages were actually obvious already earlier, but there was the hindrance of low microbubble generation cos. Considering the water containing environment it has been also desirable to avoid in the microbubble generator any operations by electric current.

The simplest and seemingly fail safe generation method is percolating the gas through an aerator – a body having a large number of parallel exit channels of very small cross section areas. Experience with this approach, however, were generally a failure. As demonstrated in the example Fig. 1, the bubbles obviously tend to grow far beyond the size of aerator exits.

A promising new solution was recently found (Tesař, 2007; Zimmerman et al., 2008) in pulsating the gas flow supplied into the aerator. Especially attractive is using for this purpose a no-moving-part fluidic oscillator - robust, inexpensive, with long life, high reliability, no maintenance demands, and operation without driving electric current. The oscillator is practically nothing more than just a special shaping of the gas (air) aerator entrance. Practical results obtained were, however, rather uncertain. Some experiments have demonstrated successful microbubble production — while in other attempts this approach failed. The main obstacle in the way towards success has been the lack of understanding the bubble generation mechanism and the way it is influenced by the fluidic oscillation. Initially, attempts focused on fragmentation effect, which is known to generate in the analogous (but, of course, inverse) problem of small liquid droplets in air (James et al., 2003; Tesař, 2014). Efficient action of the oscillation on a fragmented bubble requires applying it at natural resonant frequencies of the resultant microbubbles. These frequencies are, however, very high – in the kilohertz range, which obviously are not the frequencies at which the fluidic oscillators in the performed tests operated — which were typically 100 Hz to 200 Hz. Higher frequencies are, in principle achievable, but designing fluidic oscillators for the kilohertz range (at reasonably large size) is far from easy. Evidently, the successful cases excited (Tesař, 2013b) higher harmonics of the basic frequency.

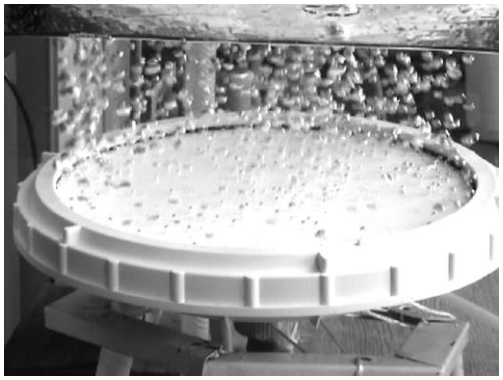

Fig. 1. An example of a typical present-day no-fluidics aerator in operation (supplied by Pfleiderer water systems GmbH, Germany). Air passes through pores of equivalent diameter 120 μm, between sintered polyethylene spheres. Bubbles are generated at only a few exits — due to the phenomenon called instability of parallel bubble formation (Tesař 2007) — and are very large: the Sauter mean 5.7 mm bubble diameter evaluated in this picture is 47-times larger than the equivalent diameter of pore exits

2. HIGH-SPEED-CAMERA IMAGE STUDIES

Because of the absence of reliable information about generation of microbubbles, author (Tesař, 2013a) begun series of experimental studies in an attempt to understand the mechanism. All previous researchers so far were satisfied in their studies of bubble (and microbubble) formation with visual observations or images obtained using a standard-speed camera. However, the repetition rates of microbubble formation are often very much higher – of the order 10^2 Hz – than what can be visually captures. Author was able to use for his study of microbubble formation a high-speed camera, capable of taking images at 4000 frames per second or more – the limiting factor being the available light that had to be focused onto the very small millimetre-sized picture scene. The key component of the image taking was a long-distance macro-lens Machine Vision “Navitar” 12X. This made possible photographs of sub-millimetre objects from a distance as large as 100 mm from the front lens. This allowed taking the high-speed video sequences from outside of the water tank, through its glass walls. Also, this special lens made possible clear recognition of details at extremely small distances from the exits of the aerator passages. It was in particular the phenomena observed in this region that provided an explanation to the apparent paradox of the microbubble diameters much larger than the equivalent diameter

of the aerator passage exit (Tesař, 2013a).

The explanation was found in conjunctions of freshly formed microbubbles – merging a certain number of microbubbles to form a single much larger bubble. The key factor is the fact that ascent velocity of bubbles decreases rapidly with decreasing size. Microbubbles move so slow they do not get far from the passage exit before the next, follower microbubble appears, gets into touch with the already present one, and merge with it. The merging is favoured from the energy point of view – some energy is released as is seen from the following consideration of a spherical bubble of diameter d_j has volume:

$$V = \frac{\pi}{6} d_j^3 \tag{1}$$

and its surface area is:

$$F = \pi d_j^2 \tag{2}$$

so that its surface energy is:

$$E = \pi d_j^2 \sigma \tag{3}$$

where σ[N/m2] is the surface tension.

Conjunction of two equal-sized bubbles of diameter d_j thus results in a single bubble of diameter dc and volume:

$$V_c = \frac{\pi d_j^3}{3} = \frac{\pi d_c^3}{6} \tag{4}$$

and hence surface area:

$$F_c = \pi d_c^2 = 2^{\frac{2}{3}} \pi d_j^2 \tag{5}$$

while the total surface of the two small pre-conjunction primary microbubbles was:

$$F_{total} = 2\pi d_j^2 \tag{6}$$

This was $2^{(-\frac{1}{3})} = 0.794$-times larger. Thus, there is energy:

$$\Delta E = (2 - 2^{\frac{2}{3}}) \pi d_j^2 \sigma \tag{7}$$

released during this conjunction. It is not small – its magnitude is more than one fifth of the available total sum of surface energy of the two pre-conjunction microbubbles. The energy eq. (7) is dissipated by viscous effects during the strong oscillation that takes place immediately after the conjunction. Analysis of high-speed camera images has shown, as documented in the example presented in Fig. 2, that the after-conjunction oscillating motion effectively stops the upwards motion of the larger bubble formed in the process. This larger bubble thus stays for some time practically at the same height above the aerator top surface – and, as a result, inevitably takes place in another conjunction with the subsequently formed next bubble. In the example presented in Fig. 2 there were five microbubbles taking part in the four conjunctions A, B, C, and D before the resultant bubble was finally released and moved away. In other observed cases the number of repeated conjunctions was even much higher. Note in Fig. 2 that all this happened at very small distances – merely around 0.2 mm - above the aerator exit and the conjunctions followed one another at ~ 6 millisecond intervals. Both the position and speed made it impossible to watch the processes visually. No wonder the phenomenon has so far escaped attention of earlier researchers.

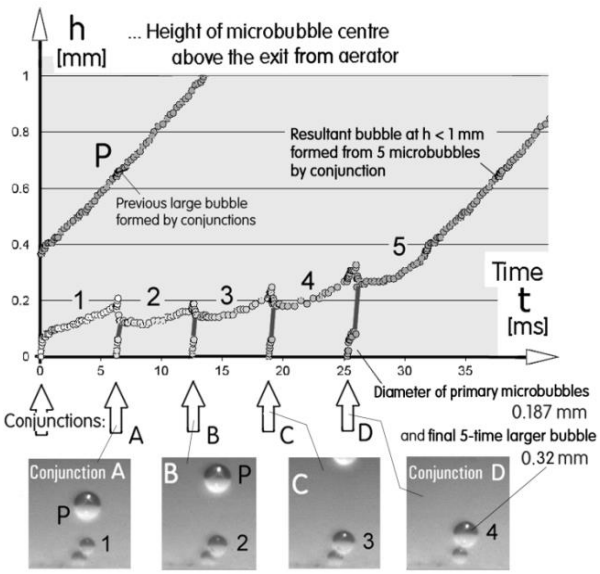

Fig. 2. An example of high-speed camera images (bottom) of freshly produced microbubbles 1, 2, 3, 4, and 5 – and a diagram of evaluated heights h above the aerator exit as a function of time *t*. Microbubbles move upwards so slowly that they get into contact and subsequent conjunction with the next, later generated microbubble. The conjunctions may be repeated several times before the microbubble is finally released

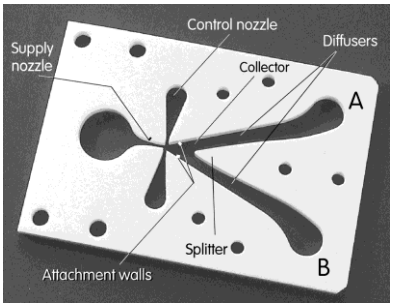

Fig. 3. A typical example of a fluidic amplifier (Tesař, 2009) of the jet-deflection type. When provided with suitable de-stabilising feedback loop channels it may be the essential part of a fluidic oscillator

3. STANDARD FLUIDIC OSCILLATORS

3.1. Amplifier and feedback loop

According to Zimmerman et al., 2008, the bubble growth caused by the conjunctions may be eliminated if the gas flow is pulsed, preferably by a fluidic no-moving-part oscillator. The problem that remained was the uncertainty: sometimes the pulsation did help, sometimes not. The reason is in the character of the action of the oscillator.

The self-excited fluidic oscillators in general use the hydrodynamic instabilities in the flowfield. There is a large number of alternative possibilities how to create the instabilities. Most often used are version consisting (Tesař, 2013b) of two components. The first component is a fluidic amplifier – a device responding by large changes of the conditions in its output terminal to a rather weak control fluid flow into its input. The second component are destabilising negative feedback loops connecting the amplifier inputs and outputs, Fig. 4.

DOI 10.1515/ama-2015-0032

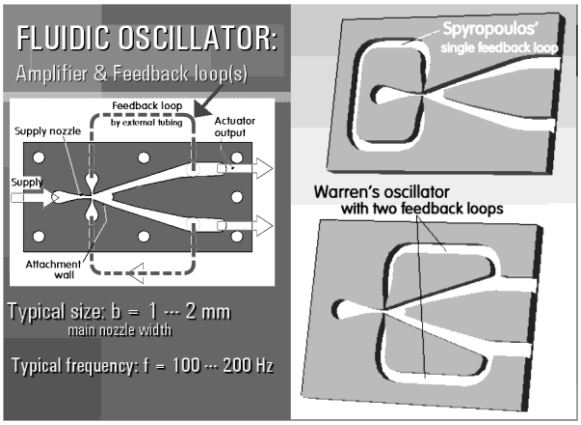

Fig. 4. Usual versions of fluidic oscillators with two alternative layouts of feedback loops, both invented in the 1960's by Warren. These oscillators sometimes did produce microbubbles – but sometimes did not. To discover the reasons, author investigated the mechanism of bubble formation using a high-speed camera

An example of typical amplifier is presented in Fig. 3. It shows the main plate in which are made cavities for air flows. In operation, the cavities are closed by being covered by flat top and bottom cover plates. The amplifier shown is of the jet-deflection Coanda-effect bistable type. At left in Fig. 3 is supply nozzle into which is fed a constant flow of air. This flow leaves the supply nozzle as a jet issuing into the cavity between two mutually opposed attachment walls. The apex angle of these two walls is so large that the jet cannot follow both. Instead, by a phenomenon known as the Coanda effect, the jet attaches to only one attachment wall — and is led through one of the two diffusers into either A or B output terminal, seen at the right-hand side of the picture. On each side of the supply nozzle exit in Fig. 3 there are control nozzles. Air flow admitted into one of these nozzles – the one at the side to which the jet is attached - causes the main jet (the one leaving the supply nozzle) to switch from the ON one attachment wall to the other, opposite one that was so far in the OFF state.

Converting a fluidic amplifier into an oscillator is achieved by the feedback loops. Two most popular loop versions are presented in Fig. 4. Both lead to a de-stabilising effect: if the flow passes through the amplifier in Fig. 3 to the terminal A, then a signal is fed into the control nozzle on the same. This switches – after a certain time delay - the main jet flow into the other terminal B. The roles of the terminals are then exchanged and this is a beginning of another oscillation period.

It should be noted that the Coanda-effect attachment of the main jet to the attachment wall requires a low resistance load connected to the amplifier output terminals. If the flow through e.g. the terminal A encounters a high-resistance loading (e.g., is to pass through a connected device with small channel cross sections), the Coanda effect fails to keep the main jet deflected. If there is no such load connected to the other output terminal, the jet switches to that easier flow path – and becomes attached to the other attachment wall. The load-switched fluidic amplifiers therefore need no control nozzles.

3.2. Flow reversal caused by jet pumping

It is useful to note that the main jet (as all jets do, especially if their Reynolds number is high enough so that the flow is turbulent) entrains the air from its surrounding space and carries it away. Let us assume that the jet leaves the amplifier through the output terminal A in Fig. 3. Its entrainment action removes the surrounding fluid from the amplifier – where it is replaced by a suction inflow into the amplifier body through the other terminal B. This suction effect of the ON jet flow acting in the other, OFF terminal is called jet-pumping.

If the amplifier is provided with the feedback and oscillates, this jet-pumping effect generates in its output terminals an alternation of suction and blowing, each for a part of oscillation period. This temporary flow reversal, however, requires low-resistance loads connected to the terminals. The lack of success some microbubble researchers encountered with their fluidic oscillators was due to the high resistance of their aerators (too small and too long passages). What took place instead of the jet pumping was spillover flow of periodically varied intensity through the OFF terminal. The adjustment of the oscillator and load for their proper collaboration requires a matching similar to the one discussed in Tesař (2009).

4. SUPPRESSING THE CONJUNCTION BY THE OSCILLATOR

4.1. High-speed camera images of successful cases

For the studies of processes at (as well as in) the aerator passages was designed a laboratory model aerator with well ordered passages, made by drilling (rather than the chaotically arranged passages usually made by sintering of small particles, as is the example case shown in Fig. 1). The organised aerator layout is, of course, amenable to better description and study. In the model aerator there was a set of parallel drilled holes. To avoid expected problems with breaking the very small drill bits, the holes were of relatively large, 0.6 mm diameter – Fig. 5. Also, to make the process of microbubble generation easily adjustable, the fluidic oscillator was for this study replaced by a pulsation generator with a generator of harmonic electric signal and a loudspeaker.

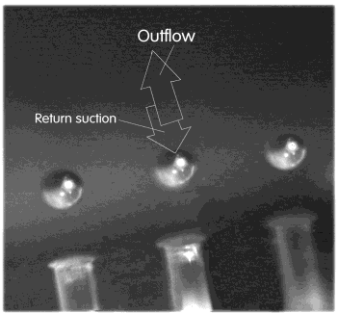

Fig. 5. An example of high-speed camera images of freshly produced microbubbles that just left the row of 0.6 mm diameter aerator passages. The conjunctions shown in Fig. 2 were in this case eliminated because the used oscillator caused flow direction reversal for a part of the cycle. Thus the newly formed microbubbles having returned into their aerator passage are protected from contact with the microbubble previously made

Successful generation of microbubbles with this model is seen in the microphotograph in Fig. 5. The amplitude of the oscillation was so large that the microbubble motion was not at all dependent upon the small steady ascent velocity. Instead, the microbubble motion was governed by a mechanism similar to the processes

in a synthetic jet (Trávníček et al. 2007, Tesař 2007): entrainment of fluid near to the exit and a rectified one-direction flow at larger distances. The freshly produced microbubble after its emergence from the aerator is in the subsequent part of the oscillatory period sucked back into the aerator passage — while its predecessor microbubble at a larger axial distance from the passage exit is not influenced by the suction a and moves away. The motion is governed by the inertia of water also moved (this water gets into the aerator passage during the previous suction part of the cycle from locations near to the passage exit.

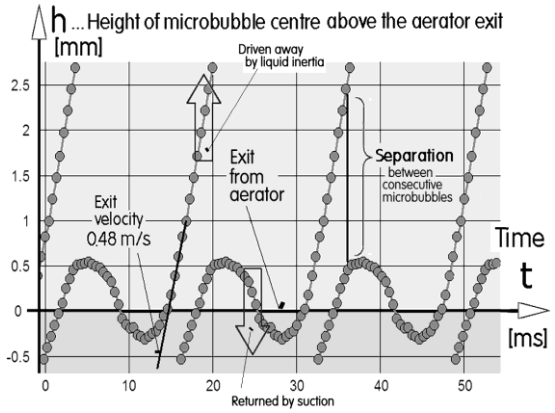

Fig. 6. Height vs. time trajectories of freshly formed microbubbles seen in Fig. 5 – i.e. those influenced by the temporary flow reversals caused by the jet-pumping in the fluidic oscillator

The model generated small microbubbles of the diameter 0.6 mm, the same as that of the passage exits – and very much smaller than the typical bubbles obtained with contemporary steady-flow aerators (Fig. 1). The generation of microbubbles was also studied by analysis of high-speed camera images (analogous to those described above in Section 2 for the steady, non-pulsating air flows). With the applied pulsation, there were no observable microbubble conjunctions. It was soon found that this absence of conjunctions (which keeps the bubbles small) is due to the temporarily reversing character of the flow direction in the aerator passages. The reversal is seen in the time history diagram presented in Fig. 6. The pulsation amplitude is seen to be so large that during a part of the oscillation cycle the suction moving the microbubble back into the aerator passage prevents it from getting in touch with the previously generated ones. Also of importance is the suction of the water from the vessel into the passage – as is shown e.g. in the regime C in Fig. 7. In the following part of the oscillation cycle this water column from the passage is expulsed, together with the microbubble. It is essential to note that the density of the bubble is roughly three orders of magnitude smaller than density of water. It would be therefore wrong to think about acceleration of the bubble. Instead, it is the water column inside the aerator passage that is accelerated (in the regime D in Fig. 7). Its inertia moves it together with the microbubble quite far from the aerator. This way is suppressed the effect of the small ascent velocity and consequent mutual contact that without oscillation leads to the conjunctions.

It should be noted that the diagram in Fig. 6 shows the vertical position of the bubble centre as a function of time. The lines connecting in Fig. 6 the locations of the microbubble centres may suggest that the microbubbles having left the passages are not particularly much separated in space in the horizontal direction. This would be a wrong impression, on the horizontal co-ordinate is time. What really influences the possibility of the mutual conjunctions are the vertical separations of the bubbles – and these separations are large.

4.2. Failures caused by improper loading the oscillator

With this demonstrated elimination of conjunctions – and the clear explanation of the elimination phenomenon – it became a question why the positive results were obtained only in some tests. The reason was found in disappearance of the jet-pumping phenomenon if the oscillator is loaded by high hydraulic resistance.

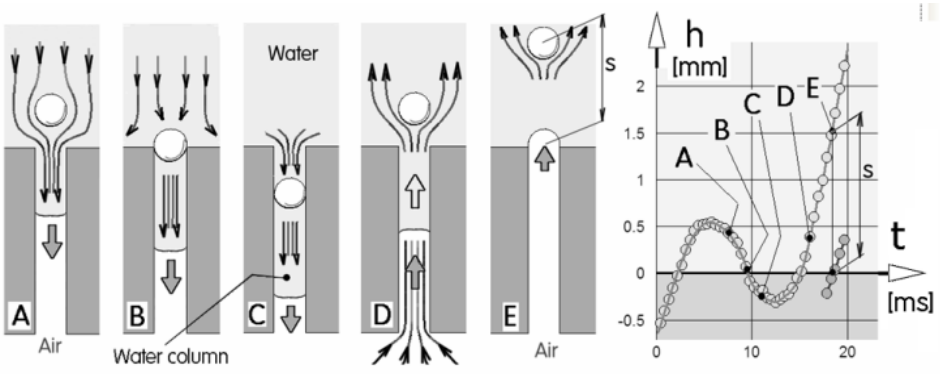

Fig. 7. The states from A to E eat left show schematically the water pathlines and positions of a microbubble and water column during the oscillation cycle – the instants are identified in the diagram from Fig. 6.

In the successful tests discussed in Section 4.1 the jet pumping did occur due to two factors. First, the used oscillator was quite small in relation to the rather large aerator's drilled passages. The aerator thus represented a low-resistance load. Second, the hydrostatic pressure acting on the submerged aerator passage exits did not add much to the loading because - for easier observation - the aerator was placed to only a small depth under the water surface. These two favourable factors disappeared in the unsuccessful tests with larger amplifiers (the size chosen for generating more microbubbles) and aerators with relatively long, tortuous passages positioned in the usual large depths.

DOI 10.1515/ama-2015-0032

5. ELIMINATING THE CONJUNCTIONS

5.1. Fluidic circuit with jet pump and accumulator

The solution that made the reverse flow for a part of oscillation cycle reliably present was provided with the fluidic oscillator designed specifically for generation of micro-bubbles. It is a subject of author's recent patent application (Tesař, 2015). The flow reversal in this device does not depend on the rather weak, generally unreliable and sometimes non-reproducible effect of jet pumping inside the amplifier. Instead, the return flow is driven by energy of air accumulated inside a fluidic accumulator, which is a part of the circuit. Also, this available driving effect is employed in an efficient, full-scale jet pumping.

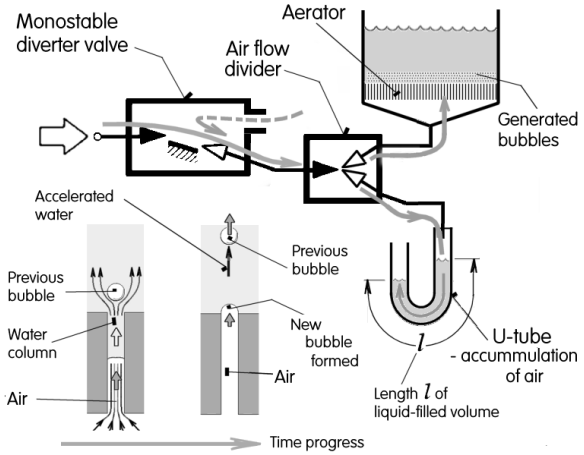

Fig. 8. Schematic representation of the fluidic generator according to the author's patent application (Tesař, 2015). The two details drawings in the bottom left are the cases D and E from Fig. 7. They show the character of the flow in an aerator passage in the half-period characterised by generation of the microbubbles

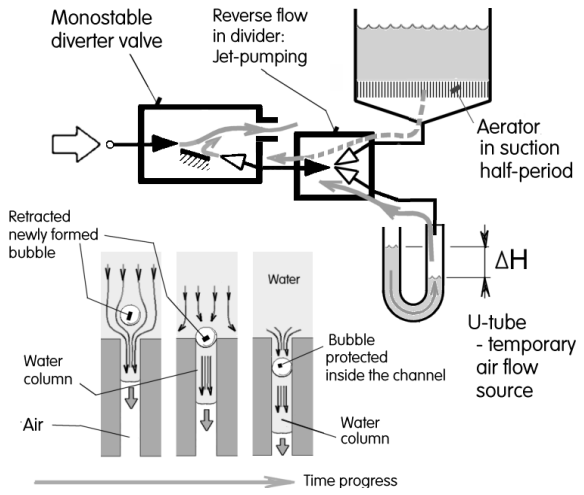

Fig. 9. Schematic representation of the same generator as in previous Fig. 8 - here, however, showing the half-period of air flow back from the water tank into the aerator passages

In one of its simplest versions the new layout is presented schematically in Figs. 8 and 9. The air flows are there indicated gray arrows. The components of the schematically presented devices are nozzles, drawn as black (fully filled) triangles, — and diffusers, drawn schematically as white (not filled) triangles. The first picture, Fig. 8, shows the arrows in the expulsion half-period, i.e. in the part of the cycle during which air is percolated through the aerator passages into the water in a large vessel, with the aerator at its bottom. The other Fig. 9 shows the air flow arrows in the other, suction half-period. In both pictures in their left-hand lower part are added the corresponding representations of the flow in the aerator passages from Fig. 7.

The air supplied into the microbubble generator comes first into a device drawn in the upper left corner of the circuit. It is a load-switched monostable diverter. In principle it may be described as akin to jet-deflection type fluidic diverter amplifiers discussed in Section 3 – the difference being in there being only one attachment wall and also in the absence of control nozzles. This device is switched by the load-switching effect discussed above. The monostability means that the air jet generated in the supply nozzle tends to attach always to the single attachment wall. There is also only one output terminal – apart from it, there is in this device a vent outlet, connecting the internal cavities of the device with the atmosphere outside.

The other part is the jet pump device, located in the centre of the picture. It possesses one nozzle and two diffusers, with their smaller cross section ends at the nozzle. The nozzle is connected to the output of the diverter device. One output terminal of the jet pump (i.e. the larger cross-section end of the diffuser) is connected to the aerator at the bottom of the water-filled vessel. The other output terminal is connected to the fluidic accumulator. There are many alternative designs of fluidic accumulators. The one chosen for schematic presentation in Figs. 8 and 9 is the U-tube with two vertical columns – one of them open into atmosphere.

In the situation presented in Fig. 8, air jet issuing from the supply nozzle at left attaches to the attachment wall and is guided into the nozzle of the jet pump – which in this regime does not operate as a jet pump at all — its role may be described as divider, dividing the supplied ait flow into two output flows. The dashed arrow line passing through the vent outlet of the diverter indicates that there may be some jet pumping suction effect. It is an effect, however, which is here unimportant; the discussed fluidic circuit is capable of performing its task even if the pressure inside the device is higher than atmospheric and some air actually leaves the cavity through the vent as a spillover flow.

One of the output flows leaving the exits of the jet-pump /f low-divider progresses to the aerator where it generates the small bubbles. The flow from the other exit continues into the active arm of the U-tube, where it gradually pushes down the water level. This, of course, is associated with rising water level in the other arm. Thus the pressure in the active arm gradually increases and finally reaches the level at which the load-switching occurs in the monostable diverter valve.

After the switching, the air jet in the diverter separates from the attachment wall – as shown in Fig. 9 – and leaves through the vent into atmosphere. This is the beginning of the other half-period. Between the both arms of the U-tube now exists the pressure difference:

$$\Delta P = g\Delta H, \tag{8}$$

where g = 9.81 m/s^2 is the gravitational acceleration. This difference drives the air away from the U-tube into the jet pump/ divider which now behaves as the usual jet pump, i.e. entrains the air

from the aerator and takes it along to the switched divider. . There this return flow prevents the main air jet from attaching to the attachment wall (i.e. keeps the air flow deflected into the vent). This is the desirable regime with removal of the freshly made microbubbles back into the aerator passages. Of course, as the time progresses, the height ΔH (as well as ΔP, eq. (8)) in the U-tube decreases. Finally the influence of this flow from the U-tube accumulator ceases completely. There is no more the reverse flow that could maintain the main air jet in the monostable diverter separated from the attachment wall. The jet clings back to the wall — and the next oscillation cycle may begin.

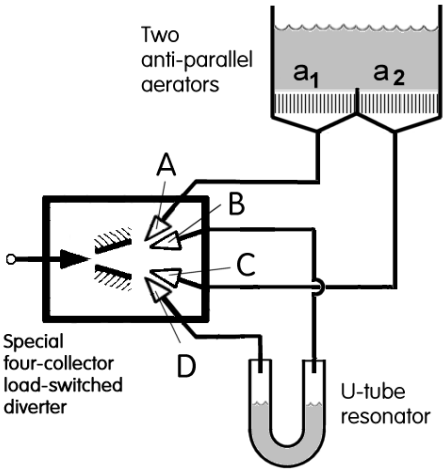

Fig. 10. Schematic representation of the double-acting fluidic generator of microbubbles with prevention of the conjunctions. The diffusers A to D are the ones presented in Fig. 11

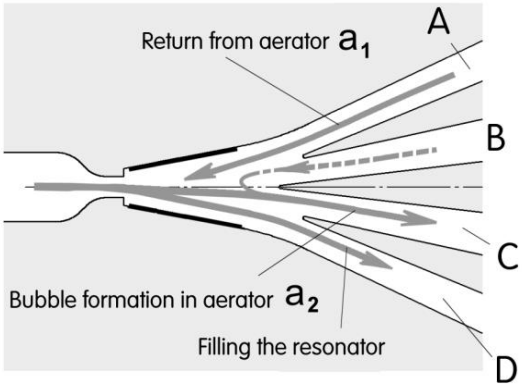

Fig. 11. Interaction cavity of the special diverter with four collectors A to D. Grey arrows indicate the character of air flow in the half-period of formation of microbubbles in the aerator a_2

The periodic switching between the two regimes is in tune with the oscillatory motions of the liquid in the U-tube – the frequency of which is:

$$f = \frac{1}{2\pi}\sqrt{\frac{g}{l}}, \tag{9}$$

where l is the length of the liquid column in the U-tube, as shown in Figs. 9, 14.

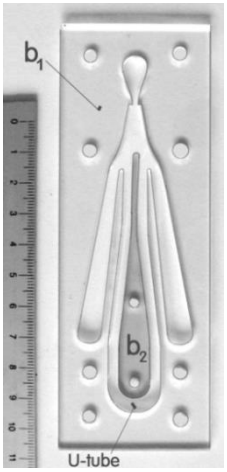

Fig. 12. Photograph of the two components (b_1 and separate inner component b_2) of the laboratory model of the double-acting microbubble divider — which now really operated as the jet pump. From there it generator with integral U-tube resonator. The air and water flow cavities were laser-cut in 3 mm thick polymethylmethacrylate plate

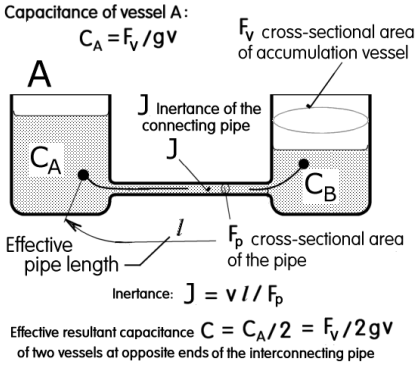

Fig. 13. The principle of the CJC oscillator: two accumulation cavities (of capacitance values CA and CB respectively) are connected by a pipe of inertance J

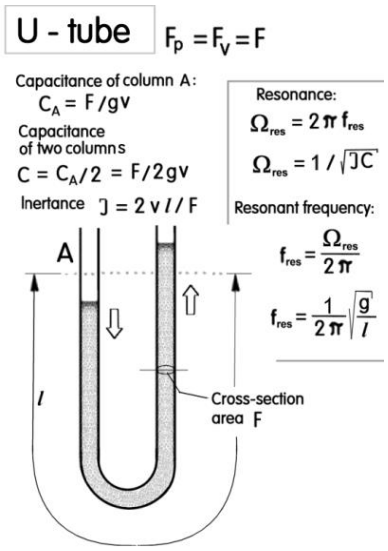

Fig. 14. The U-tube oscillator: contrary to the separate accumulation and inertia components in Fig. 14, here the two vertical columns share the capacitance as well as inertance properties

DOI 10.1515/ama-2015-0032

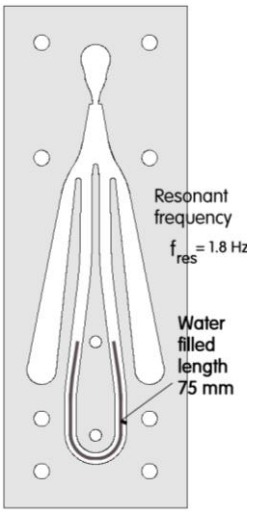

Fig. 15. Early tests with the U-tube integrated into a load-switched fluidic jet-type oscillator verified the capability of self-excited oscillation at very low frequencies

5.2. Integral design

Obvious disadvantage of the circuit discussed in the previous Sect 5.1 is the energetic loss associated with allowing the compressed air to leave into the atmosphere (through the vent of the divider) during approximately one half of the oscillation cycle. This is actually not necessary. The monostable layout was chosen for discussion here only because of its simplicity and ease of explanation of its action. There may be a double-acting configuration with a single U-tube resonator – but with two aerators, operating in anti-parallel (i.e. in opposite phases).

Another source of losses that may be eliminated is the connection between the monostable diverter valve and the jet pump device. The air flow is first slowed down in the diffuser of the monostable device – only to be accelerated in the nozzle of the jet pump a short distance downstream. Of course, these two conversions are inevitably associated with hydraulic losses.

Figs. 10, 11, 12, and 13 present an example of layout also discussed in Tesař (2015) that removes both above mentioned shortcomings. Of course, while the devices used in the circuit presented in Figs. 8 and 9 may be standard fluidic devices, the multi-collector integral design in Figs. 10 and 11 are unusual, specially designed for the purpose. The development of the oscillator thus may be perhaps more difficult.

6. CONCLUSIONS

Generation of microbubbles has very large potential importance for future process engineering. Especially, the potential importance of producing renewable automobile fuels may be very high. Particularly attractive – inexpensive and reliable - are microbubble generation methods based on pulsating the gas flow by fluidic oscillators. Until recently, however, this generation method was not always successful, the generated bubbles being large. High-speed camera studies pinpointed the reason: it was the consequence of multiple conjunction of microbubbles immediately after their formation. Also found was the solution of the problem: reversing the flow direction for a part of the oscillation period. An oscillator design is described producing this desirable effect by a U-tube resonator integral within the oscillator body. It is a subject of a recent patent application as well as tests in laboratory.

REFERENCES

1. **Allouch A., Bourmine K., Monmayrant A., Gauthier-Lafaye o., Geoffroy S., Guo A.-M., Joseph P.** (2014), Microbubbles for optofluidics: controlled defects in bubble crystals, *Microfluidics and Nanofluidics*, 549-560.
2. **Al-Mashhadani M.K.H., Wilkinson S.J., Zimmerman W.B.** (2015), Airlift bioreactor for biological applications with microbubble mediated transport processes, *Chemical Engineering Science*, Vol. 137, 243-253.
3. **Al-Mashhadani M.K.H., Bandulasena H.C.H., Zimmerman W.B.** (2012), CO2 mass transfer induced through an airlift loop by a microbubble cloud generated by fluidic oscillation, I*ndustrial and Engineering Chemistry Research*, Vol. 51, 1864-1877.
4. **Bogdevich V.G.,** Evseev A.R,., Mljuga A.G., Migirenko G. S. (1978), Gas saturation effect on near-wall turbulence characteristics, *Proc of 2nd International Conference on Drag Reduction*, Cambridge, BHRA, 25-34.
5. **Coward T., Lee J. G. M., Caldwell G.S.** (2015), The effect of bubble size on the efficiency and economics of harvesting microalgae by foam flotation, *Journal of Applied Phycology*, Vol. 27, 733-742.
6. **Demirbas A., Demirbas M.F.** (2011) Importance of algae oil as a source of biodiesel, *Energy Conversion and Management*, Vol. 52, 163-170.
7. **Hanotu J., Bandulasena H.C.H., Zimmerman W.B.** (2012), Microflotation performance for algal separation, *Biotechnology and Bioengineering*, Vol. 109, 1663-1673.
8. **Hanotu J., Bandulasena H.C.H., Chiu T. Y., Zimmerman W.B. t**(2013), Oil emulsion separation with fluidic oscillator generated microbubbles, *International Journal of Multiphase Flow*, Vol. 56, 119-l125.
9. **Hashimoto M.,** Mayers B., Garstecki P., Whitesides G. M. (2006), Flowing lattices of bubbles as tunable, self-assembled diffracting gratings, *Small*, Vol. 2, 1292-1298
10. **Hu X., Liu B., Zhou J., Jin R. Qiao S., Liu G.** (2015), CO_2 fixation, lipid production, and power generation by a novel air-lift-type microbial carbon capture cell system, *Environmental Science and Technology*, Vol. 49, 10710-10717.
11. **James A., Vukasinovic B., Smith M. K.,Glezer A,** (2003), Vibration-induced drop atomization and bursting, *Journal of Fluid Mechanics*, Vol. 476, 1-28.
12. **Jones S.M.J., Harrison S.T.L.** (2014), Aeration energy requirements for lipid production by Scenedesmus sp. in airlift bioreactors, *Algal Research*, Vol. 5, 249-257.
13. **Kanagawa T.** (2013), Focused ultrasound propagation in water containing many therapeutical microbubbles, Paper OS6-04-4, P*roc. of FLUCOME 2013*, 12th Intern. Conf., Nara, Japan
14. **Kargbo D.M.** (2010), Biodiesel production from municipal sewage sludges, *Energy and Fuels*, Vol. 24, 2791-2797.
15. **Kooiman K., Foppen-Harteveld M., Der Steen A.F.W.V., De Jong N.**(2011), Sonoporation of endothelial cells by vibrating targeted microbubbles, *Journal of Controlled Release*, Vol. 154, 35-41..
16. **Kuznetsova L.A., Coakley W.T.** (2007), Applications of ultrasound streaming and radiation force in biosensors, *Biosensors and Bioelectronics*, Vol. 22, 1567-1572.
17. **Lam M.K., Lee K.T,** (2012) Microalgae biofuels: a critical review of issues, problems and the way forward, *Biotechnology Advances*, Vol. 30, 673-678.
18. **Lee J.H., Lee K. H., Won J. M., Rhee K., Chung S. K.** (2012), Mobile oscillating bubble actuated by AC-electrowetting-on-dielectric for microfluidic mixing enhancement , *Sensors and Actuators A: Physical*, Vol. 182, 153-162.

19. **Leite G.B., Abdelaziz A.E., Hallenbeck P.C**. (2013), Algal biofuels: challenges and opportunities, *Bioresource Technology*, Vol. 145, 134-139.
20. **Madavan N.K., Deutsch S., Merkle C. L.** (1984), Reduction of turbulent skin friction by microbubbles, *Physics of Fluids*, Vol.27, 356-363.
21. **McCormick M.E, Bhattacharyya R.** (1973), Drag reduction of a submersible hull by electrolysis, *Naval Engineers Journal*, Vol. 85, 2973-2978.
22. **Moriguchi Y., Kato H.** (2002), Influence of microbubble diameter and distribution on frictional resistance reduction, *Journal of Marine Science and Technology*, Vol. 7, 79-85.
23. **Oh J.S., Kwon Y. S., Lee K. H., Jeong W., Chung S. K., Rhee K.** (2014), Drug perfusion enhancement in tissue model by steady streaming induced by oscillating micro-bubbles, *Computers in Biology and Medicine*, Vol. 44, 37-43
24. **Pang M.J., Wei J.J., Yu B.** (2014), Numerical study on modulation of microbubbles on turbulence frictional drag in a horizontal channel, *Ocean Engineering*, Vol. 81, 58-64.
25. **Prevenslik T.** (2011), Stability of nanobubbles by quantum mechanics, *Proceedings of conference 'Topical Problem of Fluid Mechanics'*, Prague, 113-116.
26. **Rawat I., Ranjith Kumar R., Mutanda T., Bux F.** (2011) Dual role of microalgae: phycoremediation of domestic wastewater and biomass production for sustainable biofuels production, *Applied Energy*, Vol. 88, 3411-3424.
27. **Rehman F., Medley G. J. D., Bandulasena H.C.H., Zimmerman W. B.** (2015) Fluidic oscillator-mediated microbubble generation to provide cost effective mass transfer and mixing efficiency to the wastewater treatment plants, *Environmental Research*, Vol.137, 32-39.
28. **Rodríguez-Rodríguez J., Sevilla A., Martinez-Bazán C., Gordillo J. M.** (2015), Generation of microbubbles with applications to industry and medicine, *Annular Review of Fluid Mechanics*, 405-429.
29. **Shams M.M., Dong M., Mahinpey N.** (2014), Friction factor of microbubbles in capillary tubes at low Reynolds numbers, *Chemical Engineering Science*, Vol.112, 72-77.
30. **Sun R.R., Noble M. L., Sun S. S., Song S., Miao C. H.** (2014), Development of therapeutic microbubbles for enhancing ultrasound-mediated gene delivery, Journal of Controlled Release, Vol. 182, 111-120.
31. **Terasaka K., Hirabayashi A., Nishino T., Fujioka S., Kobayashi D.** (2011), Development of microbubble aerator for waste water treatment using aerobic activated sludge, *Chemical Engineering Science*, Vol. 66, 3172-3179.
32. **Tesař V., Tippetts J. R., Allen R. W. K., Low Y.-Y.** (2005), Subdynamic asymptotic behavior of microfluidic valves, *Journal of Microelectromechanical Systems*, Vol. 14, 335-347.
33. **Tesař V.** (2007), Configurations of fluidic actuators for generating hybrid-synthetic jet, *Sensors and Actuators A: Physical*, Vol. 138, 394-403.
34. **Tesař V.** (2007), Fluidics applied to generating small aeration bubbles, *Proc. of 9th Int. Symp. FLUCOME 2007*, Tallahassee, FLA USA.
35. **Tesař V.** (2009) Fluidic control of reactor flow – Pressure drop matching, *Chemical Engineering Research and Design*, Vol. 87, 817-832.
36. **Tesař V.** (2009), Enhancing impinging heat or mass transgfer by fluidically generated flow pulsation, *Chemical Engineering Research and Design*, Vol. 87, 181-192.
37. **Tesař V.** (2010), No-moving-part valve for automatic flow switching, *Chemical Engineering Journal*, Vol. 162, 278-295.
38. **Tesař V.** (2013), Microbubble smallness limited by conjunctions, *Chemical Engineering Journal*, Vol. 231, 526-536.
39. **Tesař V.** (2014), Microbubble generator excited by fluidic oscillators´s third harmonic frequency, *Chemical Engineering Research and Design*, Vol. 92, 1603-1615.
40. **Tesař V.** (2014a) New concept: Low-pressure wide-angle atomiser, *Chemical Engineering and Processing: Process Intensification*, Vol. 82, 19-29.
41. **Tesař V.** (2014b), Shape oscillation of microbubbles, *Chemical Engineering Journal*, Vol. 235, 368-378.
42. **Tesař V.** (2015), *Fluidic generator of microbubbles* (in Czech), Czech Rep. Patent Application, PV 2015-204 filed March 2015.
43. **Tesař V., Hung C.-H., Zimmerman W.B.J.** (2006), No-moving-part hybrid-synthetic jet actuator, *Sensors and Actuators, A: Physical*, Vol. 125, 159-169.
44. **Tesař V., Zhong S.** (2003), Efficiency of Synthetic Jet Generation, *Transactions of the Aeronautical and Astronautical Society of the Republic of China*, Zhongguo Hangkong Taikong Xuehui Huikan, Vol. 35, 45-53.
45. **Tesař V., Zhong S., Fayaz R.** (2013) New fluidic oscillator concept for flow separation control, *AIAA Journal*, Vol. 51, 397-405
46. **Trávníček Z., Tesař V., Kordk J.** (2007), Performance of synthetic jet actuators based on hybrid and double-acting principles, *Journal of Visualization*, Vol.11, 221-l220.
47. **Tremblay-Darveau C., Williams R., Burns P.N.** (2014), Measuring absolute blood pressure using microbubbles, *Ultrasound in Medicine and Biology*, Vol. 40, 775-781.
48. **Tsuge H., Li P., Shimatani N., Shimamura Y., Nakata H., Ohira M.** (2009) Fundamental study on disinfection effect of microbubbles, *Kagaku Kogaku Ronbunshu*, Vol. 35, 548-552.
49. **Wang C., Yalikop S. V., Hilgenfeldt S.** (2012), Efficient manipulation of microparticles in bubble streaming flows, *Biomicrofluidics*, Vol. 6, 012801
50. **Watanabe O., Masuko A., Shirose Y.** (1998), Measurements of drag reduction by microbubbles using very long ship models, *Journal of Soc. Naval Architects*, Vol. 183, 53-59.
51. **Watanabe Y., Aoi A., Horie S., Tomita N., Mori S., Morikawa H., Matsumura Y., Vassaux G., Kodama T.** (2008), Low-intensity ultrasound and microbubbles enhance the antitumor effect of cisplatin, *Cancer Science*, Vol. 99, 2525-2531.
52. **Wataneabe K.,** (2013), Washing effect of microbubbles, Paper OS1-01-1, *Proc. of FLUCOME 2013, 12th Intern. Conf.*, Nara, Japan, November 2013
53. **Xi X.** (2012), *Controlled translation and oscillation of microbubbles near a surface in an acoustic standing wave field*, PhD Thesis, Mechanical Engineering Department, Imperial College London.
54. **Yanuar, Gunawan, Sunaryo, Jamaluddin A.** (2012), Micro-bubble drag reduction on a high-speed vessel model, *Journal of Marine Science and Technology*, Vol. 17, 301-304.
55. **Zimmerman W.B., Tesař V., Butler S., Bandulasena H.C.H.** (2008), Microbubble generation, *Recent Patents in Engineering*, Vol. 2, 1-8
56. **Zimmerman W.B., Al-Mashhadani M.K.H., Bandulasena H.C.H.** (2013) Evaporation dynamics of microbubbles, *Chemical Engineering Science*, Vol. 101, 865-877.
57. **Zimmerman W.B., Zandi M., Bandulasena H.C.H.** (2011), Towards energy efficient nanobubble generation with fluidic *oscillation, Current Opinion in Colloid & Interface Science*, Vol. 16, 350-356.
58. **Zimmerman W.B., Zandi M., Bandulasena H.C.H., Tesa5 V., Gilmour J.D., Ying K.** (2011), Design of an airlift bioreactor and pilot scale studies with fluidic oscillator induced micro bubbles for growth of a microalgae Dunaliella Salina, *Applied Energy*, Vol. 88, 3357-3369.

Acknowledgements: Author gratefully acknowledges the support by grant Nr. 13-23046S obtained from the GACR – Grant agency of the Czech Republic, and the institutional support RVO: 61388998.

DOI 10.1515/ama-2015-0033

MODELING AND PARAMETER IDENTIFICATION OF VIBRATIONS OF A DOUBLE TORSION PENDULUM WITH FRICTION

Ernest CZERWIŃSKI*, Paweł OLEJNIK*, Jan AWREJCEWICZ*

*Department of Automation, Biomechanics and Mechatronics, Lodz University of Technology, ul. Stefanowskiego 1/15, 90-924 Łódź, Poland

ernest.czerwinski@dokt.p.lodz.pl, pawel.olejnik@p.lodz.pl, jan.awrejcewicz@p.lodz.pl

received 23 August 2015, revised 9 December 2015, accepted 10 December 2015

Abstract: The purpose of this paper is to investigate a double torsion pendulum with planar frictional contact. The single torsion pendulum with one-degree-of-freedom is an angular equivalent of the linear harmonic oscillator. The second degree of freedom has been obtained by adding a free body to the inverted single torsion pendulum. The free body's angular displacement is caused by frictional forces appearing in the interface (contact zone) between the free body and the pendulum column's head kinematically excited at its base by a mechanism with torsion spiral spring. An experimental station has been set up and run to find most unknown parameters of the pendulum from the time series of state variables taken as inputs to the Nelder-Mead method of identification. The obtained results proved significant usability of the identification method in the case of numerical simulation of the pendulum's dynamical model. It has not been satisfactorily proved in the case of time characteristics coming from a real system that exhibits also some unrecognized physical effects.

Keywords: Friction, Planar Contact, Numerical Modeling, Double Torsion Pendulum, Parameter Identification, Nonlinear Vibrations, Kinematic Excitation, Kinematic Forcing Mechanism, Nelder-Mead Method

1. INTRODUCTION

The friction in nature exists in the form of external friction occurring at the interface of two bodies. Two kinds are distinguished: a static friction between the two mutually not moving bodies; a kinetic friction between the two mutually moving bodies: friction sliding, wherein the speed of the two bodies in their mutual contact points are different; friction bearings, wherein the resistance movement occurs in turning one body after another. The friction may have a structural form that is related to a dissipation of energy released in the contact surface of mutually fixed parts. Finally, the friction may be internal being observed in solids and fluids in the form of mechanical energy loss (Awrejcewicz and Olejnik, 2005).

The first full friction model was presented by Charles Coulomb, who showed that the static friction is not constant, and pointed to the variability of kinetic friction. It is often used in engineering practice. The concept of friction can incorporate the friction effects such as: a viscous friction increasing linearly while the speed increases; the Stribeck effect observed when a friction force decreases at a low speed, which is called the Stribeck speed; the friction dependent on angular position of the contact surface in rotational motion (Awrejcewicz and Olejnik, 2007).

Steady states of a nonlinear discrete three-degree-of-freedom system containing a torsional damper are investigated in Skup (2002). The system under consideration is harmonically excited. The analysis takes into account structural friction and linear viscous friction of a ring floating in a plunger filled with a high density silicon oil. The influence of external loading amplitude, unit pressures, linear viscous damping, geometric parameters and amplitude-frequency characteristics is analyzed. The equations of motion of the examined power transmission system are solved by a slowly-varying parameter method and digital simulation.

The described system is related to our work too, in a few key points, i.e. by regarding to the influence of friction in the two-degrees-of-freedom system as well as in the forced oscillation of the torsion pendulum caused by harmonic excitation.

In Bassan et al. (2013) an analysis of a simple torsion pendulum's motion is presented. Usual basic dynamical model is investigated in the context of some unexpected features found in experimental data. Comparison with observed values yields estimates for the misalignment angles and other parameters of the model. The authors developed a more flexible model for the torsion pendulum.The basic feature of that is to consider a rigid body suspended to the fibre at an arbitrary point, therefore, not necessarily associated to any particular symmetry of the body. Despite maximum experimental accuracy, some misalignment can occur when the fibre is fastened to the test mass. A detailed mechanical model of the torsion pendulum with geometrical imperfections can explain two unexpected features, ie.: the modulation of the torsion signal at the natural frequency of the swinging motion and the splitting of the swinging resonance.

Analysis of a torsion pendulum is also conducted in some experimental works. For instance, the dynamic process from period-doubling bifurcations to chaos is observed in Miao et al. (2014) by changing the driving period of a modified Pohl's torsion pendulum that formally exhibits periodical dynamics. A data acquisition system with a CCD camera connected to a computer and corresponding image processing software is designed to exhibit the dynamics of the modified pendulum by recording the oscillating angle of the copper rotating wheel. As a result, abundant chaotic sequence diagrams and phase diagrams can be clearly seen in real time.

The described system is related to our work by a similar form of kinematic forcing. With regard to the method of tunable parameters of periodic forcing and the free body being in a frictional contact with the second body, our experimental model is capable to exhibit any irregular behavior, including various ways of parameter dependent bifurcation diagrams and chaotic motion.

An eight-degrees-of-freedom Lagrangian model that provides a suitable account for the motion of the double torsion pendulum is described in De Marchi et al. (2013). The model fully describes its free dynamics and its response to external disturbances, and can accurately predict the torsion, swinging pendulum and bouncing resonances. The number and location of resonance peaks are correctly predicted and are used for a first validation of the model with preliminary data. There is possible to extend the Lagrangian formalism, via the Rayleigh dissipation function, to account for frictional forces. Dissipative effects are taken into account in order to predict, via the fluctuation-dissipation theorem, the fundamental limits of sensitivity of the system.

The described system is related to our work in two key points: (a) parameter identification during validation of the investigated pendulum's model; (b) estimation of frictional forces that act in the contact interface described in Section 2.

Physical systems such as an inverted pendulum driven by a spiral spring, an unbalanced Euler elastica with a travelling mass, a heavy body with a parabolic section and an Ising ferromagnet are very different. In Coullet et al. (2009) a nonlinear oscillator close to its supercritical bifurcation that oscillates with a period inversely proportional to its angular amplitude is presented. The authors performed experiments with a Holweck-Lejay-like pendulum which was used to measure the gravity field during the twentieth century. Main conclusions prove, that the spiral spring, parabolic heavy body and Holweck-Lejay oscillators belong to the same class of universality as the Ising ferromagnet close to their symmetry-breaking bifurcation. The Larmor's law was confirmed experimentally with a good accuracy.

The described system is related to our work in the key point: kinematic forcing of the investigated double torsion pendulum is made with the use of a spiral spring. Thanks to that, the dynamics may be investigated using similar methods taken into consideration in Coullet et al. (2009).

The real application of torsional dynamics can be found in Liu et al. (2014) showing modeling and analysis of a drilling system discretized into several components with lumped inertia properties and with the inertia elements interconnected with axial and torsional springs. The work extends the model of one coupling of two mutually rotating bodies onto a set of multiple couplings modelling the dynamics of a drill string.

The described system is related to our work only in its particular connection, but it brings a real application that could be investigated using elementary couplings with a frictional interface and a torsional spiral spring.

In other fields of science like in textile metrology or biology the double torsion pendulum is found as the basic model for the derivation of principles governing description of dynamics of complex hybrid systems.

In Michalak and Krucińska (2004), the influence of chemical treatment on bending and torsional rigidity of flax and hemp fibers was studied. The double pendulum's mathematical model is useful for the determination of fibre bending rigidity, and the torsional pendulum is helpful in a subsequent determination of fibre torsional rigidity in investigation of bast fibre rigidities.

The nonlinear dynamics of DNA relevant to the transcription process in terms of a chain of coupled pendulums was described in Cadoni et al. (2013). The authors provided a simple model for a nonlinear double chain showing some features which are quite interesting both in the frame of nonlinear dynamics for discrete systems and for applications, in particular, to DNA torsional dynamics.

2. A PHYSICAL MODEL OF THE DOUBLE TORSION PENDULUM WITH FRICTION

Fig. 1 shows a three-dimensional simplified visualization of the double torsion pendulum without any excitation mechanism. It consists of main and auxiliary parts such as screws and pins. The construction is inverted as compared with the general models of torsion pendulums so that on the pendulum column's head it is possible to freely place a next body. Rotational displacement of the free body depends on the pendulum column's dynamics and the friction in the interface of the two contacting bodies. The lower part of the sleeve is connected to the movable cam with the torsion spiral spring imitated by a handmade bar spring. A dynamic kinematic forcing of the free end of the spring attached to the slider causes the pendulum's torsion about an angle. The construction provides an angular contact bearing, allowing the rotation of the column with minimizing the adverse effects of friction occurring in that part of the construction (see Fig. 3).

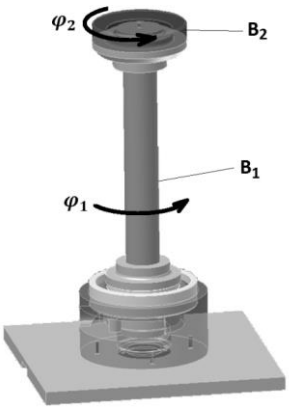

Fig. 1. The double torsion pendulum's CAD in Inventor with marked generalized coordinates φ_1 and φ_2

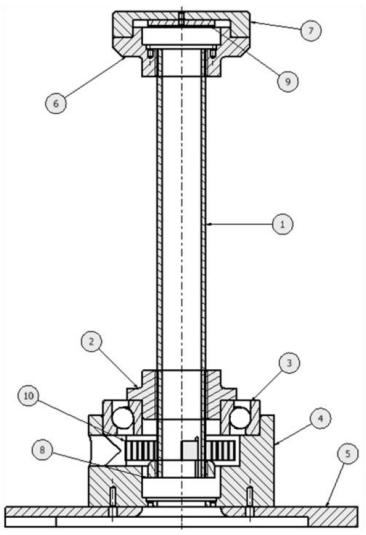

Fig. 2. Scheme of the double torsion pendulum

DOI 10.1515/ama-2015-0033

In Fig. 2 it can be seen a cross-section taken along the vertical axis of the pendulum with the numbered particular elements. The construction is placed on the plate (5) on which the pendulum's base (4) is mounted. The base is designed so that one can attach the lower measuring circuit board of circular shape, bearing (3) and the torsion spiral spring (10). Angular contact bearing that is used in the project transmits the rotation to the lower mounting ring (2), which is screwed onto the sleeve (1). Rotational movement is generated by the spiral spring mounted between the body and the sleeve. At the end of the sleeve there is concealed a plastic cap (8), while the other end of the sleeve is engaged with an upper mounting ring (6 – head of the pendulum's column), wherein the second measuring circuit board with the angular motion sensor is placed. A free body (7) with a screwed plastic cap (9) containing two small circular magnets is placed on the upper surface of the mounting ring. Two rotating magnets attached to the free body create a contactless measurement by means of the Hall-effect sensor of magnetic field. Therefore, any angular relative displacement of the bodies can be measured.

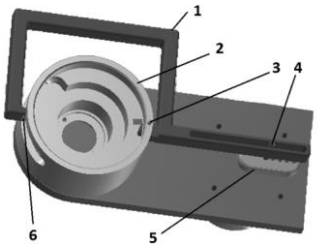

Fig. 3. A mechanism generating the dynamic kinematic sinusoidal forcing (see $f_e(t)$ given by equation (3b)) of one end of the torsion spiral spring

The design provides some space for installation of the two mentioned circuit boards with the Hall-effect sensors, which measure angles of rotation of the torsion pendulum's column formed by elements (1, 2 and 6) and the internal sleeve bearing (3), as well as an angle of rotation of the free body (7).

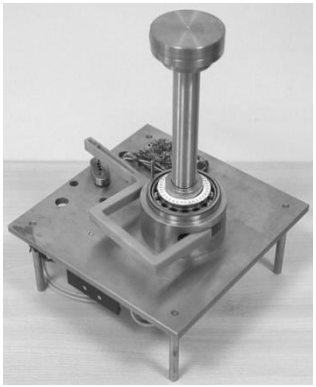

Fig. 4. View of the experimental stand with electronics and a stepper motor mounted below the base plate

The torsion pendulum's kinematic forcing mechanism visible in Fig. 3 consists of a few mechanical parts (1-5) and a stepper motor attached to the cam (5). The cam (5) which is put on the stepper motor's shaft enables movement of the arm (1) via an intermediate pin (4). The point of rotation of the arm is the axis of the fastening pin (3) in the pendulum's base (2 – it is the same base marked by 4 in Fig. 2). At the end of the arm there is a roller (6) used to attach one end of the spiral spring. The second end is attached to the sleeve (1) visible in Fig. 2.

Finally, the described design has been physically realized, and a view of the experimental stand for investigation of dynamics of the two-degrees-of-freedom mechanical system with friction is shown in Fig. 4.

3. ELECTRONIC SYSTEM FOR MEASUREMENT OF THE VECTOR OF GENERALIZED COORDINATES

The vector of real measurement data used for the identification purposes has been subject to an acquisition by means of a measurement system shown in Fig. 5.

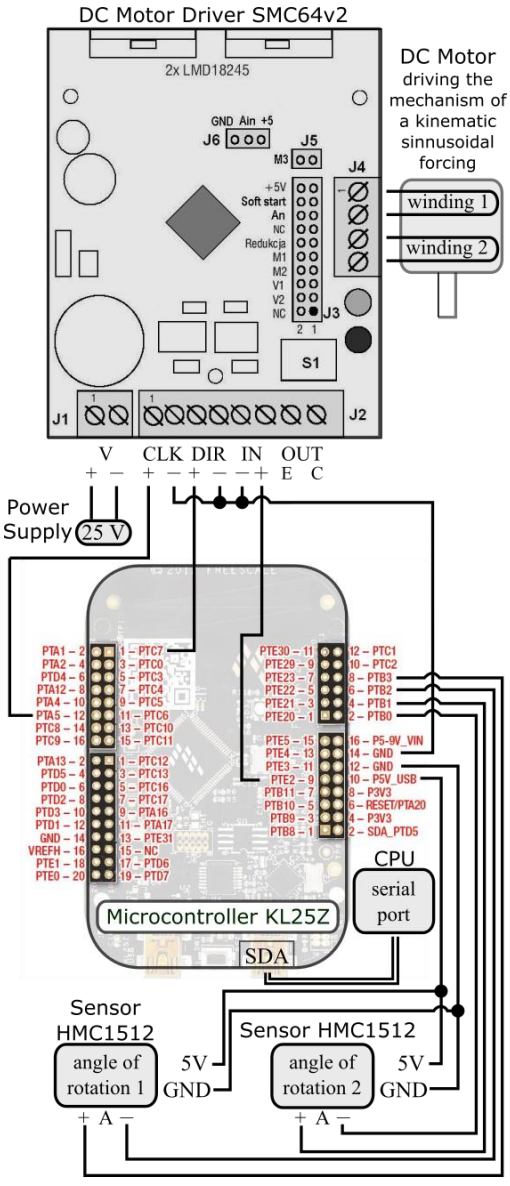

Fig. 5. The measurement and motor driving electronic system

The measurement and motor driving system of the torsion pendulum cosists of the following elements: two angular position sensors HMC1512 embedded in a dedicated electronic circuit based on the LM358 amplifier; Freescale microcontroller FRDM-KL25Z for data acquisition and control; the DC stepper motor

driver SMC64v2 controlled by the microcontroller; the 2-phase DC stepper motor 57BYG081 (55Ncm, 5V, 1A, 1.8° – basic step); a computer (CPU in Fig. 5) for data reading in a serial connection with the SDA port of the microcontroller. After reading, the two series of data corresponding to the angles of rotation were presented in the Terminal in a column form and after a single experiment saved in a text file for further presentation on the graphs (see Fig. 11-13).

4. MATHEMATICAL MODEL OF THE DOUBLE TORSION PENDULUM WITH FRICTION

4.1. Introduction

The investigated double torsion pendulum with friction is an extension of a single torsion pendulum. The construction has been inverted, compared to the general models of torsion pendulum so that on the pendulum column's head there is possible to place a next body, of which free motion dynamics will depend on the base pendulum's dynamics and the friction forces acting in an interface of the two contacting bodies. This implies that the resulting frictional coupling with the two movable bodies establishes the two-degrees-of-freedom mechanical system with friction.

In Fig. 1 we have introduced two variables $\varphi_1$and φ_2 that constitute the vector of generalized coordinates:

$$q = \begin{bmatrix}\varphi_1 \\ \varphi_2\end{bmatrix}, \tag{1}$$

where φ_1 [rad] is the angular displacement of the pendulum's column relative to its base, φ_2 [rad] – the angular displacement of the free body relative to the column.

The zero position of the column is determined by the neutral position of the kinematically forced end of the spiral spring, which is attached at the center of the hollow bore's opening in the base. The column can rotate clockwise and counter-clockwise, contrary to the range indicated by the opening angle of the hollow bore.

4.2. Derivation of the double torsion pendulum's equations of motion using the Lagrange method

Kinetic energy of the double torsion pendulum is given by:

$$T = \frac{1}{2}B_1\dot{\varphi}_1^2 + \frac{1}{2}B_2(\dot{\varphi}_1 + \dot{\varphi}_2)^2, \tag{2}$$

where B_1[kg·m^2] is the mass moment of inertia of the sleeve with two rings constituting the pendulum's column, B_2 [kg·m^2] – the mass moment of inertia of the free body.

The potential energy is given by:

$$V = \frac{1}{2}k(f_e(t) - \varphi_1)^2, \tag{3a}$$

where$k$ [N·m/rad] is the torsion spring's stiffness, $f_e(t)$ – function of the kinematic sinusoidal forcing (external excitation) of one end of the torsion spring given by the formula:

$$f_e(t) = Asin(\omega t), \tag{3b}$$

where ω [rad/s] is the angular frequency of kinematic forcing, A [rad] – amplitude of the kinematic forcing.

Vector Q of generalized forces can be written as follows

$$Q = \begin{bmatrix}\tau_1 \\ \tau_2\end{bmatrix} = \begin{bmatrix}-M_L + M_T \\ -M_T\end{bmatrix}, \tag{4}$$

where M_L [N·m] is the frictional resistance torque of the bearing, in which the first pendulum's body (the column) is mounted, M_T [N·m] – the frictional resistance torque between both pendulum's bodies of inertia B_1 and B_2.

We assume, that the frictional resistance torque of the bearing depends on unknown viscous friction and the Coulomb friction expressed by the maximum static friction torque M_1 acting in the contact zone Michalak and Krucińska (2004). Moreover, the discontinuity introduced by Coulomb model of dry friction is smoothened by the smoothing function $arctg$ approximating function $sgn(\dot{\varphi}_1)$ of sign of the angular velocity $\dot{\varphi}_1$ of the column

$$M_L = c_1\dot{\varphi}_1 + M_1\frac{2}{\pi}arctg(\varepsilon_1\dot{\varphi}_1), \tag{5}$$

where c_1 [N·m·s/rad] is the coefficient of viscous friction in bearing, M_1 [N·m] – maximum torque of the static friction of the bearing in the contact zone, ε_1 [s] – a parameter determining accuracy of smoothing of the static friction torque's Coulomb term acting in the bearing's contact zone. The larger the value of ε_1 is the closer the $arctan$ function approximates the frictional effects caused by Coulomb friction.

For further use in the text, the term "contact zone" will denote a contact zone in the frictional coupling between the pendulum's bodies of inertia B_1 and B_2.

One takes into account more frictional effects existing in the contact zone between both pendulum's bodies. The frictional resistance torque between bodies of inertia B_1 and B_2 depends on the viscous friction $T_v\dot{\varphi}_2$, smoothened relation for Coulomb dry friction $T_{s1}\frac{2}{\pi}arctg(\varepsilon_2\dot{\varphi}_2)$, the free body's angular position dependent friction $T_{s2}(1 - sgn|\dot{\varphi}_2|)$ and the Stribeck effect that is characterized by a Stribeck curve $T_{st}\left(1 - e^{-T_0|\dot{\varphi}_2|}\right)sgn(\dot{\varphi}_2)$. Therefore, concatenating the possible frictional effects we obtain:

$$\begin{aligned}M_T = {} & T_v\dot{\varphi}_2 + T_{s1}\frac{2}{\pi}arctg(\varepsilon_2\dot{\varphi}_2) \\ & + T_{s2}(1 - sgn|\dot{\varphi}_2|) + T_{st}\left(1 - e^{-T_0|\dot{\varphi}_2|}\right)sgn(\dot{\varphi}_2),\end{aligned} \tag{6}$$

where T_v [N·m·s/rad] is the viscous friction coefficient in contact zone, T_{s1}[N·m] – the maximum static friction torque in the contact zone, T_{s2} [N·m] – the maximum static friction torque,T_{st} [N·m] – friction coefficient associated with the exponential curve appearing due to the Stribeck effect, T_0 [s] – the parameter of exponential curve, ε_2 [s] – a parameter of static friction torque in the analyzed contact zone.

Expressing the kinetic and potential energies in generalized coordinates, a Lagrange function L is defined as the difference of the kinetic energy T and the potential energy V:

$$L = T - V, \tag{7}$$

which after substituting equations (2) and (3) leads to the formula

$$L = \frac{1}{2}B_1\dot{\varphi}_1^2 + \frac{1}{2}B_2(\dot{\varphi}_1 + \dot{\varphi}_2)^2 - \frac{1}{2}k(f_e(t) - \varphi_1)^2. \tag{8}$$

Then, for the function L, the Lagrange equation is used

$$\frac{d}{dt}\left(\frac{\partial L}{\partial \dot{q}_i}\right) - \frac{\partial L}{\partial q_i} = Q, \tag{9}$$

where Q – vector of generalized forces, q_i – i-th generalized coordinate.

The Lagrange equation for the coordinate φ_1 is given by:

DOI 10.1515/ama-2015-0033

$$\frac{d}{dt}\left(\frac{\partial L}{\partial \dot{\varphi}_1}\right) - \frac{\partial L}{\partial \varphi_1} = \tau_1. \tag{10}$$

Considering only the left-hand side of equation (10) and equation (8), one obtains:

$$\frac{d}{dt}\left(\frac{\partial L}{\partial \dot{\varphi}_1}\right) - \frac{\partial L}{\partial \varphi_1} = B_1\ddot{\varphi}_1 + B_2(\ddot{\varphi}_1 + \ddot{\varphi}_2) - k(f_e(t) - \varphi_1). \tag{11}$$

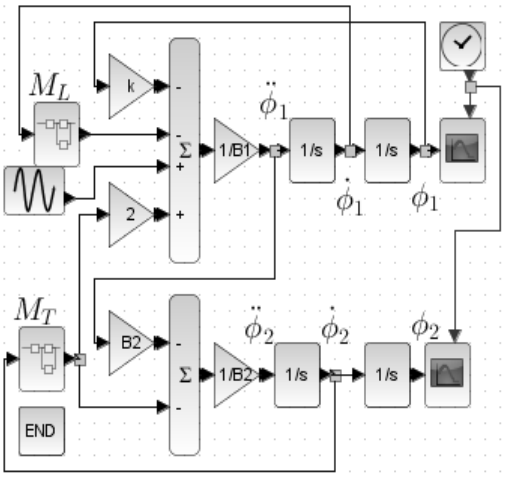

Fig. 6. Complete simulation diagram of the double torsion pendulum.

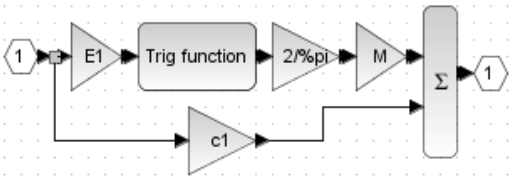

Fig. 7. Simulation diagram of a subsystem modelling the equation of the frictional resistance torque M_L

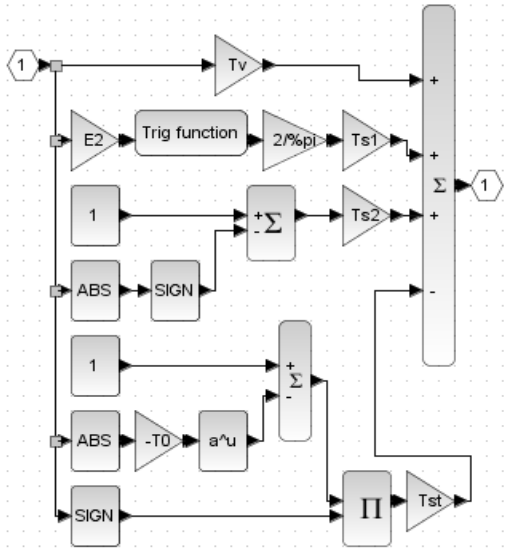

Fig. 8. Simulation diagram of a subsystem modelling the equation of the frictional resistance torque M_T

The Lagrange equation for the coordinate φ_2 is given in the form:

$$\frac{d}{dt}\left(\frac{\partial L}{\partial \dot{\varphi}_2}\right) - \frac{\partial L}{\partial \varphi_2} = \tau_2. \tag{12}$$

Combining the left-hand side of equation (12) and equation (8), one gets:

$$\frac{d}{dt}\left(\frac{\partial L}{\partial \dot{\varphi}_2}\right) - \frac{\partial L}{\partial \varphi_2} = B_2(\ddot{\varphi}_1 + \ddot{\varphi}_2). \tag{13}$$

Substituting the generalized forces τ_1 and τ_2, which are defined in (4) into the equations (10) and (12), and taking into account the formulas (11) and (13), the two ordinary differential equations of second order describing the dynamics of the double inverted torsion pendulum with the dynamic kinematic forcing are found:

$$B_1\ddot{\varphi}_1 + B_2(\ddot{\varphi}_1 + \ddot{\varphi}_2) - k(f_e(t) - \varphi_1) = -M_L + M_T \tag{14}$$

and:

$$B_2(\ddot{\varphi}_1 + \ddot{\varphi}_2) = -M_T. \tag{15}$$

Finally, the double torsion pendulum with a plane frictional coupling is represented by a two-degrees-of-freedom dynamical system and described by the system of two second-order ordinary differential equations:

$$\begin{cases} B_1\ddot{\varphi}_1 - k(f_e(t) - \varphi_1) = -M_L + 2M_T, \\ B_2(\ddot{\varphi}_1 + \ddot{\varphi}_2) = -M_T. \end{cases} \tag{16}$$

Equations (16) were implemented in Scilab to build the simulation diagram of the analyzed physical model visible in Fig. 6-8.

5. PARAMETER IDENTIFICATION OF THE REAL OBJECT

Prior to the process of identification, the objective function was assumed as the arithmetic average of squares of the differences between the measured and estimated angles in the following form

$$y = \frac{\frac{1}{N}\sum_{i=1}^{N}(\varphi_1 - \hat{\varphi}_1)^2 + \frac{1}{N}\sum_{i=1}^{N}(\varphi_2 - \hat{\varphi}_2)^2}{2}, \tag{17}$$

where $\varphi_1(t)$, $\varphi_2(t)$ are the actual measurements of angles, $\hat{\varphi}_1(t)$, $\hat{\varphi}_2(t)$ – the estimates of angles, N – number of samples in the series. The objective function (17) was implemented in Scilab (see Listing 1 in Appendix).

To identify the unknown parameters of the pendulum the Nelder-Mead simplex method for finding a local minimum of a function of several variables has been used. It allows to determine the local minimum without using the derivatives, so it can be applied when the function is not differentiable at a point. In the numerical analysis we used an identification algorithm available in the Scilab (see Listing 1). Exemplary references extending the problem of finding of unknown parameters with the use of the Nelder-Mead simplex method can be found in Luersen and Le Richie (2004).

In the identification process there are assumed some known parameters: ω, $\varepsilon_1, \varepsilon_2$, while the unknowns are as follows: $k, A, B_1, B_2, c_1, M_1, T_v, T_{s1}, T_{s2}, T_{st}, T_0$.

5.1. An identification based on the numerical solution – example

Before the target identification of parameters of the real torsion pendulum will be made, a test of the assumed method in an exemplary simulation has to be carried out with the use of a nu-

merically computed solution. The identification procedure was initiated with all values of parameters, i.e.: $\omega = 0.5,\ \varepsilon_1 = 1000, \varepsilon_2 = 1000,\ \mathrm{B}_1 = 20,\ \mathrm{B}_2 = 1, \mathrm{k} = 100, \mathrm{A} = \frac{\pi}{6}, \mathrm{c}_1 = 10,\ \mathrm{M}_1 = 3, \mathrm{T}_\mathrm{v} = 1, \mathrm{T}_{\mathrm{s1}} = 2,\ \mathrm{T}_{\mathrm{s2}} = 2,\ \mathrm{T}_{\mathrm{st}} = 0.5,\ \mathrm{T}_0 = 10.$ As a result, the trajectories of state variables visible in Fig. 9 and 10 were obtained.

Figs. 9a and 9b show a time histories of system variables in a response of the pendulum to the sinusoidal function of the kinematic forcing $f_a(t)$. According to the specificity of the externally forced two-degrees-of-freedom dynamical system, the angular velocities and accelerations are difficult to predict within a time period of applied forcing. This irregularity is caused by the effects of a rolling friction present in the bottom bearing and the inertia of the free body acting reversely on the column at the stick-slip frictional contact interface of both bodies of the pendulum. In Fig. 9 we can see a temporal slippings as well as close to zero relative velocities of the free body against the column. Also in this case, the angular velocity and acceleration of both bodies are difficult to predict. It is caused by the frictional effects occurring at the frictional contact interface of both pendulum bodies of inertias B_1 and B_2.

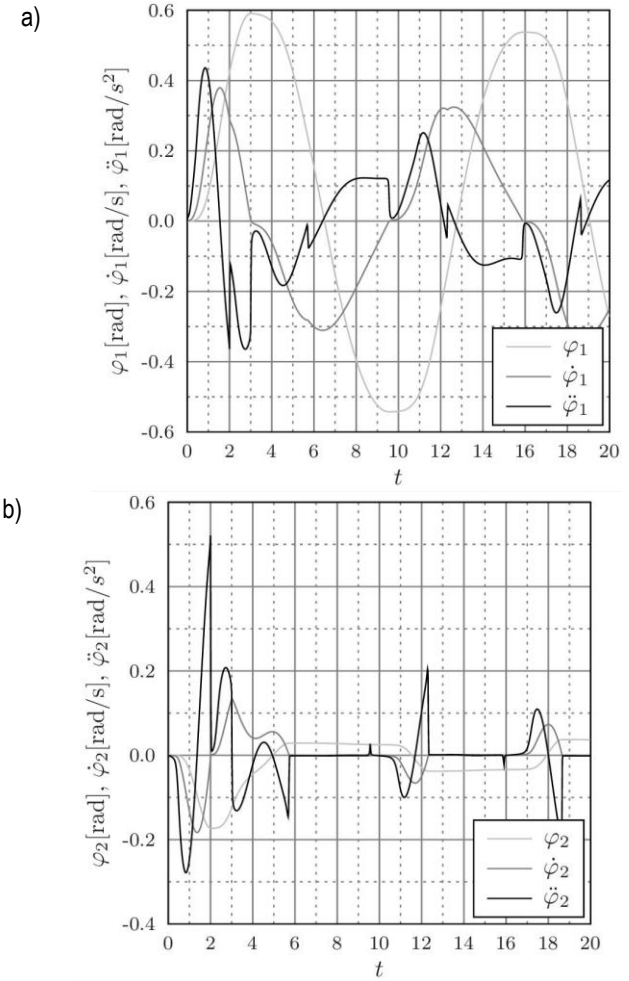

Fig. 9. Time histories of the angular displacements $[\varphi_1, \varphi_2]$, velocities $[\dot{\varphi}_1, \dot{\varphi}_2]$ and accelerations $[\ddot{\varphi}_1, \ddot{\varphi}_2]$ of the column and the free body

The set of parameters which were described as unknowns was slightly modified in relation to the simulation, i.e.: $B_1 = 22$, $B_2 = 11$, $k = 10$, $A = \pi/4, c_1 = 5$, $M_1 = 2$, $T_v = 0.1$, $T_{s1} = 3, T_{s2} = 1, T_{st} = 0.2, T_0 = 1000$.

It is seen, that after a few steps of the identification procedure of parameters of the pendulum, the time trajectories are significantly different (see Fig. 10a and 10b). However, after several thousands of iterations, there was obtained better set of parameters. The angular velocity and acceleration are difficult to predict by unrecognized effects of friction occurring in contact zone of the pendulum's bodies.

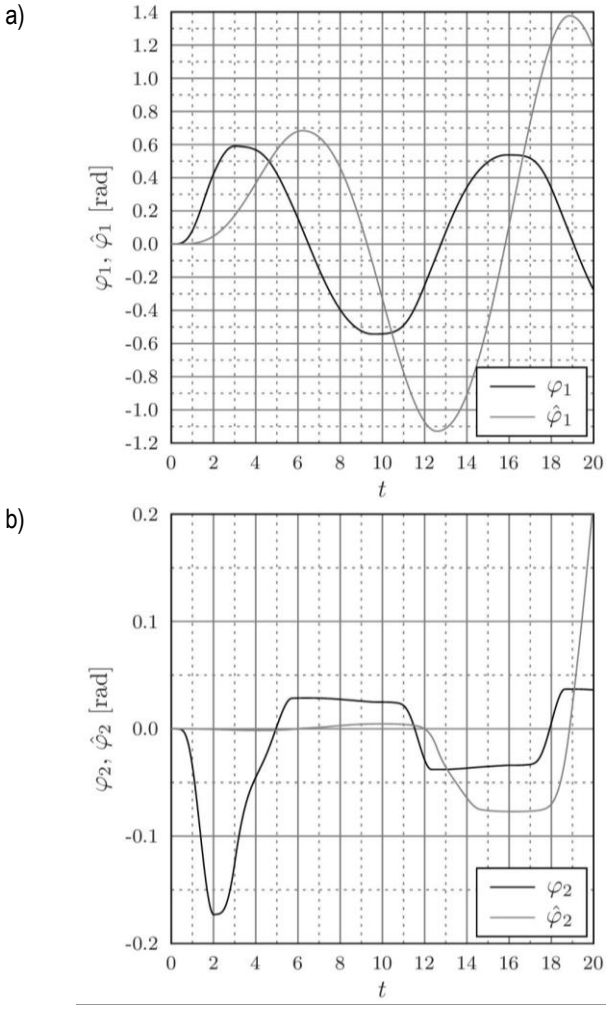

Fig. 10. Time histories of the actual $[\varphi_1, \varphi_2]$ and partially estimated $[\hat{\varphi}_1, \hat{\varphi}_2]$ dynamical variables of the pendulum before the final identification parameters are found. In the presented view, the model's parameters are not finally identified (the procedure of identification is still in progress)

It has guaranteed almost perfectly identified model of the inverted double torsion pendulum with friction and a dynamic kinematic forcing (see Fig. 11a and 11b).

5.2. The target identification based on the data acquired from measurement

In previous section a numerical solution of the pendulum's model was taken into consideration leading to the successful identification. Correctness of our methodology has been proved.

Now, beginning with the identification of the measurement series, three parameters were assumed as known. Frequency of the dynamic kinematic forcing $\omega = 2\pi/T = 2\pi/0.48 = 13.09$ is assumed. A parameter of static friction torque in the slip zone of

DOI 10.1515/ama-2015-0033

the bearing and the static friction torque in the analyzed frictional contact of the pendulum's bodies are as follows: $\varepsilon_1 = 1000, \varepsilon_2 = 1000$, respectively. After a few thousand of iterations, the smallest possible value of objective function was obtained: $y = 0.01171$.

a) b)

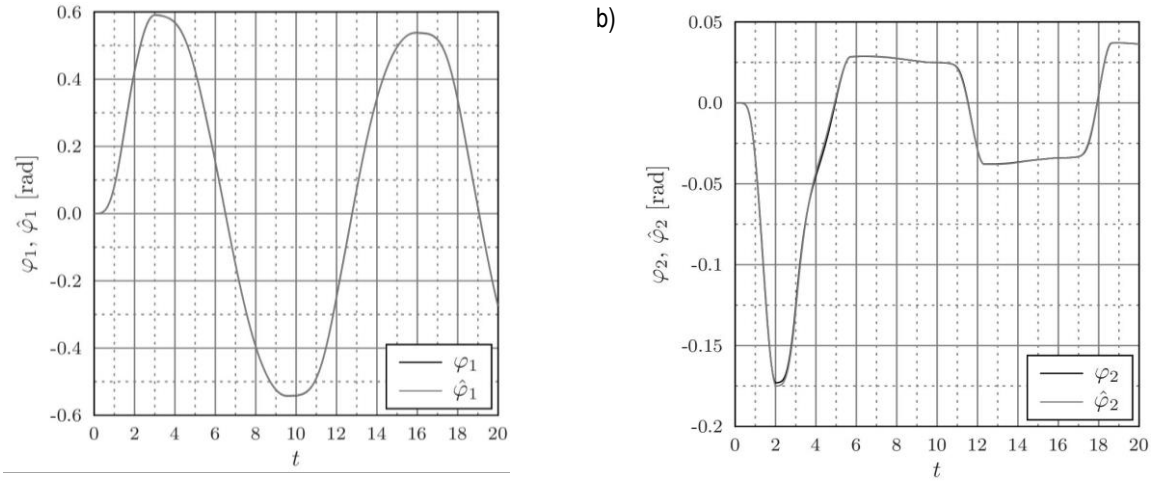

Fig. 11. Time histories of the actual $[\varphi_1, \varphi_2]$ and estimated $[\hat{\varphi}_1, \hat{\varphi}_2]$ dynamical variables of the pendulum after final identification of parameters. In the presented view, the model's parameters are identified (the procedure of identification is finished)

a) b)

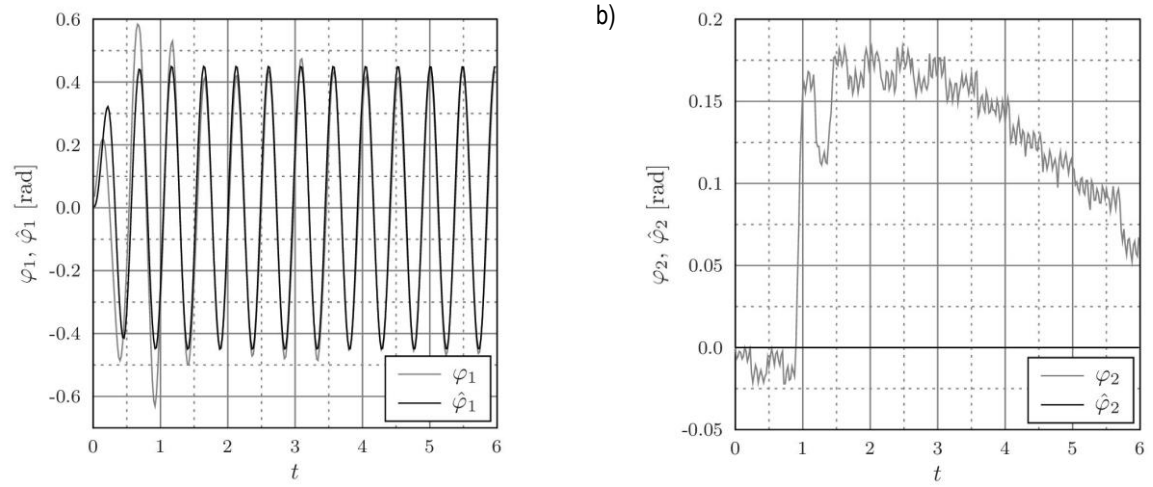

Fig. 12. Time histories of the actual $[\varphi_1, \varphi_2]$and estimated $[\widehat{\varphi}_1, \widehat{\varphi}_2]$ dynamical variables of the pendulum after final identification of parameters

a) b)

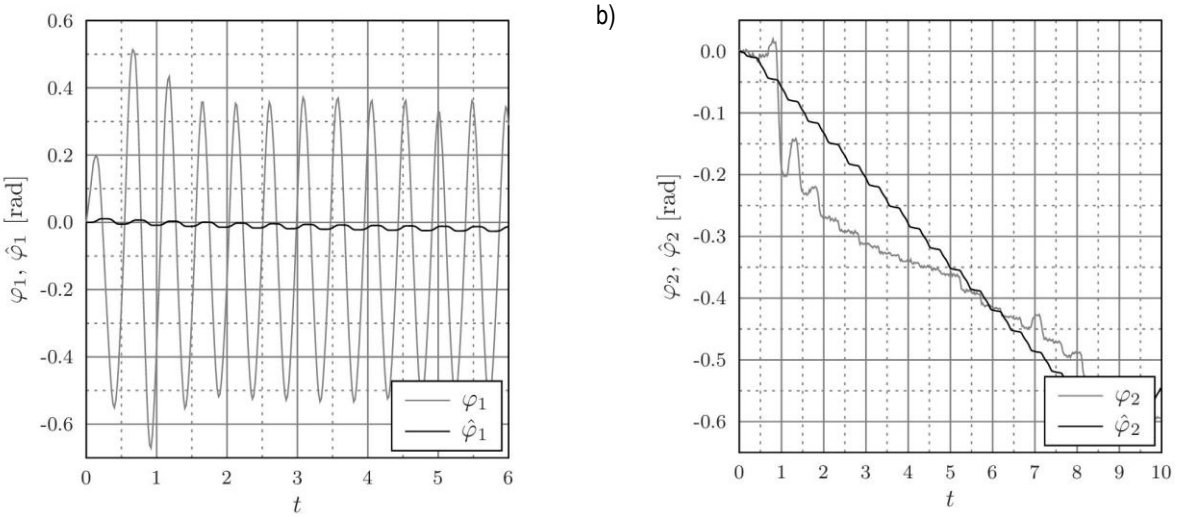

Fig. 13. Time histories of the actual $[\varphi_1, \varphi_2]$ and estimated $[\hat{\varphi}_1, \hat{\varphi}_2]$ dynamical variables of the analyzed pendulum after final identification of parameters

Given the time history in Fig. 12b, which shows the matching, it can be concluded, that the presented numerical solution of the double torsion pendulum's model with friction does not match the measurement series obtained from our real experiment. The time history of actual value and the estimated value of the angle φ_1 tends to correct convergence, however, the φ_2 angle's time history does not show any acceptable convergence.

Then, the second real identification was performed. As previously, three parameters were assumed as known and set to the same values. After a few thousand of iterations, the smallest possible value of objective function was obtained: $y = 0.05328$.

Given the time history in Fig. 13, which shows the matching, it can be concluded, that the presented numerical solution of the double torsion pendulum's model with friction does not satisfctorily match the measurement series of data obtained from our real experiment as in the previous case.

6. CONCLUSIONS

The introduced mathematical model of the torsion double pendulum with a spiral spring allows to simulate complex dynamics of the mechanical system. The time histories of angular displacement, velocity and acceleration of the pendulum's column were shown in Fig. 9. According to the given time history of external excitation of the pendulum, the kinematic forcing takes the form of sine wave. It is one of the reasons causing main complexity of the system, so the angular velocity and acceleration are difficult to predict. This irregularity of responses is caused by the effects of dry and viscous friction acting on the column and the free body placed on its head. In turn, we had shown in Fig. 10 a time history of the angular displacement, velocity and acceleration of the free body, that is forced via a plane frictional contact by the column's head. We can see the restraint of the free body against the column. Also in this case, if we consider a noise in the measured series of data, then the velocity and acceleration will be impossible to observe. After the first sample simulations, it was decided to carry out the identification of model parameters using a slightly modified form in relation to the simulation model. It has led to some satisfactory fitting, even though not all the parameters have been fully identified. This may be due to the fact that this particular solution was possible with several different values of unknown parameters. It is worth noting that even a small change in the parameters dramatically changes the behavior of our mechanical system.

The next step was to perform the identification of pendulum's parameters. Considering the real and the estimated angular displacements of the pendulum's bodies, as well as assuming that the parameters obtained with known parameters B_1 and B_2 should be equal to each other, it can be concluded, that the matching of the double torsion pendulum's model with a planar frictional contact to the measurements obtained from the real experiment is not sufficiently correct. There are several aspects that have a direct impact on such divergence.

Firstly, it should be pointed out that the system is very sensitive and has a lot of local solutions dependent on initial conditions. Free body of the torsion pendulum can move relatively to the column, where it can exhibit an oscillatory rotational motion to the right and then to the left, it can move only in one direction and suddenly stop to move with the column, it can sometimes exhibit rapid stick-slip behavior in relation to the pendulum's head and others. Even with the same initial conditions, the system may behave differently as shown by measurements. Another problem is devoted to the number of unknown parameters. To many unknown parameters were reported, so that the same co-existing solutions may be obtained at their different sets of values. It is also essential that the parameters of the model do not need to be constant in time, as it has been assumed at the beginning, and may vary in time.

The spiral spring is worth a comment. Its stiffness during winding and unwinding is slightly different, although it is assumed constant. Another imperfections can be introduced by small vibrations visible on the graphs of the angular displacement of the free body. Such discrepancy may be caused by insufficiently precise manufacturing of the mechanical parts of the laboratory stand, the type of bearing and insufficient parallelism between the base and the column, which causes vibration of the column in a vertical plane. Another problem could be deduced from the mathematical model, in which, there could not be taken into account the unknown dynamical effects that occur in the adequate real object, or even the idealized mathematical model could include too many frictional effects that complicate the identification. A small change of the parameters may result in a large change in the waveforms of the double torsion pendulum's states. In most considered cases, the estimated displacement of the column adjusts to a measured position as the parameters in the equation of the position of the columns are easier to estimate, and the second equation depends only on both the movement of the column and the friction between the column and the free body.

Another aspect may be connected with the Nelder-Mead method. Despite the fact that it is a simple and easy implementing method allowing the determination of extremes of nonlinear function of several variables without the use of derivatives, the objective function can reach local minima during the identification algorithm, so it is not always possible to find the correct set of identified parameters.

The last aspect that one needs to consider is the fact that the arm of the mechanism realizing the dynamic kinematic forcing is greater than the spring hook arm, which can cause unnatural deformation of the spring and the fact, that angle-voltage characteristics of two sensors are not ideal to measure the rotational movement of the column and the free body in a range greater than $\pm 45°$. This prevents a full examination of the model, as in other cases. In the measurements, it was necessary to adopt high frequency of excitation, which leads to the observed rapid dynamic changes of state variables.

Despite the not fully correct identification of parameters of the double torsion pendulum with friction, we have achieved a good basis for further work on the subject. It is possible to consider several possible paths, such as simplifications based on reduction of system variables, or the extension of the model to take into account more effects, including a time-dependent uncertainty of model parameters, which were originally assumed as constants. One should also tend to improve accuracy of the angle sensors to be able to measure the states more correctly. Performance of certain mechanical parts should be raised by eliminating unwanted vibrations of the column or by replacing the bearing with another one of a higher enough tolerances, as well as by using a spiral spring with a greater stiffness. The identification method could be supplemented with partial analytical solutions to identify some unknown parameters.

DOI 10.1515/ama-2015-0033

REFERENCES

1. **Awrejcewicz J., Olejnik P.** (2005), Analysis of dynamic systems with various friction laws, *Applied Mechanics Reviews – Transactions of ASME*, Vol. 58 (6), 389-411.
2. **Awrejcewicz J., Olejnik P.** (2005), Friction pair modeling by 2-dof system: numerical and experimental investigations, *International Journal of Bifurcation and Chaos*, Vol. 15 (6), 1931-1944.
3. **Awrejcewicz J., Olejnik P.** (2007), Occurrence of stick-slip phenomenon, *Journal of Theoretical and Applied Mechanics*, Vol. 45(1), 33-40.
4. **Bassan M., De Marchi F., Marconi L., Pucacco G., Stanga R., Visco M.** (2013), Torsion pendulum revisited, *Physics Letters A*, Vol. 377 (25-27), 1555-1562.
5. **Cadoni M., De Leo R., Gaeta G.** (2013), Solitons in a double pendulums chain model, and DNA roto-torsional dynamics, *Journal of Nonlinear Mathematical Physics*, Vol. 14(1), 128-146.
6. **Coullet P., Gilli J.-M., Rousseaux G.** (2009), On the critical equilibrium of the spiral spring pendulum, *Proceedings of the Royal Society A*, Vol. 466, 407-421.
7. **De Marchi F., Pucacco G., Bassan M., De Rosa R., Di Fiore L., Garufi F., Grado A., Marconi L., Stanga R., Stolzi F., Visco M.** (2013), A quasi-complete mechanical model for a double torsion pendulum, *Physical Review D*, Vol. 87(122006).
8. **Liu X., Vlajic N., Long X., Meng G., Balachandran B.** (2014), State-dependent delay influenced drill-string oscillations and stability analysis, *ASME Journal of Vibration and Acoustics*, Vol. 136(5), 051008.
9. **Luersen M.A., Le Riche R.** (2004), Globalized Nelder–Mead method for engineering optimization, *Computers & Structures*, Vol. 82(23-26), 2251-2260.
10. **Miao C., Luo W., Ma Y., Liu W., Xiao J.** (2014), A simple method to improve a torsion pendulum for studying chaos, *European Journal of Physics*, Vol. 35, 055012.
11. **Michalak M., Krucińska I.** (2004), Studies of the effects of chemical treatment on bending and torsional rigidity of bast fibres, *Materials Science*, Vol. 10(2), 182-185.
12. **Skup Z.** (2002), Structural friction and viscous damping in a frictional torsion damper, *Journal of Theoretical and Applied Mechanics*, Vol. 2(40), 497-511.

The work has been supported by the Polish National Science Centre, MAESTRO 2, No. 2012/04/A/ST8/00738 and it was presented during the 3rd International Conference on MECHATRONICS – Ideas for Industrial Applications, Gdansk, 2015.

APPENDIX

Listing 1. A procedure in Scilab of using the Nelder-Mead identification method

```
ExpData = fscanfMat("data_in_rad.txt");
fip1.time = ExpData(:,1);
fip1.values = ExpData(:,2);
fip2.values = ExpData(:,3);

function y=Fobj(x);
importXcosDiagram("xcos_model_pendulum.zcos")
Context.w=13.09;Context.E1=1000;Context.E2=1000;
   Context.B1=x(1);Context.B2=x(2); Context.k=x(3);
Context.A=x(4);Context.c1=x(5);Context.M=x(6);
Context.Tv=x(7);Context.Ts1=x(8);Context.Ts2=x(9);
Context.Tst=x(10);Context.T0=x(11);

Context.tmax=10;Context.tini=0;Context.S=2;
scicos_simulate(scs_m,Context);

y= (mean((fip1.values-fi1.values)^2) + mean((fip2.values-
fi2.values)^2))/2;

clf(1); figure(1)
plot(fip1.time, [fip1.values,fi1.values]);
clf(2); figure(2)
plot(fip1.time, [fip2.values,fi2.values]);
endfunction

x=[1, 1, 1, 1, 1, 1, 1, 1, 1, 1, 100]
y=Fobj(x)
opt = optimset("MaxIter",50,"PlotFcns",optimplotfval);
x = fminsearch(Fobj,x,opt)
```

A CONCEPT OF MODIFICATION AND SIMULATION STUDIES OF A MECHATRONIC STAIR TRANSPORTER FOR THE DISABLED

Sławomir WUDARCZYK*, Artur MURASZKOWSKI*

*Faculty of Mechanical Engineering, Department of Biomedical Engineering, Mechatronics and Theory of Mechanisms, Wroclaw University of Technology, Wybrzeże Wyspiańskiego 27, 50-370 Wrocław, Poland

slawomir.wudarczyk@pwr.edu.pl, artur.muraszkowski@pwr.edu.pl

received 27 January 2015, revised 10 December 2015, accepted 11 December 2015

Abstract: A numerical model of existing stair climber with its passenger was built and its operation was analysed through simulations. A modification of the stair climber has been developed on a basis of the simulation studies. The modification depends on equipping the device with additional controllable mechanism the function of which is to change the position of the passenger's centre of gravity. Comparative simulation studies were carried out for the standard version and the modified version of the stair transporter in a system for the dynamic.

Keywords: Computational Model, Stair Transporter, Operator Relief System

1. INTRODUCTION

The problem of the locomotion of persons with impaired mobility on a flat terrain has been quite effectively solved through various wheelchairs. One of the major difficulties for those people is to overcome architectonic barriers, mainly stairs (Laffont et al., 2008). This problem is being solved chiefly through approach ramps or special lifts. Such solutions enable locomotion impaired persons to independently overcome stairs. They are psychologically important since the disabled person can get to another level in a building without asking other people for help. Unfortunately, there are still many places, e.g. the aircraft boarding ramp or very narrow stairs, in which the use of such devices is impossible or costly. In such situations the solution is the use of stair transporters, commonly called stair climbers.

Depending on the way they overcome stairs the devices are divided into driving (usually tracked) devices (Yu et al., 2013) and walking devices (in which a proper mechanism enables the translocation of their particular members at a momentary absence of contact of the members with the base).

From the point of view of kinematics, a device which is to overcome obstacles (e.g. stairs) must have a proper mechanism (Bałchanowski et al., 2012; Bałchanowski et al., 2010) whose geometric features enable overcoming obstacles of particular type and size. Moreover, the stability of the device during obstacle overcoming must be ensured. The R&D work on stair transporters has resulted in various technical solutions.

This paper presents an analysis of the motion of the AAT S-Max Aviation stair climber for transporting disabled persons up and down the stairs. First a numerical model of the actual device was created in a system for the dynamic analysis of multilink systems and then simulations were run. The results of the simulation studies were used to develop a modification of the device in order to facilitate the work of the operator.

2. STRUCTURE OF STANDARD WALKING STAIR TRANSPORTER

Designed stair climbers are different in design depending on their purpose (Gonzalez et al., 2009; Shriwaskar et al., 2013;Fang et al, 2011; Trochimczuk et al., 2014). The S-Max Aviation stair climber made by AAT is an example of a device which uses walking to climb stairs. It was designed to service persons with impaired mobility at airports. The device can be operated exclusively by a trained operator. The stair climber consists of a frame on which a seat and adjustable operator handle are mounted and a driving-walking mechanism supplied from a battery. The device is shown and described in Fig. 1.

Fig. 1. S-max Aviation walking stair climber made by ATT (http://www.aatgb.com/)

Stair climbing is effected by means of the lifting foot which by moving downwards lifts the device with the passenger. During this time the wheels move to the next stair. The device ascends the stairs with its back to the latter. When the device descends

DOI 10.1515/ama-2015-0034

the stairs the passenger faces the direction in which it moves. Driving on a flat terrain is effected solely by the operator's muscles. The operator operates the device via a proper control panel. The drive unit is a 275 W motor supplied with 24 V direct current, with a maximum lifting capacity of 160 kg. The other basic specifications of the device are as follows.

- Overall dimensions: height 1.1-1.5 m, width 0.38 m, length with footrest 1 m;
- Mass parameters: total weight 36 kg, lifting mechanism 17 kg, the seat with the backrest 11 kg, handle 3 kg, battery set 3 kg,
- Stairs overcoming speed: 8-23 stairs per minute;
- Maximum stair height: 25 cm.

The S-Max Aviation stair climber is operated by a single operator and enables the transport of a disabled person up and down the stairs. It is a wheeled-walking device in which walking up/down the stairs is effected by a proper electrically powered walking mechanism. The main difficulty which the operator has to cope with is to keep the whole device (with its passenger) in equilibrium. Unfortunately, this requires considerable effort and skill. Somewhat oversimplifying it, the operator must bear the person sitting in the device which is supported only in one point. In addition, at a certain moment the point of support changes quite abruptly: first the whole device rests on the foot situated on the lower stair and then the whole weight is carried by the wheel resting on the higher stair. In order to keep the transported person in the stability field the operator must use considerable force.

3. CREATION OF MECHATRONIC MODEL OF STAIR TRANSPORTER

In order to define the characteristics of walking transporter mechanism a numerical model of the existing device for transporting disabled persons up/down the stairs had to be built and several simulations had to be run. The kinematic scheme of S-max Aviation walking transporter which was the basis for the model is shown (in scale) in Fig. 2.

The numerical model was built on the basis of the technical documentation and measurements performed by the authors. The interactions of the foot and the wheels with the base were modelled as contact forces (Bałchanowski, 2012). The transported person's mass was assumed to amount to 90 kg.

The aim of this part of the simulation studies was to determine the kinematic and dynamic parameters of the device during overcoming the stairs. At this stage of the studies the focus was on the changes in the position of the device and passenger's centre of gravity. View of the device and its walking sequence is shown in Fig. 3.

Moving up the stairs takes place with passenger rear-facing. Pressing the "UP" button on the control panel will start the process of entering implemented in two stages. It begins with foot moving downward (Fig. 3a). After touching base, foot takes load from the wheels (Fig. 3b), which together with the entire chassis are raising. Simultaneously wheels axis is moving circularly relative to chassis in the direction of the next stair. Afterwards, wheels touch the surface of the next stair (Fig. 3c). At this point, wheels abruptly takes the load, which was previously on the foot (Fig. 3d), and the step of retracting the foot to the chassis begins. In the presented procedure it is evident, that to maintain the device in balance it is necessary to put in work by the operator, who is omitted in Fig. 3. To overcome the following stair process is repeated with the same sequence.

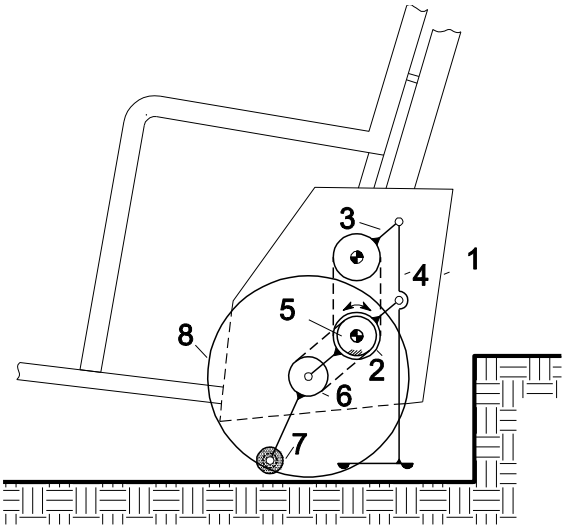

Fig. 2. Kinematic scheme of standard version of stair climber: 1 – frame, 2 – driving chain wheel, 3 – parallelogram chain wheel, 4 – foot (parallelogram connecting link), 5 – stationary chain wheel, 6 – satellite chain wheel, 7 – braking wheel, 8 – driving-walking wheel

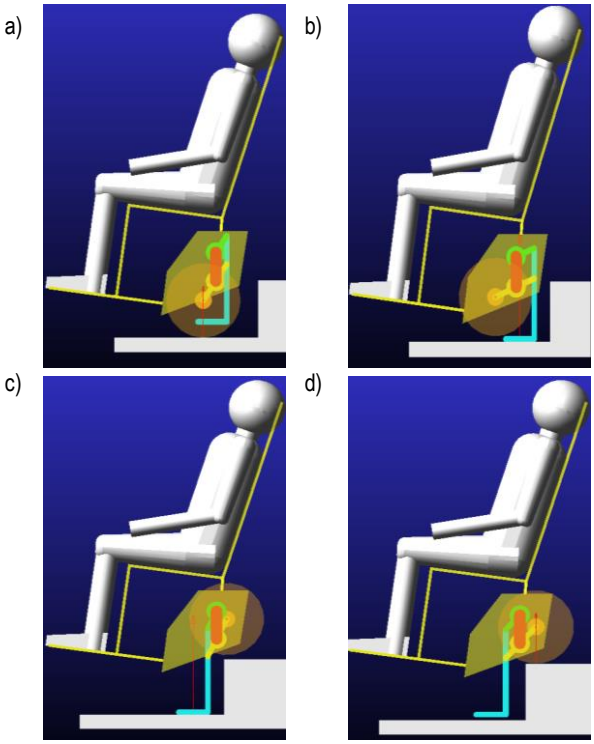

Fig. 3. Stairs walking procedure shown on example of one stair upcoming

Carried out simulations allowed to define quantitative assessment of the operator's applied force during transporter operation and indicate the necessity of modification toward its reduction.

Having in mind operator work facilitation the authors undertook to equip the device with an additional kinematic system whose purpose is to change the position of the centre of gravity of the passenger. The essence of good design of such system is to appropriately develop structure and geometry so as to acquire horizontal movement of seat with passenger in the range sufficient for necessary centre of gravity of man-device system position change relative to actual fulcrum.

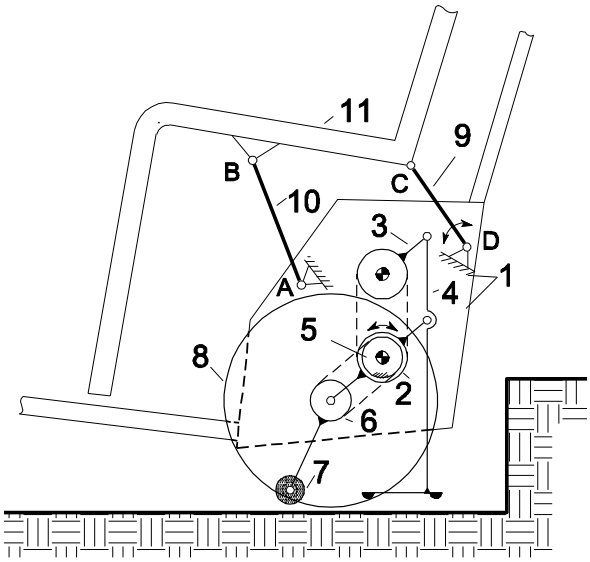

Fig. 4. Kinematic scheme of stair climber with mechanism changing passenger's gravity centre position: 1 – frame, 2 – driving chain wheel, 3 – parallelogram chain wheel, 4 – foot (parallelogram connecting link), 5 – stationary chain wheel, 6 – satellite chain wheel, 7 – braking wheel, 8 – driving-walking wheels 9 – control mechanism crank, 10 – control mechanism rocker, 11 – seat

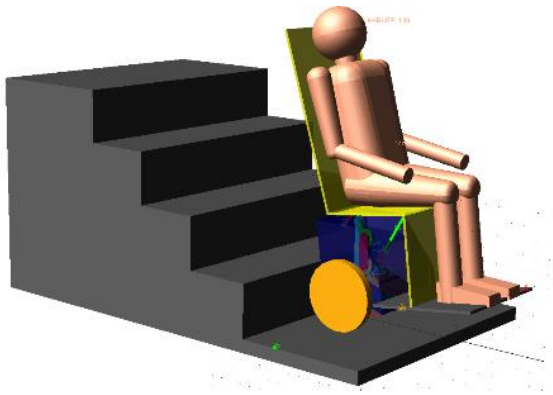

Fig. 5. Model of stair transporter

The authors decided to use four-bar linkage mechanism, whose main advantage is to occur only rotational joint. Geometric synthesis of four-bar linkage was performed using extreme position of seat relative to frame. Next condition was the change of seat angle from horizontal position within ten degrees. The parallelogram mechanism obviously fulfils above assumptions. Unfortunately usage of this mechanism was impossible because of the construction restriction. It was only used as the base for geometric synthesis of four-bar linkage. It consisted of searching AB length and the position of joint B on part 11 (seat) for different position of joint A on frame. Therefore, the synthesis process was brought to a classic task of defining dimensions of the basic four-bar linkage with three coupler position synthesis with alternate attachment points (Miller S., 1987) and additional design criteria. The procedure for dimensions design of the basic four-bar linkage is a separate issue and is not the subject of this work.

Kinematic diagram of the stair transporter mechanism equipped with the changing passenger mass centre position is shown in Fig. 4. The results of the first part of the simulation studies provided the basis for development of control algorithm whose function is to position the centre of gravity of the transported person as close as possible to the point of support of the system.

To sum up, the task of the additional mechanism equipped with a control system is to change the position of the seat so as to make it easier for the operator to keep the passenger in the stability field. The model together with the disabled person in the seat is shown in Fig. 5.

4. MECHATRONIC CONTROL SYSTEM OF STAIR TRANSPORTER

The aim of the next stage in the research was to develop a model and carry out numerical analyses of the device equipped with the mechanism automatically adjusting the position of the centre of gravity. The obtained results were the base for developing a proper mechanical control algorithm (Bałchanowski, 2012; Morales et al., 2010). Fig. 6 shows the procedure of overcoming stairs by the stair transporter. The function of the control system is to properly position the centre of gravity of the passenger relative to one of the two points of support. The location of the point of support depends on the current device configuration (it can be the contact between the base and the driving wheel or the foot).

The purpose of passenger centre of gravity control is to minimize the handle moment needed to achieve balance and thus to reduce the force needed to hold the stair climber by the operator. The moment should have the same sense during the whole work cycle so that the vehicle's handle does not pull the operator down the stairs. Thanks to this requirement the danger that the operator will be pulled towards the base of the stairs, which may result in the fall of and serious injury to both the operator and the transported person, is minimized.

Control is effected through the adjustment, according to relationship (1) of the driving torque in the rotational joint connecting the device casing with crank 9 of the four-bar linkage (Fig. 4) supporting the seat. Control task, which is to consist in keeping the transported person's centre of gravity in the permissible range of positions relative to the support point, is effected by means of two PD controllers. The set value for the first controller is the position of the seat relative to the foot while the position of the seat relative to the driving wheel is the set value for the second controller. Application of two regulators allows to set control parameters independently for control with the foot or wheels as an active fulcrum. A scheme of the control algorithm is shown in Fig. 7. For each regulator, the set value has been matched independently to achieve the control aim described above. At a given instant only one controller is active. The choice of a controller depends on the current point of support – the device can stand on its foot or driving wheel. The base function of PD regulator is to minimize the control error $e(t)$.

$$M = k_P^i \cdot e(t) + k_D^i \cdot \frac{\mathrm{d}e(t)}{\mathrm{d}t} \tag{1}$$

where: $M -$ the crank torque, $e(t) = q_{set}^i - q -$ control error, $\frac{de(t)}{dt} = \frac{d(q_{set}^i - q)}{dt} = \frac{dq_{set}^i}{dt} - \frac{dq}{dt}$, $q_{set}^i -$ the set position for the i-th controller, $q -$ the actual value of passenger's centre of gravity relative to chassis, $\frac{dq_{set}^i}{dt} -$ derivative of set value for i-th controller, $\frac{dq}{dt} -$ derivative of actual value, $i = \begin{cases} 1 \\ 2 \end{cases} for \begin{matrix} F_n > 0 \\ F_n \leq 0 \end{matrix}$, where: $F_N -$ the pressure force measured in the foot base, $\mathrm{i} = 1$ for the controller connected with the leg, $i = 2$ for the controller connected with the driving wheel.

DOI 10.1515/ama-2015-0034

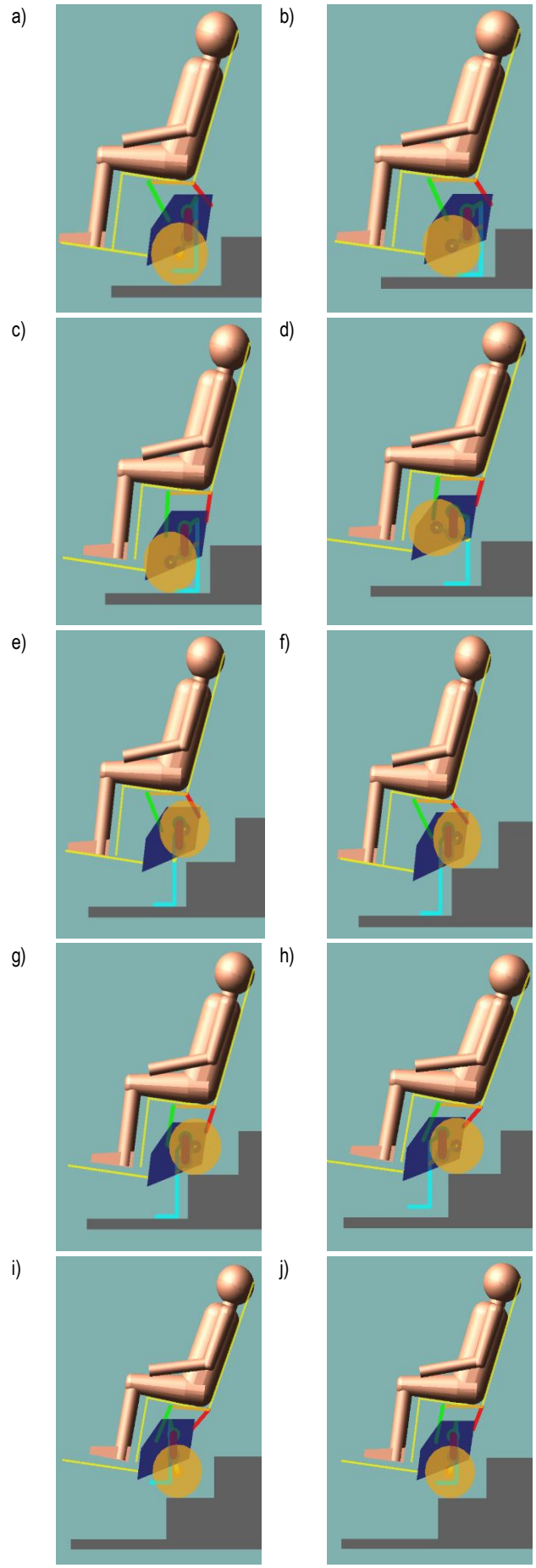

Fig. 6. Procedure of overcoming stairs, illustrated for single stair

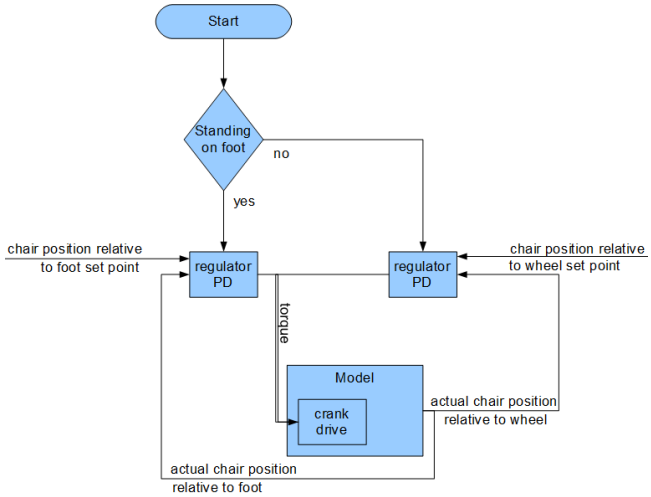

Fig. 7. Block diagram of control

In the climbing process repeating cycles can be distinguished. Each cycle consists of four phases. During first phase weight of device with passenger lay on driving wheels. In control algorithm, PD regulator, whose set value is determined by position of seat relative to driving wheels, is active. The crank torque is computed, according to equation (1), for keeping passenger in the appropriate position relative to chassis of the mechanism. Value of the control signal depends on value of the error signal e(t). The greater the error, the greater the control signal is, according to the value of proportional part parameter. Additionally, derivative part of the regulator is used. It is assumed to correct control signal in situation when the error signal is changing quickly. When error signal is increasing, value that is product of error derivative and derivative part parameter, is added to control signal. As a result, the regulator's output signal is increased as a reaction to increasing error. In case of decreasing error the reaction of regulator is similar. The derivative part of regulator decreases value of control signal. According to that, the over-regulation is eliminated in control algorithm. This over-regulation would cause yaw of seat, which would be very unpleasant for the passenger. After initiation of gait sequence in stair climber, driving wheel changes position relative to chassis. Seat also changes position according to maintain its and passenger centre of gravity above the wheel and base fulcrum. In certain moment the foot of mechanism touches the base and second fulcrum is created. This is the second phase of cycle, in which weight of device and passenger lay on both driving wheel and foot. At this moment controller changes active regulator to that which present value is measured relative to foot. Seat is moving, so that centre of gravity is above the foot. Driving wheel is moving of the base.

The third phase begins, in which the weight lay only on foot. Working of algorithm is similar to phase one but control error is substrate of seat position and position of foot and base fulcrum. Next, mechanism comes into fourth phase, in which weight lay on foot and driving wheel simultaneously. Algorithm works similarly to phase two. Controller changes active regulator to that, which set value is relative to position of driving wheel. Seat is moving so that its and passenger's mass centre is above driving wheel and base fulcrum. Next, algorithm comes into phase one and the cycle is looped.

5. RESULTS OF SIMULATION STUDIES

The numerical model of the stair transporter equipped with the mechanism for changing the position of the passenger's centre of gravity, and with a control system was used to study the dynamics of the whole device together with its passenger for one full work cycle. In the model the force put in by the operator was replaced with constraints keeping the device in a specified orientation. The moment of force which needs to be applied to the handle in order to keep the position of balance was treated equally with the moment applied to the stair climber body by the operator.

In the simulations a single cycle time of 6.5 s was assumed. In the first 0.5 s the position of balance would be reached. Fig. 6 shows the graphs of changes in the moments which need to be applied to the device body in order to keep it balanced for the standard device and the one equipped with a controllable mechanism aiding the operator work. It appears from Fig. 6 that during most of the working period the balancing moment value in the model with control is lower. The peaks visible in Fig. 8 are caused by changes in the point of support, which are practically stepwise. The demand for moment in the control mechanism is shown in Fig. 9, but its maximum value in the control system was limited to 100 Nm. The pattern of changes in torque in the main drive (Fig. 10) is practically the same for the two models.

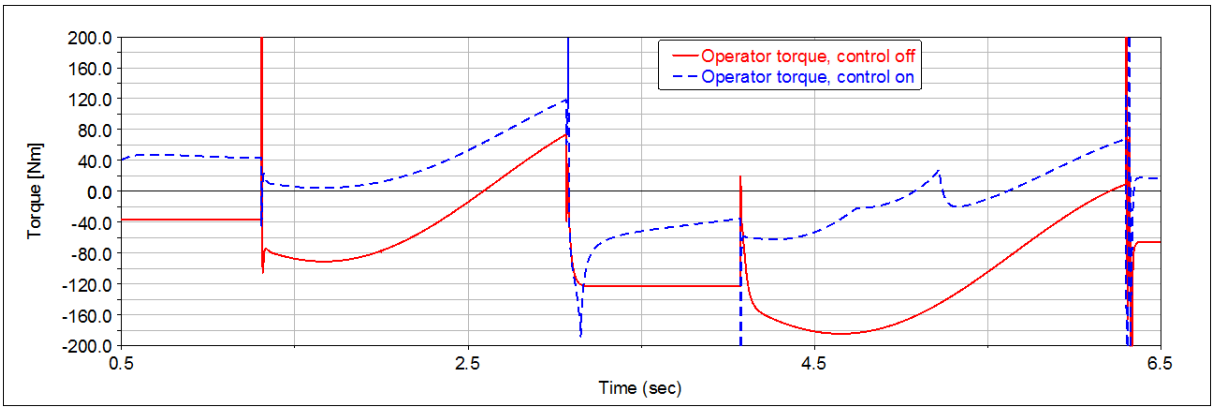

Fig. 8. Changes in moment applied to device body

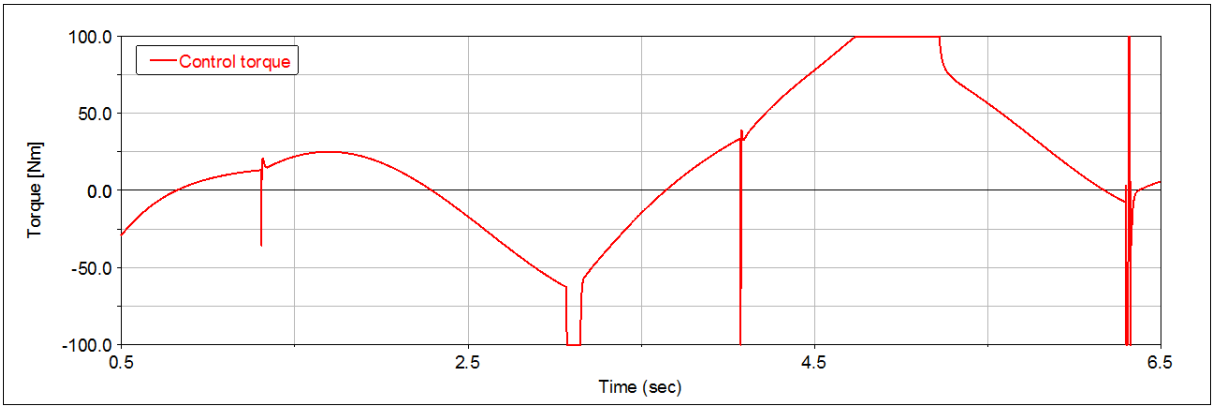

Fig. 9. Changes in torque in controlling drive

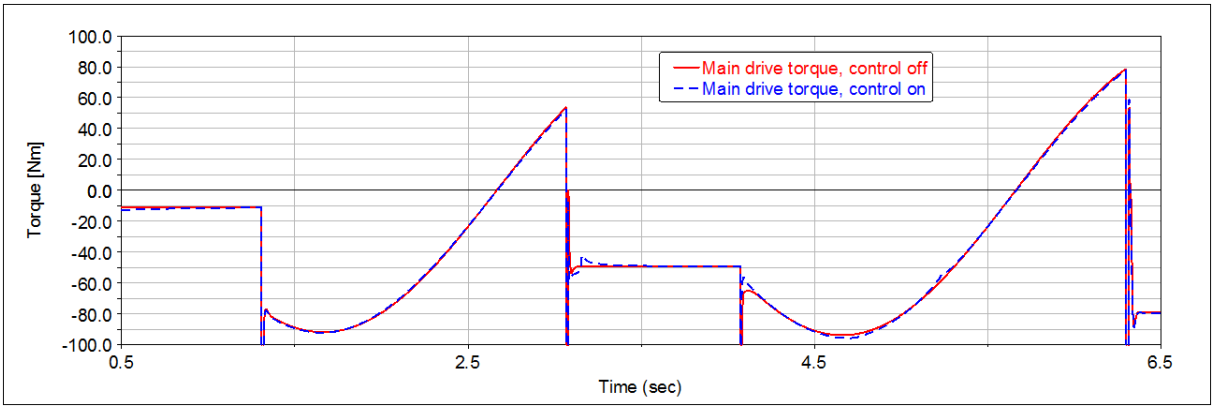

Fig. 10. Changes in torque in main drive

DOI 10.1515/ama-2015-0034

6. CONCLUSION

The results of the simulation studies have shown, that the design of the easing mechanism added to standard stair climber, is correct. Control is effected through adjusting the torque of the four-bar linkage crank.

Two PD controllers are used for this purpose. One of the controllers is input with the set position of the seat relative to the foot, whereas the other is input with the set position of the driving-walking wheel (only one controller operates at a time). The selection of the active controller depends on the point of support (the driving-walking wheel/the foot).

The proposed equipment of the stair climber with the additional mechanism changing the position of the passenger's centre of gravity significantly aids the work of the operator. Thanks to this solution the operator's effort is considerably reduced. The results of the kinematics and dynamics simulation studies show that a battery powered electric drive can be used for the mechanism. The operation of the device equipped with a sensor and control system can significantly improve the operator's work comfort.

A drawback of the solution is that a change in the position of the passenger's centre of gravity requires an additional time for the change of the mechanism configuration.

The simulation studies were carried out for a constant transporter orientation. In reality the operator changes this orientation continuously, seeking an orientation which requires the least effort. In further research the effect of the decisions made by the operator should be included in the model.

REFERENCES

1. **Bałchanowski J., (**2012**),** Mobile Wheel-Legged Robot: Researching of Suspension Leveling System, *Advances in Mechanisms Design*, eds. Jaroslav Beran et al., Dordrecht et al., Springer, 3-12.
2. **Bałchanowski J., Gąsieniec P.,** (2010), Design and Simulation Researches of mobile Walking Robot (in Polish), Acta Mechanica et Automatica, 4(2), 9-16.
3. **Bałchanowski J., Gronowicz A., (**2012**),** Design And Simulations of Wheel-Legged Mobile Robot**,** *Acta Mechanica et Automatica*, 6(2), 11-16.
4. **Fang L., Lu T., Yuan K., Shen X., Li L**. (2011), Design and Development of an Electric-Powered Stair Climbng Wheelchair, *Proccedings of 9th World Congress on Intelligent Control and Automation (WCICA)*, Tai Pei, Taiwan, 474-479.
5. **Gonzalez A, Ottaviano E., Ceccarelli M.** (2009), On the kinematic functionality of a four-bar based mechanism for guiding wheels in climbing steps and obstacles, *Mechanism and Machine Theory*, 44, 1507–1523.
6. **Laffont I., Guillon B., Fermanian C., Pouillot S., Even-Schneider A., Boyer F., Ruquet M., Aegerter P., Dizien O., Lofaso F.,** (2008), Evaluation of a Stair-Climbing Power Wheelchair in 25 People with Tetraplegia, *Arch Phys Med Rehabil*, 89, 1958-1964.
7. **Miller S.,** (1987), Kinematic Systems. Design Fundamentals (in Polish), WNT.
8. **Morales R., Feliu V., González A.,** (2010), Optimized Obstacle Avoidance Trajectory Generation for a Reconfigurable Staircase Climbing Wheelchair, *Robotics and Autonomous Systems*, 58, 97-114.
9. **Shriwaskar A.S., Choudhary. S.K.,** (2013). Synthesis, Modeling & Simulation of Stair Climbing Mechanism, *International Journal of Engineering Research & Technology*, 2(8), 413-419.
10. **Trochimczuk R., Kuźmierowski T.** (2014), Kinematic Analysis of CPM Machine Supporting To Rehabilitation Process After Surgical Knee Arthroscopy And Arthroplasty, *International Journal of Applied Mechanics and Engineering*, 19(4), 841-848.
11. **Yu S., Wang T., Wang Z., Wang Y., Yao C., Li X.** (2013), Wheelchair Robot Equipped with Variable Geometry Single Tracked Mechanisms, *Journal of Mechanical Engineering*, 49(13), 40-47.
12. http://www.aatgb.com/downloads/pdf/smax_aircraft_de.pdf

CYCLIC LINEAR RANDOM PROCESS AS A MATHEMATICAL MODEL OF CYCLIC SIGNALS

Sergiy LUPENKO*, Nadiia LUTSYK*, Yuri LAPUSTA**

*Ternopil Ivan Pul'uj National Technical University,46001, Ruska str. 56, Ternopil, Ukraine.
**French Institute of Advanced Mechanics, Institut Pascal / UBP / IFMA / CNRS / Clermont Université, BP 265, 63175 Aubière CEDEX, France.

lupenko@ua.fm, lutsyk.nadiia@gmail.com, yuri.lapusta@ifma.fr

received 21 April 2015, revised 11 December 2015, accepted 14 December 2015

Abstract: In this study the cyclic linear random process is defined, that combines the properties of linear random process and cyclic random process. This expands the possibility describing cyclic signals and processes within the framework of linear random processes theory and generalizes their known mathematical model as a linear periodic random process. The conditions for the kernel are given and the probabilistic characteristics of generated process of linear random process in order to be a cyclic random process. The advantages of the cyclic linear random process are presented. It can be used as the mathematical model of the cyclic stochastic signals and processes in various fields of science and technology.

Keywords: Linear Cyclic Random Process, Mathematical Model, Rhythm Function, Factorized Kernel

1. INTRODUCTION

Linear stochastic processes are widely studied in different fields of science, particularly in radio signals modeling, in technical and medical diagnostics, hydroacoustics, geophysics etc. (Yurekli et al., 2005; Blake and Thomas, 1968; Bartlett, 1955; Medvegyev, 2007; Bhansali, 1993; Giraitis, 1985; Olanrewaju and Al-Arfaj, 2005). A characteristic feature of linear random process (LRP) is its constructiveness, namely LRP is specified as a structure − stochastic integral Stieltjes of the process of independent (or not correlated) increments. Furthermore, it is possible to implement the description and analysis of signals using the multivariate distribution functions on the basis of LRP and to perform simulations using computers. The problem of identifying the elements of its structure from the known (given) probability characteristics of the signals and processes is somewhat difficult in applying LRP simulation to model real signals and processes.

In the scientific literature there exist two important subclasses of linear stochastic processes. These are stationary linear random processes (Bartlett, 1950) and linear periodic random processes (Martchenko, 1998; Zvarich and Marchenko, 2011; Pagano, 1978). Stationary linear random processes are used as appropriate models of stochastic signals with time-invariant probability characteristics. The linear periodic random processes allow to take into account randomness and recurrence of the studied cyclic signals that is provided by the periodicity of the process probabilistic characteristics.

In many cases, when the rhythm of a cyclic signal varies, the hypothesis about the periodicity of its probability characteristics is inadequate to the structure of the real signal. Therefore, it is not quite correct to apply a linear periodic random process. In this case, it is more correct to apply the class of cyclic random processes (CRP), defined in the work (Lupenko, 2006). This class includes class of periodic random processes (PRP) as its particular cases and accounts for the variability of cyclic signals rate (Naseri et al.,2013).

Since the class of cyclic random processes is wider class of processes than the class of periodic random processes, it is useful to define a class of random processes which is the intersection of cyclic classes of random processes and linear random processes. In this work a linear cyclic random process (LCRP) is defined. It combines the properties of linear random process and cyclic random process, in order to broaden the possibility of using a constructive approach to the description of cyclic signals and processes in the theory of linear stochastic processes. The conditions are given to be met by the kernel and probabilistic characteristics of generated process of linear random process to be a cyclic random process. An example of linear cyclic random process and its probabilistic characteristics are given.

2. DEFINITIONS AND BASIC PROPERTIES OF LINEAR RANDOM PROCESS

Let's present briefly some main equations for the LRP and CRP. LRP can be presented in the form of a stochastic Riemann integral (Berkes and Horváth, 2006):

$$\xi(\omega,t)=\int_{-\infty}^{\infty}\varphi(t,\tau)\zeta(\omega,\tau)d\tau,\omega\in\Omega,\ t\in R, \tag{1}$$

or as an Stieltjes integral over the stochastic measure (Protter, 2005):

$$\xi(\omega,t)=\int_{-\infty}^{\infty}\varphi(t,\tau)d\eta(\omega,\tau),\omega\in\Omega,\ t\in R, \tag{2}$$

where $\varphi(t,\tau)$ is a square-integrable deterministic function with respect to variable τ, which is called the kernel of LRP $\xi(\omega,t)$, the random process $\eta(\omega,t),\ \omega\in\Omega,\ t\in R$ is a process with independent (uncorrelated) increments, which is named as a generated process, the generalized derivative of which is a white noise $\zeta(\omega,t),\ \omega\in\Omega,\ t\in R$ in the narrow (broad) sense (Ω is a set of elementary events). From the application

DOI 10.1515/ama-2015-0035

point of view, LRP is a process from the output of a linear system with impulse response $\varphi(t,\tau)$, if white noise $\zeta(\omega,t),\ \omega\in\Omega,\ t\in R$ acts on its input (Fig. 1).

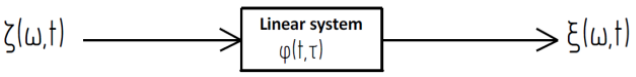

Fig. 1. The schematic presentation of LRP generation

Note that a random process $\eta(\omega,t),\ \omega\in\Omega,\ t\in R$ is the process with independent (uncorrelated) increments if for some fixed t_0 for all $t_{-m}<t_{-m+1}<\ldots<t_{-1}<t_0<t_1<\ldots<t_{n-1}<t_n$ $(m,n\in \mathrm{Z})$ from R the random values:

$$\begin{aligned}&\eta(\omega,t_{-m})-\eta(\omega,t_{-m+1}),\ldots,\eta(\omega,t_0)-\eta(\omega,t_{-1}),\\&\eta(\omega,t_0),\eta(\omega,t_1)-\eta(\omega,t_0),\ldots,\eta(\omega,t_n)\\&\qquad-\eta(\omega,t_{n-1})\end{aligned}\tag{3}$$

are independent (uncorrelated).

In case of LRP, one can write the logarithm of its multidimensional characteristic function $f_{k_\xi}(u_1,\ldots,u_k;t_1,\ldots,t_k)$ in the form of Levy:

$$\begin{aligned}&lnf_{k_\xi}(u_1,\ldots,u_k;t_1,\ldots,t_k)=\\&=i\textstyle\sum_{j=1}^{k}u_j\int_{-\infty}^{\infty}\varphi(\tau,t_j)d\mu(\tau)-\\&-\textstyle\sum_{i,j=1}^{k}u_iu_j\int_{-\infty}^{\infty}\varphi(\tau,t_i)\varphi(\tau,t_j)d\sigma(\tau)+\\&+\textstyle\int_{-\infty}^{\infty}\int_{-\infty}^{\infty}[e^{ix\sum u_j\varphi(\tau,t_j)}-1-\\&-\frac{ix}{1+x^2}\textstyle\sum_{k=1}^{n}u_j\varphi(\tau,t_j)]d_xd_\tau L(x,\tau)\end{aligned}\tag{4}$$

where $L(x,\tau)$ is a function, undefined at zero that is called Poisson spectrum jumps in the form of Levi. This function is defined as:

$$L(x,\tau)=\begin{cases}M(x,\tau), & x<0,\\ N(x,\tau), & x>0,\end{cases}\tag{5}$$

where $M(x,\tau)$ and $N(x,\tau)$ ($M(-\infty,\tau)$=$N(\infty,\tau)$=0) are non-decreasing functions that set negative and positive jumps (increments) of generating process, respectively.

Functions $\mu(\tau)$ and $\sigma(\tau)$ are defined as follows:

$$d\mu(\tau)=d\chi_1(\tau)-d\tau\cdot\textstyle\int_{-\infty}^{\infty}xd_xL(x,\tau)\tag{6}$$

$$d\sigma(\tau)=d\chi_2(\tau)-d\tau\cdot\textstyle\int_{-\infty}^{\infty}(1+x^2)d_xL(x,\tau)\tag{7}$$

where $\chi_1(\tau)$ and $\chi_2(\tau)$ are first and second cumulant functions of generated process $\eta(\omega,\tau)$.

3. DEFINITIONS AND BASIC PROPERTIES OF CYCLIC RANDOM PROCESS

The cyclic random process of a continuous argument is characterized by the fact that its family of distribution functions satisfies the following equation:

$$\begin{aligned}&F_{k_\xi}(x_1,\ldots,x_k,t_1,\ldots,t_k)=\\&=F_{k_\xi}(x_1,\ldots,x_k,t_1+T(t_1,n),\ldots,t_k+T(t_k,n)),\\&x_1,\ldots,x_k,t_1,\ldots,t_k\in R,n\in Z,k\in N.\end{aligned}\tag{8}$$

The rhythm function $\mathrm{T(t,n)}$ has the following properties:

1. $T(t,n)>0$, if $n>0$ $(T(t,1)<\infty)$;
   $T(t,n)=0$, if $n=0$; (9)
   $T(t,n)<0$, if $n<0$, $t\in \mathrm{R}$.
2. For any $t_1\in R$ and $t_2\in R$ for which $t_1<t_2$, the strict inequality holds for the function $T(t,n)$:
   $$T(t_1,n)+t_1<T(t_2,n)+t_2,\ \forall n\in Z.\tag{10}$$
3. Function $T(\mathrm{t,n})$ is the smallest by absolute value $(|T(t,n)|\le|T_\gamma(t,n)|)$ among all such functions $\{T_\gamma(t,n),\ \gamma\in\Gamma\}$ satisfying the conditions (9) and (10).

In other words, the cyclic random process is a random process, the distribution functions of which are invariant to cyclic countable discontinuous group of transformations $\Gamma=\{\mathrm{T_n(t)=t+T(t,n),\ n\in Z}\}$ for a set of time arguments.

Note that the family of characteristic functions and moment functions (if they exist) of cyclic random process also satisfy the condition of invariance, which is similar to the condition (8). Thus, they are invariant to cyclic countable discontinuous group of transformations $\Gamma=\{\mathrm{T_n(t)=t+T(t,n),\ n\in Z}\}$.

In particular, according to reference (Giraitis, 1985), we will give the definition of the process with the independent cyclical increments.

The stochastically continuous process with independent increments $\eta(\omega,\mathrm{t})$ will be called the process with independent cyclic increments if there is a function $\mathrm{T(t,n)}$ that satisfies the rhythm functions conditions, that is, for a fixed $\mathrm{h>0}$ the distributions of increments (differentials) $\Delta_\mathrm{h}\eta(\omega,\mathrm{t})(\mathrm{d}\eta(\omega,\mathrm{t}))$ and $\Delta_\mathrm{h}\eta(\omega,\mathrm{t+T(t,n)})$ $(\mathrm{d}\eta(\omega,\mathrm{t+T(t,n)}))$ are the same for any $\mathrm{n\in Z}$ and for any $\mathrm{t\in R}$.

4. LINEAR CYCLIC RANDOM PROCESS

To take into account the cyclicity of the probabilistic characteristics of LRP, we can impose relevant conditions on its kernel $\varphi(t,\tau)$ and probabilistic characteristics of the generated process $\eta(\omega,t),\ \omega\in\Omega,\ t\in R$. Namely, a linear stochastic process $\xi(\omega,t)$ is cyclic in the following cases:

1. When $\varphi(t,\tau)=\varphi(t-\tau)$, that is, a linear system is stationary (time-invariant) with the same parameters, and the generated random process $\eta(\omega,t),\ \omega\in\Omega,\ t\in R$ is a process with independent (uncorrelated) cyclic increments, with the function of rhythm $\mathrm{T(t,n)}$;
2. When $\varphi(t,\tau)=\varphi(t+T(t,n),\tau)$, that is a linear system is described by a cyclic linear operator, and the generated process is a homogeneous random process with independent (uncorrelated) increments;
3. When $\varphi(t,\tau)=\varphi(t+T(t,n),\tau)$, that is a linear system is described by a cyclic linear operator, and the generated random process $\eta(\omega,t),\ \omega\in\Omega,\ t\in R$ is a process with independent (uncorrelated) cyclic increments of the rhythm function $T(t,n)$.

If the condition of generated process $\eta(\omega,t),\ \omega\in\Omega,\ t\in R$ increments non-correlatedness holds true, we have a linear cyclic random process in a broad sense. This means that its expectation and correlation function are cyclic on the set of its two arguments. If you require an independence of generated process

increments, we obtain a linear cyclic random process in the narrow sense, for which its multidimensional distribution functions and characteristic functions are cyclic on the set of all time arguments.

We will show the correctness of formulated conditions of the cyclical linear random process only for the second case when the generated process is homogeneous. In this case $L(x,\tau) = L(x)$,$\mu(\tau) = m\sigma(\tau) = \sigma$, and the kernel of a linear process is a cyclic function for argument τ. Then, for the characteristic function (4) we have:

$$\begin{aligned}
&lnf_k(u_1,\dots,u_k;t_1,\dots,t_k) = \\
&= im\sum_{j=1}^{k} u_j \int_{-\infty}^{\infty} \varphi(\tau,t_j)d\tau - \\
&-\sigma^2 \sum_{i,j=1}^{k} u_i u_j \int_{-\infty}^{\infty} \varphi(\tau,t_i)\varphi(\tau,t_j)d\tau + \\
&+ \int_{-\infty}^{\infty}\int_{-\infty}^{\infty}[e^{ix\sum u_j\varphi(\tau,t_j)} - 1 - \\
&-\frac{ix}{1+x^2}\sum_{k=1}^{n} u_j\varphi(\tau,t_j)]dL(x)d\tau = im\sum_{j=1}^{k} u_j \times \\
&\times \int_{-\infty}^{\infty} \varphi\left(\tau,t_j+T(t_j,n)\right)d\tau - \sigma^2\sum_{i,j=1}^{k} u_i u_j \times \\
&\times \int_{-\infty}^{\infty} \varphi(\tau,t_i+(T(t_i,n))\varphi(\tau,t_j+T(t_j,n))d\tau + \\
&+ \int_{-\infty}^{\infty}\int_{-\infty}^{\infty}[e^{ix\sum u_j\varphi\left(\tau,t_j+T(t_j,n)\right)} - 1 - \frac{ix}{1+x^2}\sum_{k=1}^{n} u_j \times \\
&\times \varphi\left(\tau,t_j+T(t_j,n)\right)dL(x)d\tau = lnf_k(u_1,\dots,u_k;t_1 + \\
&+T(t_1,n),\dots,t_k+T(t_k,n))
\end{aligned} \tag{11}$$

That is, the linear random process $\xi(\omega,t)$ is a cyclic random process with a rhythm function $T(t,n)$. The moment functions of such a linear random process are also cyclic. Consider this only for its two first moment functions − mathematical expectation and correlation function. These moment functions fully exhaust the description of a LRP in the broad sense, when only the non-correlatedness of the generated process increments is required, rather than their independence. In this case, we can write the following expression for the expectation function LCRP:

$$\begin{aligned}
&m_\xi(t) = M\{\xi(\omega,t)\} = m\int_{-\infty}^{\infty}\varphi(t,\tau)d\tau = \\
&= m\int_{-\infty}^{\infty}\varphi(t+T(t,n),\tau)d\tau = M\{\xi(\omega,t+T(t,n))\}, \\
&t\in R, n\in Z,
\end{aligned} \tag{12}$$

where m is the homogeneous process $\eta(\omega,t),\ \omega\in\Omega,\ t\in R$ increments expectation with uncorrelated increments.

For the correlation function LCRP, we have:

$$\begin{aligned}
&R_\xi(t_1,t_2) = M\{\dot{\xi}(\omega,t_1)\dot{\xi}(\omega,t_2)\} = \\
&\sigma^2\int_{-\infty}^{\infty}\varphi(t_1,\tau)\varphi(t_2,\tau)d\tau = \\
&= \sigma^2\int_{-\infty}^{\infty}\varphi(t_1+T(t_1,n),\tau)\varphi(t_2+T(t_2,n),\tau)d\tau = \\
&= R_\xi(t_1+T(t_1,n),t_2+T(t_2,n)), \qquad t_1,t_2\in R, n\in Z,
\end{aligned} \tag{13}$$

where σ is standard deviation of increments homogeneous process $\eta(\omega,t),\ \omega\in\Omega,\ t\in R$ with uncorrelated increments.

That is, LCRP expectation is a cyclic deterministic function with the rhythm function $T(t,n)$, and its correlation function is cyclic with the rhythm function $T(t,n)$.

5. PARTICULAR CASE OF CYCLIC LINEAR RANDOM PROCESS WITH FACTORIZED KERNEL

In a particular case when the LRP kernel $\varphi(t,\tau)$ can be factorized, it is represented as a product of two functions:

$$\varphi(t,\tau) = \varphi_1(t)\varphi_2(\tau),\ t,\ \tau\in R, \tag{14}$$

then a LRP looks like:

$$\begin{aligned}
&\xi(\omega,t) = \int_{-\infty}^{\infty}\varphi_1(t)\varphi_2(\tau)d\eta(\omega,\tau) = \\
&= \varphi_1(t)\int_{-\infty}^{\infty}\varphi_2(\tau)d\eta(\omega,\tau),\ \omega\in\Omega,\ t\in R
\end{aligned} \tag{15}$$

This presentation is equivalent to the presentation of a random process as a product of deterministic function $\varphi_1(t)$ and random variable $A(\omega)$, namely:

$$\xi(\omega,t) = \varphi_1(t)\cdot A(\omega), \omega\in\Omega,\ t\in R \tag{16}$$

where $A(\omega) = \int_{-\infty}^{\infty}\varphi_2(\tau)d\eta(\omega,\tau)$ is a random functional.

If, in this case, the function $\varphi_1(t) = \varphi_1\left(t+T(t,n)\right)$ is a cyclic numerical function, then the formulae (12) and (13) take the following form:

$$\begin{aligned}
&m_\xi(t) = M\{\xi(\omega,t)\} = m\int_{-\infty}^{\infty}\varphi(t,\tau)d\tau = \\
&= m\int_{-\infty}^{\infty}\varphi_1(t)\varphi_2(\tau)d\tau = m\varphi_1(t)\int_{-\infty}^{\infty}\varphi_2(\tau)d\tau, \\
&t\in R, n\in Z,
\end{aligned} \tag{17}$$

$$\begin{aligned}
&R_\xi(t_1,t_2) = \sigma^2\int_{-\infty}^{\infty}\varphi(t_1,\tau)\varphi(t_2,\tau)d\tau = \\
&= \sigma^2\int_{-\infty}^{\infty}\varphi_1(t_1)\varphi_1(t_2)\varphi_2(\tau)\varphi_2(\tau)d\tau = \\
&= \sigma^2\varphi_1(t_1)\varphi_1(t_2)\int_{-\infty}^{\infty}\left(\varphi_2(\tau)\right)^2 d\tau, \\
&t_1,t_2\in R, n\in Z.
\end{aligned} \tag{18}$$

The problem of identifying the elements of its structure from the known probability characteristics of the studied signals and processes is somewhat difficult in applying LRP simulation to model real signals and processes. In this case, the probability characteristics cyclicity of a LRP is due to cyclical numerical function $\varphi_1(t)$.

Consider an example of LCRP and its probability characteristics in the case of LCRP kernel factorizing. Let LCRP kernel has the form:

$$\varphi(t,\tau) = sin(2t^2)e^{-0.3\tau}cos(\tau),\ t\in(0,\infty),\ \tau\in R, \tag{19}$$

and the generated stochastic process $\eta(\omega,t),\ \omega\in\Omega,\ t\in R$ is a homogeneous process with independent increments with expectation m and standard deviation σ of its increments. Then, the linear cyclic random process will look like:

$$\begin{aligned}
&\xi(\omega,t) = sin(2t^2)\int_{-\infty}^{\infty}e^{-0.3\tau}cos(\tau)d\eta(\omega,\tau), \\
&\omega\in\Omega, \qquad t\in(0,\infty)
\end{aligned} \tag{20}$$

and its expectation and correlation function will be:

$$\begin{aligned}
&m_\xi(t) = msin(2t^2)\int_{-\infty}^{\infty}e^{-0.3\tau}cos(\tau)d\tau, \\
&t\in(0,\infty), \quad n\in Z,
\end{aligned} \tag{21}$$

$$\begin{aligned}
&R_\xi(t_1,t_2) = \\
&\sigma^2 sin(2t_1{}^2)sin(2t_2{}^2)\int_{-\infty}^{\infty}\left(e^{-0.3\tau}cos(\tau)\right)^2 d\tau, \\
&t_1,t_2\in(0,\infty), \qquad n\in Z.
\end{aligned} \tag{22}$$

Fig. 2 and 3 show plots of kernel sections $\varphi(t,\tau)$ (19) for fixed values of t and τ.

Fig. 4 presents a plot of the expectation function, and Fig. 5 represents the plot of section correlation function LCRP.

It can be seen from Fig. 4 and 5, that the respective probabilistic characteristics of LRP are cyclic.

DOI 10.1515/ama-2015-0035

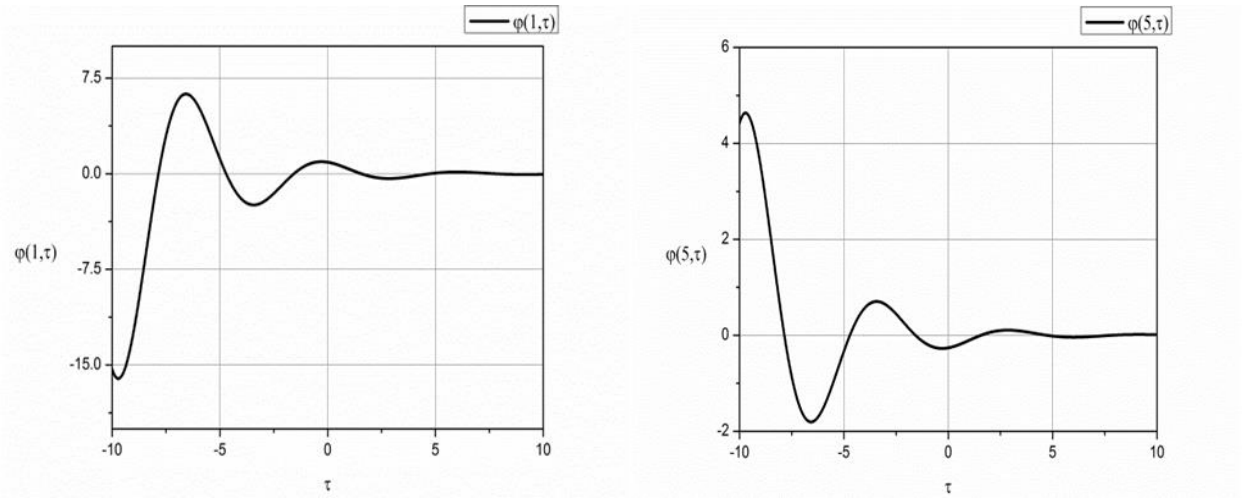

Fig. 2. Plots of kernel sections $\varphi(t,\tau)$ for some fixed values of t (t =1 left and t =5 right)

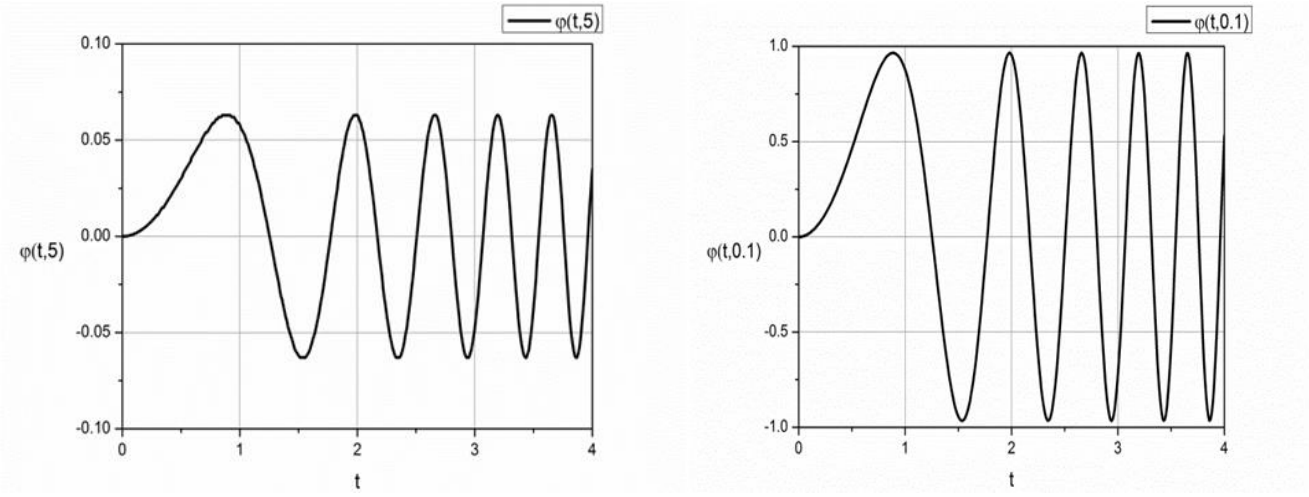

Fig. 3. Plots of kernel sections $\varphi(t,\tau)$ for fixed values of $\tau(\tau = 0.1$ left and $\tau = 5$ right)

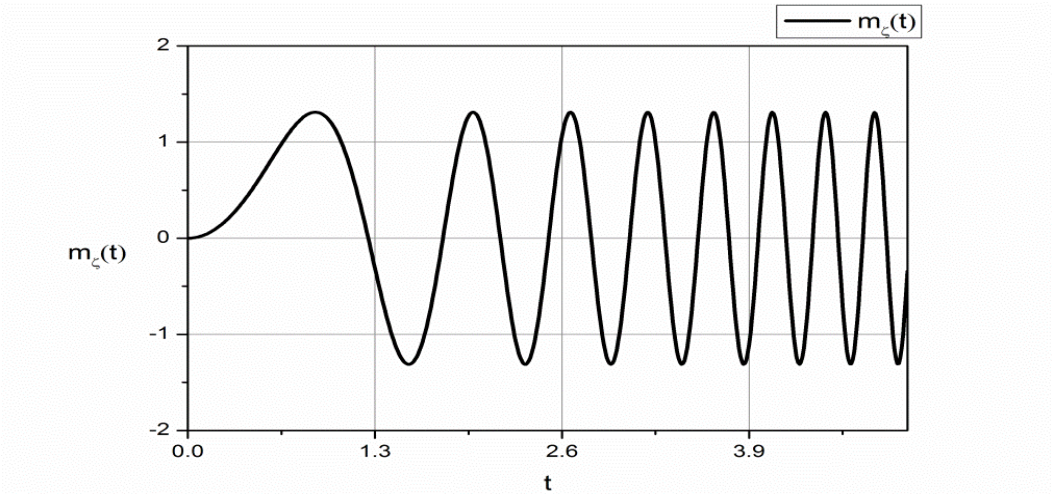

Fig. 4. Plot of linear cyclic random process expectation

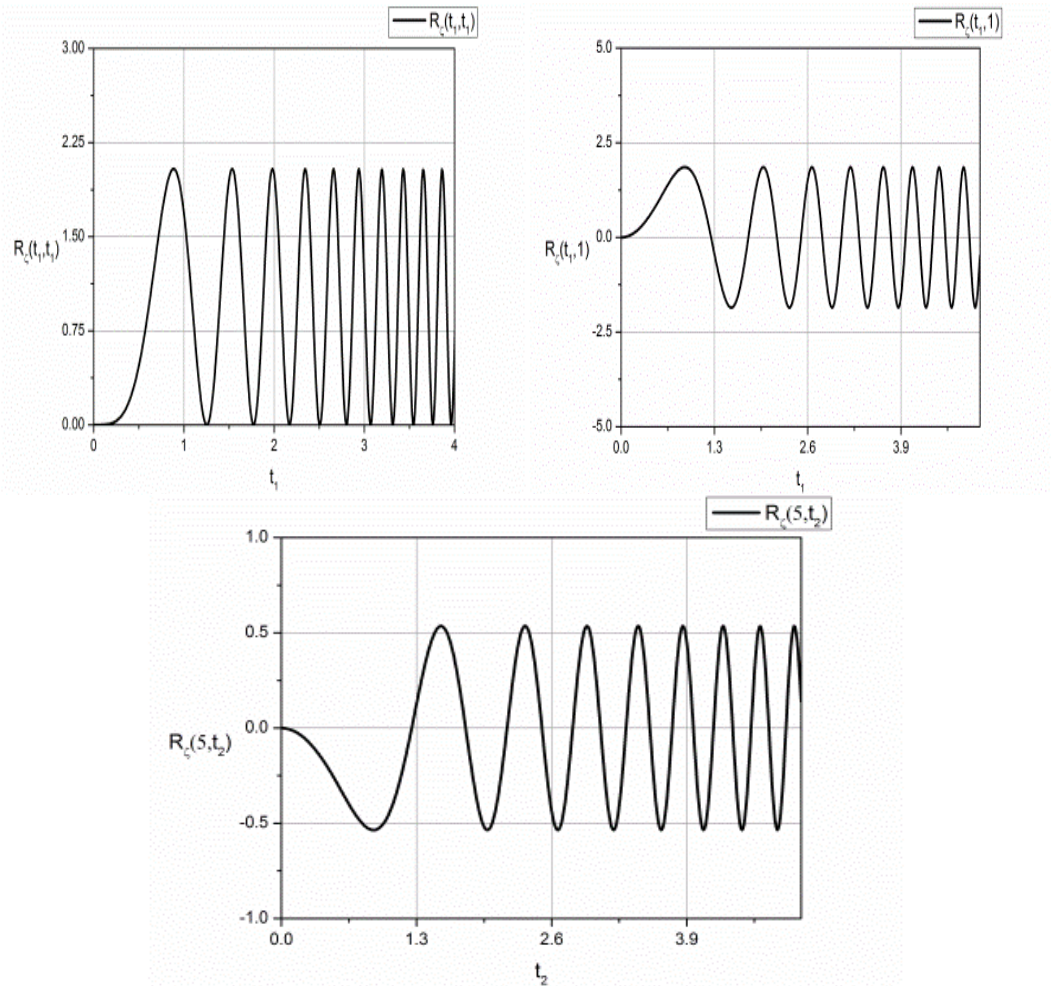

Fig. 5. Plots of correlation function $R_\xi(t_1, t_2)$ section of linear cyclic random process a) $R_\xi(t_1, t_1)$, *b)* $R_\xi(t_1, 1)$, *c)* $R_\xi(5, t_2)$

6. SOME ADVANTAGES OF LINEAR CYCLIC RANDOM PROCESS

The LCRP that is proposed in this study has the advantage, that allows to take into account the variation of rhythm of the investigated signals and processes as compared with known mathematical models of random cyclic signals and processes such as periodically correlated random process (cyclic stationary random process) (Gardner et al., 2006; Hurd and Miamee, 2006), periodically distributed random process, linear periodic random process.

Namely the following advantages in modeling of cyclic signals and processes can be mentioned in comparison with the known cyclic random process.

1. The entire probabilistic structure of LCRP is completely determined by the deterministic kernel $\varphi(t, \tau)$ and characteristics $L(x, \tau)$, $\mu(\tau)$, $\sigma(\tau)$ of its generated process, which can be parameterized in many applied problems. This allows a compact and economical description of the studied stochastic signals of the cyclic structure.
2. Using LCRP as the mathematical model, cyclic stochastic signals and processes can be explored in a broad range of probability characteristics, namely within the framework of the spectral correlation theory of random processes, within the framework of the higher orders moment distribution functions, within the framework of the multivariate distribution functions and characteristic functions.
3. LCRP remains LCRP after transformation by a linear dynamic system. This LCRP has unchanged characteristics of the generated process. It has the changed kernel only. This property simplifies the study of the transformations of cyclic stochastic signals in the linear systems that often arise in the problems of radio engineering, technical and medical diagnostics, geophysics and mechanics.
4. The result of the LCRP constructiveness is the ability to display the mechanisms of the studied signals formation in the LCRP structure that allows to study the influence of various parameters of generation process mechanism on its probabilistic characteristics.
5. The construction of the LRCP is directly suitable for generating and simulating cyclic stochastic signals and processes by modern software and hardware systems.

7. CONCLUSIONS

1. The linear cyclic random process is defined. It combines the properties of linear random process and cyclic random process. This enables the extension of a constructive approach to the description of cyclic signals within the linear theory of random processes and summarizes their mathematical model as a linear periodic random process.
2. The conditions are given for the kernel and the probabilistic characteristics of generated process of linear random process

DOI 10.1515/ama-2015-0035

in order to be a cyclic random process.

3. The advantages of the LCRP allow to use it as mathematical models of the cyclic stochastic signals and processes in various fields of science and technology, particularly as mathematical models of a wide class of human body heart and respiratory system cyclic signals, as models of the data transmission channels process, as models of vibrating processes in rotating mechanical structures of different types of generators, turbines, propellers, as models of the cyclical economic processes.
4. Presented results open some perspectives such as development of discrete analogues of cyclic linear stochastic processes, including definitions and study of classes of cyclic moving average (MA), autoregressive (AR), autoregressive moving average (ARMA). This will permit to create further effective models and methods of analysis, simulation and prediction of cyclic processes with the use of modern digital technology.

REFERENCES

1. **Yurekli K., Kurunc A., Ozturk F.**, (2005) Application of linear stochastic models to monthly flow data of Kelkit Stream, *Ecological Modelling*, 183 (1), 67–75.
2. **Blake I., Thomas J.** (1968), The Linear Random Process, *Proc. Of IEEE*, 56 (10) 1696–1703.
3. **Bartlett M.** (1955), *An introduction to stochastic processes with special reference to methods and applications*, Cambridge University Press.
4. **Medvegyev P.** (2007), *Stochastic Integration Theory*, Oxford University Press, New York.
5. **Bhansali R**. (1993), Estimation of the impulse response coefficients of a linear process with infinite variance, *Journal of Multivariate Analysis*, 45, 274-290.
6. **Giraitis L.** (1985), Central limit theorem for functionals of a linear process, *Lithuanian Mathematical Journa*l, 25, 25–35.
7. **Olanrewaju J., Al-Arfaj M.** (2005), Development and application of linear process model in estimation and control of reactive distillation, *Computers and Chemical Engineering*, 30, 147–157.
8. **Bartlett M.** (1950) Periodogram Analysis and Continuous Spectra, *Biometrika*, 37(1/2), 1–16.
9. **Martchenko B**. (1998) Concerning on a theorem for periodic in Slutskiy sense linear random processes, *International Congress of Mathematicians*, *Berlin*.
10. **Zvarich V., Marchenko B.** (2011), Linear autoregressive processes with periodic structures as models of information signals, *Radioelectronics and Communications Systems*, 54(7), 367–372.
11. **Pagano M.** (1978), On periodic and multiple autoregressions, *The Annals of Statistics*, 6, 1310–1317.
12. **Lupenko S.** (2006), Deterministic and random cyclic function as a model of oscillatory phenomena and signals: the definition and classification*, Electronic Modeling, Institute of modeling problems in power of H.E Pukhov NAS*, 28, 29–45.
13. **Naseri H., Homaeinezhad M.R., Pourkhajeh H**., (2013), Noise/spike detection in phonocardiogram signal as a cyclic random process with non-stationary period interval, *Computers in Biology and Medicine*, 43, 1205–1213.
14. **Berkes I., Horváth L**., (2006), Convergence of integral functionals of stochastic processes, *Econometric Theory*, 22, 304–322.
15. **Protter P.E.**, (2005), Stochastic integration and differential equations, *Second edition, New York*.
16. **Gardner W., Napolitano A., Paura L.,** (2006) Cyclostationarity: Half a century of research*, Signal Processing*, 86, 639–697.
17. **Hurd H., Miamee A.** (2006), *Periodically Correlated Random Sequences*, Spectral Theory and Practice, Wiley, New York.

MINIMUM ENERGY CONTROL OF POSITIVE TIME-VARYING LINEAR SYSTEMS

Tadeusz KACZOREK*

*Faculty of Electrical Engineering, Bialystok University of Technology, Wiejska 45D, 15-351 Bialystok, Poland

kaczorek@isep.pw.edu.pl

received 22 May 2015, revised 11 December 2015, accepted 14 December 2015

Abstract: The minimum energy control problem for the positive time-varying linear systems is formulated and solved. Sufficient conditions for the existence of solution to the problem are established. A procedure for solving of the problem is proposed and illustrated by a numerical example.

Keywords: Positive, Continuous-Time, Minimum Energy Control, Procedure

1. INTRODUCTION

A dynamical system is called positive if its trajectory starting from any nonnegative initial state remains forever in the positive orthant for all nonnegative inputs. An overview of state of the art in positive system theory is given in the monographs (Farina and Rinaldi,2000; Kaczorek, 2001b). Variety of models having positive behavior can be found in engineering, economics, social sciences, biology and medicine, etc.

The positive fractional linear systems have been investigated in Kaczorek (2008a, 2011c,d, 2012). Stability of fractional linear 1D discrete–time and continuous-time systems has been investigated in the papers (Busłowicz, 2008; Dzieliński and Sierociuk, 2008; Kaczorek, 2012) and of 2D fractional positive linear systems in Kaczorek (2009). The notion of practical stability of positive fractional discrete-time linear systems has been introduced in Kaczorek (2008b). The minimum energy control problem for standard linear systems has been formulated and solved by Klamka (1976, 1977, 1983, 1991, 1993, 2010) and for 2D linear systems with variable coefficients in Kaczorek and Klamka (1986). The controllability and minimum energy control problem of fractional discrete-time linear systems has been investigated by Klamka (2010). The minimum energy control of fractional positive continuous-time linear systems has been addressed in Kaczorek (2014b) and for descriptor positive discrete-time linear systems in Kaczorek (2014a).

In this paper the minimum energy control problem for positive time-varying linear systems will be formulated and solved.

The paper is organized as follows. In section 2 the basic definitions and theorems of the positive time-varying linear systems are recalled and the necessary and sufficient conditions for the reachability of the positive systems are given. The minimum energy control problem of the positive time-varying linear systems is formulated and solved in section 3. Sufficient conditions for the existence of solution of the problem are established and a procedure for computation of the optimal inputs and the minimum value of the performance index are also presented. Concluding remarks are given in section 4.

The following notation will be used: $\Re$ – the set of real numbers, $\Re^{n\times m}$ – the set of $\mathrm{n}\times\mathrm{m}$ real matrices, $\Re_+^{n\times m}$ – the set of $n\times m$ matrices with nonnegative entries and $\Re_+^n=\Re_+^{n\times 1}$, M_n – the set of $n\times n$ Metzler matrices (real matrices with nonnegative off-diagonal entries), I_n – the $n\times n$ identity matrix, A^T – the transpose matrix A.

2. POSITIVE TIME-VARYING LINEAR SYSTEMS AND THEIR REACHABILITY

Consider the time-varying linear system

$$\dot{x}(t)=A(t)x(t)+B(t)u(t) \tag{2.1}$$

where $x(t)\in\Re^n$ and $u(t)\in\Re^m$ are the state and input vectors and $A(t)\in\Re^{n\times n}$, $B(t)\in\Re^{n\times m}$ with continuous-time entries.

The solution of equation (2.1) has the form

$$x(t)=\Phi(t,t_0)x_0+\int_0^t\Phi(t,\tau)B(t)u(\tau)d\tau,\quad x(t_0)=x_{t_0} \tag{2.2}$$

where $\Phi(t,t_0)$ is the fundamental matrix defined by

$$\Phi(t,t_0)=I_n+\int_{t_0}^t A(\tau)d\tau+\int_{t_0}^t A(\tau)\int_{t_0}^{\tau}A(\tau_1)d\tau_1\,d\tau+\ldots \tag{2.3a}$$

If $A(t_1)A(t_2)=A(t_2)A(t_1)$ for $t_1,t_2\in[t_0,\infty)$, then (2.3a) takes the form (Gantmacher, 1959)

$$\bar{\Phi}(t,t_0)=exp\left(\int_{t_0}^t A(\tau)d\tau\right). \tag{2.3b}$$

The fundamental matrix $\Phi(t,t_0)$ satisfies the matrix differential equation

$$\dot{\Phi}(t,t_0)=A(t)\Phi(t,t_0) \tag{2.4}$$

DOI 10.1515/ama-2015-0036

and the initial condition $\Phi(t_0, t_0) = I_n$.

Lemma 2.1. The fundamental matrix satisfies

$$\Phi(t, t_0) \in \Re_+^{n\times n} \text{ for } t \geq t_0 \tag{2.5}$$

if and only if the off-diagonal entries a_{ij}, $i \neq j$, $i,j = 1,2,\ldots,n$ of the matrix $A(t)$ satisfy the condition

$$\int_{t_0}^{t} a_{ij}(\tau)d\tau \geq 0 \text{ for } i \neq j,\ i,j = 1,2,\ldots,n. \tag{2.6}$$

Proof is given in Kaczorek (2001a).

Definition 2.1. The system (2.1) is called the (internally) positive if and only if $x(t) \in \Re_+^n$, $t \geq t_0$ for any initial conditions $x_{t_0} \in \Re_+^n$ and all inputs $u(t) \in \Re_+^m$, $t \geq t_0$.

Theorem 2.1. The time-varying linear system (2.1) is positive if and only if the off-diagonal entries of the matrix $A(t)$ satisfy the condition (2.6) and $B(t) \in \Re_+^{n\times m}$ for $t \geq t_0$.

Definition 2.2. The system (2.1) is called reachable in time $t_f - t_0$ if for any given final state $x_f \in \Re_+^n$ there exists an input $u(t) \in \Re_+^m$, for $t \in [t_0, t_f]$ that steers the state of the system from zero initial state $x(t_0) = x_{t_0}$ to the state x_f, i.e. $x(t_f) = x_f$.

A real square matrix is called monomial if each its row and each its column contains only one positive entry and the remaining entries are zero.

Theorem 2.2. The positive system (2.1) is reachable in time $t_f - t_0$ if and only if

$$R_f = \int_{t_0}^{t_f} \Phi(t_f,\tau)B(\tau)B^T(\tau)\Phi^T(t_f,\tau)d\tau \tag{2.7}$$

is a monomial matrix. The input vector which steers the state of the system (2.1) from $x(t_0) = x_{t_0}$ to x_f is given by

$$u(t) = B^T(\tau)\Phi^T(t_f,t)R_f^{-1}x_f \text{ for } t \in [t_0,t_f]. \tag{2.8}$$

Proof. It is well-known (Kaczorek, 2001b) that the inverse matrix $R_f^{-1} \in \Re_+^{n\times n}$ if and only if the matrix R_f is monomial. In this case the input $u(t) \in \Re_+^m$ given by (2.8) steers the state of the system from $x(t_0) = x_{t_0}$ to the state x_f. Substituting (2.8) into (2.2) for $t = t_f$ and $x(t_0) = x_{t_0}$ we obtain

$$\begin{aligned} x(t_f) &= \int_{t_0}^{t_f} \Phi(t_f,\tau)B(\tau)B^T(\tau)\Phi^T(t_f,\tau)R_f^{-1}x_f d\tau \\ &= \left[\int_{t_0}^{t_f} \Phi(t_f,\tau)B(\tau)B^T(\tau)\Phi^T(t_f,\tau)d\tau\right] R_f^{-1}x_f = x_f. \end{aligned} \tag{2.9}$$

Therefore, the positive system (2.1) is reachable in time $t_f - t_0$ if and only if the matrix (2.7) is monomial. □

3. MINIMUM ENERGY CONTROL PROBLEM

Consider the positive system (2.1) reachable in time $t_f - t_0$. If the system is reachable in time $t \in [t_0, t_f]$, then usually there exists many different inputs $u(t) \in \Re_+^n$ that steers the state of the system from $x(t_0) = x_{t_0} = 0$ to $x_f = x(t_f) \in \Re_+^n$. Among these inputs we are looking for an input $u(t) \in \Re_+^n$ that minimizes the performance index

$$I(u) = \int_{t_0}^{t_f} u^T(\tau)Qu(\tau)d\tau \tag{3.1}$$

where $Q \in \Re_+^{n\times n}$ is a symmetric positive defined matrix and $Q^{-1} \in \Re_+^{n\times n}$.

The minimum energy control problem for the positive time-varying linear systems (2.1) can be stated as follows: Given the matrices $A(t), B(t)$ and $Q \in \Re_+^{n\times n}$ of the performance index (3.1), $x_f \in \Re_+^n$, t_0, and $t_f > 0$, find an input $u(t) \in \Re_+^n$ for $t \in [t_0, t_f]$ that steers the state vector of the system from $x_{t_0} = 0$ to $x_f \in \Re_+^n$ and minimizes the performance index (3.1).

To solve the problem we define the matrix

$$\begin{aligned} W &= W(t_f, Q) \\ &= \int_{t_0}^{t_f} \Phi(t_f,\tau)B(\tau)Q^{-1}B^T(\tau)\Phi^T(t_f,\tau)d\tau \end{aligned} \tag{3.2}$$

From (3.2) and Theorem 2.2 it follows that the matrix (3.2) is monomial if and only if the fractional positive system (2.1) is reachable in time $[t_0, t_f]$. In this case we may define the input

$$\hat{u}(t) = Q^{-1}B^T(t)\Phi^T(t_f,t)W^{-1}x_f \text{ for } t \in [t_0,t_f]. \tag{3.3}$$

Note that the input (3.3) satisfies the condition $u(t) \in \Re_+^n$ for $t \in [t_0, t_f]$ if

$$Q^{-1} \in \Re_+^{n\times n} \text{ and } W^{-1}x_f \in \Re_+^n. \tag{3.4}$$

Theorem 3.1. Let the positive system (2.1) be reachable in time $[t_0, t_f]$ and let $\bar{u}(t) \in \Re_+^n$ for $t \in [t_0, t_f]$ be an input that steers the state of the positive system (2.1) from $x_{t_0} = 0$ to $x_f \in \Re_+^n$. Then the input (3.3) also steers the state of the system from $x_{t_0} = 0$ to $x_f \in \Re_+^n$ and minimizes the performance index (3.1), i.e. $I(\hat{u}) \leq I(\bar{u})$.

The minimal value of the performance index (3.1) is equal to

$$I(\hat{u}) = x_f^T W^{-1} x_f. \tag{3.5}$$

Proof. If the conditions (3.4) are met then the input (3.3) is well defined and $\hat{u}(t) \in \Re_+^n$ for $t \in [t_0, t_f]$. We shall show that the input steers the state of the system from $x_{t_0} = 0$ to $x_f \in \Re_+^n$. Substitution of (3.3) into (2.2) for $t = t_f$ and $x_{t_0} = 0$ yields

$$\begin{aligned} x(t_f) &= \int_{t_0}^{t_f} \Phi(t_f,\tau)B(\tau)\hat{u}(\tau)d\tau \\ &= \int_{t_0}^{t_f} \Phi(t_f,\tau)B(\tau)Q^{-1}B^T(\tau)\Phi^T(t_f,\tau)d\tau\, W^{-1}x_f \\ &= x_f \end{aligned} \tag{3.6}$$

since (3.2) holds. By assumption the inputs $\bar{u}(t)$ and $\hat{u}(t)$, $t \in [t_0, t_f]$ steers the state of the system from $x_{t_0} = 0$ to $x_f \in \Re_+^n$. Hence

$$\begin{aligned} x_f &= \int_{t_0}^{t_f} \Phi(t_f,\tau)B(\tau)\bar{u}(\tau)d\tau \\ &= \int_{t_0}^{t_f} \Phi(t_f,\tau)B(\tau)\hat{u}(\tau)d\tau \end{aligned} \tag{3.7a}$$

or

$$\int_{t_0}^{t_f} \Phi(t_f,\tau)B(\tau)[\bar{u}(\tau) - \hat{u}(\tau)]d\tau = 0. \tag{3.7b}$$

By transposition of (3.7b) and postmultiplication by $W^{-1}x_f$ we obtain

$$\int_{t_0}^{t_f} [\bar{u}(\tau) - \hat{u}(\tau)]^T B^T(\tau)\Phi^T(t_f,\tau)d\tau W^{-1}x_f = 0. \tag{3.8}$$

Substitution of (3.3) into (3.8) yields

$$\int_{t_0}^{t_f}[\bar{u}(\tau)-\hat{u}(\tau)]^T B^T(\tau)\Phi^T(t_f,\tau)d\tau W^{-1}x_f = \int_{t_0}^{t_f}[\bar{u}(\tau)-\hat{u}(\tau)]^T Q\hat{u}(\tau)d\tau = 0. \quad (3.9)$$

Using (3.9) it is easy to verify that

$$\int_{t_0}^{t_f}\bar{u}(\tau)^T Q\bar{u}(\tau)d\tau = \int_{t_0}^{t_f}\hat{u}(\tau)^T Q\hat{u}(\tau)d\tau + \int_{t_0}^{t_f}[\bar{u}(\tau)-\hat{u}(\tau)]^T Q[\bar{u}(\tau)-\hat{u}(\tau)]d\tau . \quad (3.10)$$

From (3.10) it follows that $\mathrm{I}(\hat{\mathrm{u}}) < \mathrm{I}(\bar{\mathrm{u}})$ since the second term in the right-hand side of the inequality is nonnegative.

To find the minimal value of the performance index (3.1) we substitute (3.3) into (3.1) and we obtain

$$I(\hat{u}) = \int_0^{t_f}\hat{u}^T(\tau)Q\hat{u}(\tau)d\tau = x_f^T W^{-1}\int_0^{t_f}\Phi(t_f,\tau)B(\tau)Q^{-1}B^T(\tau)\Phi^T(t_f,\tau)d\tau\, W^{-1}x_f = x_f^T W^{-1}x_f \quad (3.11)$$

since (3.2) holds. □

From the above considerations we have the following procedure for computation the optimal inputs that steers the state of the system from $x_{t_0}=0$ *to* $x_f \in \Re_+^n$ and minimize the performance index (3.1).

Procedure 3.1.

Step 1. Knowing the matrix $A(t)$ compute $\Phi(t)$.

Step 2. Using (3.2) compute the matrix W.

Step 3. Using (3.3) compute the input $\hat{u}(t)$.

Step 4. Using (3.5) compute the minimal value of the performance index.

Example 3.1. Consider the positive system (2.1) for $t_0 = 0$ with matrices

$$A(t)=\begin{bmatrix}2 & 0\\ 0 & t\end{bmatrix},\quad B(t)=\begin{bmatrix}0 & e^t\\ \sqrt{t} & 0\end{bmatrix} \quad (3.12)$$

and the performance index (3.1) with

$$Q=\begin{bmatrix}2 & 0\\ 0 & 2\end{bmatrix}. \quad (3.13)$$

By Theorems 2.1 and 2.2 the system is positive and reachable in time $t_f - t_0$. Therefore, there exists an input $\mathrm{u}(\mathrm{t})$ that steers the state of the system from zero state to $x_f = [2 \quad 1]^T$ in time $t_f - t_0$ for $t_0 = 0, t_f = 1$.

Using the Procedure 3.1 we obtain the following:

Step 1. Using (2.3a) we obtain

$$\bar{\Phi}(1,\tau) = exp\left(\int_\tau^1 A(\tau)d\tau\right) = \begin{bmatrix}exp(2(1-\tau)) & 0\\ 0 & exp(0.5(1-\tau^2))\end{bmatrix}. \quad (3.14)$$

Step 2. Using (3.2), (3.13) and (3.14) we obtain

$$W = \int_0^{t_f}\bar{\Phi}(1,\tau)B(\tau)Q^{-1}B^T(\tau)\bar{\Phi}^T(1,\tau)d\tau = \begin{bmatrix}0.25e^2(e^2-1) & 0\\ 0 & 0.25(e-1)\end{bmatrix}. \quad (3.15)$$

Step 3. Using (3.3) and (3.15) we have

$$\hat{u}(t) = Q^{-1}B^T(t)\bar{\Phi}^T(1,t)W^{-1}x_f = \begin{bmatrix}\frac{2\sqrt{t}}{e-1}exp(0.5(1-\tau^2))\\ \frac{4exp(-t)}{e^2-1}\end{bmatrix}. \quad (3.16)$$

Step 4. The minimal value of the performance index

$$I(\hat{u}) = x_f^T W^{-1}x_f = [2 \quad 1]\begin{bmatrix}0.25e^2(e^2-1) & 0\\ 0 & 0.25(e-1)\end{bmatrix}^{-1}\begin{bmatrix}2\\1\end{bmatrix} = \frac{16}{e^2(e^{-2}-1)}+\frac{4}{e-1}. \quad (3.17)$$

4. CONCLUDING REMARKS

Necessary and sufficient conditions for the reachability of the positive time-varying linear systems have been established (Theorem 2.2). The minimum energy control problem for the positive time-varying linear systems has been formulated and solved. Sufficient conditions for the existence of a solution to the problem has been given (Theorem 3.1). A procedure for computation of optimal input and the minimal value of performance index has been proposed. The effectiveness of the procedure has been demonstrated on the numerical example. The presented method can be extended to positive discrete-time linear systems and to fractional positive time-varying linear systems with bounded inputs.

REFERENCES

1. **Busłowicz M.** (2008), Stability of linear continuous time fractional order systems with delays of the retarded type, *Bull. Pol. Acad. Sci. Tech.*, Vol. 56(4), 319-324.
2. **Dzieliński A., Sierociuk D.** (2008), Stability of discrete fractional order state-space systems, *Journal of Vibrations and Control*, Vol. 14(9/10), 1543-1556.
3. **Dzieliński A., Sierociuk D., Sarwas G.** (2009), Ultracapacitor parameters identification based on fractional order model, *Proc ECC'09*, Budapest.
4. **Farina L., Rinaldi S.** (2000), *Positive Linear Systems; Theory and Applications*, J. Wiley, New York.
5. **Gantmacher F.R.** (1959), *The Theory of Matrices*, Chelsea, New York.
6. **Kaczorek T.** (1992), *Linear Control Systems*, Research Studies Press and J.Wiley, New York.
7. **Kaczorek T.** (2001a), Externally and internally positive time-varying linear systems, *Int. J. Appl. Math. Comput. Sci.*, Vol. 11(4), 957-964.
8. **Kaczorek T.** (2001b), *Positive 1D and 2D systems*, Springer Verlag, London.
9. **Kaczorek T.** (2008a), Fractional positive continuous-time systems and their Reachability, *Int. J. Appl. Math. Comput. Sci.*, Vol. 18(2), 223-228.
10. **Kaczorek T.** (2008b), Practical stability of positive fractional discrete-time linear systems, *Bull. Pol. Acad. Sci. Tech.*, Vol. 56(4), 313-317.
11. **Kaczorek T.** (2008c), Reachability and controllability to zero tests for standard and positive fractional discrete-time systems, *Journal Européen des Systèmes Automatisés*, JESA, Vol. 42(6-8), 769-787.
12. **Kaczorek T.** (2009), Asymptotic stability of positive fractional 2D linear systems, *Bull. Pol. Acad. Sci. Tech.*, Vol. 57(3), 289-292.
13. **Kaczorek T.** (2011a), Checking of the positivity of descriptor linear systems by the use of the shuffle algorithm, *Archive of Control Sciences*, Vol. 21(3), 287-298.
14. **Kaczorek T.** (2011b), Controllability and observability of linear electrical circuits, *Electrical Review*, Vol. 87(9a), 248-254.
15. **Kaczorek T.** (2011c), Positive linear systems consisting of n subsystems with different fractional orders, *IEEE Trans. Circuits and Systems*, Vol. 58(6), 1203-1210.
16. **Kaczorek T.** (2011d), Positivity and reachability of fractional electrical circuits, *Acta Mechanica et Automatica*, Vol. 5(2), 42-51.

DOI 10.1515/ama-2015-0036

17. **Kaczorek T.** (2012), *Selected Problems of Fractional Systems Theory*, Springer-Verlag, Berlin.
18. **Kaczorek T.** (2014a), Minimum energy control of descriptor positive discrete-time linear systems, *COMPEL: The International Journal for Computation and Mathematics in Electrical and Electronic Engineering*, Vol. 33(3), 976 - 988.
19. **Kaczorek T.** (2014b), Minimum energy control of fractional positive continuous-time linear systems, *International Journal of Applied Mathematics and Computer Science*, Vol. 24(2), 335-340.
20. **Kaczorek T., Klamka J.** (1986), Minimum energy control of 2D linear systems with variable coefficients, *Int. J. of Control*, Vol. 44(3), 645-650.
21. **Klamka J.** (1976), Relative controllability and minimum energy control of linear systems with distributed delays in control, *IEEE Trans. Autom. Contr.*, Vol. 21(4), 594-595.
22. **Klamka J.** (1977), Minimum energy control of discrete systems with delays in control, *International Journal of Control*, Vol. 26(5), 737-744.
23. **Klamka J.** (1983), Minimum energy control of 2D systems in Hilbert spaces, *System Sciences*, Vol. 9(1-2), 33-42.
24. **Klamka J.** (1991), *Controllability of Dynamical Systems*, Kluwer Academic Press, Dordrecht.
25. **Klamka J.** (1993), Controllability of dynamical systems-a survey, *Archives of Control Sciences*, Vol. 2(3-4), 281-307.
26. **Klamka J.** (2010), Controllability and minimum energy control problem of fractional discrete-time systems, Chapter in "N*ew Trends in Nanotechology and Fractional Calculus*", Eds. Baleanu D., Guvenc Z.B., Tenreiro Machado J.A., Springer-Verlag, New York, 503-509.

Acknowledgment: This work was supported under work S/WE/1/11.

COMPARATIVE ANALYSIS FOR KINEMATICS OF 5-DOF INDUSTRIAL ROBOTIC MANIPULATOR

Shiv MANJAREE[*], Bahadur Chand NAKRA[*], Vijyant AGARWAL[*]

[*]Department of Mechanical Engineering, The Northcap University (Formerly ITM University), Sector 23 A, Gurgaon, India
[*]Department of Mechanical Engineering, IIT Delhi, Hauz Khas, New Delhi, India
[**]Department of MPAE, NSIT, Sector 3, Dwarka, New Delhi, India

shivmanjree@gmail.com, bcnakra@hotmail.com, vijayant@nsit.ac.in

received 2 December 2014, revised 11 December 2015, accepted 14 December 2015

Abstract: This paper gives the kinematic analysis of a 5-DOF industrial robotic manipulator while considering wrist in motion. Analytical solutions have been obtained for forward kinematics and inverse kinematics to accurately position the end-effector of robotic manipulator in three dimensional spaces. For the first time, a hybrid neuro-fuzzy intelligent technique with two different membership functions has been studied and their performances are comparatively evaluated with analytical solutions. An experiment has been performed for a desired trajectory. It is seen that the results for the intelligent technique are reasonably in agreement with experiment. Also, the results obtained highlight the importance of selection of a particular membership function for robotic manipulators of industrial use.

Keywords: Kinematic Analysis, Wrist, ANFIS, Membership Function, Degree of Freedom

1. INTRODUCTION

Robotic manipulators exhibit an important role in industrial automation and applications. A number of industrial tasks such as pick and place operation, assembly, welding, spray painting etc. is performed by several complex robotic systems. Since any task is performed within the pre-defined work space of a robotic manipulator, the position of end-effector plays an important role in the quality of the final product. To put it another way, the point of interest is the accuracy of reaching desired coordinates by the end-effector which leads to the successful manufacturing of a product. The end-effector positioning of any robotic manipulator can be very well understood with the help of kinematic analysis. The kinematic analysis of any robotic manipulator can be carried out by forward and inverse kinematics. While the presence of Denavit-Hartenberg convention makes the forward kinematics an easy task; calculation of inverse kinematic solutions is complex and time consuming due to non-existence of unique solution.

In terms of literature available on kinematic analysis, the well-known Denavit-Hartenberg convention for position analysis was proposed (Denavit, 1955) and has been widely adopted. The kinematic solutions for industrial manipulator PUMA 560 has been presented (Elgazzar, 1985). Based upon the convention, software programs for five or six degrees-of-freedom (DOF) robotic manipulators of general geometry have been developed (Manseur, 1996; Koyuncu, 2007) along with their theoretical analysis. The performance of different robotic manipulators has been studied for pick and place and assembly operations (Kim, 1987; Azadivar 1987). The calculation of home position of a robotic manipulator has been given (Shah et al., 2013). The theoretical background for the calculations of forward and inverse kinematics has been described exhaustively (Niku, 2009; Mittal, 2003; Saha, 2008). A geometrical approach for inverse kinematics of hyper redundant manipulators has been proposed (Yahya et al., 2011).

For complex structures of robotic manipulators, traditional methods are inadequate, highly iterative and time consuming. The difficulties of traditional methods to calculate inverse kinematic solutions can be avoided by using artificial intelligent techniques, which gives an advantage of fast computation. Most of the work presented in literature has used different artificial intelligent techniques: fuzzy logic (Agarwal et al., 2005; Homaifar et al. 1994; Bingul, 2011) and neural network (Tejomurtula, 1999; Karlik, 2000) to calculate inverse kinematic solutions of planar two-DOF and three-DOF robotic manipulators.

In recent times, the complexities of research are tried to be solved with the use of adaptive and hybrid artificial intelligent techniques. The widely used artificial intelligent techniques are fuzzy logic and neural networks. Fuzzy logic approach provides quantitative value to verbal communication. Neural networks approach provides mathematical computations of a brain. It is interesting to work on certain applications like robotic manipulators involving the proper combination of these two approaches resulting in a hybrid system. ANFIS (Adaptive Neuro-Fuzzy Intelligent System) is a hybrid combination of fuzzy logic and neural networks, mostly used to find inverse kinematic solutions of robotic manipulators (Jang, 1993). The literature search shows that ANFIS has been used for two and three DOF planar robotic manipulator (Alavander, 2008). For ANFIS implementation, even the industrial manipulators like PUMA 560 and PUMA 600 have been reduced to three DOF link movement only (Bachir, 2012; Aghajarian, 2011). A comparative study on the development and application of three main artificial intelligent techniques, namely neural networks, fuzzy logic and combination of neural networks and fuzzy logic on different robotic manipulators has been presented (Er et al., 1997; Mohan, 2007; Efe, 2000). The kinematic study for 2-DOF, 3-DOF and 5-DOF planar robotic systems using artificial intelligence techniques and analytical approach have been performed (Manjaree et al., 2010). A comparative analysis for inverse kinematic solutions obtained using

DOI 10.1515/ama-2015-0037

ANFIS method, geometrical approach and experimental validation has been carried out for a 3-DOF robotic manipulator (Manjaree, 2013). The inverse kinematic solutions for 3-DOF robotic manipulator using ANFIS method moving in three dimensional spaces have been presented (Manjaree et al., 2013). In this paper, experimental validation has been carried out by plotting a desired trajectory. One of the fundamental problems of robotic manipulators is in trajectory planning. The issues of trajectory planning have been discussed and resolved by various methods (Gasparetto, 2007; Kuo, 1991; Chen, 2010; Conkur, 2003). After reviewing the available literature, it can very well be concluded that inverse kinematic analysis used for multi-DOF robotic manipulators have considered restricted wrist motion and have applied ANFIS method on links movement only. The issue of accurate end-effector positioning arises when wrist in motion is also considered.

This paper focuses on three important aspects, namely analytical analysis, use of ANFIS method and experimental validation of 5-DOF pick and place type industrial robotic manipulator while considering wrist in motion. For the very first time, ANFIS method has been used on an industrial robotic manipulator involving two different membership functions. A comparative analysis for better performance by used membership functions for all possible multiple solutions of 5-DOF robotic manipulator have been presented. The research work presented in this paper have very first time incorporated wrist movement while applying ANFIS method on 5-DOF robotic manipulator which is duly validated with experimental results as well. Along with this, the paper also acts as a single platform for analyzing the 5-DOF robotic manipulator using analytical methods, intelligent methods and experiments.

2. DESCRIPTION OF 5-DOF ROBOTIC MANIPULATOR

In this paper, a 5-DOF pick and place type robotic manipulator (Pravak make) of industrial use has been considered. The robotic manipulator under study consists of 3-DOF at joints and 2-DOF at wrist. The available degree of freedom in links is sufficient to bring the end effector to the required position; however, the wrist movement provides additional flexibility to reach a particular position by the end effector. The extra degrees of freedom made available at the wrist provide greater flexibility and applicability to the complete robotic system. It also enhances the accuracy of experiments performed.

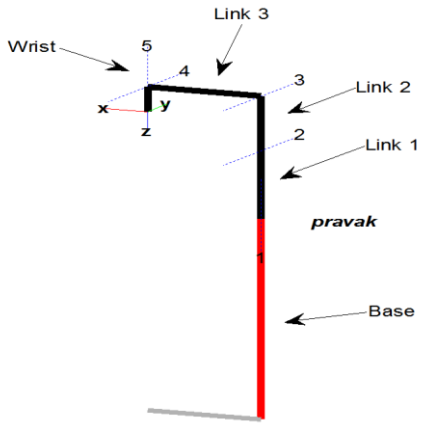

Fig. 1. Representation of 5-DOF (Pravak make) robotic manipulator

Tab. 1. Description of movement of robotic manipulator

S. No.	Type	Part of Manipulator	Movement	Rotation
1	Link 1	Waist	Left/Right	-90° – 90°
2	Link 2	Shoulder	Forward/Backward	0° – 180°
3	Link 3	Elbow	Up/Down	0° – 180°
4	Wrist	Wrist pitch	Sky-turn/Earth-turn	0° – 180°
5	Wrist	Wrist Roll	Clock-wise/Anti-clock-wise	0° – 360°

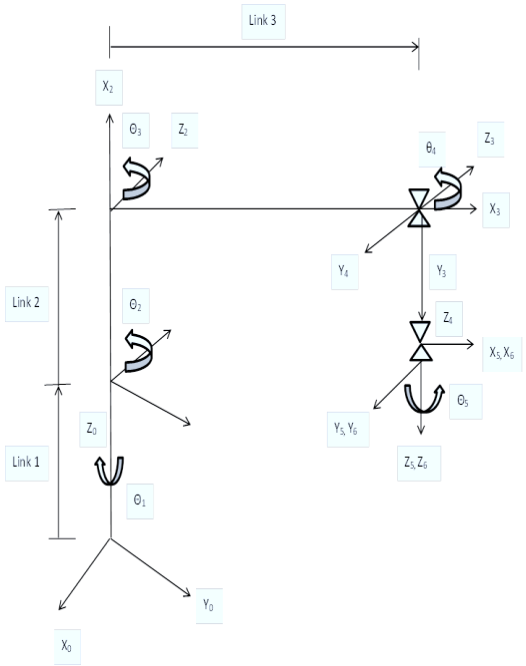

Fig. 2 Schematic representation of Denavit-Hartenberg convention for 5-DOF robotic manipulator

The 5-DOF robotic manipulator considered in present work is shown in Fig. 1. The robotic manipulator has been plotted using Peter Corke Robotics Toolbox for MATLAB (release 9.8) (Corke 2011). The complete description about the movement of each link of robotic manipulator is as quoted in Tab. 1. The schematic representation of Denavit-Hartenberg convention is as shown in Fig. 2.

3. ANALYTICAL ANALYSIS FOR FORWARD AND INVERSE KINEMATICS

The kinematic analysis of any robotic system is performed in two ways i.e. forward kinematics and inverse kinematics. The forward kinematics problem is to find the position and orientation as a function of joint variables, achieved by end-effector of robotic manipulator, as given in equation (1). The forward kinematics of multi-DOF robotic manipulators is an easy task due to the availability of Denavit-Hartenberg convention.

$$x(t) = f(\theta(t)) \tag{1}$$

The calculation of joint variables to bring the end-effector of robotic manipulator to the required position and orientation is defined by inverse kinematics problem, as given in equation (2).

$$\theta(t) = f'(x(t)) \tag{2}$$

As compared to forward kinematics, calculation of inverse kinematic solutions is a complex task since there is no possible unique solution due to non-linear and time-varying nature of its governing equation. The inverse kinematics of multi-DOF robotic manipulator can be obtained using three different techniques, viz. algebraic approach, geometric approach and iterative approach. In this paper, analytical kinematic analysis for 5-DOF pick and place type robotic manipulator has been performed using algebraic approach. The Denavit-Hartenberg convention has been used to obtain the forward kinematic equations, as given in Tab. 2.

Tab. 2. Denavit-Hartenberg convention table for Pravak manipulator

Joint	θ_i (°)	α_i (°)	a_i	d_i
1	θ_1	-90	0	L_0
2	θ_2	0	L_1	0
3	θ_3	0	L_2	0
4	θ_4 - 90	-90	0	0
5	θ_5	0	0	L_3

By substituting the Denavit-Hartenberg parameters (θ_i, d_i, a_i, α_i) in the general matrix given in equation (3); the transformation matrices A_1 to A_5 are obtained as below:

$$A_{n+1} = \begin{bmatrix} C\theta_{n+1} & S\theta_{n+1}C\alpha_{n+1} & S\theta_{n+1}S\alpha_{n+1} & a_{n+1}C\theta_{n+1} \\ S\theta_{n+1} & C\theta_{n+1}C\alpha_{n+1} & -C\theta_{n+1}S\alpha_{n+1} & a_{n+1}S\theta_{n+1} \\ 0 & S\alpha_{n+1} & C\alpha_{n+1} & d_{n+1} \\ 0 & 0 & 0 & 1 \end{bmatrix}$$

$$A_1 = \begin{bmatrix} C_1 & 0 & -S_1 & 0 \\ S_1 & 0 & C_1 & 0 \\ 0 & -1 & 0 & L_0 \\ 0 & 0 & 0 & 1 \end{bmatrix} \quad A_2 = \begin{bmatrix} C_2 & -S_2 & 0 & L_1C_2 \\ S_2 & C_2 & 0 & L_1S_2 \\ 0 & 0 & 1 & 0 \\ 0 & 0 & 0 & 1 \end{bmatrix} \tag{3}$$

$$A_3 = \begin{bmatrix} C_3 & -S_3 & 0 & L_2C_3 \\ S_3 & C_3 & 0 & L_2S_3 \\ 0 & 0 & 1 & 0 \\ 0 & 0 & 0 & 1 \end{bmatrix} \quad A_4 = \begin{bmatrix} C_4 & 0 & -S_4 & 0 \\ S_4 & 0 & C_4 & 0 \\ 0 & -1 & 0 & 0 \\ 0 & 0 & 0 & 1 \end{bmatrix}$$

$$A_5 = \begin{bmatrix} C_5 & -S_5 & 0 & 0 \\ S_5 & C_5 & 0 & 0 \\ 0 & 0 & 1 & L_3 \\ 0 & 0 & 0 & 1 \end{bmatrix}$$

Mathematically, the forward kinematics equations can be obtained by multiplying A1 to A5 matrices as given in equation (4):

$$A_5^0 = A_1 \dots \dots A_5 \tag{4}$$

which results to, $A_5^0 = \begin{bmatrix} R_{3\times3} & p_{1\times3} \\ 0\ 0\ 0 & 1 \end{bmatrix}$.

After applying the above steps, the forward kinematic equations for 5-degree of freedom robotic manipulator under study has been obtained as given in equations (5-7):

$$p_x = -L_3 \times C_1 \times S_{234} + L_2 \times C_1 \times C_{23} + L_1 \times C_1 \times C_2 \tag{5}$$

$$p_y = -L_3 \times S_1 \times S_{234} + L_2 \times S_1 \times C_{23} + L_1 \times S_1 \times C_2 \tag{6}$$

$$p_z = -L_3 \times C_{234} - L_2 \times S_{23} - L_1 \times S_2 + L_0 \tag{7}$$

where $S_{23} = sin(\theta_2 + \theta_3) = S_2C_3 + C_2S_3$ and $C_{23} = cos(\theta_2 + \theta_3) = C_2C_3 - S_2S_3$.

The orientation of end-effector of 5-DOF robotic manipulator has been given below in equations (8-16):

$$n_x = C_1S_{234}C_5 + S_1S_5 \tag{8}$$

$$n_y = S_1C_{234}C_5 - C_1S_5 \tag{9}$$

$$n_z = -C_{234}C_5 \tag{10}$$

$$o_x = -C_1S_{234}S_5 + S_1C_5 \tag{11}$$

$$o_y = -S_1S_{234}S_5 - C_1C_5 \tag{12}$$

$$o_z = C_{234}S_5 \tag{13}$$

$$a_x = C_1C_{234} \tag{14}$$

$$a_y = S_1C_{234} \tag{15}$$

$$a_z = -S_{234} \tag{16}$$

The 5-DOF robotic manipulator used in this study comprises of a 2-DOF wrist motion. The sufficient condition to solve inverse kinematics is that it has two intersecting axes. For these types of manipulators it is possible to separate inverse kinematic problem into two sub-problems: position and orientation. To put it in another way, the 5-DOF robotic manipulator has 3-DOF available at links to find the end position of wrist and 2-DOF available at wrist to find the orientation of the wrist. It implicates that the robotic manipulator under study has closed form solutions. Thus, the wrist position p_W can be calculated as:

$$p_W = p_e - L_3a_e \tag{17}$$

where p_e denotes the end-effector position and orientation is specified in terms of $R_e = [n_e \quad o_e \quad a_e]$, respectively.

Equation (17) gives the generalized form of expression for calculation of wrist position. The components of above equation in x, y and z directions is given in equation (18).

$$\begin{bmatrix} p_{wx} \\ p_{wy} \\ p_{wz} \end{bmatrix} = \begin{bmatrix} p_{ex} - L_3a_{ex} \\ p_{ey} - L_3a_{ey} \\ p_{ez} - L_3a_{ez} \end{bmatrix} \tag{18}$$

The inverse kinematics solution for the complete 5-DOF robotic manipulator has been obtained by a closed solution of the above equation (18). Thus, the general solutions for the joint angles have been given below in equations (19-23) as:

$$\theta_1 = a\tan2(p_y, p_x) \tag{19}$$

$$\theta_2 = a\tan2\left(\frac{L_0 - p_z}{p_xC_1 + p_yS_1}\right) - a\tan2\left(\frac{L_2S_3}{\sqrt{(p_xC_1 + p_yS_1)^2 + (L_0 - p_z)^2 - (L_2S_3)^2}}\right) \tag{20}$$

where $S_1 = \pm\sqrt{1 - C_1^2}$

$$\theta_3 = a\tan2(S_3, C_3) \tag{21}$$

where

$$C_3 = \frac{(p_xC_1 + p_yS_1)^2 + (L_0 - p_z)^2 - L_1^2 - L_2^2}{2L_1L_2}, S_3 = \pm\sqrt{1 - C_3^2}$$

DOI 10.1515/ama-2015-0037

Also, the general solutions for wrist rotations are obtained as:

$$\theta_4 = a\tan2\left(\left(a_xC_1S_{23} + a_yS_1S_{23} + a_zC_{23}\right), \left(a_zS_{23} - a_xC_1C_{23} - a_yS_1C_{23}\right)\right) \quad (22)$$

$$\theta_5 = a\tan2\left(\left(n_yC_1 - n_xS_1\right), \left(o_yC_1 - o_xS_1\right)\right) \quad (23)$$

The above inverse kinematic solution gives one value of θ_1 and two values of θ_2 and θ_3 each as per the rotations of link 1, link 2 and link 3 given in Tab. 1. Two solutions are possible for θ_4 and one solution exist for θ_5 as per wrist rotations. It is clear from the obtained solutions that a number of multiple solutions are possible. It can be seen from equations (5-7) that a total of 8 multiple solutions exist for all possible combinations of joint angles with wrist rotation for the robotic manipulator under study. In this case, traditional mathematical computations for multiple data sets are almost impossible to perform due to their highly iterative and time-consuming nature. This disadvantage opens up way for the use of artificial intelligence techniques in the field of robotics. This paper has used a hybrid neuro-fuzzy intelligence technique known as ANFIS method to obtain end-effector position of 5-DOF (Pravak make) robotic manipulator.

4. ANFIS ARCHITECTURE WITH TWO DIFFERENT MEMBERSHIP FUNCTIONS

ANFIS method is a hybrid neuro-fuzzy intelligent technique which is functionally equivalent to Sugeno fuzzy inference system. It is a hybrid combination of artificial neural networks and fuzzy logic which basically exploits the individual advantages. It constructs a fuzzy inference system whose membership functions are tuned either by back propagation method alone or by a combination of least square method. The learning capabilities of artificial neural networks are brought into fuzzy inference system.

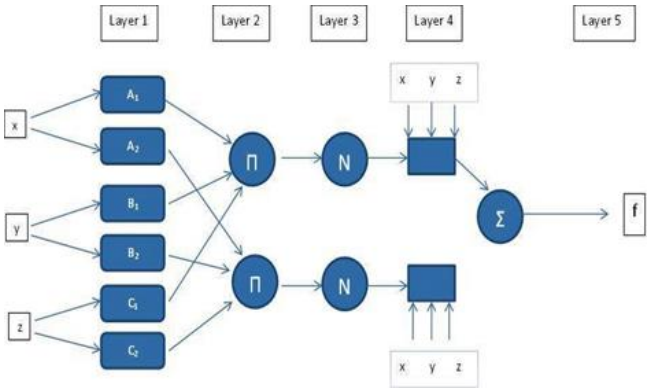

Fig. 3. ANFIS architecture

ANFIS method works in five layers (as shown in Fig. 3). The role of each layer is described as follows:

Layer 1: Calculation of membership function value for input parameter.

Each node in the first layer is an adaptive node where the node function O_i^k (for i^{th} position of k^{th} layer) is calculated as:

$$O_i^1 = u_{Ai}(x);\ O_i^1 = u_{Bi}(y);\ ;\ O_i^1 = u_{Ci}(z) \quad (24)$$

where (x, y, z) is input vector and $(u_{Ai},\ u_{Bi},\ uu_{Ci})$ is the membership function for that particular input.

Layer 2: Firing strength of rule or output of every node is the product of all incoming signals.

Here, the output of each node is the product of membership functions.

$$O_i^2 = W_i = u_{Ai}(x)u_{Bi}(y)u_{Ci}(z), i = 1,2,3 \quad (25)$$

Layer 3: Normalize firing strength. In other words, each of firing strengths of rules is compared with sum of all firing strengths.

It contains fixed nodes which calculate the ratio of the firing strengths of the rules:

$$\overline{O_i^3} = W_i = (W_i\ /W_1 + W_2 + W_3) \quad (26)$$

Layer 4: Consequent parameter or linear combination of input variables of ANFIS with constant terms to form the output of each IF-THEN rule.

The nodes in this layer are adaptive and perform the consequent of the rules:

$$\overline{O_i^4} = W_i f_i \quad (27)$$

Layer 5: It performs the defuzzification process.

There is a single node here that computes the overall output:

$$\overline{O_i^5} = \sum W_i f_i \quad (28)$$

The reported literature consists of ANFIS method being applied on planar robotic manipulators only. In this paper, for the first time, ANFIS method has been used to find the position of end-effector of 5-DOF robotic manipulator including 2-DOF wrist motion and moving in three dimensional spaces. For the first time, two ANFIS architectures of first order Sugeno fuzzy inference system based upon two different membership functions (MF's) have been considered. An attempt has been made for the very first time, to clearly demonstrate the effect of different MF's on the functioning of robotic manipulator. The paper also highlights the significance of selection of a particular MF. Here, the selection of MF's is primarily based on their feature of being smooth and non-zero at all points. Based on this criterion, generalized bell (gbellmf), Gaussian (gaussmf and gauss2mf), sigmoidal (dsigmf and psigmf) and spline based curve (pimf) MF's qualify for selection. Out of these six, only two namely Gaussian MF and generalized bell MF are showing acceptable results. The details related to used MF's has been given below:

Case a: The generalized bell MF's with product inference rule have been used in fuzzification level while defuzzification has been performed using weighted average method. A bell MF is given by equation (29), where parameter 'c' gives distance from origin, parameter 'a' shows curve width and parameter 'b' is normally positive. Its representation is shown in Fig. 4 (a).

$$\mu(x; a, b, c) = \frac{1}{1 + \left|\frac{x - c}{a}\right|^{2b}} \quad (29)$$

Case b: In this case Gaussian MF's with product inference rule have been used for fuzzification while defuzzification has been performed using weighted average method. A symmetric Gaussian MF is given by equation (30), where parameter 'c' gives the distance from origin and 'σ' shows curve width. Its representation is shown in Fig. 4 (b).

$$\mu(x;\sigma,c) = e^{\frac{-(x-c)^2}{2\sigma^2}} \quad (30)$$

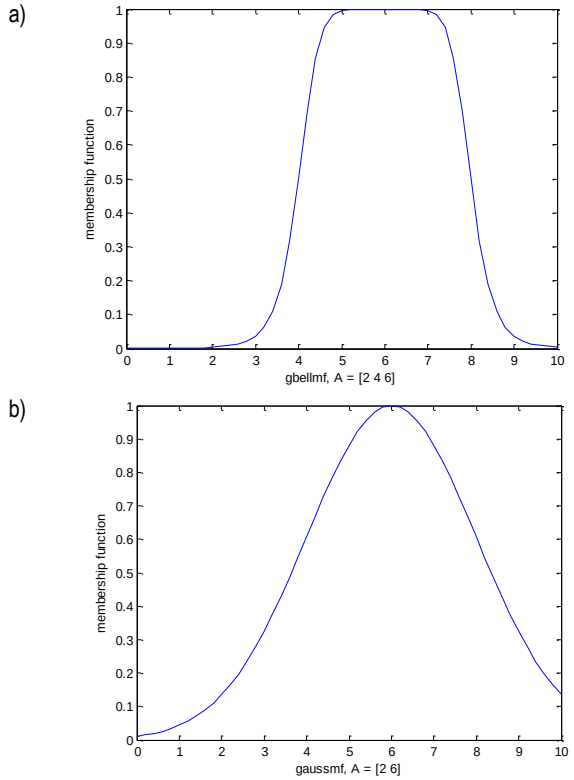

Fig. 4 Representation of generalized bell MF and Gaussian MF

Two ANFIS architectures with two different MF's (as discussed earlier) have been used individually on 5-DOF robotic manipulator. A comparative analysis of these two MF's of ANFIS method based on positioning error for end-effector coordinates has been presented in later paragraphs.

5. IMPLEMENTATION OF ANFIS METHOD ON 5-DOF ROBOTIC MANIPULATOR

In this section of paper, the complete process of implementing ANFIS method on used 5-DOF robotic manipulator has been discussed. The basic procedure of ANFIS method is defined in four steps:

Step (1): Initialization of fuzzy inference system using *genfis1* or *genfis2* command.

Step (2): Define learning parameters such as membership functions, number of epochs and so on

Step (3): Start the learning process using *anfis* command and

Step (4): Validation of individual data set, respectively.

ANFIS method works in two phase viz. training phase and testing phase. In trained ANFIS data, the (x, y, z) coordinates of end-effector of 5-DOF robotic manipulator and joint angles act as the input. Here, five training data sets comprising of coordinates and joint angles has been considered as (x, y, z, θ_1), (x, y, z, θ_2), (x, y, z, θ_3), (x, y, z, θ_4) and (x, y, z, θ_5), respectively.

The respective MF's and number of rules have been assigned for each training data set. Data set 1 consists of seven MF for each end-effector coordinate leading to a total of 343 rules. Data set 2 consists of six MF for each coordinate leading to a total of 216 rules. Data set 3 have five MF each and total 125 rules. Four MF for each coordinate and 64 rule in total has been assigned to data set 4. Dataset 5 has three MF for each coordinate and a total of 27 rules. In this paper, these five data sets have been used on two ANFIS architectures concerning two different MF. The number of epochs used is 10.

The adaptive nature of ANFIS method means that both the premise and consequent parameters are adjustable. The complete adaptive process of ANFIS method is divided into two steps. Consequent parameter training is the first step which uses least square method because the ANFIS output is a linear combination of consequent parameters. During this step, the premise parameters are fixed. In the second step, approximation error is back propagated through every layer to update premise parameters. This part of learning procedure is based on gradient descent principle which is equivalent to training of back propagation neural network. The consequence parameters identified by least square method are optimal as the premise parameters are fixed. This hybrid learning algorithm is more effective than gradient descent method as it reduces the search space dimensions of original back propagation neural network. With this hybrid learning algorithm, ANFIS converges with smaller number of iterations.

The output of ANFIS method has been obtained in the form of variations in (x, y, z) coordinates for 5-DOF robotic manipulator. The variations in coordinates help us to understand the necessity of proper positioning of end-effector of a robotic manipulator. The difference between the (x, y, z) coordinates calculated using forward kinematic equations and (x, y, z) coordinates calculated using ANFIS acts as the individual data set for validation of proper functioning of ANFIS. Out of 0.1 million points generated as coordinate, a total of 500 observation points have been considered to plot the error of end-effector in achieving x-coordinate, y-coordinate and z-coordinate, respectively.

5.1. Membership functions analysis of ANFIS method for positioning error

Here, ANFIS method has been used to find the error obtained in achieving defined coordinates by the end-effector of robotic manipulator. For the very first time, two different MF's, generalized bell MF and Gaussian MF have been used with ANFIS method on 5-DOF robotic manipulator. The accurate positioning of end-effector of robotic manipulator (with wrist in motion) plays an important role in any industrial application. With this point of interest, dataset involving all possible combinations of multiple solutions with respect to joint angles and wrist rotations have been formed. To reach x and y coordinates by end-effector of robotic manipulator, eight set of multiple solutions {(θ_{11}, θ_{21}, θ_{31}, θ_{41})……., (θ_{12}, θ_{22}, θ_{32}, θ_{42})…….and so on} are possible. To reach z coordinate, eight set of multiple solutions {(θ_{21}, θ_{31}, θ_{41})……., (θ_{22}, θ_{32}, $\theta\theta_{42}$)…….and so on} are possible.

In the training phase of ANFIS method, the end-effector coordinates have been calculated for each data set using forward kinematic equations, better known as 'deduced' coordinates. The obtained values of end-effector coordinates in training phase have been taken as reference values. Then the joint angles have been predicted by ANFIS method which in turn has been used to predict end-effector coordinates of 5-DOF robotic manipulator. In this case, the coordinates obtained using ANFIS method is known as 'predicted' coordinates. The above process has been used

DOI 10.1515/ama-2015-0037

for both generalized bell MF and Gaussian MF.

The difference between deduced coordinates and predicted coordinates gives the error in proper positioning of end-effector of robotic manipulator. In the end, the average % errors have been calculated by dividing the error in positioning of end-effector by deduced coordinates of robotic manipulator. For each dataset, average percentage error has been obtained in x, y, z axes using two MF's individually, has been given in Tab. 3.

Tab. 3. Average % error obtained in coordinates using ANFIS method with two different MF's

Dataset	% error using Generalized bell MF			% error using Gaussian MF		
	x	y	z	x	y	z
1	0.41	0.67	2.40	0.4	0.13	0.52
2	0.3	0.35	2.84	0.28	0.44	0.29
3	0.30	1.01	1.57	0.29	0.20	1.05
4	0.35	1.13	0.96	0.34	0.33	1.36
5	0.36	1.16	0.90	0.35	0.36	1.32
6	0.37	0.27	2.46	0.36	0.52	0.43
7	0.26	0.57	3.00	0.25	0.23	0.12
8	0.33	1.24	1.58	0.32	0.44	0.97

As quite evident from Tab. 3, average % error varies from (maximum – 0.4104, minimum – 0.2690) in x axis, (maximum – 1.1672, minimum – 0.2789) in y axis and (maximum – 3.0098, minimum – 0.9073) in z axis using generalized bell MF. The average % error varies from (maximum – 0.4, minimum – 0.2586) in x axis, (maximum – 0.5234, minimum – 0.1323) in y axis and (maximum – 1.3635, minimum – 0.1286) in z axis using Gaussian MF. It can be clearly seen that generalized bell MF gives least average % error for dataset 4 combination. Similarly, Gaussian MF gives least average % error for dataset 7 combination.

The error in all eight set of multiple solutions for x-axis coordinates have been plotted in Fig. 5 (a to h). Similarly, the errors in y-coordinates and z-coordinates have been plotted in Fig. 6 (a to h) and Fig. 7 (a to h), respectively. Fig. 5 (d) and Fig. 7 (d) shows that for dataset 4, generalized bell MF gives better results than Gaussian MF for error in x -coordinates and z-coordinates, respectively. Fig. 5 (g) and Fig. 7 (g) shows that for dataset 7, Gaussian MF gives better results than generalized bell MF for x and z coordinates errors. Fig. 6 (d) and Fig. 6 (g) shows almost similar variations for y-coordinates in dataset 4 and dataset 7, respectively. The selection of dataset has been done on the basis of least average % error obtained in coordinates using ANFIS method with two different MF's. It can be clearly seen that overall Gaussian MF provide better results as compared to generalized bell MF of ANFIS method in end-effector positioning. Since the results during the present study have been obtained in 3D space while considering wrist in motion for the very first time using ANFIS method, the range of error is quite acceptable.

a)

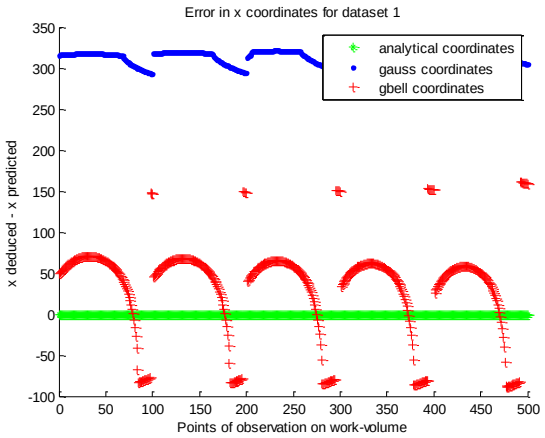

b)

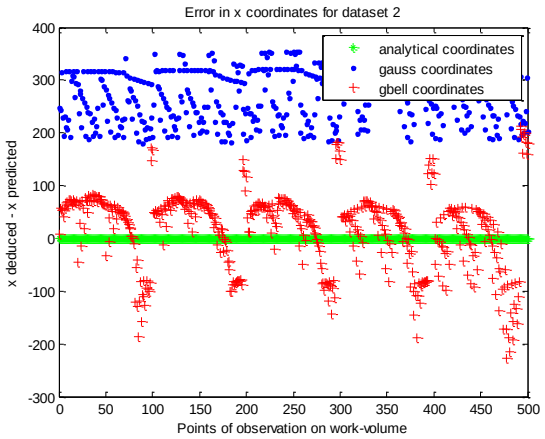

c)

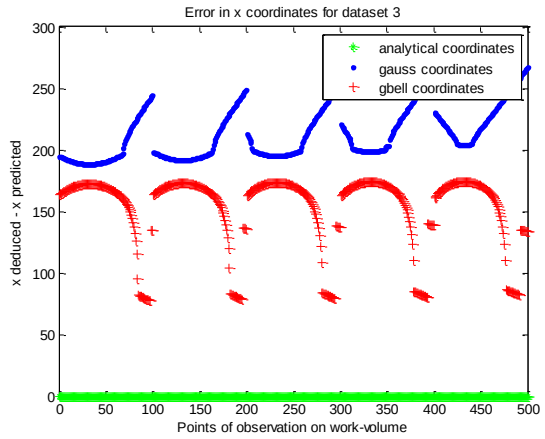

d)

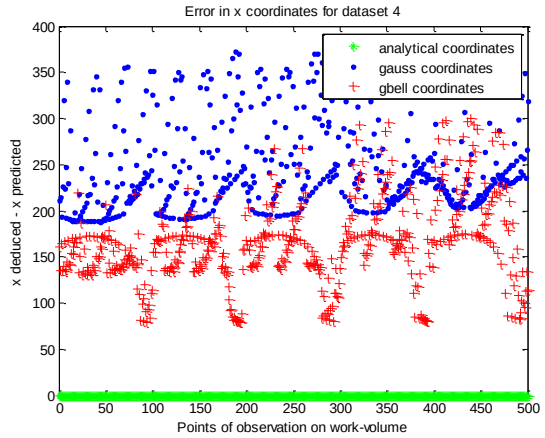

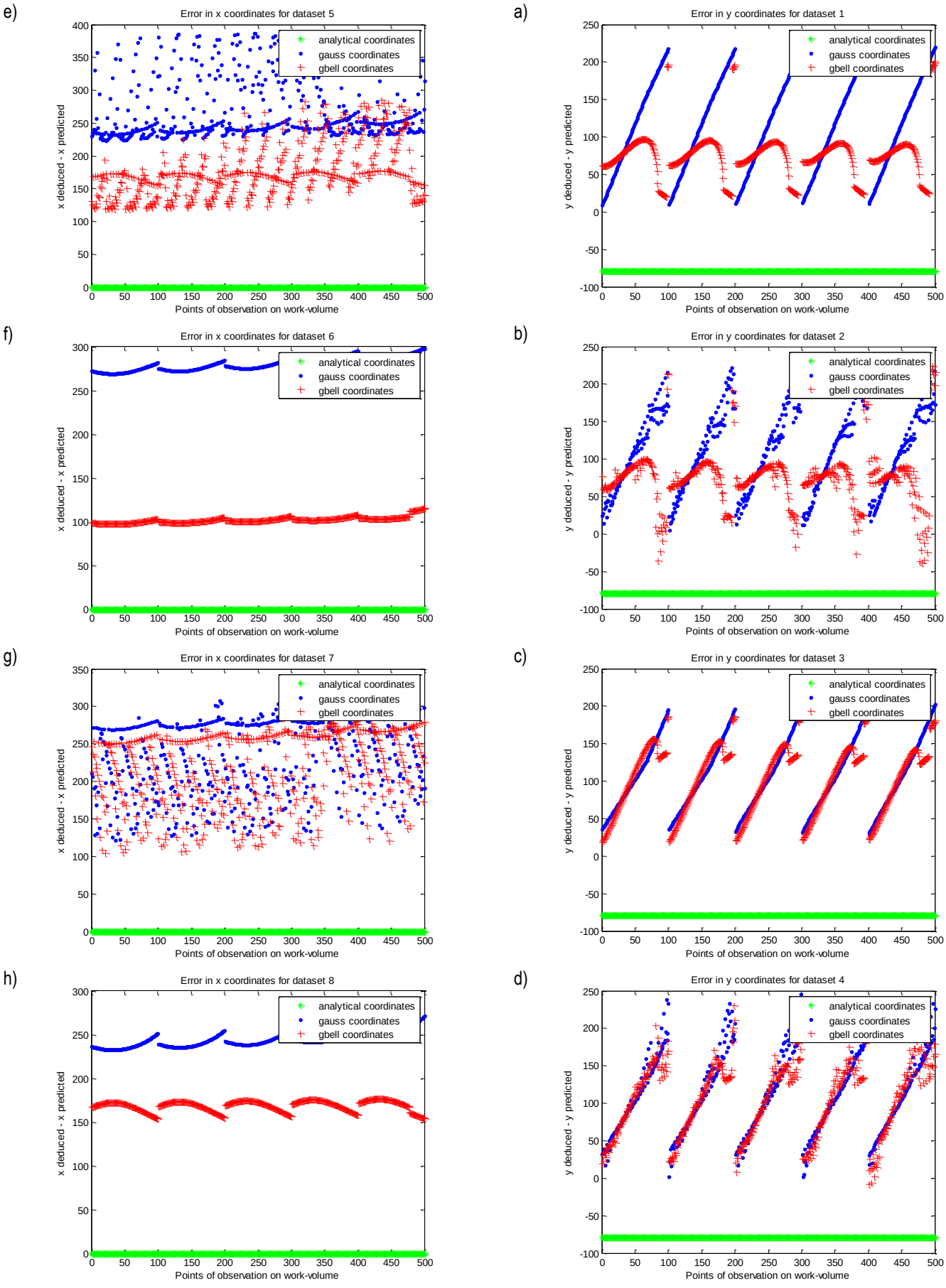

Fig. 5. Comparison of error in x coordinates for eight set of solutions using analytical method and ANFIS method with two MF's

DOI 10.1515/ama-2015-0037

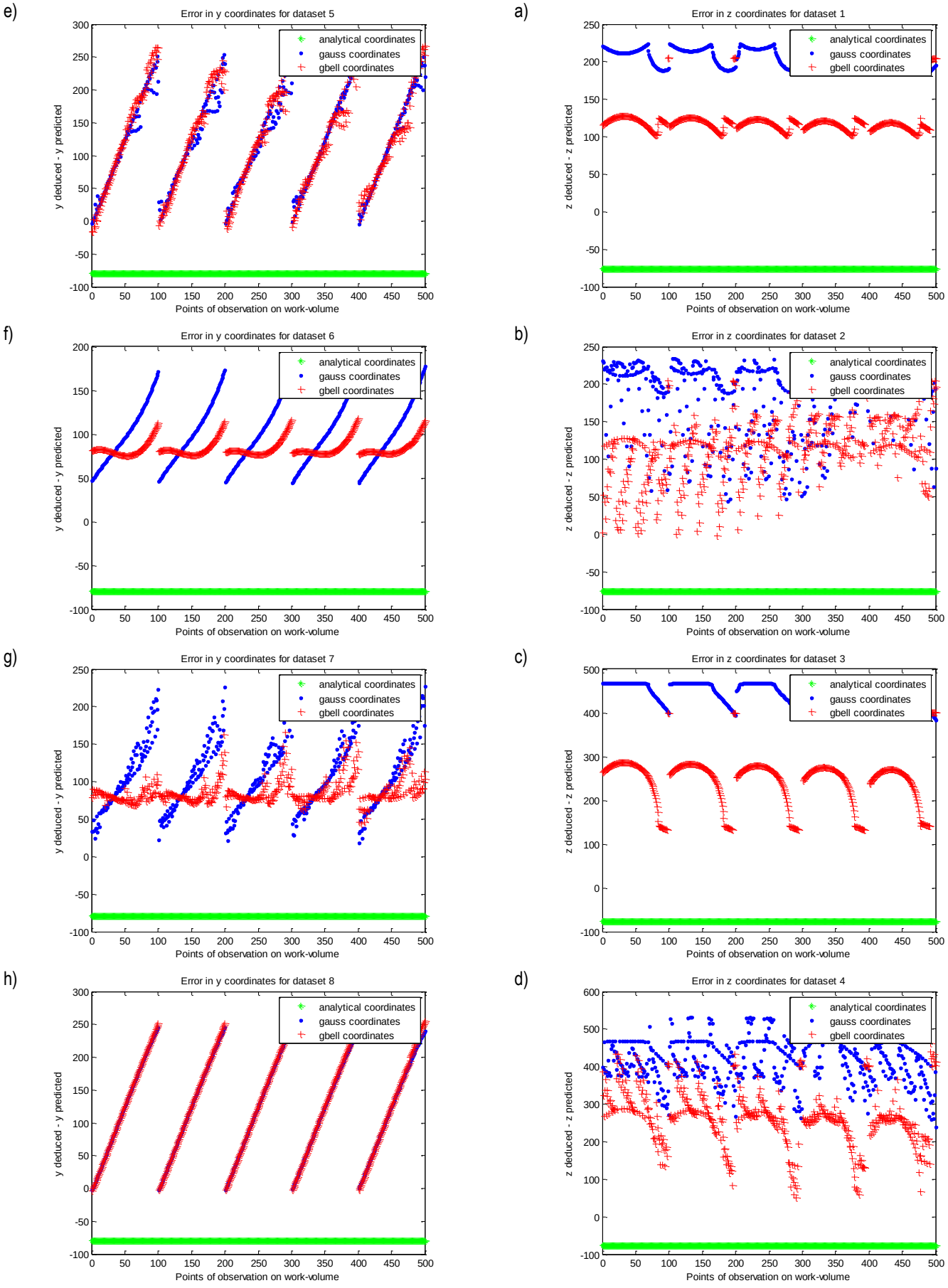

Fig. 6. Comparison of error in y coordinates for eight set of solutions using analytical method and ANFIS method with two MF's

e)

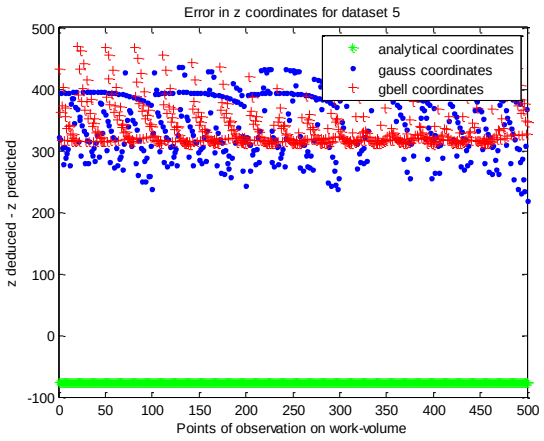

f)

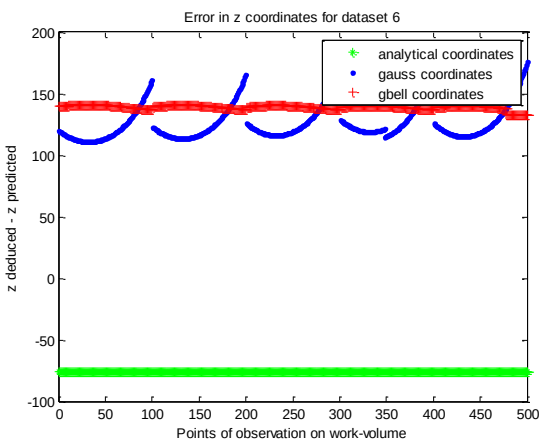

g)

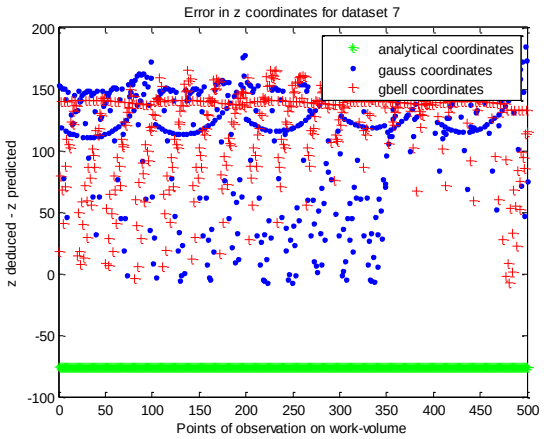

h)

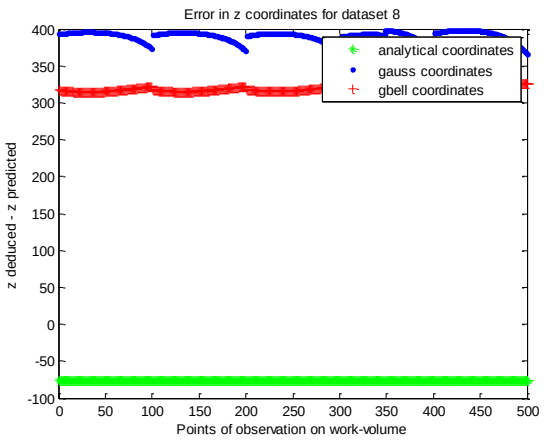

Fig. 7 Comparison of error in z coordinates for eight set of solutions using analytical method and ANFIS method with two MF's

The use of artificial intelligence techniques may be considered as methods for conducting experiments on digital computers, as substitutes for experiments that are impossible in reality or as special case of experiments. However, the use of computer simulations with different methods in experimental activities related to robotic manipulators involves a number of problems: (a) to what extent can we 'trust' results coming from simulations? and (b) is it reasonable to simulate a real robot by operating it in a scale environment? The above raised problems can be solved by validating the results obtained using analytical method and artificial intelligence method with the help of experiments. Experiments form the essential part of science/engineering with a role to either confirm or decline a theory and to find out new theories. It is also reasonable to expect that it can be useful in engineering, especially when the behavior and performance are difficult to characterize analytically, as it has often been the case in robotics. The experiment performed also gives insight of the actual movements of links and joints of robotic manipulator which is of utmost importance for any industrial/medical application. In this paper, the results obtained using analytical method and ANFIS method have been experimentally validated by moving the end-effector of 5-DOF robotic manipulator on desired trajectory.

6. EXPERIMENTAL SET UP

The effectiveness of ANFIS method using two different membership functions along with analytical method has been experimentally verified by 5-DOF robotic manipulator. For experimentation, it is desired to move the end-effector of robotic manipulator on the circumference of a 'circle' trajectory. The trajectory has been selected in such a way that the end-effector of robotic manipulator is free to move on the desired coordinates without getting struck to any singular condition. It is evident that multiple solutions exist for the robotic manipulator under study. The end-effector coordinates obtained using analytical and ANFIS methods have been validated experimentally for all the eight set of possible multiple solutions.

The complete experimental set up for 5-DOF robotic manipulator is as shown in Fig. 8 (a). The robotic manipulator under study has three links where L_o = 226 mm, L_1 = 177 mm, L_2 = 179 mm are the respective link lengths and L_3 = 80 mm, is the distance between wrist center and end-effector center (as given in Tab. 2). The 'circle' trajectory as drawn by the 5-DOF robotic manipulator is shown in Fig. 8 (b).

The complete trajectory is divided into two parts namely, outer half and inner half with two quadrants each having 15 reading points in total. Here, the robotic manipulator is controlled by six stepper motors (Pravak 2008), where five motors are used to move the joints while the sixth motor opens and closes the gripper. The stepper motors move by an angle of 7.5° in each step, which subsequently moves the joints. Thus, the position of the joint can be calculated by counting the number of steps. The 5-DOF Pravak make of robotic manipulator has a dedicated micro-controller located in the base of the robot, which controls all the operations of the robot. The micro-controller communicates with a computer through serial port. It is a closed loop control system where, the feedback is sent by the robot every 100 ms.

DOI 10.1515/ama-2015-0037

a)

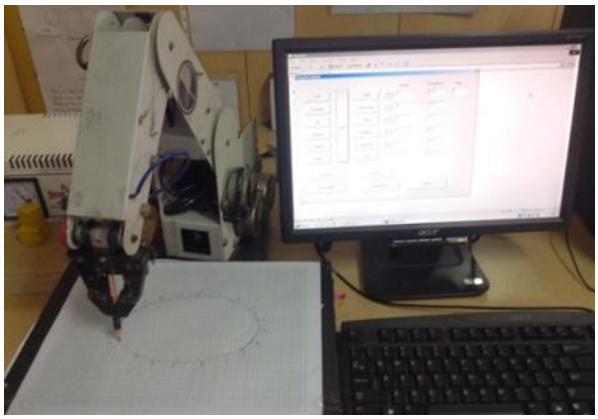

b)

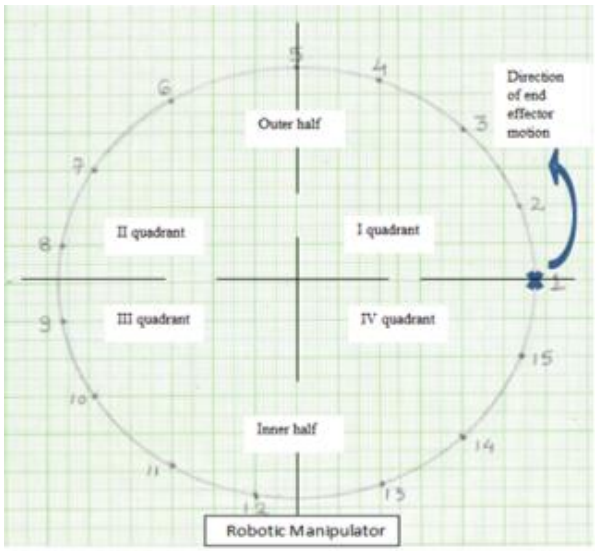

Fig. 8. a) Actual photograph of experimental set
b) Labelled diagram of 'circle' trajectory

6.1. Positioning error analysis using analytical and ANFIS methods with experiment validation

In this paper, the end effector position of robotic manipulator for a 'circle' trajectory has been obtained using analytical and ANFIS methods which are duly validated by experimental data obtained in the laboratory as per the set up discussed above. As discussed in section 6, the joints of robotic manipulator are operated by stepper motors which move by a precise amount of 7.5° with each step, thereby, counting the number of steps moved gives a very good idea of position of the joint. Then with reference to the home position of robotic manipulator, the coordinates of end-effector at each point on trajectory has been calculated. The forward kinematic equations have been used to obtain analytical solutions of coordinates of end-effector at each point on desired trajectory, where experimentally obtained joint angles for specific points on 'circle' trajectory act as the input.

ANFIS method has been used once with generalized bell MF and secondly with Gaussian MF. From the set of multiple solutions obtained (as given in Tab. 3), dataset 4 for generalized bell MF and dataset 7 for Gaussian MF have been used for experimental validation. The reason for dataset selection is based upon the criteria of least error to reach the desired coordinates by the end-effector of the robotic manipulator. Here, the analytical solutions for end-effector coordinates have been taken as reference values; using which the average % error for generalized bell MF, Gaussian MF and experiment has been calculated. Tab. 4 gives the average percentage error obtained in ANFIS method with generalized bell MF, ANFIS method with Gaussian method and experimental data for desired 'circle' trajectory. It clearly shows that Gaussian MF provide better results as compared to generalized bell MF for a 5-DOF robotic manipulator with wrist movement, moving in three-dimensional spaces.

The end-effector coordinates for all the specific points on 'circle' trajectory obtained using analytical method, ANFIS method with two different MF's and experiment have been plotted along x-axis, y-axis and z-axis, as shown in Fig. 9. It lays the background in order to understand the difference between analytical movement and actual movement of industrial robotic manipulators.

Tab. 4. Comparison of average % error obtained in coordinates of 'circle' trajectory

Coordinates	Generalized bell MF	Gaussian MF	Experiment
x	3.28	0.81	10.18
y	29.17	4.62	01.82
z	1.60	0.03	12.48

Fig. 9 (a, b and c) show a comparative analysis of all the used methods. The end effector positioning is highly influenced with the movement of each link and wrist depending upon the complexity of robotic manipulator. Here also, the obtained results can be well understood with the help of motion of each link and wrist of robotic manipulator, as shown in the experimental set up. This analysis also helps in identifying the importance of rigidity of links and end effector required for improved performance during industry use.

Fig. 9 (a) gives a comparison of end effector positioning along x -axis obtained using all three methods. It can be seen that the results obtained using analytical and ANFIS methods (with generalized bell MF and Gaussian MF) are matching quite accurately with each other throughout the 'circle' trajectory. Apart from this, these results are also showing good agreement with experimental results in the outer half of 'circle' trajectory. However, small deviations from experimental results can be seen in the inner half of the 'circle' as compared to other two methods.

Fig. 9 (b) shows a comparison of end effector positioning along y-axis obtained using all three methods. It can very well be concluded that the results obtained using analytical and ANFIS method (with Gaussian MF) are showing good agreement with the experimental results at all points along 'circle' trajectory. The results for ANFIS method with generalized bell MF are little deviated as compared with the results of other methods.

Fig. 9 (c) shows a comparison of end effector positioning along z-axis obtained using all three methods. It can be seen that the results obtained using analytical and ANFIS methods are showing deviations at some points along 'circle' trajectory which are not significant. The Gaussian MF of ANFIS method is matching quite accurately with analytical method as compared to generalized bell MF. However, these results are showing considerable deviations from experimental results at all points along 'circle' trajectory especially in the last three quadrants.

A good agreement between results obtained using analytical and ANFIS methods supports the equations and methodology presented in this paper. On the other hand, deviations in these results from experimental results are due to inherent irregular motion in the links and wrist by the virtue of physical constraint of experimental set up used in this research work. This physical

constraint results in erroneous plotting of 'circle' trajectory coordinates on the graph. Whereas joint angles required as inputs for analytical and ANFIS methods are calculated using step count of stepper motors of robotic manipulator only which remains unaffected by these constraints observed at end effector. This limitation of experimental set up is showing its effect largely while plotting inner half of the 'circle' trajectory resulting due to end-effector being closer to the body of the robotic manipulator.

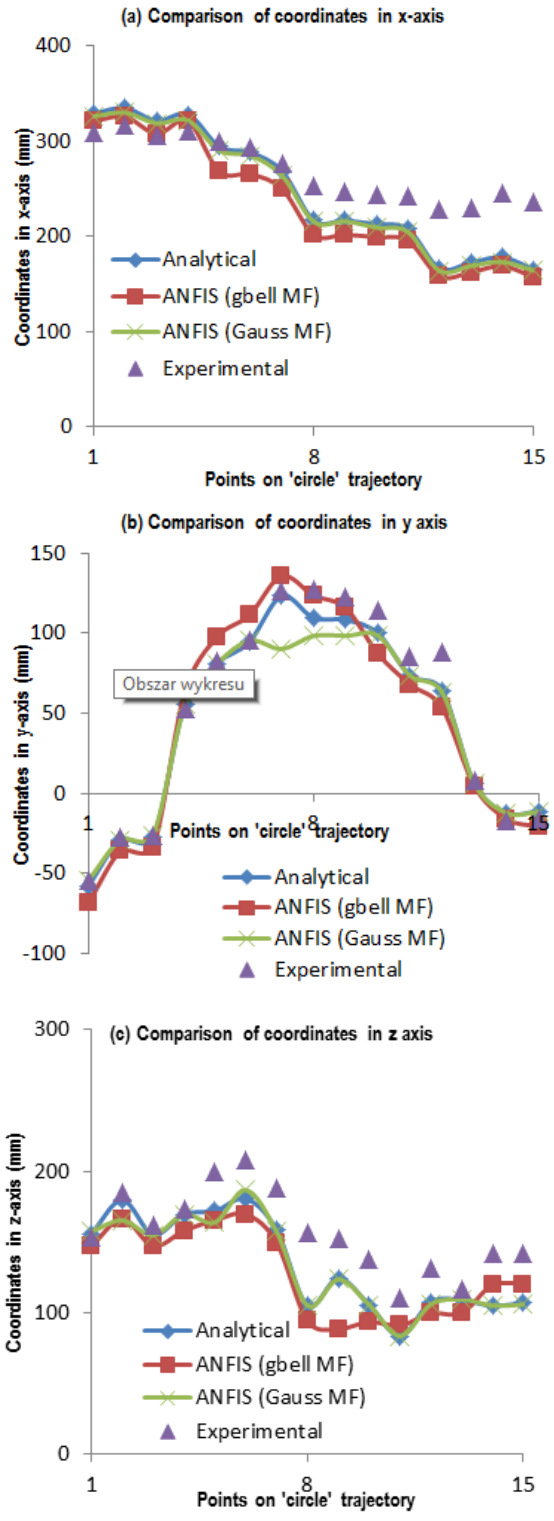

Fig. 9. Comparison of positioning errors of end-effector of robotic manipulator

7. CONCLUSIONS

The work presented in this paper has been tried to provide a single platform for analytical analysis, simulation and experimental methods for a 5-DOF robotic manipulator with wrist in movement. The experimental validation has been performed for a 'circle' trajectory.

The following specific conclusions are drawn from the research work:

i. Forward and inverse kinematic equations have been derived for analytical solution of a 5-DOF robotic manipulator with 2-DOF wrist movement in consideration.
ii. ANFIS method with two different MF's i.e. generalized bell MF and Gaussian MF have been applied for the very first time on a 5-DOF robotic manipulator considering wrist in movement.
iii. The average percentage error obtained to reach desired coordinate shows that Gaussian MF provides better results than generalized bell MF for a 5-DOF robotic manipulator moving in three-dimensional spaces.
iv. A good agreement between results obtained using analytical and ANFIS methods supports the equations and methodology presented in this paper.
v. Analytical and ANFIS results show good agreement with experimental results in first and fourth quadrants along 'circle' trajectory for x and z coordinates. However, deviations in these results are observed in y coordinates.

The future scope of the work can be as follows:

i. Further studies can be made to more complex architectures of robotic manipulators.
ii. Various other hybrid or non-hybrid artificial intelligent techniques can be applied which may produce far more accurate results.

Nomenclature: a_i, d_i, α_i, θ_i (i = 1,2,3,4,5) – the Denavit-Hartenberg parameters; L_i (i = 0,1,2,3) – respective link lengths; p_e – end-effector coordinates; p_w – coordinates of wrist; p_x, p_y, p_z – translation about x-axis, x -axis and x -axis; n_x, n_y, n_z, o_x, o_y, o_z, a_x, a_y, a_z – rotation about x -axis, x -axis and x -axis; C_i (i = 1, 2, 3, 4, 5) – cosine; S_i (i = 1, 2, 3, 4, 5) – sine; A_i – the transformation matrix; DOF – degree of freedom; MF – membership function.

REFERENCES

1. **Aghajarian M., Kiani K.** (2011), Inverse Kinematics Solution of PUMA 560 Robot Arm using ANFIS, *8th International Conference on Ubiquitous Robots and Ambient Intelligence*, Songdo Conventia, Korea.
2. **Agarwal V., Mittal A.P., Nakra B.C.** (2005), A Study of Fuzzy Logic Based Inverse Kinematics Solution, *Proceedings of International Conference on Computer Applications in Electrical Engineering*, IIT Roorkee, India.
3. **Alavander S., Nigam M.J.** (2008), Inverse Kinematics Solution of 3-DOF Planar Robot using ANFIS, *International Journal of Computers, Communication and Control*, 3,150-155.
4. **Azadivar F.** (1987), The Effect of Joint Position Errors of Industrial Robots on Their Performance in Manufacturing Operations, *IEEE Journal of Robotics and Automation*, RA-3 (2), 109-114.

DOI 10.1515/ama-2015-0037

5. **Bachir O., Zoubir A.** (2012), Adaptive Neuro-fuzzy Inference System based Control of PUMA 600 Robot Manipulator, *International Journal of Electrical and Computer Engineering*, 2 (1), 90-97.
6. **Bingul Z, Karahan O.** 2011, A Fuzzy Logic Controller tuned with PSO for 2 DOF robot trajectory control, *Expert Systems with Applications*, 38, 1017-1031.
7. **Chen C, Wu T, Peng C.** 2010, Robust trajectories following control of a 2-link robot manipulator via coordinate transformation for manufacturing applications, *Robotics and Computer-Integrated Manufacturing*, 27, 569-580.
8. **Conkur E.** (2003), Path following algorithm for highly redundant manipulators, *Robotics and Autonomous Systems*, 45, 1-22.
9. **Corke P.I.** (2011), *Robotics Toolbox for MATLAB (Release 9)*, http://petercorke.com/Robotics_Toolbox.html.
10. **Denavit J, Hartenberg R.S.** (1955), A kinematic notation for lower pair mechanisms based on matrices, *ASME Journal of Applied Mechanics*, 77, 215-221.
11. **Efe M.O., Kaynak O.** (2000), A comparative study of soft-computing methodologies in identification of robotic manipulators, Robotics and Autonomous Systems, *Elsevier*, 30, 221-230.
12. **Elgazzar S.** (1985), Efficient Kinematic Transformations for the PUMA 560 Robot, *IEEE Journal of Robotics and Automation*, RA-1 (3),142-151.
13. **Er M.J., Yap S.M., Yeaw C.W., Luo F.L.** (1997), A Review of Neural-Fuzzy Controllers for Robotic Manipulators, *Conference Record of the IEEE Industry Applications*.
14. **Gasparetto A, Zanotto V.** (2007), A new method for smooth trajectory planning of robotic manipulators, *Mechanism and Machine Theory*, 42, 455-471.
15. **Homaifar A, Sayyarrodsari B, Hogans J.** (1994), Fuzzy Controller for Robot Arm Trajectory, *Information Sciences*, 2, 69-83.
16. **Jang J.S.R.** (1993), ANFIS: Adaptive Network based Fuzzy Inference System. IEEE Transactions on Systems, *Man and Cybernetics*, 665-685.
17. **Karlik B, Aydin S.** (2000), An improved approach to the solution of inverse kinematics problems for robot manipulators, *Engineering Applications of Artificial Intelligence*, 13, 159-164.
18. **Kim W.S., Tendick F., Stark L.W.** (1987), Visual Enhancements in Pick-and-Place Tasks: Human Operators Controlling a Simulated Cylindrical Manipulator, *IEEE Journal of Robotics and Automation*, RA-3 (5), 418-425.
19. **Koyuncu B., Guzel M.** (2007), Software development for the kinematic control of Lynx6 Robot Arm, *World Academy of Science*, Engineering and Technology, 252-257.
20. **Kuo C, Wang S.** (1991), Robust Position Control of Robotic Manipulator in Cartesian Coordinates, *IEEE Transactions on Robotics and Automation*, 7, 653-659.
21. **Manjaree S., Shah J., Nakra B.C.** (2010), *Studies on Kinematics of Robotic Systems Using Artificial Intelligence Techniques*, M Tech Thesis, Maharishi Dayanand University, Rohtak.
22. **Manjaree S.** (2013), Inverse Kinematic Analysis of 3-degree-of-freedom Robotic Manipulator using three different methods, *International Journal of Advances in Science and Technology*, 6(3), 71-80.
23. **Manjaree S., Agarwal V., Nakra B.C.** (2013), Inverse Kinematics using Neuro-Fuzzy Intelligent Technique for Robotic Manipulator, *International Journal of Advanced Computer Research*, 3(4), 160-165.
24. **Manseur R.** (1996), A software package for computer-aided robotics education, *Proceedings of 26th Annual Conference on Frontiers in Education*, Salt Lake City, UT.
25. **Mittal R.K., Nagrath I.J.** (2003), *Robotics and Control*, Tata Mc Graw Hill Publishing Company Limited.
26. **Mohan S., Bhanot S.** (2007), Comparative Study of Some Adaptive Fuzzy Algorithms for Manipulator Control, *International Journal of Computational Intelligence*, 3(4), 303-311.
27. **Niku S.B**. (2009), *Introduction to Robotics: Analysis, Systems, Applications*, PHI Learning Private Limited, India.
28. **Pravak Manual** (2008), *Model 1055*, Pravak Cybernetics, New Delhi.
29. **Saha S.K.** (2008), *Introduction to Robotics*, Tata McGraw Hill Education Private Limited.
30. **Shah J., Rattan S.S., Nakra B.C.** (2013), End-Effector Position Analysis Using Forward Kinematics For 5 Dof Pravak Robot Arm, *IAES International Journal of Robotics and Automation*, 2(3), 112-116.
31. **Tejomurtula S., Kak S.** (1999), Inverse kinematics in robotics using neural networks, *Information Sciences, Elsevier*, 116 (2), 147-164.
32. **Yahya S., Moghavvemi M, Haider A.F. Mohamed** (2011), Geometrical approach of planar hyper-redundant manipulators: Inverse kinematics, trajectory planning and workspace, *Simulation Modeling Practice and Theory*, 19, 406-422.

STRESS-STRAIN STATE OF ELASTIC PLATE WITH AN ARBITRARY SMOOTH NOTCH

Ihor KUZ*, Olga KUZ, Heorgij SULYM*****

*Department of Mechanics and Mathematics, Ivan Franko National University of Lviv, 1 Universitetska Str., 79000 Lviv, Ukraine
**Vyacheslav Chornovil Institute of Ecology, Nature Protection and Tourism, National University "Lviv Polytechnic", 12 Bandery Str.,79013 Lviv,Ukraine
***Faculty of Mechanical Engineering, Bialystok University of Technology, 45C Wiejska Str., 15-351 Bialystok, Poland

ihorkuz24@gmail.com, olyakuzon@gmail.com, sulym@pb.edu.pl

received 4 May 2015, revised 15 December 2015, accepted 16 December 2015

Abstract: The paper contains comparing calculations of the stress fields in an elastic plate with notch along the arc of a circle, ellipse or parabola obtained by analytic method based on complex Kolosov-Muskhelishvili potentials and by numerical variation-difference method. These fields differ by no more than 2%, which, in particular, indicates the reliability of such numerical implementation. This discrepancy can be explained by the fact that in the analytical solution domain is unbounded, while the numerical calculation was carried out, obviously, for a finite field. The given stresses at the top of the notch along the arc of an ellipse or a parabola significantly increase with increasing of the relative depth of the notch (while increasing its depth or decreasing width).

Keywords: Semi-Plane, Plate, Notch, Variation-Difference Method, Stress Field

1. INTRODUCTION

Investigation of the stress-strain state of the plate structural elements weakened by notch (Lazzarin and Tovo, 1996, Savruk and Kazberuk, 2006-2014, Savruk et al., 2012) is a necessary step in the prediction of their strength and safety. Since these structural elements have finite dimensions or curvilinear boundary, the possibility of the application of analytical methods for solving the corresponding boundary value problems (Muskhelishvili, 2003) is significantly limited, and in most cases impossible.

In this paper, we provide comparison of the obtained solutions of plane elasticity problems on uniaxial loading of a plate structural element with notch of an arbitrary smooth contour by analytic method using the complex Kolosov-Muskhelishvili potentials (Kuz, 2005) and numerical method on base of the variation-difference method (Kuz, 2008, Kuz et al., 2014).

2. ANALYTIC METHOD FOR SOLVING THE PROBLEM

Let us find the stress state of a plate of the thickness$h$, which is simulated by the half-plane, on the surface of which a notch is made of an arbitrary smooth contour. We assume that the half-plane extends to infinity by normal stress of value P (Fig. 1), and the boundary of the half-plane with notch is free from stresses.

Choose a Cartesian coordinate system Oxy, directing the axis Ox along the straight edge, and the vertical axis – upwards. The curve traced by the notch is denoted by L, the straight line portionof the boundary of the half-plane by L'. The lower half-plane of the plane xOy is denoted by S^-, the upper one by S^+.

According to the formulation of the problem we have the following boundary conditions:

$$\Sigma_{yy} = 0, \quad \Sigma_{xy} = 0, \quad x \in L'; N = T = 0, \quad t \in L,$$

where N and T are the normal and tangential components of the vector of stresses on L respectively.

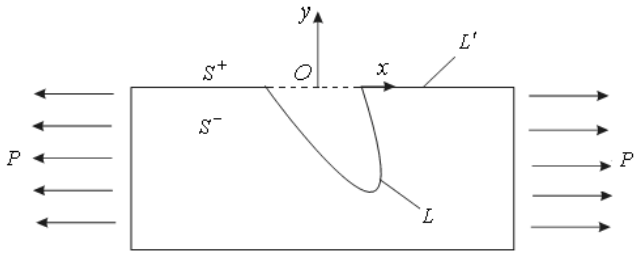

Fig. 1. Plate with the notch under uniaxial loading

To solve the problem, we introduce the complex Kolosov-Muskhelishvili potentials $\Phi(z)$ and $\Psi(z)$and present them in the form:

$$\Phi(z) = \Phi_1(z) + \Phi_2(z) + \frac{p}{4}, \quad \Psi(z) = \Psi_1(z) + \Psi_2(z) - \frac{p}{2}.$$

Here $\Phi_2(z)$ and $\Psi_2(z)$ are complex potentials which are holomorphic in the lower half-plane and must ensure that the zero boundary conditions on the axis $y = 0$, are fulfilled, and corrective complex potentials $\Phi_1(z)$ and $\Psi_1(z)$ are responsible for the implementation of the boundary conditions on the surface of the notch.

Analytically extending the function $\Phi_2(z)$ from the region S^- over the region S^+ and solving the corresponding problem of conjugation of boundary values on the line, we obtain a singular integral equation, which we solve numerically using the method of mechanical quadratures (Panasiuk et al., 1976).

DOI 10.1515/ama-2015-0038

3. VARIATION-DIFFERENCE METHOD FOR SOLVING THE PROBLEM

We also consider the plane problem of elasticity theory in a finite region V with curved boundary Σ (see Fig. 1), which simulates the stress-strain state in a plate with notch of an arbitrary smooth contour. From the mathematical point of view it consists in solving equations of equilibrium in a plate (Bozydarnik and Sulym, 2012):

$$\left(C_{ijkl}u_{k,l}\right)_{,j} = 0 \tag{1}$$

using mixed boundary conditions on the surfaceΣ

$$C_{ijkl}u_{k,l}n_j \quad |_{\Sigma} = P_i \ . \tag{2}$$

Here C_{ijkl} are the components of the elastic modulus tensor; u_i, P_i , n_j are the components of the displacement vector, surface forces, and the external normal to the surfaceΣ respectively; $u_{i,j} \equiv \partial u_i/\partial x_j$. We assume the summation from one to two by the same indices that occur twice in one expression.

For numerical solution of problem (1) – (2) it is convenient to use its variation formulation (Pobedria, 1981), which is to minimize the Lagrangian:

$$L = \int_V W\, dV - \int_{\Sigma} P_i \ \ u_i d\Sigma, \tag{3}$$

where $W = \frac{1}{2}C_{ijkl}u_{i,j}u_{k,l}$ is the energy density of elastic deformation.

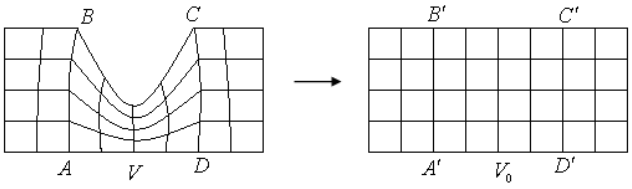

Fig. 2. Mapping of a grid in the curvilinear region V onto the uniform rectangular grid in the region V_0

We write the Lagrangian (3) in the canonical region V_0, which can be a rectangle or a region composed of rectangles. For this purpose we use a discrete bijection mapping of the grid in a curvilinear region V to a uniform rectangular grid $N_1 \times N_2$ of the region V_0 (Fig. 2):

$$x_i = x_i(\beta^1, \beta^2) \quad (i = 1,2). \tag{4}$$

Then $J = det(A_i^j)$, $g_{ij} = A_i^m A_j^m$, where $A_i^j = \partial x_i/\partial \beta^j$ is the Jacobi matrix of this mapping. Using (4) we write the density energy of the deformation W in the coordinates $\vec{\beta}$

$$W = \frac{1}{2}C^{ijkl}u_{i,j}u_{k,l} = \frac{1}{2}C^{ijkl}\left(\vec{\beta}\right)B_j^m B_l^n u_{i|m}u_{k|n} = \frac{1}{2}D^{imkn}\left(\vec{\beta}\right)\mathrm{u_{i|m}u_{k|n}}$$

where $u_{i|m} \equiv \partial u_i/\partial \beta^m$, $B_j^m = \partial \beta^m/\partial x_j$, $D^{imkn} = C^{ijkl}B_j^m B_l^n$.

Thus, the Lagrangian in the rectangle V_0 will look like:

$$L_0 = \frac{1}{2}\int_{V_0} JD^{imkn}\, u_{i|m}u_{k|n}dv - \int_{\Sigma_0} q\left(\vec{\beta}\right) P_i u_i d\Sigma, \tag{5}$$

where $q(\vec{\beta}) = \begin{cases}\sqrt{g_{11}}, & \beta^2 = \{0, l_2\},\\ \sqrt{g_{22}}, & \beta^1 = \{0, l_1\}.\end{cases}$

Replacing in (5) all continual function by grid ones, integrals by finite sums, and derivatives by difference derivatives, we obtain the difference analogue of the Lagrangian L_0^h using the discrete analogue of mapping (4), which should not be given analytically, in particular, to be conformal. It is sufficient to have one correspondence between nodes in the curvilinear V_1 and model V_0 regions. To determine the stationary point L_0^h we obtain a system of linear algebraic equations:

$$\partial L^h/\partial v_\beta^h\,(i_1, i_2) = 0, \quad i_\alpha = 1,2,\ldots,N_\alpha, \quad \alpha, \beta = 1,2. \tag{6}$$

This approach leads to the impossibility of the use of direct methods for solving the system (6) due to the accumulation of errors of rounding. However, it was done with a combined iterative process that implements the scheme of the gradient method and the method with Chebyshev set of iterative parameters. The complexity of its practical implementation is selection of iterative parameters.

The described variation-difference method in domains with curved boundary is implemented as a software on FORTRAN.

4. RESULTS

For example, the calculations of the components of the stress tensor on the notch and near it done, if its boundary is an arc of the circle, ellipse or parabola.

In Fig. 3 and Fig. 4 there are shown the graphs of dimensionless stresses $\sigma_{\theta\theta}^0 \equiv \sigma_{\theta\theta}/P$, $\sigma_{xx}^0 \equiv \sigma_{xx}/P$ and $\sigma_{yy}^0 \equiv \sigma_{yy}/P$ for the notches along the arc of the circle. Here and after, 2lis the width of the notch (along the axis Ox); δis the depth of the notch (along the axis Oy); $a = \delta/l$ is a dimensionless parameter relative absorption; $\sigma_{\theta\theta}^0$ is dimensionless circumferential stress on the notch, σ_{xx}^0, σ_{yy}^0 are dimensionless normal stresses on a segment $x^0 \equiv x/l = 0$, $y^0 \equiv y/\delta \in [-5, -1]$ (along the axis Oy below the groove). The hatched lines represent stress obtained by the analytic method, and the solid lines by variation-difference method.

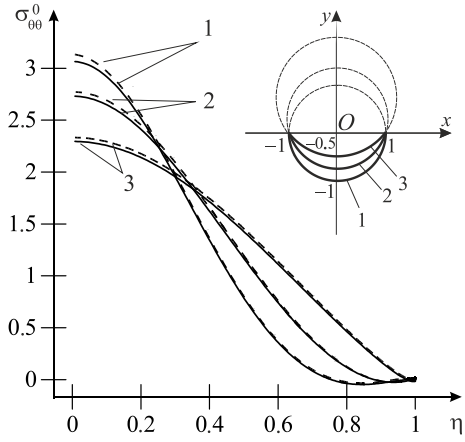

Fig. 3. Stress $\sigma_{\theta\theta}^0$ on the notch in an arc of the circle for $l = 1$ at different values of δ

In Fig. 3, the curves 1 are obtained for $\delta = 1$, curves 2 for $\delta = 0.75$, curves 3 for $\delta = 0.5$. As seen from this figure, the stress $\sigma^0_{\theta\theta}$ (actually the coefficient of stress concentration) in the top of the notch ($\eta = 0$) achieves its greatest value in the case of notch along the semicircle (curve 1). And it is only slightly higher than typical for the Kirsch problem value 3.

Here and after, the accuracy of the results is of four significant digits (the error of about 0,1%). Monitoring convergence and accuracy of analytic and numerical solution is conducted by comparing the studied parameters on the grids with single and double number of nodes.

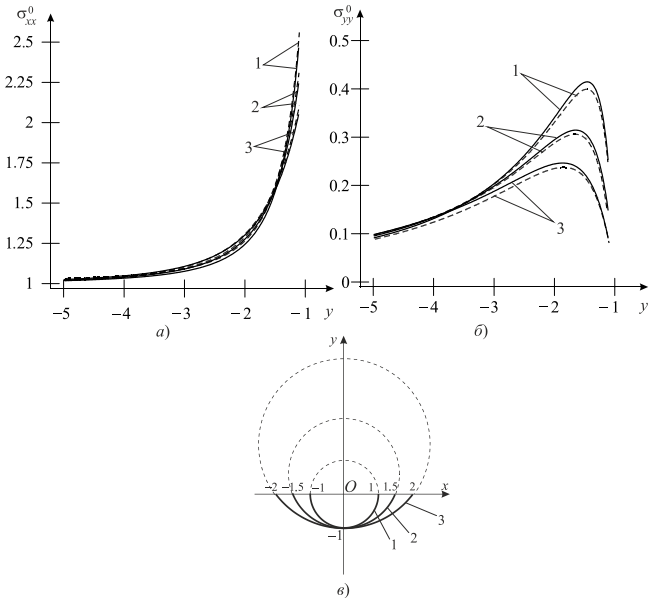

Fig. 4. Stresses σ^0_{xx} and σ^0_{yy} on extension of the axis of symmetry of the notch along the arc of a circle $\delta = 1$ for various values of l

In Fig. 4, the curves 1 are obtained for $l = 1$, curves 2 for $l = 1.5$, curves 3 for $l = 2$. As shown in Fig. 4, the normal stress σ^0_{xx} much lower of the notch ($y = -5$) is almost equal P, and at the top of the notch it is obvious that $\sigma^0_{xx} = \sigma^0_{\theta\theta}$.

Fig. 5 and Fig. 6 show the relevant graphs of stresses $\sigma^0_{\theta\theta}$, σ^0_{xx} and σ^0_{yy} for the notches along the arc of the ellipse.

In Fig. 5 the curves 1 are obtained for $\delta = 0.5$, curves 2 for $\delta = 0.75$, curves 3 for $\delta = 1$, curves 4 for $\delta = 1.5$.

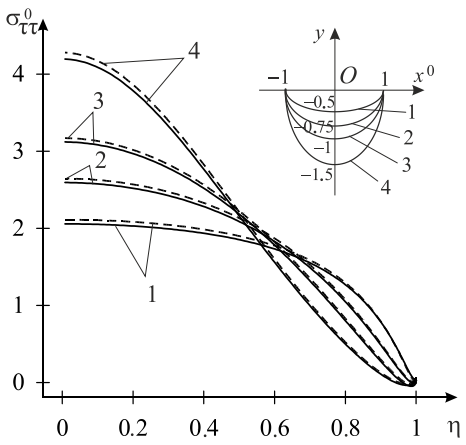

Fig. 5. Stress $\sigma^0_{\tau\tau}$ on the notch along the arc of the ellipse for $l = 1$ and various values of δ

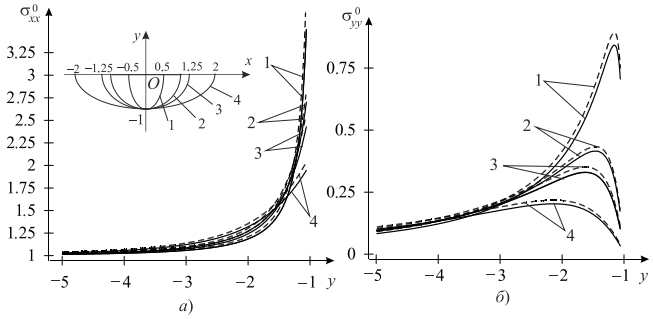

Fig. 6. Stresses σ^0_{xx} and σ^0_{yy} on the extension of the symmetry axis of the notch along the arc of the ellipse for $\delta = 1$ and various values of l

In Fig. 6, the curves *1* are obtained for $l = 0.5$, curves *2* for $l = 1$, curves *3* for $l = 1.25$, curves *4* for $l = 2$.

Fig. 7 and Fig. 8 show the relevant graphs of stresses $\sigma^0_{\tau\tau}$, σ^0_{xx} and σ^0_{yy} for the notches along the arc of the parabola.

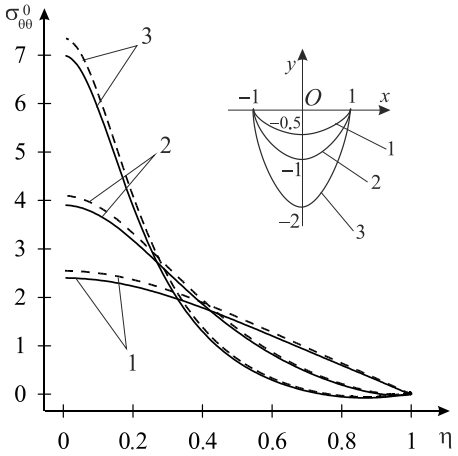

Fig. 7. Stress $\sigma^0_{\tau\tau}$ on the notch along the arc of the parabola for $l = 1$ and various values of δ

In Fig. 7, the curves *1* are obtained for $\delta = 0.5$, curves *2* for $\delta = 1$, curves *3* for $\delta = 2$.

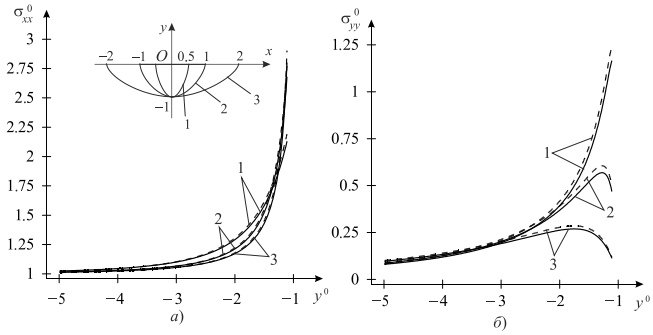

Fig. 8. Stresses σ^0_{xx} and σ^0_{yy} on the extension of the symmetry axis of the notch along the arc of the parabola for $\delta = 1$ and various values of l

In Fig. 8, the curves 1 are obtained for $l = 0.5$, curves 2 for $l = 1$, curves 3 for $l = 2$.

DOI 10.1515/ama-2015-0038

Fig. 9 shows the change of the stress $\sigma_{\tau\tau}^0$ for the three types of notches of the same depth (arces of circle, parabola and ellipse that pass through three fixed points), which enables us to identify the influence of notch shape on the stress state of the plate.

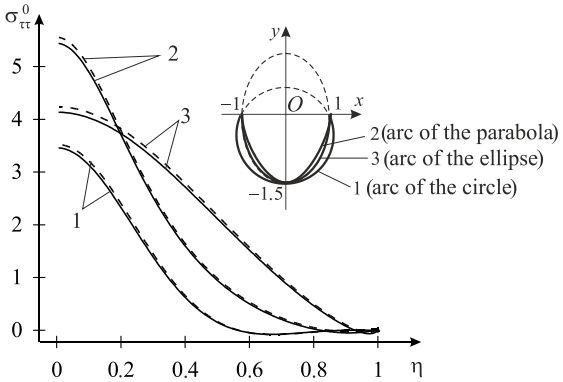

Fig. 9. Stress $\sigma_{\tau\tau}^0$ on the surface of the notches of the same depth along the arc of the circle, parabola, and ellipse for $l = 1$, $\delta = 1.5$

In Fig. 9, curve 1 concerns the circle, curve 2 the parabola, and curve 3 the ellipse.

5. CONCLUSIONS

As is shown in Fig. 5-8, the given stresses at the top of the notch along the arc of an ellipse or a parabola significantly increase with increasing of the relative depth of the notch (while increasing its depth or decreasing width). As is shown in Fig. 9, sharpness of the notch, obviously, also enlarges the level of stresses.

As is shown in Fig. 3-9, the stress fields obtained by analytic and variation-difference methods differ by no more than 2%. This discrepancy can be explained by the fact that in the analytical solution domain is unbounded, while the numerical calculation was carried out, obviously, for a finite field.

Thus, the developed method of numerical determination of stresses and their concentrations agrees at solving plane elasticity problems in the plates with notch.

REFERENCES

1. **Bozydarnik V. V., Sulym H. T**. (2012), *Theory of Elasticity*, V. 1, Publishing House of Lutsk National Technical University, Lutsk (in Ukrainian).
2. **Kuz I.** (2008), Numerical solution of plane plasticity problem about metal elbow strain, *Visnyk of Lviv University, Ser. Mech. et Math*., 69, 203–209 (in Ukrainian).
3. **Kuz I., Kuz O., Pyz N.** (2014), Influence of stress concentrators onto stress-strain state of elasto-plastic plates, *Visnyk of the Ternopil National Technical University,* 4(76), 79-88 (in Ukrainian).
4. **Kuz O. (**2005), Stress state of semi-plane with notch under uniform extension, *Abstract of the Sixth Polish-Ukrainian Conference "Current problems of mechanics of nonhomogeneous media",* Warsaw, 76–77 (in Ukrainian).
5. **Lazzarin P., Tovo R.** (1996), A unified approach to the evaluation of linear elastic stress fields in the neibourhood of cracks or notches, *International Journal of Fracture,* 78, 3-19.
6. **Muskhelishvili N.I.** (2003), *Some Basic Problems of the Mathematical Theory of Elasticity,* Springer.
7. **Panasiuk V. V., Savruk M. P., Datsyshyn O. P.** (1976), *Distribution of Stresses near Cracks in Plates and Shells*, Naukova Dumka, Kyiv (in Russian).
8. **Pobedria B. E.** (1981), *Numerical Methods in Theory of Elasticity and Plasticity*, Publishing House of Moscow University, Moscow (in Russian).
9. **Savruk M.P., Kazberuk A.** (2006), Relationship between the stress intensity and stress concentration factor for sharp and rounded notches, *Material Science (Springer),* 42(6), 725-738.
10. **Savruk M.P., Kazberuk A.** (2007), A unified approach to problems of stress concentration near V-shaped notches with sharp and rounded tip, *International Applied Mechanics,* 43(2), 182-187.
11. **Savruk M.P., Kazberuk A.** (2007), Stress concentration near a rounded v-notch with arbitrary vertex curvature, *Acta mechanica et Automatica,* 1(1), 99–102 (in Polish).
12. **Savruk M.P., Kazberuk A.** (2010), Two-dimensional fracture mechanics problems for solids with sharp and rounded V-notches, *International Journal of Fracture*, 161, 79-95.
13. **Savruk M.P., Kazberuk A.** (2011), Antisymmetric stress distribution in an elastic body with a sharp or a rounded v-shaped notch, *Material Science (Springer),* 46(6), 711-722.
14. **Savruk M.P., Kazberuk A.** (2012), Distribution of stresses near V-shaped notches in the complex stressed state, *Material Science (Springer),* 47(4), 476-487.
15. **Savruk M.P., Kazberuk A.** (2014), Curvilinear cracks in the anisotropic plane and the limit transition to the degenerate material, *Material Science (Springer),* 50(2), 189-200.
16. **Savruk M.P., Kazberuk A.** (2014), Plane elgenvalue problems of the elasticity theory for orthotropic and quasi-orthotropic wedges, *Material Science (Springer),* 50(6), 707-714.
17. **Savruk M. P., Kazberuk A., Tarasiuk G.** (2012), Distribution of stresses over the contour of rounded V-shaped notch under antiplane deformation, *Material Science (Springer),* 47(6), 717-725.

KOITER ASYMPTOTIC ANALYSIS OF THIN-WALLED COLD-FORMED STEEL MEMBERS

Viorel UNGUREANU[*,], Dan DUBINA[*,**], Andrei CRISAN[*], Antonio MADEO[***], Giuseppe ZAGARI[***], Giovanni ZUCCO[***], Raffaele ZINNO[***]**

[*]Faculty of Civil Engineering, Department of Steel Structures and Structural Mechanics, Politehnica University of Timisoara, Timisoara, Romania
[**]Laboratory of Steel Structures, Romanian Academy – Timisoara Branch, Timisoara, Romania
[***]MODELING Department, University of Calabria, Cosenza, Italy

viorel.ungureanu@upt.ro, dan.dubina@upt.ro, andrei crisan@upt.ro, antonio.madeo81@unical.it
giuseppe.zagari@unical.it, giovannizucco@gmail.com, raffaele.zinno@unical.it

received 6 September 2015, revised 11 December 2015, accepted 14 December 2015

Abstract: An imperfection sensitivity analysis of cold-formed steel members in compression is presented. The analysis is based on Koiter's approach and Monte Carlo simulation. If the modes interaction is correctly accounted, than the limit load and the erosion of critical buckling load can be easily evaluated. Thousands of imperfection can be analysed with very low computational cost and an effective statistical evaluation of limit performance can be carried out. The analysis is done on pallet rack uprights in compression, based on an intensive experimental study carried out at the Politehnica University of Timisoara.

Key words: Koiter Asymptotic Approach, Instability Problems, Thin-Walled Cold-Formed Steel Members, Imperfection Sensitivity Analysis, Monte Carlo

1. INTRODUCTION

The finite element implementation of Koiter's asymptotic approach allows to evaluate the pre-critical and initial post-critical behaviour of slender elastic structures, also in the presence of strong non-linear for pre-critical and in the case of interactive buckling (Casciaro, 2005). The method is considered very attractive for its advantages in respect to path-following approach (Riks, 1979). These consist in an accurate post-buckling analysis and in an efficient imperfection sensitivity analysis with low computational cost (Casciaro, 2005). The main difficulties arise in the availability of geometrically coherent structural model and in an accurate evaluation of their high order energy variations (Garcea et al., 2012a, 2012b). The use of co-rotational formulation, within a mixed formulation, allows to have a general finite element implementation of Koiter analysis (Zagari et al., 2013).

Our recent technology (Barbero et al., 2014, 2015), in terms of numerical implementation is applied for the evaluation of performance of slender cold-formed steel members especially for the case of modal interaction. In particular, an efficient and robust imperfection sensitivity analysis is performed. Using a Monte Carlo simulation, for a random sequence of imperfections assumed with the shape as linear combination of buckling modes, the equilibrium paths for the imperfect structures are recovered. The load carrying capacity is evaluated statistically. The worst imperfections are detected and the limit load is obtained, allowing the evaluation of erosion of critical bifurcation load (Dubina and Ungureanu, 2014).

2. THEORETICAL BACKGROUND

A summary of the FE asymptotic analysis proposed by Casciaro et al. is presented (Casciaro, 2005; Garcea et al., 2014a, 2014b). The described implementation is called quadratic algorithm. The method is based on the expansion of the potential energy, in terms of load factor λ and buckling mode amplitudes ξ_i, which is characterized by fourth-order accuracy. It provides an approximation of the equilibrium path by performing the following steps:

1. The fundamental path is obtained as a linear extrapolation, from a known equilibrium configuration:

$$u^f[\lambda] = \lambda\hat{u} \tag{1}$$

where u is the field of configuration variables in terms of stress and displacement and û is the tangent obtained as a solution of the linear equation

$$\Phi_0''\hat{u}\delta u = \hat{p}\delta u,\ \forall\delta u \in \mathcal{J} \tag{2}$$

where Φ'' is the strain energy while an index denotes the point along u^f which the quantities are evaluated, that is $\Phi_0'' \equiv \Phi''\left[u^f[\lambda_0]\right]$.

2. A cluster of buckling loads $\{\lambda_0 \dots \lambda_m\}$ and associated buckling modes $(\dot{v}_1 \dots \dot{v}_m)$ are defined along $u^f[\lambda]$ by the critical condition

$$\Phi''[u^f[\lambda_i]]\dot{v}_i\delta u = 0,\ \forall\delta u \in \mathcal{J}. \tag{3}$$

Buckling loads are considered to be sufficiently close to each other to allow the following linearization

$$\Phi_b''\dot{v}_i\delta u + (\lambda_i - \lambda_b)\Phi_b'''\hat{u}\dot{v}_i\delta u = 0,\ \forall\delta u \in \mathcal{J}. \tag{4}$$

λ_b being an appropriate reference value of λ (e.g. the first of λ_i or their mean value). Normalizing we obtain $\Phi_b'''\hat{u}\dot{v}_i\dot{v}_j = \delta_{ij}$, where δ_{ij} is Kroneker's symbol.

3. The tangent space $\mathcal{J}$ is decomposed into the tangent $\mathcal{V} \equiv \{\dot{v} = \sum_i \dot{v}_i\}$ and orthogonal $\mathcal{W} \equiv \{w : \Phi_b'''\hat{u}\dot{v}_i w = 0\}$ subspaces so that $\mathcal{J} = \mathcal{V}\oplus\mathcal{W}$. Denoting $\xi_0 = \lambda$ and

$\dot{v}_0 = \hat{u}$, the asymptotic approximation for the required path is defined by the expansion

$$u[\lambda, \xi_k] \equiv \sum_{i=0}^{m} \xi \dot{v}_i + \frac{1}{2}\sum_{i=0}^{m} \xi_i \xi_j w_{ij} \tag{5}$$

where w_{ij} are the quadratic corrections introduced to satisfy the projection of eqn. (1) onto $\mathcal{W}$ and obtained by the linear orthogonal equations

$$\Phi_b'' w_{ij} \delta w = -\Phi_b''' \dot{v}_i \dot{v}_j \delta w, w_{ij} \quad \delta w \in \mathcal{W} \tag{6}$$

where, because of the orthogonality condition, $w_{0i} = 0$.

4. The following energy terms are computed for $i, j, k = 1 \ldots m$:

$$\mu_k[\lambda] = \frac{1}{2}\lambda^2 \Phi_b''' \hat{u}^2 \dot{v}_k + \frac{1}{6}\lambda^2(\lambda - 3\lambda_b)\Phi_b''' \hat{u}^3 \dot{v}_k$$

$$A_{ijk} = \Phi_b''' \dot{v}_i \dot{v}_j \dot{v}_k \tag{7}$$

$$B_{ijhk} = \Phi_b'''' \dot{v}_i \dot{v}_j \dot{v}_h \dot{v}_k - \Phi_b'' \left(w_{ij} w_{hk} + w_{ih} w_{jk} + w_{ik} w_{jh}\right)$$

$$B_{00jk} = \Phi_b'''' \hat{u}^2 \dot{v}_i \dot{v}_k - \Phi_b'' w_{00} w_{ik}$$

$$B_{0ijk} = \Phi_b'''' \hat{u} \dot{v}_i \dot{v}_j \dot{v}_k$$

$$C_{ik} = \Phi_b'' w_{00} w_{ik}$$

where the implicit imperfection factors μ_k are defined by the 4th order expansion of the unbalanced work on the fundamental (i.e. $\mu_k[\lambda] = (\lambda \hat{p} - \Phi'[\lambda \hat{u}])\dot{v}_k$).

5. The equilibrium path is obtained by satisfying the projection of the equilibrium eqn. (1) onto $\mathcal{V}$. According to eqns. (7) and (8), we have

$$\begin{aligned}(\lambda_k - \lambda)\xi_k - \lambda_b\left(\lambda - \frac{\lambda_b}{2}\right)\sum_{i=1}^{m} \xi_i C_{ik} + \frac{1}{2} \\ \sum_{i,j=1}^{m} \xi_i \xi_j A_{ijk} + \frac{1}{2}(\lambda - \lambda_b)^2 \sum_{i=1}^{m} \xi_i B_{00ik} \\ + \frac{1}{2}(\lambda - \lambda_b)\sum_{i,j=1}^{m} \xi_i \xi_j B_{0ijk} + \frac{1}{6}\sum_{i,j,k=1}^{m} \xi_i \xi_j \xi_h B_{ijhk} \\ + \mu_k[\lambda] = 0, \quad k = 1 \ldots m\end{aligned} \tag{8}$$

Equation (8) corresponds to a highly nonlinear system in the m+1 unknowns, $-\xi_i$, and can be solved using a standard path-following strategy. It provides the initial post-buckling behaviour of the structure including modal interactions and jumping-after-bifurcation phenomena (see Fig. 1).

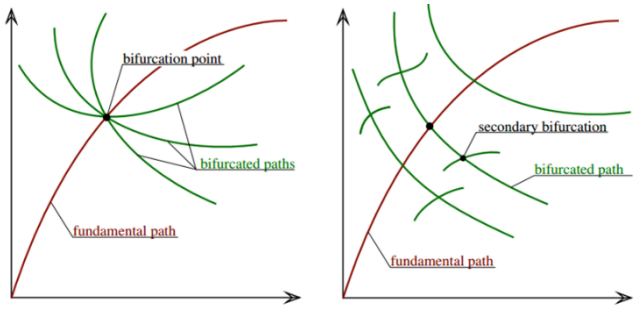

Fig. 1. Interactive buckling for coincident/nearly coincident buckling loads

In the analysis of thin-walled members the characterization of imperfection is often difficult. The presence of imperfections changes some aspects of structural response and often causes an erosion of the load carrying capacity, especially in the interactive buckling range. In the asymptotic algorithm the presences of imperfections expressed by a load $\tilde{p}[\lambda]$ and/or an initial displacement $\tilde{u}$, affect eqn. (9) only with the imperfection term $\mu_k[\lambda]$ that becomes (Casciaro, 2005).

$$\begin{aligned}\mu_k[\lambda] = \frac{1}{2}\lambda^2 \Phi_b''' \hat{u}^2 \dot{v}_k + \frac{1}{6}\lambda^2(\lambda - 3\lambda_b)\Phi_b''' \hat{u}^3 \dot{v}_k \\ + \lambda \phi''' \tilde{u} \hat{u} \dot{v}_k - \tilde{p} \dot{v}_k\end{aligned} \tag{9}$$

The aim of the imperfection sensitivity analysis is to link the presence of geometrical and load imperfections to the reduction in the limit load. For structures presenting coupled buckling even a small imperfection in loading or geometry can represent a significant reduction in ultimate load with respect to the bifurcation load (Garcea et al., 2014a, 2014b). So an effective safety analysis should include an investigation of all possible imperfection shapes and sizes to identify the worst imperfection cases.

3. NUMERICAL RESULTS

On the following, an imperfection sensitivity analysis for upright pallet racks in compression, with and without perforations, is presented. The geometry of the cross-section is shown in Fig. 2, while details related to cross-section, perforations, lengths, material, experimental tests and numerical simulations can be found in (Crisan et al., 2012a, 2012b). The member will be denoted on the following as RS125×3.2, as in (Crisan et al., 2012a, 2012b). The RS125×3.2 specimen has a perforated-to-brut cross-section ratios, A_N/A_B, of 0.806.

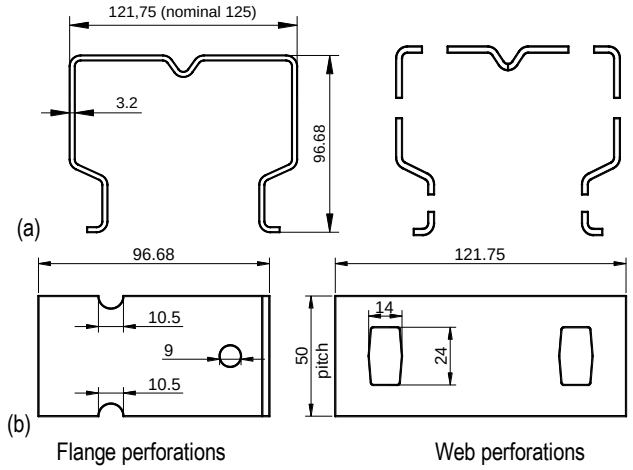

Fig. 2. (a) Geometry of RS125×3.2 section with and without perforations (dimensions are expressed in mm); (b) Perforations details

In this study, different lengths have been analysed and for each length imperfection sensitivity analyses have been performed. The minimum length considered was L = 1400 mm and the maximum one L = 2500 mm. Increments of 100 mm have been considered. The lengths range has been establish in order to include the interactive buckling range, computed based on ECBL approach (Dubina, 2001), considering the interaction of distortional and flexural buckling modes. The procedure was detailed in (Crisan et al., 2012a, 2012b).

In the imperfection sensitivity analysis only geometrical imper-

fections have been considered. In particular, the total imperfection $\tilde{u}$, as shown in eqn. (10), is assumed to be:

$$\tilde{u} = \tilde{u}^g + \tilde{u}^d \tag{10}$$

where $\tilde{u}^g$ and $\tilde{u}^d$ are the global and distortional/local imperfections, that are assumed as linear combinations of global $\dot{v}_i^g$ and distortional/local $\dot{v}_i^d$ buckling modes, that is:

$$\tilde{u}^g = \sum_i r_i \, \dot{v}_i^g \;\; i = 1..m^g$$
$$\tilde{u}^d = \sum_i r_i \, \dot{v}_i^d \;\; i = 1..m^d \tag{11}$$

In eqn. (11) r_i are random number, while m^g and m^d are the number of global and distortional/local buckling modes. The maximum values of $\tilde{u}^g_{max}$ and $\tilde{u}^d_{max}$ are assumed to be smaller than the assumed tolerances (see Fig. 3), i.e. $\tilde{u}^g_{max} < L/1000$ for global imperfection and $\tilde{u}^d_{max} < 1.5\,t$ for distortional one, where L and t are the length of the upright pallet rack and the thickness of the cross-section.

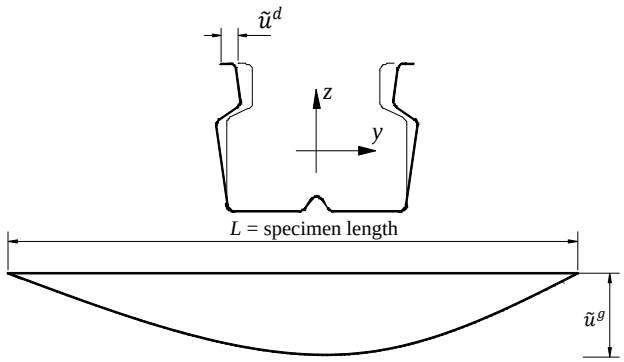

Fig. 3. Distortional and global imperfections for numerical analysis

For each length, the first four buckling modes are considered. For the simulation the rack was considered pinned at one end and simply supported at the other one. For the pinned end, all three translations together with rotation along the longitudinal axis were restrained. For the simply supported end, the translation along the section axis together and the torsional rotations were restrained. The details of the mesh are reported in Fig. 4.

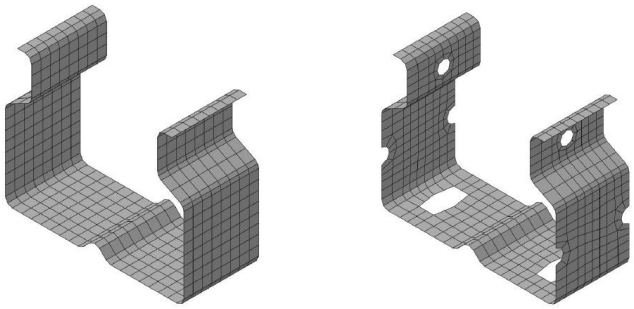

Fig. 4. Details of the mesh for RS125×3.2 brut and net section

For the range of lengths under evaluation, eight distortional buckling modes and two global buckling modes have been detected as shown in Tabs. 1 and 2 and Figs. 5 and 6.

It is easy to observe from Tables 1 and 2 that the interactive buckling range is between (2000 … 2500) mm, confirming the values obtained in (Crisan et al., 2012a).

Tab. 1. The first four buckling loads corresponding to the investigated lengths for RS125×3.2 brut section

L (mm)	λ_1 [kN]	Mode	λ_2 [kN]	Mode	λ_3 [kN]	Mode	λ_4 [kN]	Mode
1400	507.2	d_1	532.6	d_2	713.0	d_3	748.0	d_4
1500	505.6	d_1	509.7	d_2	696.8	d_4	698.6	d_3
1600	492.7	d_2	504.9	d_1	663.1	d_4	686.3	d_3
1700	481.1	d_2	501.6	d_1	643.1	d_4	677.5	d_3
1800	473.8	d_2	494.4	d_6	635.6	d_4	652.4	d_5
1900	470.0	d_2	484.8	d_6	611.6	d_4	632.3	d_5
2000	468.5	d_2	475.2	d_6	563.7	e_1	593.0	d_5
2100	467.0	d_6	468.2	d_7	516.2	e_1	550.0	e_2
2200	460.7	d_6	467.6	d_7	473.4	e_1	509.3	e_2
2300	435.1	e_1	456.4	d_6	465.9	d_7	471.9	e_2
2400	401.2	e_1	437.9	e_2	453.8	d_6	462.4	d_8
2500	370.9	e_1	407.1	e_2	452.6	d_6	458.0	d_8

Tab. 2. The first four buckling loads corresponding to the investigated lengths for RS125×3.2 net section

L (mm)	λ_1 [kN]	Mode	λ_2 [kN]	Mode	λ_3 [kN]	Mode	λ_4 [kN]	Mode
1400	441.8	d_1	474.3	d_2	627.9	d_3	652.4	d_4
1500	438.6	d_1	452.9	d_2	610.1	d_3	626.3	d_5
1600	436.1	d_2	438.0	d_1	589.3	d_5	597.5	d_3
1700	423.8	d_2	437.0	d_1	564.7	d_5	586.9	d_3
1800	415.4	d_2	433.4	d_1	551.7	d_5	573.2	d_3
1900	410.2	d_2	426.9	d_7	546.5	d_6	547.4	d_3
2000	407.6	d_2	419.0	d_7	504.7	e_1	516.3	d_3
2100	406.6	d_2	411.3	d_7	463.2	e_1	480.5	e_2
2200	404.8	d_7	406.4	d_2	425.3	e_1	446.0	e_2
2300	391.3	e_1	399.8	d_2	406.0	d_2	413.9	e_2
2400	360.9	e_1	384.5	e_2	396.3	d_7	404.4	d_2
2500	333.8	e_1	357.7	e_2	394.2	d_7	401.6	d_8

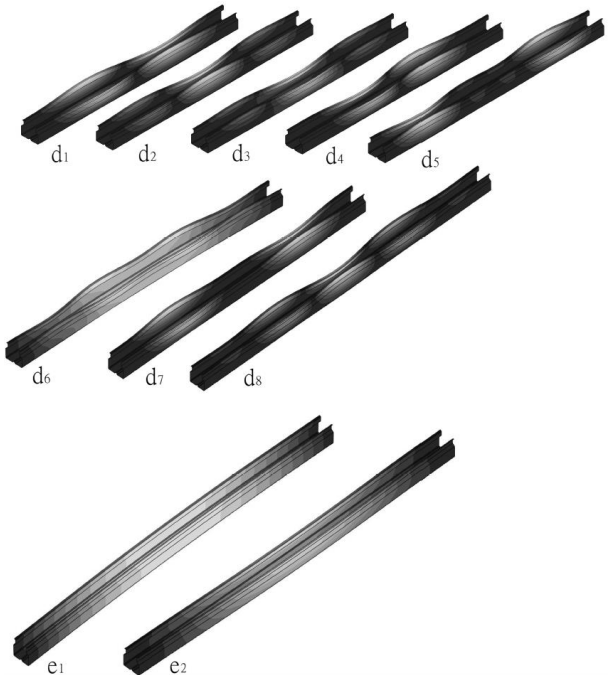

Fig. 5. Distortional d_1, d_2 ... d_8 and global e_1, e_2 buckling modes for RSB125×3.2 brut section in the range L = 1400 ... 2500 mm

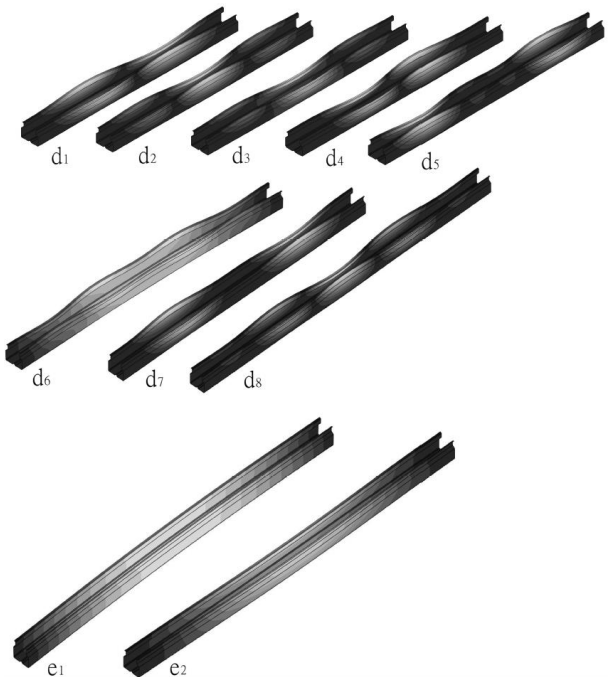

Fig. 6. Distortional d_1, d_2 ... d_8 and global e_1, e_2 buckling modes for RSN125×3.2 net section in the range L = 1400 ... 2500 mm

Fig. 7 presents the buckling loads versus the lengths of the upright members with and without perforations. The range corresponding to global/distortional interactive buckling can be clearly seen, as stated above.

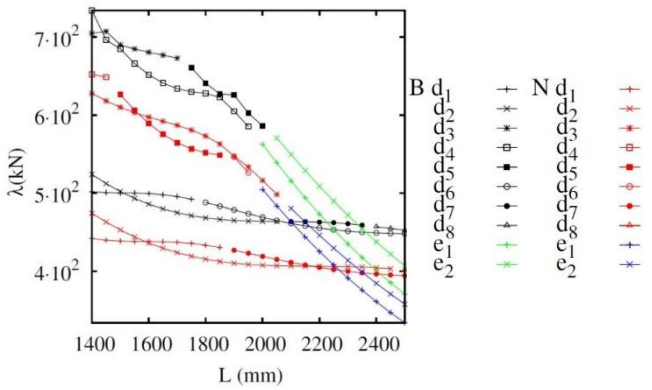

Fig. 7. Bucking load vs. corresponding length for the R125×3.2 brut (B) and net (N) sections

Fig. 8 presents the first four buckling modes for the 2200 mm length, while Fig. 9 the quadratic corrections for the same length, as was defined by eqn. (5). Note that, the aim of the paper is to find the worst imperfection case. Then, the real shape of the imperfection is not required and only the linear combinations of buckling modes are considered. Anyway, the validation of numerical model has been done according to the measured data in (Crisan et al., 2012a).

On the second step, the post-buckling analysis has been performed considering the four buckling modes presented in Tabs. 1 and 2, for the members with lengths L = 1400 ... 2500 mm. The changing of the buckling load and shape at varying lengths is shown in Fig. 5 for brut cross-sections and Fig. 6 for the section with perforations.

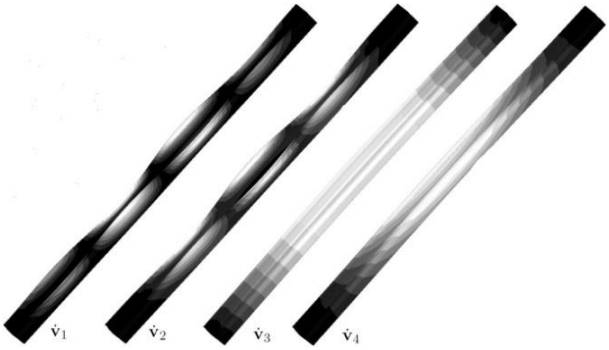

Fig. 8a. Buckling modes for the brut section with length of 2200 mm

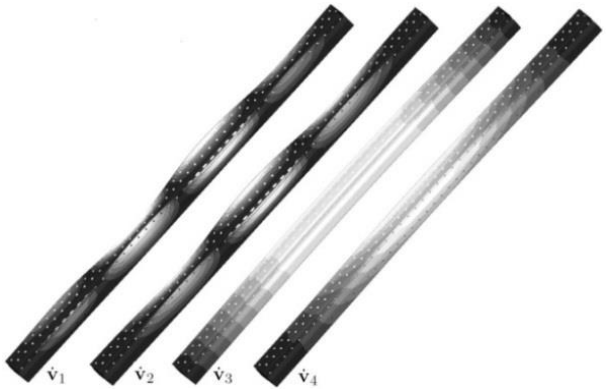

Fig. 8b. Buckling modes for the net section with length of 2200 mm

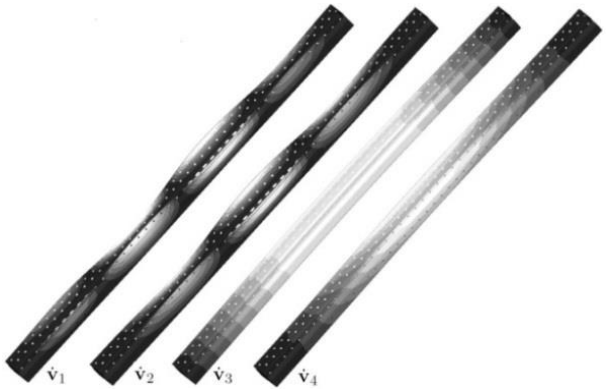

Fig. 9a. Quadratic corrections for the brut section with length of 2200 mm

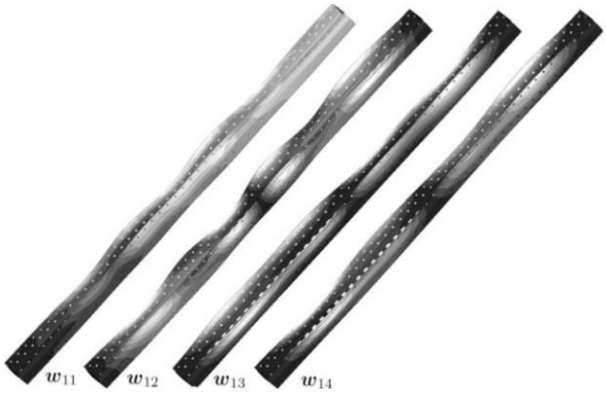

Fig. 9b. Quadratic corrections for the brut section with length of 2200 mm

The multimodal analysis has been performed considering the four buckling modes presented above. Five hundred random

geometric imperfections have been generated with a very low computational cost. The results, in terms of limit load/ displacements, for both brut and net cross-section, are shown in Fig. 10, while the worst imperfections and limit load shapes, for the length L = 2200 mm, are shown in Fig. 11.

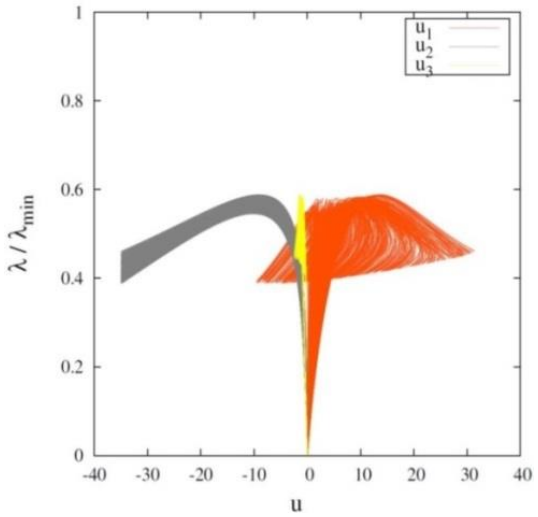

Fig. 10a. Brut section RS125×3.2 with length of 2200 mm: equilibrium paths λ versus u. The displacement components u_1, u_2 and u_3 are measured in the point of the middle of the upright pallet rack section

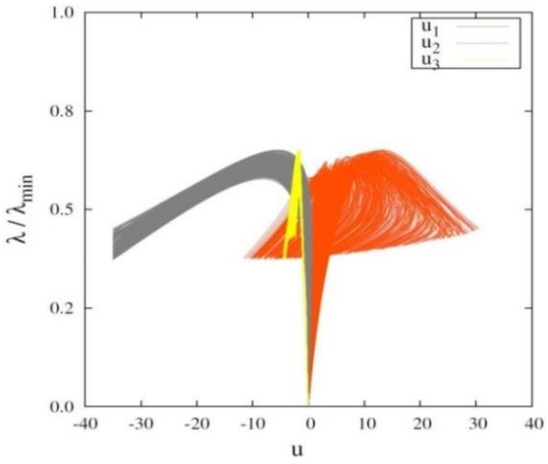

Fig. 10b. Net section RS125×3.2 with length of 2200 mm: equilibrium paths λ versus u. The displacement components u_1, u_2 and u_3 are measured in the point of the middle of the upright pallet rack section

The frequency for the limit loads and its probability distribution are reported in Fig. 12 (a and b). For the specimens with strong buckling interaction, the values are very close to the peak of the distribution. The length with strong interaction are also clearly highlighted, i.e. L = 2200 mm.

The average time required for the steps 1 to 4 have been studied (Barbero et al, 2015), and they remain of the order of seconds. This could allow users to run Monte Carlo simulations to account for other types of imperfections, i.e. load imperfection, residual stress, a.s.o., in order to obtain even more realistic evaluations of structural performance.

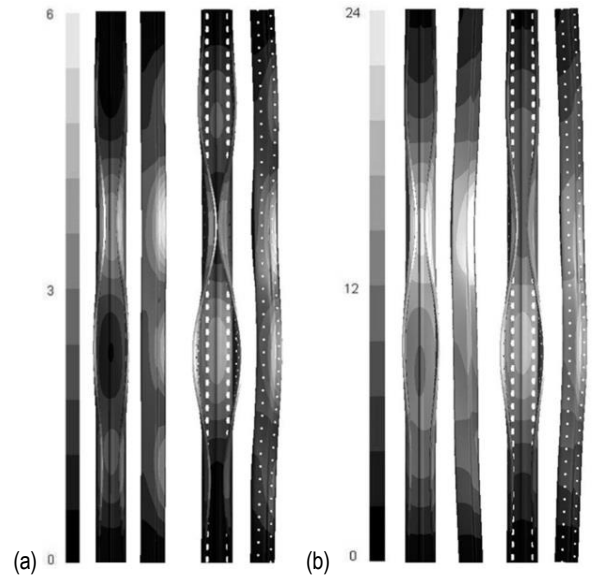

Fig. 11. Section RS125×3.2, brut and net, with the length of 2200 mm: (a) initial shapes for worst imperfection amplified by factor 5.0, (b) deformed shapes at limit load for worst imperfection amplified factor 2.5

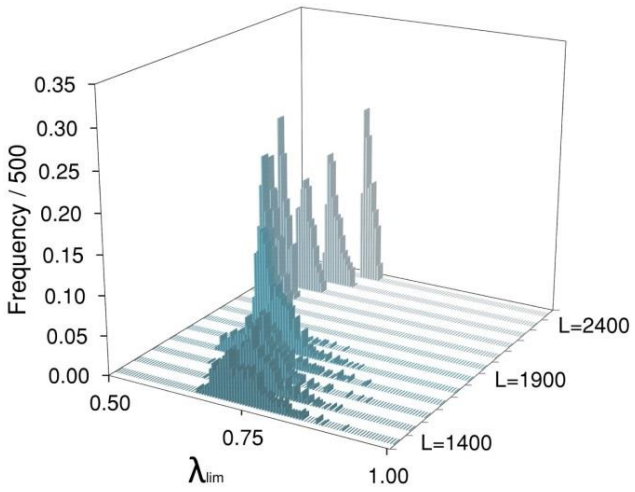

Fig. 12a. Frequency distribution of the limit load found λ_{lim} for the RS125×3.2 brut section

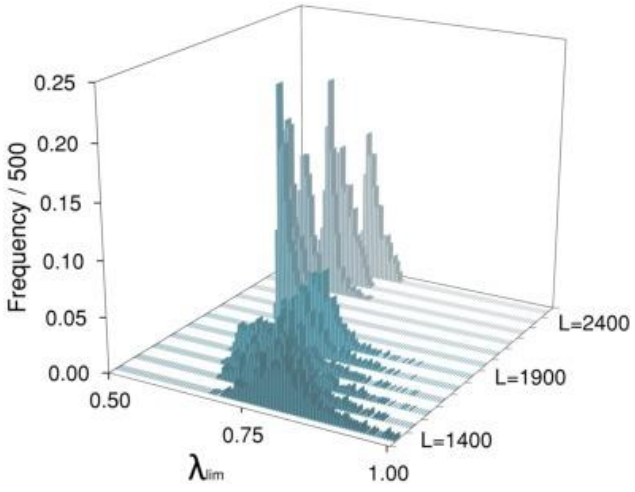

Fig. 12b. Frequency distribution of the limit load found λ_{lim} for the RS125×3.2 net section

4. EVALUATION OF ψ EROSION FACTORS

It is very well known that in the case of an ideal structure, the theoretical equilibrium bifurcation point and corresponding load, N_{cr}, are observed at the intersection of the pre-critical (primary) force-displacement curve with the post-critical (secondary) curve (see Fig. 13). For a real structure, affected by a generic imperfection, δ_0, the bifurcation point does not appear anymore and, instead, the equilibrium limit point is the one characterizing the ultimate capacity, N_u, of the structure. The difference between N_{cr} and N_u represents the *Erosion of the Critical Bifurcation Load*, due to the coupling and imperfections (Dubina, 2001).

In almost all practical cases, the mode interaction, obtained by coupling of a local instability with an overall one, is a result of design (e.g. calibration by design of mechanical and geometrical properties of member), and has a nonlinear nature.

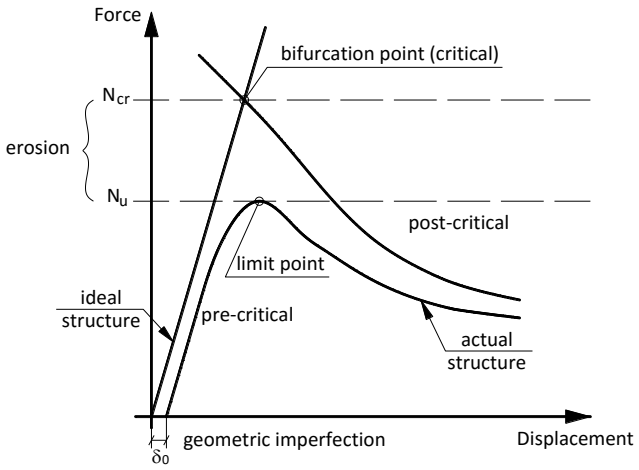

Fig. 13. Critical and post-critical behaviour

Due to the imperfections, an interaction erosion of critical bifurcation load occurs. This erosion is maximum in the coupling point vicinity. For members, an interactive slenderness range, in which sensitivity to imperfections is increased, may be identified. Depending on imperfection sensitivity, classes of interaction types, characterized by specific levels of erosion intensity, may be defined (Gioncu, 1994).

Being given a member in compression let assume two simultaneous buckling modes which might couple (see Fig. 14).

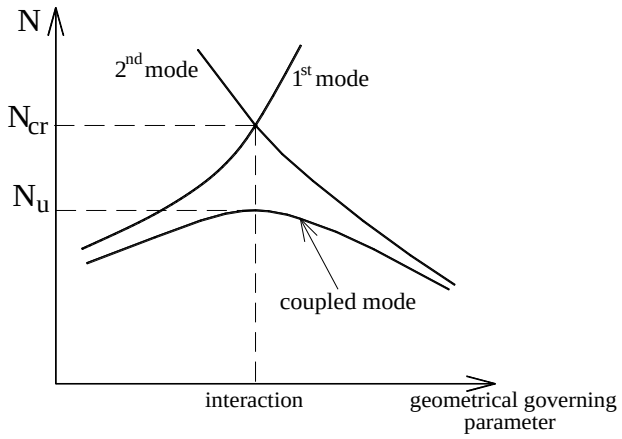

Fig. 14. Critical and post-critical behaviour

The perfect member is prone to interactive buckling, with the critical buckling load, N_{cr}, while the actual member with the ultimate load, N_u. The erosion coefficient, ψ, can be expressed as follows:

$$\psi = 1 - \bar{N}_u / \bar{N}_{cr} \tag{12}$$

and

$$\bar{N}_u = (1 - \psi)\bar{N}_{cr} \tag{13}$$

The Monte Carlo simulation also allows to found the worst imperfection case, as shown in Fig. 10, and to evaluate the erosion as shown in Fig. 15 (Dubina, 2001). The load carrying capacity is evaluated statistically. The worst imperfections are detected and the limit load is obtained so allowing the evaluation of erosion of critical bifurcation load according to eqn. (10). The evaluation of erosion is shown in Fig. 15. The maximum erosion has been detected for the specimens corresponding to the length L = 2200 mm.

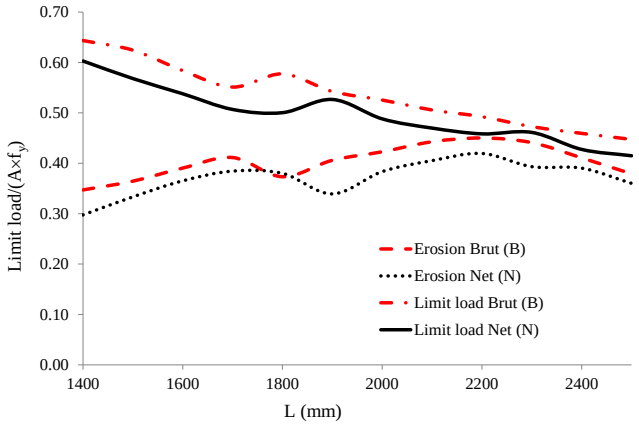

Fig. 15. The minimum limit load normalized to the cross-section capacity for brut (B) and net (N) section

The buckling modes that provide the maximum erosion and their participation are presented in Tab. 3. In Figs. 5 and 6 are defined these buckling modes.

Tab. 3. Buckling modes defining the maximum erosion and their participation, both for RS125×3.2 brut (B) and net (N) cross-section

	RS125×3.2 brut		RS125×3.2 net	
	Mode	% mode brut	Mode	% mode net
distortional	d6	99.23	d7	98.62
	d7	0.77	d2	1.38
global	e1	93.97	e1	89.08
	e2	6.03	e2	10.92

Once, evaluated the worst imperfections the sensitivity curves have been recovered (see Fig. 15). The figure shows that brut sections have a higher limit load than the net sections, however the slope of sensitivity curves is the same.

Finally, it can be observed that based on the above parametric study, the obtained maximum erosion are of 0.45 for the brut section (B) and 0.42 for the net section (N). In a direct comparison with the results obtained via ECBL approach (Dubina, 2001), it

can be observed they are in a good agreement with the ones obtained by Ungureanu and Dubina (2013), i.e. of 0.44 for the net section, but for a combination of imperfections ($\tilde{u}^{g}_{max} = \mathrm{L}/750$ and $\tilde{u}^{d}_{max} = 1.5$ t). The erosions obtained by Crisan et al. (2012b) via ECBL approach, i.e. 0.387 for the brut section and 0.395 for the net section, are also close to the ones presented above but have been obtained for different combination of imperfections, i.e. ($\tilde{u}^{g}_{max} = \mathrm{L}/1000$ and $\tilde{u}^{d}_{max} = 1$ t).

5. CONCLUSIONS

An imperfection sensitivity analysis using Koiter's approach and the Monte Carlo method has been applied for the evaluation of imperfection sensitivity of cold-formed upright members for pallet racks in compression, with and without perforations. The analysis allows to evaluate the limit loads, the erosion of the theoretical buckling due to both imperfections and the mode interaction. The main strengths of the proposed methodology are the ability to analyse thousands of random imperfections in a short time, with very low computational cost, to find the worst imperfections and to provide an accurate evaluation of the limit load and of the erosion of buckling load, with respect to theoretical case, due to buckling mode interaction.

Once again is shown and validated that the ECBL approach is an excellent and practical method that allows for the evaluation of ψ erosion coefficients and α imperfection factors, as result of interactive buckling.

REFERENCES

1. **Barbero E.J., Madeo A., Zagari G., Zinno R., Zucco G.** (2014), Koiter asymptotic analysis of folded laminated composite plates, *Composites Part B: Engineering*, 61, 267–274.
2. **Barbero E.J., Madeo A., Zagari G., Zinno R., Zucco G**. (2015), Imperfection sensitivity analysis of laminated folded plate, *Thin-Walled Structures*, 90, 128-139.
3. **Casciaro R.** (2005), *Computational asymptotic post-buckling analysis of slender elastic structures*, in *Phenomenological and Mathematical Modelling of Structural Instabilities*, M. Pignataro, V. Gioncu (eds.), Vol. 470, CISM International Centre for Mechanical Sciences, Springer Vienna, 95–276, 2005.
4. **Crisan A, Ungureanu V., Dubina D.** (2012a), Behaviour of cold-formed steel perforated sections in compression: Part 1-Experimental investigations, *Thin-Walled Structures*, 61, 86-96.
5. **Crisan A, Ungureanu V., Dubina D.** (2012b), Behaviour of cold-formed steel perforated sections in compression: Part 2-Numerical investigations and design considerations, *Thin-Walled Structures*, 61, 97-105.
6. **Dubina D.** (2001), The ECBL approach for interactive buckling of thin-walled steel members, *Steel Composite Structures*, 1(1), 75-96.
7. **Dubina D., Ungureanu V.** (2002), Effect of imperfections on numerical simulation of instability behaviour of cold-formed steel members, *Thin-Walled Structures*, 40(3), 239–262.
8. **Dubina D., Ungureanu V.** (2014), Instability mode interaction: from Van Der Neut model to ECBL approach, *Thin-Walled Structures*, 81, 39–49.
9. **Garcea G., Bilotta A., Madeo A., Casciaro R.** (2014a), Direct Evaluation of the Post-Buckling Behavior of Slender Structures Through a Numerical Asymptotic Formulation, *Direct Methods for Limit States in Structures and Materials*, Springer Netherlands, 203-228.
10. **Garcea G., Bilotta A., Madeo A., Zagari G., Casciaro R.** (2014b), A Numerical Asymptotic Formulation for the Post-buckling Analysis of Structures in Case of Coupled Instability, *Special Issue Stability And Nonlinear Analysis Of Steel Structures – Research Advances, Romanian Journal of Technical Sciences Applied Mechanics*, 59(1–2), 38-55.
11. **Garcea G., Madeo A., Casciaro R.** (2012a), The implicit corotational method and its use in the derivation of nonlinear structural models for beams and plates, *Journal of Mechanics of Materials and Structures*, 7(6), 509-538.
12. **Garcea G., Madeo A., Casciaro R.** (2012b), Nonlinear FEM analysis for beams and plate assemblages based on the implicit corotational method, *Journal of Mechanics of Materials and Structures*, 7(6), 539-574.
13. **Gioncu V.** (1994), General Theory of Coupled Instability, *Thin-Walled Structures (Special Issue on Coupled Instability in Metal Structures – CIMS'92)*, 19(2-4), 81-128.
14. **Riks E**. (1979), An incremental approach to the solution of snapping and buckling problems, *International Journal of Solids and Structures*, 15(7), 529–551, 1979.
15. **Ungureanu V., Dubina D.** (2013), Sensitivity to imperfections of perforated pallet rack sections, *Mechanics and Mechanical Engineering*, Lodz University of Technology, 17(2), 209–222.
16. **Zagari G., Madeo A., Casciaro R., de Miranda S., Ubertini F.** (2013), Koiter analysis of folded structures using a corotational approach, *International Journal of Solids and Structures*, 50(5), 755–765.

Special recognition is due to Prof. Raffaele Casciaro for his suggestions and comments. The authors from University of Calabria wish to acknowledge the International Network for the Exchange of Good Practices in Innovative, Seismically Safe and Eco-friendly Buildings (POR-FSE CALABRIA 2007-2013 RISPEISE) for the financial support. This work was partially supported by the strategic grant POSDRU/159/1.5/S/137070 (2014) of the Ministry of National Education, Romania, co-financed by the European Social Fund – Investing in People, within the Sectoral Operational Programme Human Resources Development 2007-2013."

DOI 10.1515/ama-2015-0040

ROBUST OUTPUT REGULATION OF UNCERTAIN CHAOTIC SYSTEMS WITH INPUT MAGNITUDE AND RATE CONSTRAINTS

Carlos M.N. VELOSA*, Kouamana BOUSSON*

*LAETA-UBI/AeroG & Avionics and Control Laboratory, Department of Aerospace Sciences, University of Beira Interior, 6201-001 Covilhã, Portugal

carlosvelosaeng@hotmail.com, k1bousson@yahoo.com

received 12 December 2014, revised 18 December 2015, accepted 18 December 2015

Abstract: The problem of output regulation deserves a special attention particularly when it comes to the regulation of nonlinear systems. It is well-known that the problem is not always solvable even for linear systems and the fact that some demanding applications require not only magnitude but also rate actuator constraints makes the problem even more challenging. In addition, real physical systems might have parameters whose values can be known only with a specified accuracy and these uncertainties must also be considered to ensure robustness and on the other hand because they can be crucial for the type of behaviour exhibited by the system as it happens with the celebrated chaotic systems. The present paper proposes a robust control method for output regulation of chaotic systems with parameter uncertainties and subjected to magnitude and rate actuator constraints. The method is an extension of a work recently addressed by the same authors and consists in decomposing the nonlinear system into a stabilizable linear part plus a nonlinear part and in finding a control law based on the small-gain principle. Numerical simulations are performed to validate the effectiveness and robustness of the method using an aeronautical application. The output regulation is successfully achieved without exceeding the input constraints and stability is assured when the parameters are within the specified intervals. Furthermore, the proposed method does not require much computational effort because all the control parameters are computed offline.

Keywords: Output Regulation, Actuator Constraints, Parametric Uncertainties, Robust Control, Chaos, Aeroelastic System

1. INTRODUCTION

Chaotic systems have attracted significant attention from researchers over the past twenty years and there has been since then a large effort in attempting to develop and improve control techniques for such a class of systems. Chaotic systems are known to be essentially characterized by high sensitivity to initial conditions and to parameter variations, and for that reason, any effective control technique must be robust against parameter uncertainties. On the other hand, most of real-world applications require a control not only with input magnitude constraints but also with rate constraints due to electrical, mechanical and other physical limitations.

Pecora and Carroll (1990) and Ott et al. (1990) were the pioneers in introducing techniques for the control and synchronization specifically of chaotic systems. Nevertheless, despite of their elegant strategies, actuator constraints are not considered and plant uncertainties are also not taken into account. The classical H_∞ control introduced by Zames (1981) became very popular precisely because it considers, among others, parameter uncertainties. The Quantitative Feedback Theory (QFT) developed by Horowitz (2001) is another robust technique that prevails nowadays and is quite effective for systems with parametric uncertainties. However, robust control techniques have limitations when used to control systems subject to actuator constraints. Mathematical manipulations can be obviously carried out to introduce such constraints, but its implementation requires an appropriate data structure and some precautions should be taken into account to prevent windup phenomena, (Galeani et al., 2007; Hippe, 2006). Advanced control techniques based on Linear Matrix Inequalities (LMI's) are effective and allow to include, among others, plant uncertainties and actuator constraints, (Deng and Xu, 2010; Tanaka and Wang, 2001). Meanwhile, dealing with LMI-based controller design requires modelling experience with positive definite matrices because some parameters should be relaxed in order to formulate a subsequent convex optimization problem that is not too conservative. It may occur that the control saturates while the output is still too far from the setpoint, which may lead to the instability of the closed-loop system. Bousson and Velosa (2014), Velosa and Bousson (2014, 2015) have recently tackled the problem of control and synchronization of chaotic systems with actuator constraints. But, despite of robustness against external disturbances and also to parameter uncertainties, their techniques do not consider interval-valued parameter uncertainties.

The present paper aims at proposing a generalized robust method for output regulation of nonlinear complex systems that takes into account input magnitude and rate constraints and deals explicitly with parametric uncertainties. The work is motivated by the fact that some highly demanding applications such as aerospace and aeronautical systems require this type of constraints and because in most cases the parameters of the system can be only known with a certain accuracy.

The paper is structured as follows: the problem to be solved is stated in section 2; section 3 presents a solution to problem, which is an extension of the work recently proposed by Velosa and Bousson (2015) based on the H_∞ control, more precisely, based on the small-gain principle; section 4 deals with numerical simulations to validate the effectiveness and robustness of the method coping with suppressing the undesired oscillations of an

aeroelastic system; and section 5 discusses about the simulation results with concluding remarks.

2. PROBLEM STATEMENT

Consider the problem of robust output regulation of a continuous time-invariant nonlinear system with parametric uncertainties described as (1):

$$\begin{aligned} \dot{x} &= f(x,\theta) + B(\theta)u \\ y &= C(\theta)x \end{aligned} \quad \text{Controlled system} \quad (1)$$

$$\begin{aligned} \dot{x}_r &= f_r(x_r) \\ y_r &= C_r x_r \end{aligned} \quad \text{Reference system} \quad (2)$$

where the purpose is to find an admissible control subject to magnitude and rate constraints such that its outputs follow insofar as possible reference signals generated by a given system (2).

In equations (1) and (2), $x \in \mathbb{R}^n$, $x_r \in \mathbb{R}^{n_r}$ denote the state vectors, $y,\ y_r \in \mathbb{R}^p$ the output vectors, $u \in \mathbb{R}^m$ the control vector, $\theta \in \mathbb{R}^q$ the vector of parameters which is known only with a certain degree of accuracy, $C(\theta) \in \mathbb{R}^{p\times n}$, $C_r \in \mathbb{R}^{p\times n_r}$ the output matrices, $B(\theta) \in \mathbb{R}^{n\times m}$ the control matrix, f, f_r two smooth nonlinear functions, and $\dot{x} = dx/dt$.

Writing the problem with the mathematical formalities, the objective summarizes to the following:

Problem to be solved: Find a control $u(t)$ such that conditions (3) and (4) hold for any $t \geq \tau$, $\tau > t_0$, with knowledge that the parameters of (1) may take any values within the limits specified by (5):

$$\|e_y\| = \|y(t) - y_r(t)\| \leq \varepsilon \quad (3)$$

$$\|u(t)\|_\infty \leq \eta \quad , \quad \|\dot{u}(t)\|_\infty \leq \nu \quad (4)$$

$$\theta_i \in [\theta_{i,min}\ ,\ \theta_{i,max}] \quad , \quad i = 1, \ldots, q \quad (5)$$

In inequality (3), $\|.\|$ denotes an appropriate norm and $\varepsilon \geq 0$ should be as small as possible for a proper regulation. Parameters $\eta \geq 0$ and $\nu \geq 0$ denote respectively the magnitude and rate constraints of the actuators dynamics.

3. THE PROPOSED METHOD

Consider a continuous-time, time-invariant linear system given as follows:

$$\begin{aligned} \dot{x} &= A(\theta_0)x + B_1(\theta_0)\sigma_{\eta,\nu}(u) + B_2 w + B_3 d \\ \dot{w} &= Sw + r \\ y &= C_1(\theta_0)x + D_{13}d \\ e &= C_1(\theta_0)x + D_{12}w \\ z &= C_2 x \quad\quad + D_{21}\sigma_{\eta,\nu}(u) \end{aligned} \quad (6)$$

where the first equation describes a plant, with state $x \in \mathbb{R}^n$, input $u \in \mathbb{R}^m$, and subject to the effect of external disturbances and parametric uncertainties represented respectively by $B_2 w$ and $B_3 d$. Vector θ_0 denotes the nominal value of parameter vector θ. The third equation refers to the real plant output $y \in \mathbb{R}^p$, which is also affected by parametric uncertainties represented by $D_{13}d$. The fourth equation defines the error $e \in \mathbb{R}^p$ between the plant output $C_1(\theta_0)x$ and the reference signal $-D_{12}w$ which the plant output is required to track. The second equation describes an exosystem, with state $w \in \mathbb{R}^s$, that models simultaneously the class of plant disturbances and the reference signals taken into consideration. The last equation, $z \in \mathbb{R}^{n+m}$, represents the performance outputs which are intended to be influenced in a desired way.

In the sequel, the notations $A(\theta_0) \equiv A_0$, $B_1(\theta_0) \equiv B_{1,0}$ and $C_1(\theta_0) \equiv C_{1,0}$ stand for the corresponding matrices with nominal parameter vector θ_0 taken equal to the midpoint of the parameter box in equation (5).

Let the control constraints as presented in (4) be enforced by a functional differential operator of the form $\sigma_{\eta,\nu}(u) = \lim_{\mu\to\infty} x_\mu$, with x_μ described as:

$$\begin{aligned} \dot{x}_\mu &= \sigma_\nu\left(\mu\big(\sigma_\eta(u) - x_\mu\big)\right) \\ x_\mu(t_0) &= \sigma_\eta(u(t_0)) \end{aligned} \quad (7)$$

where $\sigma_h(.)$ denotes a saturation function of limit h, defined by:

$$\sigma_h(s) = \mathrm{sgn}(s).\min\{|s|, h\} \quad (8)$$

The parametric uncertainties of system (6) can be expressed as a feedback of the performance output through an appropriate selection of matrices C_2 and D_{21}. That is, $d = \boldsymbol{\Delta} z$, with:

$$\boldsymbol{\Delta} = \begin{bmatrix} \Delta A & \Delta B_1 \\ \Delta C_1 & 0_{p\times m} \end{bmatrix} \quad (9)$$

where:

$$\begin{aligned} \|\Delta A\| &= \|A(\theta) - A(\theta_0)\| \leq a \\ \|\Delta B_1\| &= \|B_1(\theta) - B_1(\theta_0)\| \leq b \\ \|\Delta C_1\| &= \|C_1(\theta) - C_1(\theta_0)\| \leq c \end{aligned} \quad (10)$$

and it can be easily shown that $\|\boldsymbol{\Delta}\|_\infty \leq 1/\gamma$, $\gamma > 0$, where γ is computed according to the expression, (Bernhard, 2002):

$$\gamma = \frac{1}{\sqrt{\dfrac{a^2 + b^2 + c^2 + \sqrt{(a^2 + b^2 + c^2)^2 - (2bc)^2}}{2}}} \quad (11)$$

Theorem 1: The problem of robust output regulation via state-feedback for the system (6) is solvable if the following conditions are true, (Bernhard, 2002; Saberi et al., 2011):

i. The pair $(A_0, B_{1,0})$ is controllable and A_0 has all its eigenvalues in the closed left-half plane.
ii. $D_{21}^T D_{21}$ is invertible and $D_{21}^T C_2 = 0$.
iii. The pair (C_2, A_0) has no unobservable modes on the imaginary axis.
iv. There exist two matrices Π and Γ such that:
   a) they solve the regulator equations:

$$\begin{aligned} \Pi S &= A_0\Pi + B_{1,0}\Gamma + B_2 \\ 0 &= C_{1,0}\Pi + D_{12} \end{aligned} \quad (12)$$

   b) for a given $\xi > 0$ and $T \geq 0$ they satisfy the following inequalities:

$$\left\|\Gamma w + B_{1,0}^+ \Pi \dot{r}\right\|_{\infty,T} \leq \eta - \xi$$

and: $\left\|\Gamma S w + \Gamma r + B_{1,0}^+ \Pi \dot{r}\right\|_{\infty,T} \leq \nu - \xi$.

Under these conditions, the family of linear static state-feedback laws given by:

$$u = -B_{1,0}^T P x + \left(B_{1,0}^T P\Pi + \Gamma\right)w + B_{1,0}^+ \Pi r \quad (13)$$

DOI 10.1515/ama-2015-0040

where $B_{1,0}^{+}$ denotes the pseudo-inverse matrix of $B_{1,0}$ and P is a symmetric and positive semi-definite solution, if there exists, of the following algebraic Riccati equation:

$$A_0^T P + P A_0 - P B_{1,0} B_{1,0}^T P + \gamma^{-2} P B_3 B_3^T P + C_2^T C_2 = 0 \quad (14)$$

such that the matrix $A_0 - B_{1,0} B_{1,0}^T P + \gamma^{-2} B_3 B_3^T P$ is stable, i.e., all its eigenvalues have negative real parts, steers the output error $e(t)$ of system (6) to the origin when $t \to \infty$, $\lim_{t\to\infty} e(t) = 0$, and guarantees that the closed-loop transfer matrix from d to z satisfies $\|T_{z,d}\|_\infty < \gamma$ due to the small-gain theorem, (Zames, 1981).

A way to solve the regulator equations (12) and the Riccati equation (14) is presented in appendices (1) and (2) respectively.

Let matrices B_2, B_3, C_2, D_{13}, D_{12}, D_{21}, be given as:

$$\begin{aligned} B_2 &= [I_n \;\; 0_{n\times n_r}] \quad , \quad B_3 = [I_n \;\; 0_{n\times p}] \\ D_{13} &= [0_{p\times n} \;\; I_p] \quad , \quad D_{12} = [0_{p\times n} \;\; -C_r] \\ D_{21} &= \begin{bmatrix} 0_{n\times m} \\ I_m \end{bmatrix} \quad , \quad C_2 = \begin{bmatrix} I_n \\ 0_{m\times n} \end{bmatrix} \end{aligned} \quad (15)$$

Decompose now the nonlinear functions of systems (1) and (2) into the form of a linear part plus a nonlinear part so that the linear part of (1) is stable for the nominal parameters, that is:

$$\begin{aligned} f(x,\theta_0) &= A_0 x + \varphi(x,\theta_0) \\ f_r(x_r) &= A_r x_r + \varphi_r(x_r) \\ A_0 &= \left.\frac{\partial f}{\partial x}\right|_{x=x^*} \quad , \quad A_r = \left.\frac{\partial f_r}{\partial x_r}\right|_{x_r = x_r^*} \end{aligned} \quad (16)$$

with x^* chosen such that:

$$\mathrm{Re}[\lambda_i(A_0)] \le 0, \qquad i = 1, \ldots, n \quad (17)$$

and φ and φ_r written as:

$$\begin{aligned} \varphi(x,\theta_0) &= f(x,\theta_0) - A_0 x \\ \varphi_r(x_r) &= f_r(x_r) - A_r x_r \end{aligned} \quad (18)$$

Note that the first equation of (6) describes a perturbed linear system: in the absence of uncertainties, it represents the nominal model; and in the presence of uncertainties it represents all possible models better than the 'worst' model taken into consideration, i.e., the model for the maximum allowable uncertainty. Since the controlled system is described by a nonlinear function $f(x,\theta) = A(\theta)x + \varphi(x,\theta)$, when written into the form of a nominal model plus the remaining uncertainty terms, it would be $f(x,\theta) = A_0 x + \varphi_0(x) + \Delta A x + \Delta\varphi(x)$. However, certain systems, and, in particular most of the chaotic systems, have their parameters only in the linear terms of the model, and under this condition the previous expression simplifies to $f(x,\theta) = A_0 x + \varphi(x) + \Delta A x$. Lorenz, Chen, Lu systems are examples of well-known chaotic systems for which all the parameters appear exclusively in the linear terms. For such systems, the uncertainty $\Delta A x$ can be easily characterized by the term $B_3 d$ according to (9).

The arrangement above allows one to write the exosystem of (6) in its exact form $\dot{w} = Sw + r$, generating thus the nonlinear part of the controlled system, $\varphi \equiv \varphi(x,\theta_0)$, and the reference state vector, x_r:

$$\begin{bmatrix} \dot{\varphi} \\ \dot{x}_r \end{bmatrix} = \begin{bmatrix} 0_{n\times n} & 0_{n\times n_r} \\ 0_{n_r\times n} & A_r \end{bmatrix} \begin{bmatrix} \varphi \\ x_r \end{bmatrix} + \begin{bmatrix} \dot{\varphi}(x) \\ \varphi_r(x_r) \end{bmatrix} \quad (19)$$

where:

$$\dot{\varphi}(x) = \left(\frac{\partial f(x,\theta_0)}{\partial x} - A_0\right) f(x,\theta_0) \quad (20)$$

4. SIMULATION RESULTS

In this section numerical simulations are performed to validate the proposed approach. The model under consideration is an aeroelastic system with two degrees-of-freedom (Fig. 1), and the purpose is to suppress limit cycle oscillations (flutter) and eventual chaotic motion that can lead to structural failures by material fatigue.

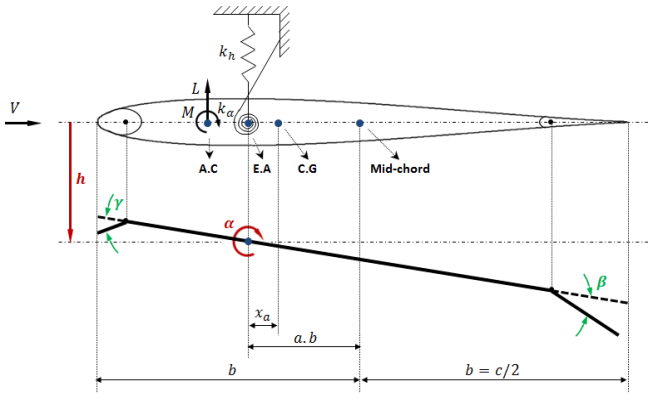

Fig. 1. Aeroelastic system with two degrees-of-freedom

The mathematical equations of motion for an aeroelastic system with two degrees-of-freedom as described in (Fig. 1) have been established in many references, (Alstrom et al., 2010; Chen et al., 2012; Demenkov, 2008; Vikhorev et al., 2008; Wang et al., 2013). Following (Demenkov, 2008), the dynamical model can be expressed, denoting the state vector by $x = [h \;\; \alpha \;\; \dot{h} \;\; \dot{\alpha}]^T$, the output vector by $y = [h \;\; \alpha]^T$ and the control vector by $u = [\beta \;\; \gamma]^T$, as:

$$\begin{aligned} \dot{x} &= f(x) + Bu \\ y &= Cx \end{aligned} \quad (21)$$

with:

$$\begin{aligned} f(x) &= \begin{bmatrix} 0_2 & I_2 \\ -F^{-1}C_\alpha(\alpha) & -F^{-1}G \end{bmatrix} x \\ B &= \begin{bmatrix} 0_2 \\ -F^{-1}L \end{bmatrix}, \qquad C = [I_2 \;\; 0_2] \end{aligned} \quad (22)$$

wherein:

$$\begin{aligned} F &= \begin{bmatrix} m_T & m_W x_\alpha b \\ m_W x_\alpha b & I_\alpha \end{bmatrix} \\ L &= \begin{bmatrix} -\rho V^2 b s C_{l\beta} & -\rho V^2 b s C_{l\gamma} \\ \rho V^2 b^2 s C_{m\beta-eff} & \rho V^2 b^2 s C_{m\gamma-eff} \end{bmatrix} \\ G &= \begin{bmatrix} c_h + \rho V b s C_{l\alpha} & \rho V b^2 s C_{l\alpha}(1/2 - a) \\ -\rho V b^2 s C_{m\alpha-eff} & c_a - \rho V b^3 s C_{m\alpha-eff}(1/2 - a) \end{bmatrix} \\ C_\alpha(\alpha) &= \begin{bmatrix} k_h & \rho V^2 b s C_{l\alpha} \\ 0 & k_\alpha(\alpha) - \rho V^2 b^2 s C_{m\alpha-eff} \end{bmatrix} \end{aligned} \quad (23)$$

and:

$$
\begin{aligned}
&k_\alpha(\alpha) = 12.77 + 53.47\alpha + 1003\alpha^2 \\
&x_\alpha = -(0.0998 + a) \quad , \quad r_{cg} = bx_\alpha \\
&I_\alpha = I_{cam} + I_{cg-wing} + m_{wing} r_{cg}^2 \\
&C_{m\alpha-eff} = (1/2 + a)C_{l\alpha} + 2C_{m\alpha} \\
&C_{m\beta-eff} = (1/2 + a)C_{l\beta} + 2C_{m\beta} \\
&C_{m\gamma-eff} = (1/2 + a)C_{l\gamma} + 2C_{m\gamma}
\end{aligned} \tag{24}
$$

The plunge displacement h and angles α, β, γ are expressed respectively in meters and radians. The parameters of the system are given in Tab. 1. One considers that the stability and control derivatives are estimated; hence they are known only with a certain degree of accuracy. Let the uncertainty be 10% around the nominal values θ_0, i.e., $\theta \in [0.90\theta_0, 1.10\theta_0]$ where $\theta = [C_{l\alpha}, C_{m\alpha}, C_{l\beta}, C_{m\beta}, C_{l\gamma}, C_{m\gamma}]^T$.

Tab. 1. Parameters of the aeroelastic system.

Parameter	Value	Tolerance
ρ	$1.225\ \mathrm{kg/m^3}$	–
a	-0.6719	–
b	$0.1905\ \mathrm{m}$	–
s	$0.5945\ \mathrm{m}$	–
k_h	$2844\ \mathrm{N/m}$	–
c_h	$27.43\ \mathrm{kg/s}$	–
c_α	$0.0360\ \mathrm{kg.m^2/s}$	–
m_{wing}	$4.340\ \mathrm{kg}$	–
m_W	$5.230\ \mathrm{kg}$	–
m_T	$15.57\ \mathrm{kg}$	–
I_{cam}	$0.04697\ \mathrm{kg.m^2}$	–
$I_{cg-wing}$	$0.04342\ \mathrm{kg.m^2}$	–
$C_{l\alpha}$	6.757	$\pm 10\%$
$C_{m\alpha}$	0	$\pm 10\%$
$C_{l\beta}$	3.774	$\pm 10\%$
$C_{m\beta}$	-0.6719	$\pm 10\%$
$C_{l\gamma}$	-0.1566	$\pm 10\%$
$C_{m\gamma}$	-0.1005	$\pm 10\%$

Notice that all uncertain parameters are only in linear terms of the model (21-24) and therefore the method proposed in the previous section can be perfectly applied. That is, the uncertainties reflect only in the linear terms $\Delta Ax + \Delta Bu$ and not in $\Delta\varphi(x)$.

Decomposing $f(x)$ as indicated in (16) considering the state $x^* = [0,\ 10.\pi/180,\ 0,\ 0]^T$, one has that:

$$
A_0 = \begin{bmatrix} 0 & 0 & 1 & 0 \\ 0 & 0 & 0 & 1 \\ -214.1 & 26.2 & -2.9 & -0.2 \\ 859.9 & -1011.3 & 8.7 & -0.2 \end{bmatrix}
$$

$$
\lambda(A_0) = \begin{Bmatrix} -0.195 + 32.247i \\ -0.195 - 32.247i \\ -1.352 + 13.593i \\ -1.352 - 13.593i \end{Bmatrix} \tag{25}
$$

$$
B_{1,0} = \begin{bmatrix} 0 & 0 \\ 0 & 0 \\ 4.225 & -0.544 \\ 49.74 & 8.013 \end{bmatrix}
$$

$$
\mathrm{rank}\left(\left[B_{1,0}\ \ A_0B_{1,0}\ \ A_0^2B_{1,0}\ \ \ldots\ A_0^{n-1}B_{1,0}\right]\right) = 4 = n
$$

and, therefore, the pair $(A_0, B_{1,0})$ is controllable (first condition of theorem 1). For matrices B_2, B_3, D_{13}, D_{12}, D_{21}, C_2 as stated in (15), the second and third conditions of theorem 1 are fulfilled as well:

$$
\begin{aligned}
&D_{21}^T D_{21} = [0_{n\times m}\ \ I_m]\begin{bmatrix} 0_{n\times m} \\ I_m \end{bmatrix} = I_m = I_m^{-1} \\
&D_{21}^T C_2 = [0_{n\times m}\ \ I_m]\begin{bmatrix} I_n \\ 0_{m\times n} \end{bmatrix} = 0_{m\times n} \\
&\mathrm{rank}([C_2\ \ C_2A_0\ \ C_2A_0^2\ \ C_2A_0^{n-1}]^T) = 4 = n
\end{aligned} \tag{26}
$$

Solving the regulator equations (12), yields:

$$
\Pi = \begin{bmatrix} 0 & 0 & 0 & 0 & 1 & 0 \\ 0 & 0 & 0 & 0 & 0 & 1 \\ -1 & 0 & 0 & 0 & 0 & 0 \\ 0 & -1 & 0 & 0 & 0 & 0 \end{bmatrix} \tag{27}
$$

$$
\Gamma \cong \begin{bmatrix} -0.302 & -0.025 & -0.132 & -0.009 & 20.48 & 5.588 \\ 2.960 & 0.127 & 0.816 & -0.069 & -234.5 & 91.53 \end{bmatrix}
$$

Computing γ for the maximum admissible uncertainty according to (9 - 11), $\theta = 1.10\theta_0$, yields $\gamma = 0.198$, and the solution of the algebraic Riccati equation (14) is:

$$
P \cong \begin{bmatrix} 15.38 & -14.10 & 0.163 & 0.040 \\ * & 13.67 & -0.192 & -0.005 \\ * & * & 0.019 & -0.013 \\ * & * & * & 0.013 \end{bmatrix} \tag{28}
$$

where two additional weighting parameters were considered to assist in finding a symmetric and positive semi-definite matrix $(P = P^T, P \geq 0)$ equal to $\varepsilon_Q = 10^{-2}$ and $\varepsilon_R = 10^4$, $(\varepsilon_Q, \varepsilon_R > 0)$, that is, matrices Q and R are defined as $Q = \varepsilon_Q . Q$ and $R = \varepsilon_R . R$ (see appendix 2 for details).

Since the control objective in this particular application is to steer the outputs to the origin, a reference system of dimension two departing from zero initial condition $x_r(0) = [0\ \ 0]^T$ is appropriate to generate the desired outputs $y_r = [h\ \ \alpha]^T = [0\ \ 0]^T$:

$$
\begin{aligned}
&\dot{x}_r = A_r x_r + \varphi_r(x_r) \\
&y_r = C_r x_r
\end{aligned} \tag{29}
$$

with:

$$
A_r = \begin{bmatrix} 0 & 0 \\ 0 & 0 \end{bmatrix}, \quad \varphi_r(x_r) = \begin{bmatrix} 0 \\ 0 \end{bmatrix}, \quad C_r = \begin{bmatrix} 1 & 0 \\ 0 & 1 \end{bmatrix} \tag{30}
$$

For simulation purposes, the differential equations of systems (6) and (7) were solved simultaneously through the RK-Butcher method between $t_0 = 0$ and $t_f = 12\ \mathrm{s}$, with a step of $dt = 0.01\ \mathrm{s}$, and departing from initial conditions (31). In (7), μ was set to $\mu = 100$. The freestream velocity was chosen as $V = 13.40\ \mathrm{m/s}$ and corresponds to 25% above the predicted flutter velocity $V_F \in [10.72,\ 10.73]\ \mathrm{m/s}$. The control is switched on at $t_{u_{on}} = 6\ \mathrm{s}$, a time-instant at which the aeroelastic system is already in a limit cycle oscillation. The amplitudes and velocities of the control surfaces are limited to $\beta, \gamma \in [-25, 25]^\circ$ and $\dot{\beta}, \dot{\gamma} \in [-1000, 1000]^\circ/\mathrm{s}$, see (32).

DOI 10.1515/ama-2015-0040

Initial conditions:

$$\begin{aligned} x_0 &= [0.02 \quad 5.\pi/180 \quad 0.00 \quad 0.\pi/180\,]^T \\ x_{r,0} &= [0.00 \quad 0.\pi/180]^T \\ \varphi_0 &= f(x_0,\theta_0) - A_0 x_0 \\ x_{\mu,0} &= \sigma_\eta([0.\pi/180 \quad 0.\pi/180]^T) \end{aligned} \tag{31}$$

Actuator constraints:

$$\begin{aligned} \|u\|_\infty &\le \eta = 25.\pi/180 \\ \|\dot{u}\|_\infty &\le \nu = 1000.\pi/180 \end{aligned} \tag{32}$$

The simulation results are depicted in Figs. 2 - 5. Figs. 2 and 3 show the time histories of the state variables $x = [h \;\; \alpha \;\; \dot{h} \;\; \dot{\alpha}]^T$, where the first two represent also the system outputs. The magnitude of the control variables, in fact, the trailing- and leading-edge control surface deflection angles $u = [\beta \;\; \gamma]^T$ are shown in Fig. 4 and their respective rates $\dot{u} = [\dot{\beta} \;\; \dot{\gamma}]^T$ in Fig. 5. The units of h and α, β, γ are presented respectively in cm and $\mathrm{degrees}$ for a better interpretation. Fig. 6 shows $\left\|\Gamma w + B_{1,0}^{+}\Pi r\right\|_\infty \equiv g_\eta$ and $\left\|\Gamma S w + \Gamma r + B_{1,0}^{+}\Pi \dot{r}\right\|_\infty \equiv g_\nu$ to verify (iv - b) of theorem 1.

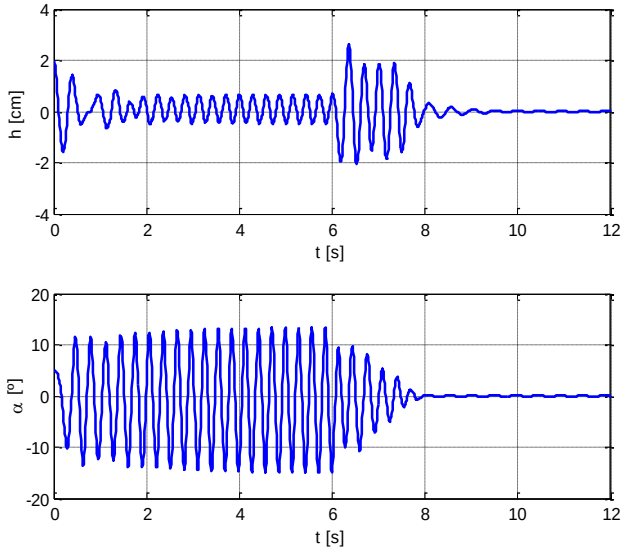

Fig. 2. State variables and outputs of the system: h and α

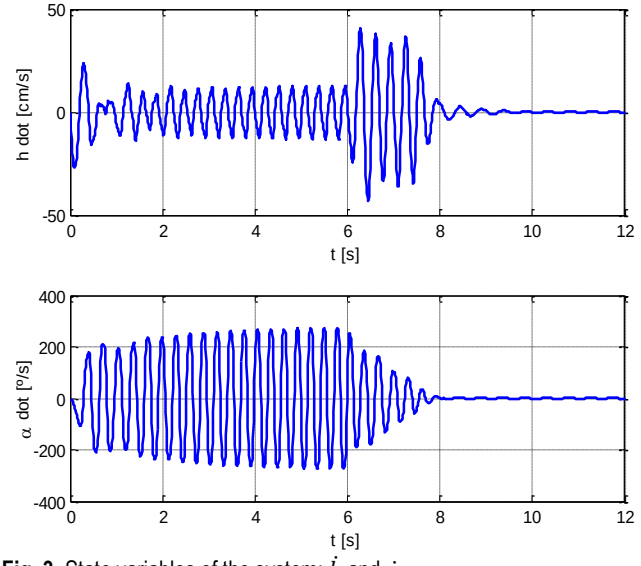

Fig. 3. State variables of the system: $\dot{h}$ and $\dot{\alpha}$

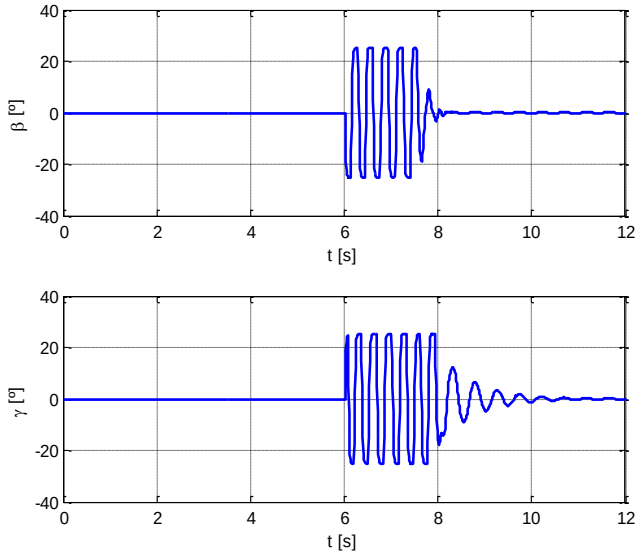

Fig. 4. Magnitude of the control variables: β and γ. $\|u\|_\infty \le 25°$

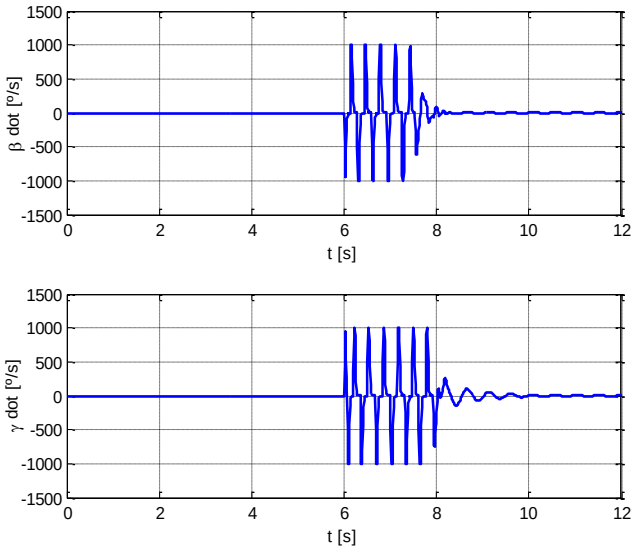

Fig. 5. Rates of the control variables: $\dot{\beta}$ and $\dot{\gamma}$. $\|\dot{u}\|_\infty \le 1000\ °/s$

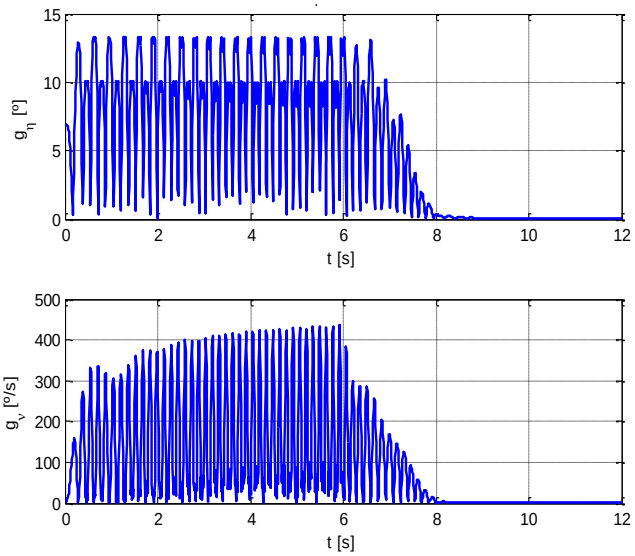

Fig. 6. $g_\eta \equiv \left\|\Gamma w + B_{1,0}^{+}\Pi r\right\|_\infty \le 25°$ and
$g_\nu \equiv \left\|\Gamma S w + \Gamma r + B_{1,0}^{+}\Pi \dot{r}\right\|_\infty \le 1000°/s$

5. DISCUSSION

The numerical simulations prove that the proposed method steers effectively the output error to the origin $\lim_{t\to\infty} e(t) = 0$ assuring that the control saturation bounds are not violated, $\|u(t)\|_\infty \leq \eta$, $\|\dot{u}(t)\|_\infty \leq \nu$. Simulations were also performed for different parameter values within the specified interval $\theta \in [0.90\theta_0, 1.10\theta_0]$, departing from different initial conditions, and for different saturation limits, η and ν, and in all cases the control was successfully achieved. Furthermore, since the criterion invoked to ensure robustness against parameter uncertainties is fairly strong (small-gain theorem), the control law can actually regulate the outputs even if the actual uncertainties are beyond the specified ones, or at least for slightly higher uncertainties.

Another point that deserves attention is the fact that the solution of the algebraic Riccati equation (14), P, should guarantee that the matrix $\tilde{A} \equiv A_0 - B_{1,0}B_{1,0}^T P + \gamma^{-2}B_3 B_3^T P$ is stable, as stated in theorem 1, and this may restrict the maximum admissible uncertainty taken into consideration. However, a given solution P is also admissible since the first two terms of $\tilde{A}$ are stable, that is, $\mathrm{Re}\left[\lambda_i\left(A_0 - B_{1,0}B_{1,0}^T P\right)\right] \leq 0$. Simulations were carried out assuming an uncertainty of $\pm 20\%$, $\theta \in [0.80\theta_0,\ 1.20\theta_0]$, condition wherein γ is too small ($\gamma = 0.099$) and $\mathrm{Re}\left[\lambda_i\left(\tilde{A}\right)\right] \leq 0$ is not satisfied, and the vibrations were suppressed.

Analysing Fig. 2, one verifies that, contrarily to what happens with the angle of attack α where it is gradually attenuated from the time-instant at which the control is turned on, $t_{u_{on}} = 6$ s, the plunge displacement h increases before starting to decrease. This means that in a critical application like the aeroelastic system presented here, some precautions should be taken into account when applying the method because the excessive increase in the plunge displacement may lead to structural failure. Nevertheless, such an undesired effect can be prevented by restricting the output, but that topic is a subject for another paper.

6. CONCLUSION

A robust output regulation method for chaotic systems which takes into account magnitude and rate actuator constraints has been proposed in the present paper. The method consists, in a first stage, in splitting the nonlinear model into a stable linear part and in a remaining nonlinear part. Then, the nonlinear part is generated simultaneously with the reference signals with the aid of an exosystem. Next, the uncertainties in the model are described as additional terms, taking into account the fact that most of the chaotic systems have their parameters exclusively in the linear terms. Besides, bounds are set on the magnitudes of the admissible uncertainties. In fact, these bounds are parameters that are used subsequently for the computation of an H_∞ state feedback control law. Lastly, a differential operator is used to enforce both magnitude and rate constraints in the controlled system.

Numerical simulations are performed to validate the method using an aeroelastic system. The results show that the undesired vibrations are effectively supressed for any parameters within the specified bounds and without exceeding the actuator constraints. Furthermore, the reference signals are tracked within a rather reduced settling time taking into account that the control is subject to magnitude and rate constraints.

The control law presented in the paper is static and all its parameters are computed offline. This is therefore a great asset, since the method can be easily implemented in a low-cost platform because it does not require high computational power. The fact that both magnitude and rate constraints are considered is another advantage since they are crucial for the proper operation of highly demanding applications, and many other control techniques do not consider them at all especially when parameter uncertainties are taken into consideration.

Extensions for the present work are possible, among which one emphasizes the hypothesis of considering asymmetric actuator constraints, an output feedback (instead of a full-state feedback) to take into account also measurement noise, and to extend the area of applicability of the method to systems whose parameters may also appear in the nonlinear terms.

REFERENCES

1. **Alstrom, B., Marzocca, P., Bollt, E., Ahmadi, G.** (2010), Controlling Chaotic Motions of a Nonlinear Aeroelastic System Using Adaptive Control Augmented with Time Delay, *AIAA Guidance, Navigation, and Control Conference*, 1–14, Toronto, Ontario Canada.
2. **Bernhard, P.** (2002), Survey of Linear Quadratic Robust Control, *Macroeconomic Dynamics*, *6*, 19–39.
3. **Bousson, K., Velosa, C.M.N.** (2014), Robust Control and Synchronization of Chaotic Systems with Actuator Constraints, P. Vasant (Ed.), *Handbook of Research on Artificial Intelligence Techniques and Algorithms*, 1–43, IGI Global.
4. **Chen, C.L., Peng, C.C., Yau, H.T.** (2012), High-order Sliding Mode Controller with Backstepping Design for Aeroelastic Systems, *Communications in Nonlinear Science and Numerical Simulation*, *17*(4), 1813–1823.
5. **Demenkov, M.** (2008), Structural Instability Induced by Actuator Constraints in Controlled Aeroelastic System. In *Proceedings of the 6th EUROMECH Nonlinear Dynamics Conference (ENOC 2008)*. Saint Petersburg, Russia.
6. **Deng, L., Xu, J.** (2010), Control and Synchronization for Uncertain Chaotic Systems with LMI Approach, *Chinese Control and Decision Conference (CCDC)*, 1695–1700.
7. **Galeani, S., Teel, A.R., Zaccarian, L.** (2007), Constructive Nonlinear Anti-windup Design for Exponentially Unstable Linear Plants, *Systems & Control Letters*, *56*(5), 357–365.
8. **Hippe, P.** (2006), *Windup In Control: Its Effects and Their Prevention*, Springer.
9. **Horowitz, I.** (2001), Survey of Quantitative Feedback Theory (QFT), *International Journal of Robust and Nonlinear Control*, *11*(10), 887–921.
10. **Huang, J.** (2004), *Nonlinear Output Regulation: Theory and Applications*, Philadelphia: Siam.
11. **Ott, E., Grebogi, C., Yorke, J.A.** (1990), Controlling Chaos, *Physical Review Letters*, *64*(11), 1196–1199.
12. **Pecora, L.M., Carroll, T.L.** (1990), Synchronization in Chaotic Systems, *Physical Review Letters*, *64*(8), 821–824.
13. **Saberi, A., Stoorvogel, A.A., Sannuti, P.** (2011), *Control of Linear Systems with Regulation and Input Constraints*, Springer; Reprint of the original 1st ed.
14. **Tanaka, K., Wang, H. O.** (2001), *Fuzzy Control Systems Design and Analysis: A Linear Matrix Inequality Approach* (1st ed.), Wiley-Interscience.
15. **Velosa, C.M.N., Bousson, K.** (2014), Suppression of Chaotic Modes in Spacecraft with Asymmetric Actuator Constraints, Submitted to the *Proceedings of the Institution of Mechanical Engineers, Part G: Journal of Aerospace Engineering*.
16. **Velosa, C. M. N., Bousson, K.** (2015), Synchronization of Chaotic Systems with Bounded Controls, *International Review of Automatic Control (IREACO)*, (To appear).

17. **Vikhorev, K. S., Goman, M. G., Demenkov, M. N.** (2008), Effect of Control Constraints on Active Stabilization of Flutter Instability, *Proceedings of The Seventh International Conference on Mathematical Problems in Engineering Aerospace and Sciences (ICNPAA 2008)*, 1–8, Genoa, Italy.
18. **Wang, C.-C., Chen, C.-L., Yau, H.-T.** (2013), Bifurcation and Chaotic Analysis of Aeroelastic Systems, *Journal of Computational and Nonlinear Dynamics*, *9*(2), 021004 (13 pages).
19. **Zames, G.** (1981), Feedback and Optimal Sensitivity: Model Reference Transformations, Multiplicative Seminorms, and Approximate Inverses, *IEEE Transactions on Automatic Control*, *26*(2), 301–320.

Acknowledgments: This research was conducted in the Aeronautics and Astronautics Research Unit of the University of Beira Interior (LAETA - UBI / AeroG) at Covilhã, Portugal, and supported by the Portuguese Foundation for Science and Technology (FCT).

Nomenclature: V – freestream velocity; h – plunge displacement; α – angle of attack / pitch angle; γ – leading-edge control surface deflection angle; β – trailing-edge control surface deflection angle; ρ – air density; a – dimensionless dist. from mid-chord to elastic axis position; b – wing section half-chord; s – wing section span; k_h – plunge displacement stiffness coefficient; k_α – pitch spring stiffness coefficient; c_h – plunge displacement damping coefficient; c_α – pitch angle damping coefficient; m_{wing} – mass of wing section; m_W – total wing section plus mount mass; m_T – total mass of pitch-plunge system; I_{cam} – pitch cam moment of inertia; $I_{cg-wing}$ – wing section moment of inertia about the center of gravity; I_α – moment of inertia; x_α – dimensionless distance between the center of gravity and the neutral axis; $C_{l\alpha}$ – lift coefficient per unit of angle of attack, $\partial l/\partial\alpha$; $C_{m\alpha}$ – moment coefficient per unit of angle of attack, $\partial m/\partial\alpha$; $C_{l\beta}$ – lift coefficient per unit of wing trailing-edge control surface deflection, $\partial l/\partial\beta$; $C_{m\beta}$ – moment coefficient per unit of wing trailing-edge control surface deflection, $\partial m/\partial\beta$; $C_{l\gamma}$ – lift coefficient per unit of wing leading-edge control surface deflection, $\partial l/\partial\gamma$; $C_{m\gamma}$ – moment coefficient per unit of wing leading-edge control surface deflection, $\partial m/\partial\gamma$; $C_{m\alpha-eff}$ – effective control moment derivative due to angle of attack; $C_{m\beta-eff}$ – effective control moment derivative due to trailing-edge control surface deflection; $C_{m\gamma-eff}$ – effective control moment derivative due to leading-edge control surface deflection.

Appendix 1: *Solving the Regulator Equations*

The following system, whose the first equation is a Sylvester equation, is known as the linear regulator equations (or also as the Francis' equations), and its resolution is essential to determine the control law presented in this paper.

$$\Pi S = A\Pi + B_1\Gamma + B_2$$
$$0 = C_1\Pi + D_{12}$$

Let $\mathrm{vec}\colon \mathbb{R}^{l\times c} \to \mathbb{R}^{lc\times 1}$ be a vector-valued function of a matrix such that, for any $X \in \mathbb{R}^{l\times c}$:

$$\mathrm{vec}(X) = \begin{bmatrix} X_1 \\ \vdots \\ X_c \end{bmatrix}$$

where, for $i = 1, \ldots, c$, X_i is the ith column of X. Applying this transformation in all terms of the system yields:

$$\mathrm{vec}(\Pi S) - \mathrm{vec}(A\Pi) - \mathrm{vec}(B_1\Gamma) = \mathrm{vec}(B_2)$$
$$\mathrm{vec}(C_1\Pi) = \mathrm{vec}(-D_{12})$$

Since $A \in \mathbb{R}^{n\times n}$, $B \in \mathbb{R}^{n\times m}$, $S \in \mathbb{R}^{s\times s}$, $B_2 \in \mathbb{R}^{n\times s}$, $C_1 \in \mathbb{R}^{p\times n}$, matrices Π and Γ have dimensions $n \times s$ and $m \times s$ respectively. Through some prepositions which can be found in (Huang, 2004), equations above can be rewritten as:

$$(S^T \otimes I_n)\mathrm{vec}(\Pi) - (I_s \otimes A)\mathrm{vec}(\Pi) - (I_s \otimes B_1)\mathrm{vec}(\Gamma) = \mathrm{vec}(B_2)$$
$$(I_s \otimes C_1)\mathrm{vec}(\Pi) = \mathrm{vec}(-D_{12})$$

where $I_s \otimes A$ denotes the Kronecker product between matrices I_s and A. Through the following mathematical manipulation:

$$\overbrace{(S^T \otimes I_n - I_s \otimes A)}^{A_*}\mathrm{vec}(\Pi) - \overbrace{(I_s \otimes B)}^{B_*}\mathrm{vec}(\Gamma) = \mathrm{vec}(B_2)$$
$$\underbrace{(I_s \otimes C_1)}_{C_*}\mathrm{vec}(\Pi) = \mathrm{vec}(-D_{12})$$

these equations can be transformed into a standard linear algebraic system of the form:

$$\underbrace{\begin{bmatrix} A_* & -B_* \\ C_* & 0_{sp\times sm} \end{bmatrix}}_{H}\underbrace{\begin{bmatrix} \mathrm{vec}(\Pi) \\ \mathrm{vec}(\Gamma) \end{bmatrix}}_{z} = \underbrace{\begin{bmatrix} \mathrm{vec}(B_2) \\ \mathrm{vec}(-D_{12}) \end{bmatrix}}_{b}$$

and matrices Π and Γ calculated as $z = H^{-1}b$.

Appendix 2: *Solving the H_∞-like Riccati Equation*

The continuous-time algebraic Riccati equation (14), transcribed below for the sake of convenience:

$$A^T P + PA - PB_1B_1^T P + \gamma^{-2}PB_3B_3^T P + Q = 0$$

can be rewritten, after a mathematical manipulation, as:

$$A^T P + PA - P\underbrace{[B_3 \;\; B_1]}_{B}\underbrace{\begin{bmatrix} -\gamma^2 I_{n+q} & 0_{(n+q)\times m} \\ 0_{m\times(n+q)} & I_m \end{bmatrix}}_{R}^{-1}\underbrace{\begin{bmatrix} B_3^T \\ B_1^T \end{bmatrix}}_{B^T}P + Q = 0$$

where I and 0 denote respectively identity and zero matrices.

Its unique solution, $P \geq 0$, $P = P^T$, can be easily computed, if there exists, by the following function provided in Matlab: $P = \mathrm{care}(A, B, Q, R)$.

LOCAL DAMAGES DURING ROLLING AND MECHANO-ROLLING FATIGUE FOR THE MECHANICAL SYSTEM SHAFT – ROLLER (0.45 CARBON STEEL – 25XGT STEEL, 20XH3A STEEL – 20XH3A STEEL)

Alexander BOGDANOVICH[*], Oleg YELOVOY[**], Leonid SOSNOVSKIY[***],Victor KOMISSAROV[***], Sergey TYURIN[***]

[*]Mechanics and Mathematics Faculty, Department of Theoretical and Applied Mechanics, Belarusian State University, Nezavisimosty av., 4,220000, Minsk, Republic of Belarus
[**]The Joint Institute of Mechanical Engineering of National Academy of Sciences of Belarus, Academicheskaya str., 12, 220072, Minsk, Republic of Belarus
[***]S&P Group TRIBOFATIGUE Ltd, Gomel, Republic of Belarus

bogal@tut.by, yelovoy@mail.ru, tribo-fatigue@mail.ru, vickom@tut.by, tribo-fatigue@mail.ru

received 4 May 2015, revised 18 December 2015, accepted 18 December 2015

Abstract: The report provides a description of local damages which are formed in the process of wear-fatigue tests. The analysis of local surface wave-like damages during rolling and mechano-rolling fatigue for the shaft-roller mechanical system under steady-state and multi-stage loading conditions is given. It is shown that the study of local wear-fatigue damage was made possible by new methods of testing and measuring wear-fatigue tests and damages, which are described in the report. New characteristics to estimate the parameters of the local wear-fatigue damage are proposed. The concept of local fatigue curves is introduced. The laws of local wear-fatigue damage for the shaft - roller system are analysed.

Key words: Local Damage, Fatigue, Tribo-Fatigue System, Microcrack, Wear-Fatigue Damage, Residual Deformation, Wave-Like Damage, Troppy Phenomena, Local Fatigue Curve

1. INTRODUCTION

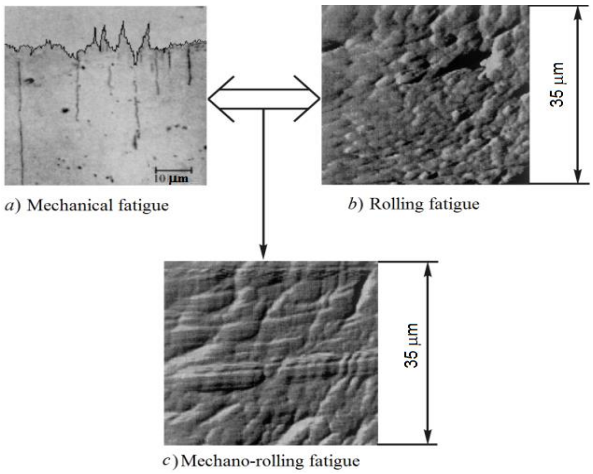

Fig. 1. Local damages under mechanical fatigue (a), rolling fatigue (b) and mechano-rolling fatigue (c) for the roller (steel 25XGT) – shaft (0.45 carbon steel) system

Risk of damage in the small volumes of material is well known to specialists in solid mechanics. Local damages in the form of microcracks, pores, corrosion pits and others lead to a breach of strength at variable loads, and even the complete destruction of structural elements as a result of the merger of microcracks in the main fatigue crack and its development (Fig. 1).Similarly, when the surface of local damage under rolling friction (Fig. 1, 2), sliding or fretting, corrosion the process of gradual degradation of the surface layer of the structural element or component of assembly friction due to damage micro volumes of material, their fusion and development leads to the depletion of the resource of structure or assembly friction (Bayer, 2004; Engel and Adams, 1987; Hogmark and Alander, 1983; Samyn et al., 2008; Yung-Li et al., 2005). An important task is to determine experimentally the local laws of wear-fatigue damage and its prediction.

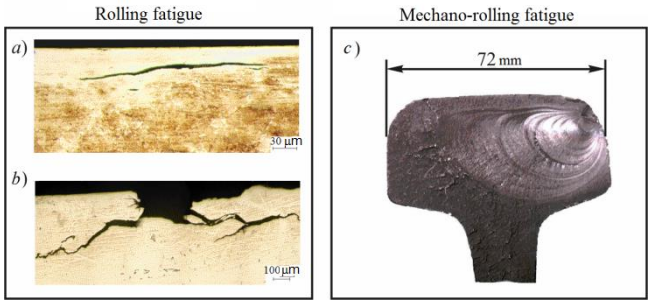

Fig. 2. Local damages - microcracks during wear peeling (a) and chipping (b) during rolling fatigue and photo of the fracture of railway rail from the transverse crack of mechano-rolling fatigue (c)

2. WAVE-LIKE DAMAGES

The tribo-fatigue system roller / shaft undergoes a mechano-rolling fatigue, to a certain extent reproduce the operating condi-

tions of wheel / rail system. It was found a special type of limiting state: formation on the raceway residual wave-like damages during such tests. Let's look at the results of the experimental analysis of this phenomenon (Sosnovskiy et al., 2014; Sosnovskiy and Shcharbakou, 2005; Turin and Sherbakov, 2005). Tested for mechano-rolling fatigue was a tribo-fatigue system 25XGT steel (roller)/0.45 carbon steel (shaft). Properties of steel 25XGT were as follows: the fatigue limit σ_{-1}= 570 MPa, the rolling fatigue limit p_f= 3100 MPa. Properties of 0.45 carbon steel were as follows: the fatigue limit σ_{-1}= 260 MPa, the rolling fatigue limit p_f = 1760 MPa. Thus, the characteristic feature of the tribo-fatigue system was that the strength of the shaft's metal is substantially less than the roller's metal so during testing it was detected residual deformation and damage only in the vicinity of the raceway on the shaft, whereas the roller dimensions remain substantially undistorted.

Bending load Q = 225 N = const corresponds to the stress amplitude σ_a = 225 MPa $< \sigma_{-1}$= 260 MPa.Contact load was varied stepwise on program, shown in Fig. 3. Rolling fatigue limit p_f =1760 MPa was exceeded at the III stage of loading.

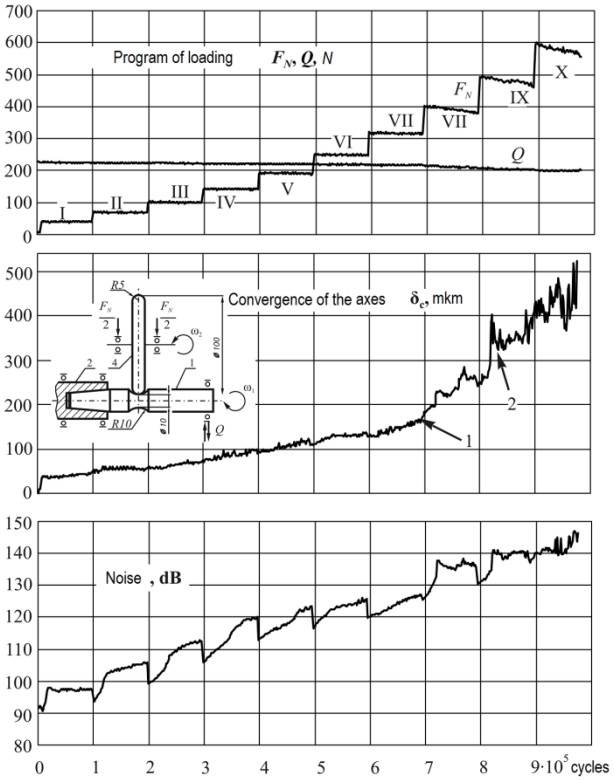

Fig. 3. The test report for the roller (steel 25XGT) – shaft (0.45 carbon steel) system on mechano-rolling fatigue (Sosnovskiy et al., 2005)

Motion of the roller on the shaft was unsteady in the transition from VII to VIII stage of contact loading, i.e. after 700 000 cycles of testing (see arrow 1 in Fig. 3). Residual radial deformations of the shaft in the area of non-stationarity are shown in Fig. 4 as bright points (750154 loading cycles, i.e. in the middle of the stage VIII).There was a loss of stability of motion at the IX stage (see arrow 2 in Fig. 3). Residual radial deformations of the shaft at the loss of stability of motion are shown in Fig. 4 by the crosses (851688 load cycles, i.e. in the middle of the stage IX).The tests were terminated at the X stage at N_Σ = 976 100 load cycles due to unacceptable vibration and noise. Deformations of the shaft after the tests are shown in Fig. 5 and 6.

What are the main features of damage for the shaft? The somewhat peculiar frozen waves of surface plastic deformation are formed on the raceway. They represent a set of irregular holes half-barrel-shaped. None of the wells is not repeated, each of them has its own, different from other sizes in all three dimensions – radial, axial, circumferential. The relative magnitude of plastic deformation (in this experiment) reaches 10% in radial direction and 30% in the axial ones.

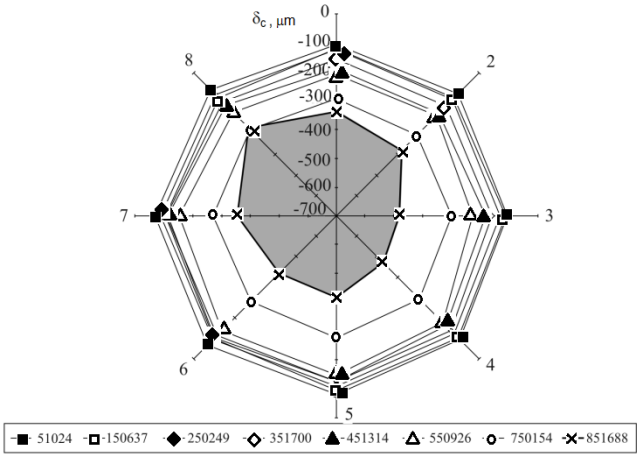

Fig. 4. Changing of radial residual deformation (μm) depending on the number of cycles in 8 points on the diameter of the shaft

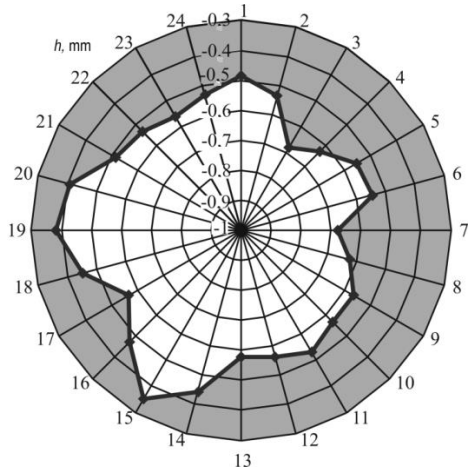

Fig. 5. Radial residual deformation (mm) on diameter of the shaft after testing on mechano-rolling fatigue (N_Σ= 976100 cycles)

Studies have shown that the described damage reversible in the sense that if the strength of the roller material is significantly less than the shaft, the residual damage undulations formed on the roller, whereas on the raceway dimensions remain substantially undistorted shaft. Thus, in these test conditions the surface wave-like residual damage can be regarded as the result of unsteady process elasto-plastic deformation in the contact zone of interaction between two elements of the system. This phenomenon is called troppy (Sosnovskiy et al., 2014; Sosnovskiy and Shcharbakou, 2005), and this nonstationary process is accompanied by three-dimensional transient distortions sizes of raceways of both elements and uneven local resistance of the material

in different "points" in the path of motion (Fig. 7). The strength of the material evaluated, e.g., hardness, is significantly different in these points, both before and after the test (Fig. 8).

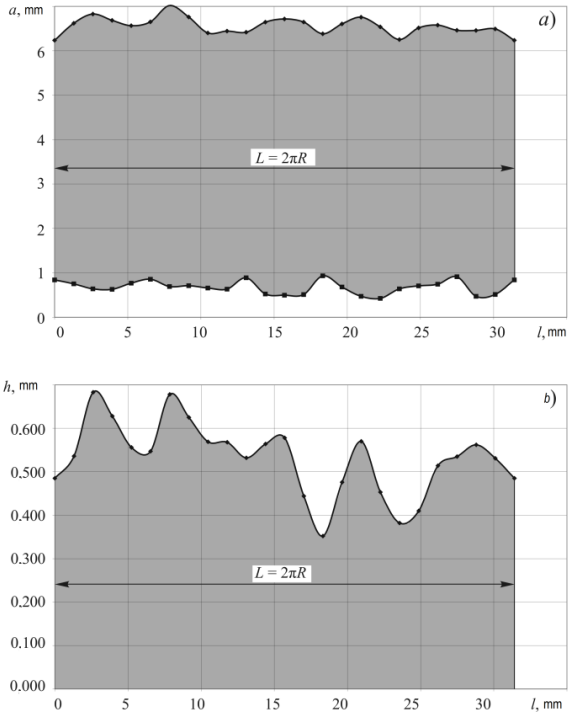

Fig. 6. Axial (a) and radial (b) residual wave-like deformations after testing on mechano-rolling fatigue (N_Σ = 976100 cycles), presented on the net of raceway

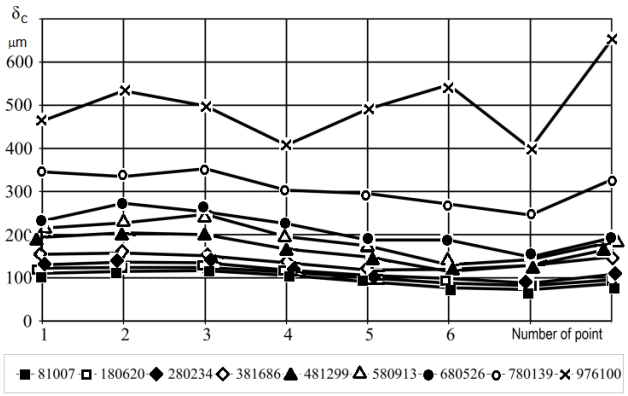

Fig. 7. The convergence of axes of shaft and roller in 8 points on the raceway depending on the number of cycles during testing on mechano-rolling fatigue

It was established experimentally geometry elements and precision in contact are factors that largely shape the emergence of wave-like damage during testing mechano-rolling fatigue.

3. THE CHARACTERISTICS OF LOCAL DAMAGE

Since there is a method of experimental measurement of local damages and some experience of their useful analysis, it was suggested several characteristics of local damage (Sosnovskiy et al., 2014). As you can see in Fig. 4 and 5 the next feature of the surface of local damage: if the circular contour of the test specimen is strictly symmetrical with respect to the center (to test), the contour of local damage, identifies eight measurement points (in these cases) is significantly asymmetric with respect to the same center (after the test).

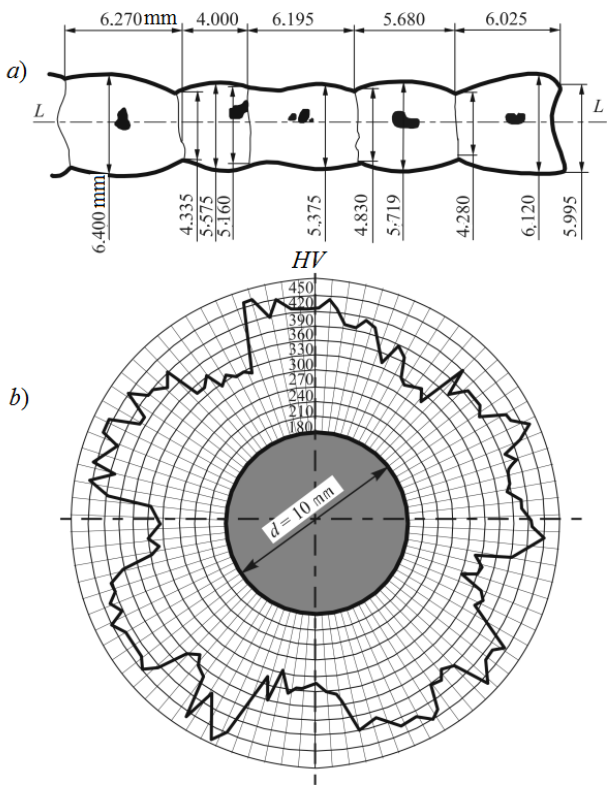

Fig. 8. Surface wave-like residual damage (chipping holes are blackened) (a) and microhardness distribution along the length L of the shaft raceways (b)

The degree of asymmetry generally increases with increasing test time and the integral damage. Let's introduce special integral characteristics of the local process of wear-fatigue damage: asymmetry factor

$$R_a = \frac{1}{4}\sum_{i=1}^{4}\frac{r_{\min(i)}}{r_{\max(i)}} \quad (1)$$

where $\mathrm{r_{min}}$ and $\mathrm{r_{max}}$ are the smaller and a larger radii of the same sample diameter, and the coefficient of unevenness

$$\eta_a = \frac{r_{\mathrm{sm.}}}{r_{\mathrm{larg.}}} \quad (2)$$

where $r_{sm.}$ and $r_{larg.}$ are the smallest and the largest radii of the sample during one revolution.

The designations specified radii of the specimen, as well as the dependence of the coefficients R_a and η_a from the level of cyclic stresses in the test of 0.45 carbon steel / steel 25XGT tribo-fatigue system on mechano-rolling fatigue at step changing of bending load (and, therefore, the stress amplitude σ_a) in the contact pressure p_0 = 0.7p_f = const. are shown in Fig. 9. It can be seen that the unevenness degree of local wear-fatigue damage increases respectively increasing of cyclic stresses. Note that the unevenness of wear-fatigue damage is greater, the smaller the values R_a and η_a.

It can be used technique of a determination of the asymmetry factor and coefficient of unevenness, namely, write them on the values δ_c:

$$R_\delta = \frac{1}{4}\sum \frac{\delta_{\min(i)}}{\delta_{\max(i)}}, \qquad \eta_\delta = \frac{\delta_{c\,sm.}}{\delta_{c\,larg.}}. \tag{3}$$

It is easy to see that the coefficients defined by the formulas (3) is not equal to the corresponding coefficients are determined by formulas (1) and (2). The choice of representation of the coefficients R and η is dictated by the specific objectives of the analysis.

The experiment showed that it is possible to detect single and associated local damages; last interconnected raceway. Formation pronounced single local damage shown in Fig. 10. It is easy to understand that the "solid" wavy-like damage is the final stage of development of local damage from a single to associatedones and then to troppy phenomena.

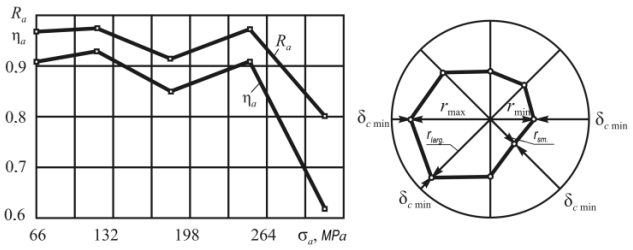

Fig. 9. Dependence of the asymmetry factor and coefficient of unevennessfrom the level of cyclic stresses in the test of 0.45 carbon steel / steel 25XGT tribo-fatigue system on mechano-rolling fatigue at step changing of bending load in the contact pressure p_0 = 0.7p_f = const.; right figure is a diagram for explaining the definition of the η_a and δ_a parameters according to the formulas (1) and (2)

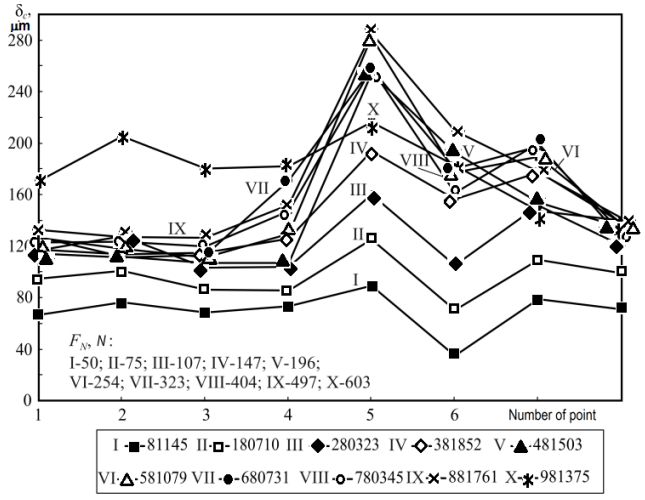

Fig. 10. The convergence of axesin 8 points on the raceway depending on the number of cycles of multystage (I, II, …, X) loading of the roller (steel 25XGT) – shaft (0.45 carbon steel) system during testing on mechano-rolling fatigue

If the limiting state is associated, for example, with a depth h of local damage $\delta_{lim} = h$, it is possible to construct a kind of fatigue curves on the criterion of local damage (Fig. 11) (Sosnovskiy et al., 2014). The numbers 1, 2, …, 8 are designated the points on the perimeter of the raceway, which reached the limiting state ($\delta_{lim} = h$) for the appropriate number of cycles N. Sequence analysis of the location of the points 1, 2, …, 8 leads to the conclusion that they are placed randomly on the graph.This conclusion does not contradict the known statistical mechanical fatigue test results of specimens: scattering increases with decreasing load. We emphasize, however, that the scattering region durability at every level of the stress is determined by the test results for only one pair of friction.

Come to the analysis of the data presented in Fig. 11, from a different perspective, let us build fatigue curves for each of the eight points individually (Fig. 12). Then the solid lines in this figure are local fatigue curves, each of which describes the limiting state at a specific point of the perimeter raceway. Thus, the Sosnovskiy – Bogdanovich – Yelovoy local fatigue curves (see Fig. 11 and 12) describe the heterogeneity of physical and mechanical properties in local areas of the test solid.

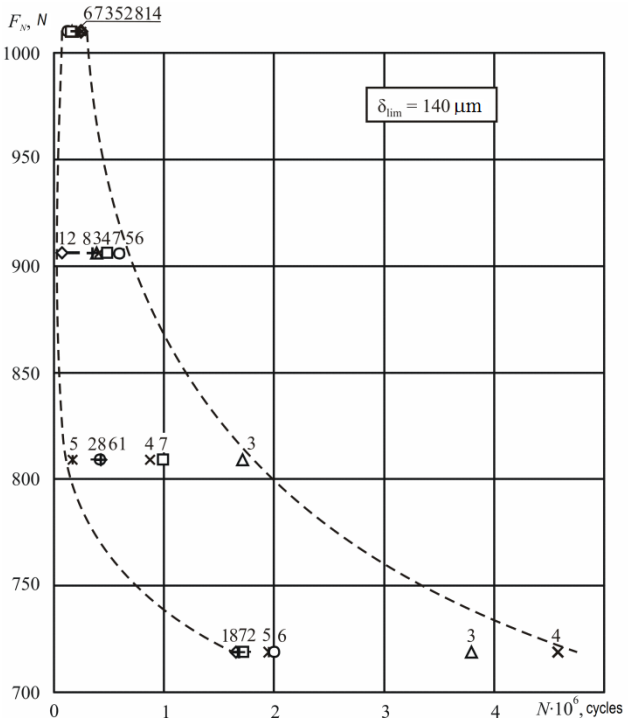

Fig. 11. The rolling fatigue curve for the roller (steel 25XGT) – shaft (0.45 carbon steel) system constructed on criterion of local damage

To learn the basic laws of formation and development of local damages, we dramatically increase the number of points of measurement (Fig. 13). The roller / shaft system made of steel 20XH3A is tested, and initial average hardness of the rolling surface was almost the same for both elements.The test results are shown in Fig. 14 and 15. It is clearly visible both single and associated local damagesin Fig. 14 and wave-like damages – in Fig. 15.

The results of statistical processing of random values of local damage (radial residual strain) are shown in Fig. 16 on normal probability paper (in coordinates of the radial permanent deformation h – the probability P corresponding to the normal distribution law). Tab.1 shows the numerical values of the minimum (h_{min}), average ($\bar{h}$) and maximum (h_{max})strain of the roller (diameter d = 100mm) and a shaft (diameter d = 10mm).

Analysis of the data presented in Fig. 15 and 16 allows us to make the following general and unexpected conclusion: under these friction conditions the roller with diameter of 100 mm is systematically damaged significantly stronger than the shaft

with diameter of 10 mm; ratio values for said objects varies in 2-10 times.

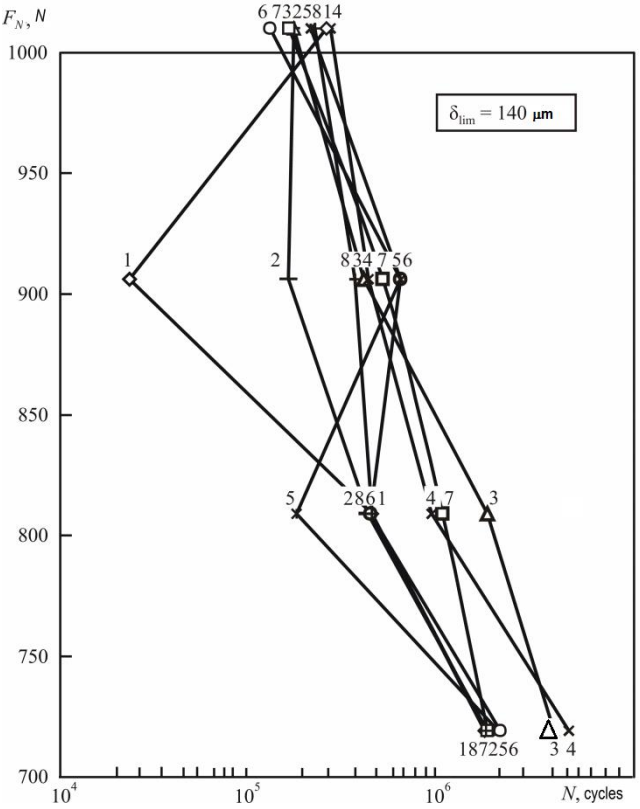

Fig. 12. The local rolling fatigue curve for the roller (steel 25XGT) – shaft (0.45 carbon steel) system

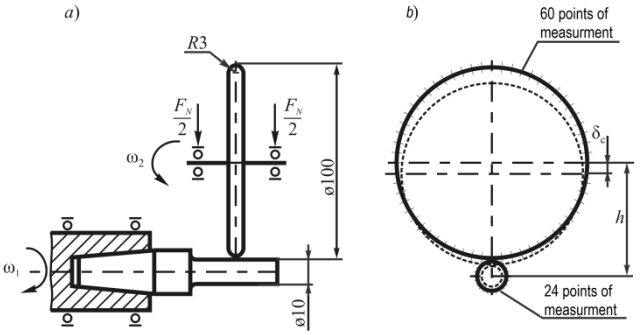

Fig. 13. Schemes of: test (a) and measurements (b) for local damages

Explanation of this fact can't be given to the theory of the scale effect; it suffices to recall that for 1 turn of roller the shaft gets 10 turns (cycles of loading). This means, for example, that when the contact load F_N = 719 N the shaft was $2 \cdot 10^7$ loading cycles (base of test), and the roller was only $2 \cdot 10^6$ cycles. Similarly, when at F_N = 809 N the shaft was $2.4 \cdot 10^6$ loading cycles (base of test) and the roller was only $2.4 \cdot 10^5$ cycles. The friction path for both elements was the same at specified load.

Thus, for equal path friction roller (diameter 100 mm) reaches the limiting state on criterion $\overline{h}$= 84 and 82 μm at the test load F_N = 719 N and 809 N (see Fig. 15), while the shaft (diameter 10 mm) reaches the average damage total only $\overline{h}$= 12 and 24 μm respectively.

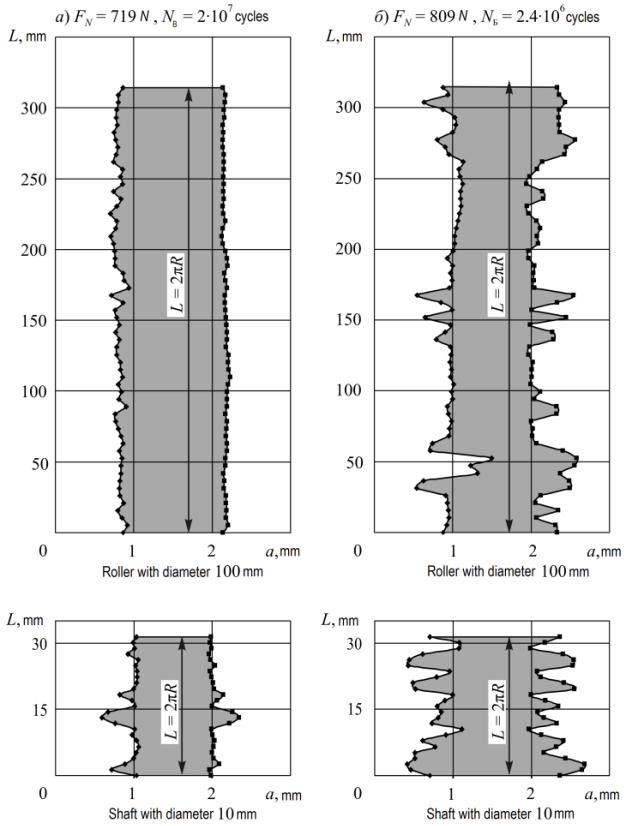

Fig. 14. The local axial residual strain (displacement)after testing of the roller (steel 20XH3A) – shaft (20XH3A) system for rolling fatigue

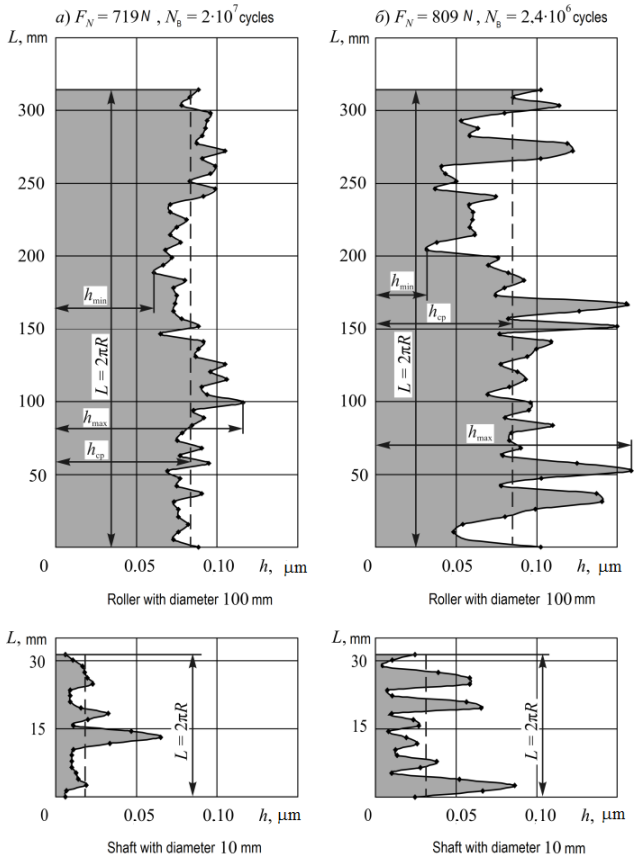

Fig. 15. The local radial residual strain (displacement) after testing of the roller (steel 20XH3A) – shaft (20XH3A) system for rolling fatigue

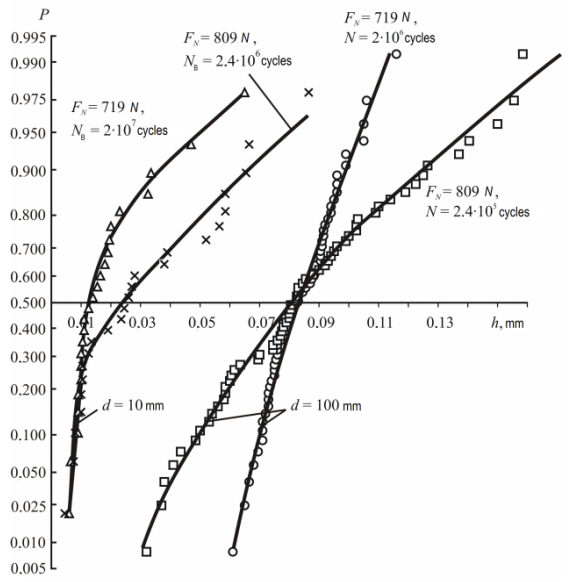

Fig. 16. The empirical distribution function of local radial residual strain after testing of the roller (with diameter 100 mm, steel 20XH3A) – shaft (with diameter 10 mm, steel 20XH3A) system for rolling fatigue

Tab. 1. Statistical parameters of the local damage for the elements of the friction pair steel 20XH3A / 20XH3A

Characteristic of local damage	F_N = 719 N		F_N = 809 N	
	d = 100mm	d = 10mm	d = 100mm	d = 10mm
h_{min}, μm	61	6	32	5
$\bar{h}$, μm	84	12	82	24
h_{max}, μm	116	65	159	87

Search for different causes of damage such two elements (of different diameters) of one pair of friction, provided that the surface hardness of the rolling surfaces for both elements substantially identical led to the hypothesis: the shaft is less damaged than the roller because it is bent during the test, whereas the roller is no.In fact, measurements have shown that in the plane of the contact load shaft deflection reaches 100 μm at F_N = 809 N and 70 μm at F_N = 719 N. This, apparently, is that some of the applied load "costs" not on the contact damage buton bending of the shaft. It follows that it is excited in bending moment counteracting to load F_N. In other words, it appears that the load applied to the conditions of this experiment as it is divided into two components: one of them causes surface damage on the raceway of shaft, and the other causes it bend.

4. CONCLUSION

1. Based on the analysis of experimental results of mechanical system shaft - roller for the 0.45 carbon steel, 25ХГТ, 20ХН3А steels basic laws of wear-fatigue damage are installed: discrete, uneven and irregular occurrence and development of entry wear-fatigue damage; the formation of wave-like residual damage during echano-rolling fatigue (and rolling friction) due to excitation of shock-cyclic loading (troppy phenomenon, this phenomenon is typical for the exploited railway and tram rails); reduction of asymmetry factor and the coefficient of unevenness for wear-fatigue damage with time trials and with increasing levels of loading; initiation of emergence and development of wear-fatigue damage in the local areas in which the minimum strength of the material is detected.
2. To build the local fatigue curves describing the limiting state in a particular point of the perimeter of the dangerous section of the test mechanical system shaft – roller it is proposed. Such local rolling fatigue curves on the parameter of the wear limit for the shaft (steel 20XH3A) - roller (steel 20XH3A) are constructed.
3. Special integral characteristics of wear-fatigue damage the asymmetry factor and coefficient of unevenness are suggested.

REFERENCES

1. **Bayer Raymond G.** (2004), *Mechanical Wear Fundamentals and Testing*, New York, USA.
2. **Engel P., Adams C.** (1987), Rolling wear study of misaligned cylindrical contacts. *Proc. Int. Conf. Wear Materials*., ASME, 181–191.
3. **Hogmark S., Alander J.** (1983), Wear of cylinder liners and piston rings, *Proc. Int. Conf. Wear Materials*, ASME, 38–44.
4. **Samyn P., Quintelier J., Schoukens G.** (2008), On the repeatability of friction and wear tests for polyimides in a hertzian line contact, *Exp. Mech.*, 48, 233–246.
5. **Sosnovskiy L.A., Bogdanovich A.V., Yelovoy O.M., Tyurin S.A., Komissarov V.V., Sherbakov S.S.** (2014), Methods and main results of Tribo-Fatigue tests, *International Journal of Fatigue*, 66, 207-219.
6. **Sosnovskiy L.A., Shcharbakou S.S.** (2005), Troppy Phenomenon, *Proceedings of the World Tribology Congress*, Washington.
7. **Tyurin S.A., Sherbakov S.S.** (2005), Experimental study ofresidual wave-like damage initiated by initial distortion of specimen form, *Vestnik of BelSUT*, 2, 88–93 (in Russian).
8. **Yung-Li L., Jwo P., Hathaway R.B., Barkey M.E**. (2005), *Fatigue testing and analysis*, Amsterdam, Elsevier Butterworth Heinemann.

.

REAL TIME TRAJECTORY CORRECTION SYSTEM OF OPTICAL HEAD IN LASER WELDING

Wojciech CIESZYŃSKI*, Michał ZIĘBA*, Jacek REINER*

*Department of Laser Technology, Automation and Organization of Production, Wroclaw University of Technology, Wybrzeże Wyspiańskiego 27 50-370 Wrocław, Poland

wojciech.cieszynski@pwr.edu.pl, zieba.nowice@gmail.com, jacek.reiner@pwr.edu.pl

received 1 October 2014, revised 17 December 2015, accepted 18 December 2015

Abstract: Application of laser welding technology requires that the laser beam is guided through the whole length of the joint with sufficiently high accuracy. This paper describes result of research on development of optomechatronic system that allows for the precise positioning of the laser head's TCP point on the edge of welded elements during laser processing. The developed system allows for compensation of workpiece's fixture inaccuracies, precast distortions and workpiece deformations occurring during the process.

Key words: Control System, Machine Vision, Image Processing, Laser Welding

1. INTRODUCTION

High precision motion in the process of laser welding involves integration of the positioning systems that control the trajectory of the laser spot with respect to the processed weld, and are able to adjust the position of the laser head. Positioning systems improve flexibility of the processing site, admit greater diversion from the assumed dimensions of the welded pieces, save time and improve quality of the assembly.

The research was aimed at development of a video positioning system for the laser head operating with the CNC machine that would improve accuracy of the trajectory by mean of real time compensation of the assembly errors of the welded pieces in the machine system.

2. CURRENT KNOWLEDGE

There were a number ideas devised over last decades of how to position the laser head. These include: (a) scanning with a pointed laser beam (Fridenfalk and Bolmsjö, 2003), b) optical recognition of the joint on a camera image taken in advance, c) triangulation with sensors measuring the distortions of the projected light profiles, d) mechanical tracking of the seam (Siciliano and Khatib, 2008).

The industry most wide spread solutions involve triangulation. These systems control the seam with 0.1 mm accuracy for straight line trajectories and 0.5 mm for the curved ones. The limited resolution arises from the inaccuracy of the image processing and the sensors' resolution (De Graaf et al., 2005, 2007, 2010). Triangulating scanners are used also for the postprocessing quality inspection (Huang and Kovacevic, 2011, 2012).

There are also extended triangulation methods - stereo triangulation (Michalos et al., 2012) where trajectory are adjusted in 3D for manifold surfaces. Michalos et al. (2012) show how a camera system is integrated on a robotic arm designed for welding. The system has been implemented in the automobile doors assembly line.

Some machine vision positioning systems determine position using the information content of images recorded with an industrial camera mounted on the laser head. A system analysing infrared (805-815 nm) images of a molten pool, provides for a 60 μm accuracy. This, however, works with the pulse lasers only, as the camera records images between the pulses.

Gao et al. (2013) proposed a method analysing the shape of the pool's front with the camera using a narrow 960 – 990 nm spectrum. The joint edge is being detected on the images taken during the welding, and the data used to adjust the trajectory of the laser head.

There is a trend to integrate the positioning system with molten pool monitoring and quality control of the seam (Dorsch et al., 2013). These methods use coaxial triangulation in front of and in the rear of the molten pool and the keyhole imaging. Thanks to the application of a infrared spectrum filter and the monochromatic projectors, the images can show both the triangulation profiles and the pool itself. These solutions are applied in the systems of laser welding of pipes and sectional metal bars.

3. DESIGN OF THE POSITION ADJUSTING SYSTEM FOR THE BEAM/LASER HEAD

3.1. Concept

The processing under consideration makes a ring shaped laser welded seam. This requires the laser head travelling along a full ring trajectory. The proposed system makes use of a stationary laser head and a rotating table of the machine.

The proposed adjustment system follows the diversions of the trajectory from the assumed shape and position. Those are detected by the optical sensor when they enter the scanning field moving in advance of the true laser beam at the preset distance. Diversions of the true joint edge from the assumed position are computed from the position of the joint edge detected in the sen-

DOI 10.1515/ama-2015-0042

sor's scanning field. The results are used to control the motion of the machine working head (Fig. 1).

a)

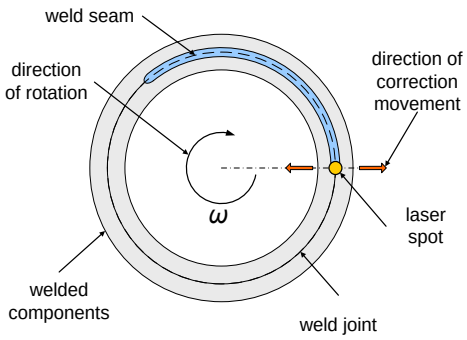

b)

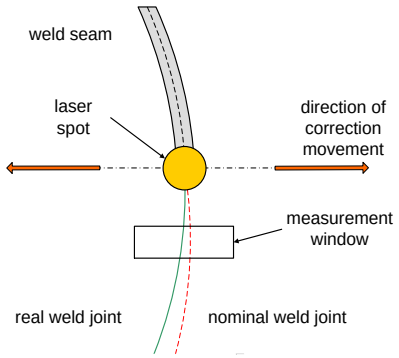

Fig. 1. Laser beam positioning system: a) general concept; b) detailed view

The adjustment motions of the machine head are perpendicular to the ideal, reference trajectory of the laser head in a coordinate system attached to the machine's table. This way, the adjustment movements do not combine with the linear speed of the head controlled in the processing script.

Computation of the adjustment signal rely on the adopted kinematic model that reflects the assumed trajectory and the motions that are drawing it.

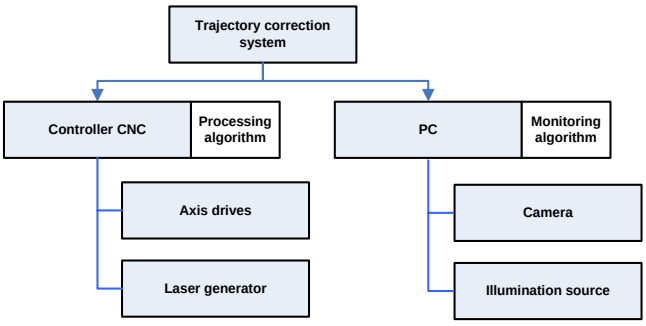

Fig. 2. Structure of the trajectory adjustment system

The concept assumes that the control algorithm will run along two parallel paths: the CNC processing script controlling the manufacturing process, and the adjustments algorithm which supervises the process and computes the adjustments, running on a PC communicated with the CNC controller (Fig. 2).

The algorithm executed on the machine includes the main technology task of controlling the kinematic system which, in turn, draws the assumed trajectory, as well as controlling of the laser beam during the machine processing. Except for that, the programme includes the elements activating and effecting communication between the machine and the PC, and the commands triggering the adjustment motions superimposed on the trajectory.

The other algorithm running on the PC supervises the process and generates the adjustment signals. Thus it processes the images created by the camera and retrieves from the machine the data concerning the head position and the job progress. Using the collected information the program computes the diversion of the machine head from the assumed position and signals the adjustments to the CNC controller in the machine.

3.2. Stages of operation

There are three specific images of the operating field that are distinguishable when a closed curve shaped seam is being drawn: (1) when only the gap is visible, (2) when the gap and the molten pool are visible, (3) when the molten pool and front of the seam are visible - the closure of the trajectory. Since there are varying algorithms of image analysis in use, 3 stages of operation have been distinguished (Fig.3).

a)

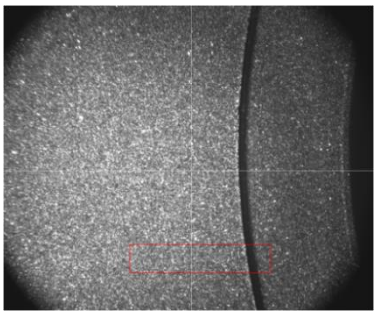

b)

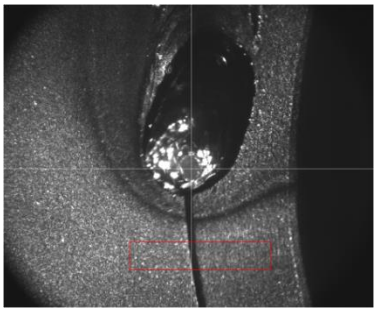

c)

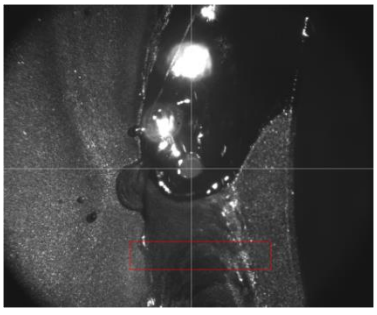

Fig. 3. Images of the elements at the subsequent process stages: a) initial stage; b) processing stage; c) finishing stage

Initial stage (Fig. 3a) - includes the table rotation when the images of the gap are recorded and the head motion adjustments determined. At this stage, the laser beam is not in use and no melting is affected. The resulting control signals are fed to the machine input thus controlling the machine head position. At the same time, the generated signals are recorded in the buffer for the later use, when the trajectory is being closed. At this stage, the table turns by 10 - 20 degrees.

Processing stage (Fig. 3b) - begins after the table reaches the assumed angle determined by the angular fore of the scanning field with respect to the laser beam angular position. The control signals that are now being computed basing on the recorded images and the current position of the beam, are fed to the CNC controller. At the start of with this stage, the laser induced melting begins. The end of this stage is marked with the table travelling the full circle from the initial position in the stage 1.

Finishing stage (Fig. 3c) - now the control signals are not generated upon the current images, but fed from the buffer where they were stored in the initial stage. The third stage ends when the full length of the seam is ready.

3.3. Hardware configuration

The operation site consisted of the following components: CNC machine, PC, data acquisition adapter, AC/DC, industrial CMOS camera, illumination (810nm laser).

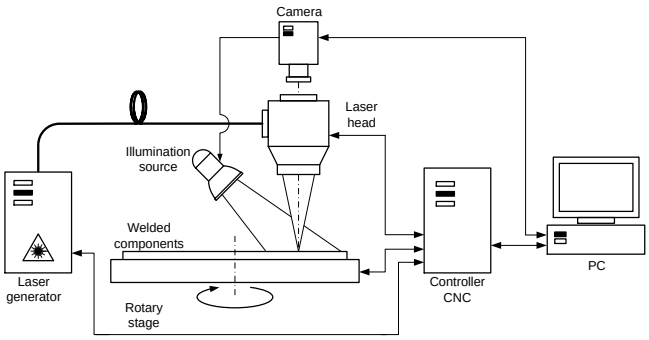

Fig. 4. Head positioning system - diagram

The following signals had to be communicated between the CNC controller and the supervising PC: reading of the laser head position data, reading by the CNC controller of the positioning diversion, reading by the PC of the synchro signals. The data concerning the position and the diversion are transferred by the analogue communication modules available in the machine control system (Siemens, 2006). The synchro signalling went through the digital output of the PLC controller that was a part of the CNC controller.

4. DETECTION OF THE JOINT EDGE

The edge detection algorithm processes images and then fits the curve to the edges detected on the image.

The first stage of image processing defines the region of interest (ROI) on the recorded image. A window set in the right position facilitates more effective image processing, limited to a piece of the the recorded image, where the junction edge and the molten pool are visible. The position of the window has been so adjusted, as to avoid the disturbances caused by the steam channel, the molten pool and the area of heat escape.

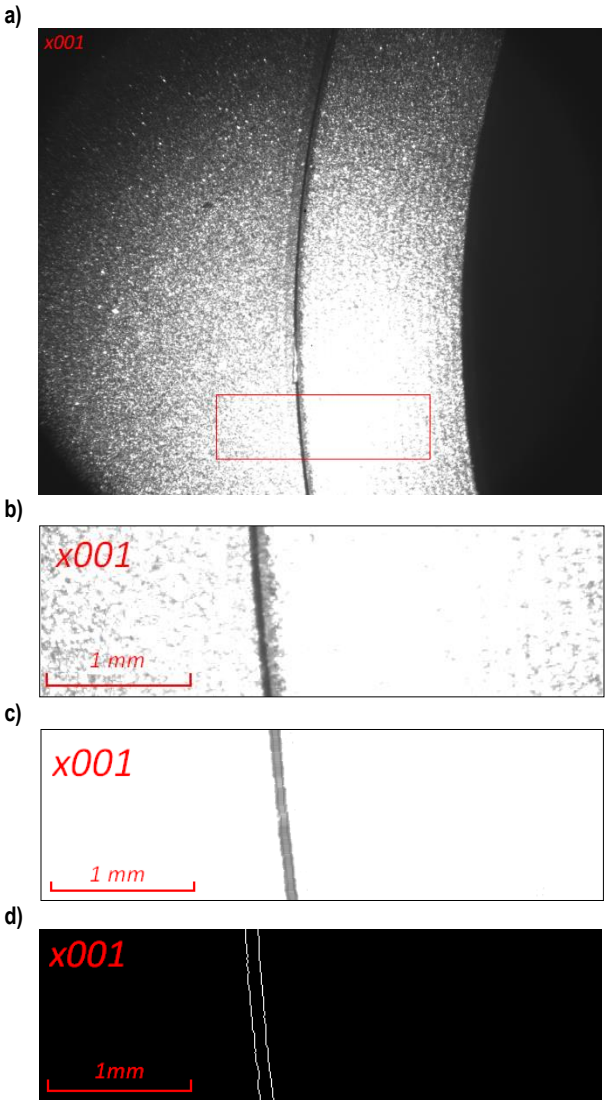

Fig. 5. Image processing: a) base image with ROI window; b) processed piece of the image; c) the image after filtering; d) the image after processing

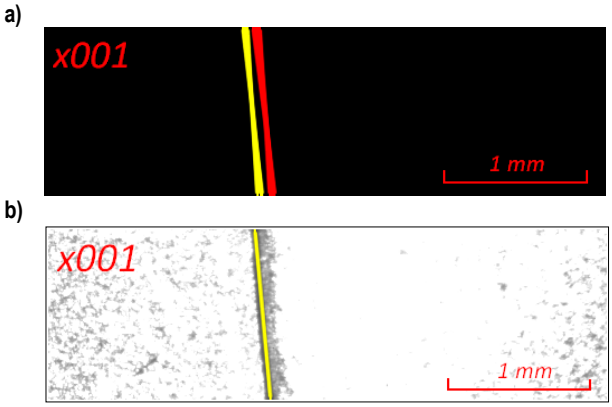

Fig. 6. Results of the edge detection algorithm with straight line model: a) edges detected with the Hough transform; b) net outcome straight line of the seam

The joint edge is visible as brighter line among the dark surroundings. In the beginning the images are subjected to filtering

DOI 10.1515/ama-2015-0042

(median, and Gauss), morphology (erosion, opening and closing) and histogram operations (adjustment of brightness, contrast) in order to remove the distortions arising from the brightness of the surface processed. Fig. 5c).

Next, the resulting image is gradient filtered to provide the ROI edges, used further by the algorithm (Fig. 5d), with visible edges of the pieces to be welded. The images showing the detected edges are used for straight line approximation of joint edge. Hough transform [14] provides for the set of lines fit to the edges visible on the image (Fig. 6a). The net fit to the joint edge is computed by averaging (Fig. 6b).

5. DETERMINATION OF THE HEAD POSITION ADJUSTMENTS

The adjustment signal is computed in a model accounting for the machine kinematics, shape of the processed item, and its position in the machine operating space.

The coordinate system is stationary with respect to the machine's body and located at the centre of the table rotations P_0, while the angular velocity of the table is constant. Coordinates of the head and the lines tracing the joint on the recorded images are relative to the P_0. The adjustment motion vectors are parallel to the X axis of the coordinate system, and the camera see this axis as a horizontal line.

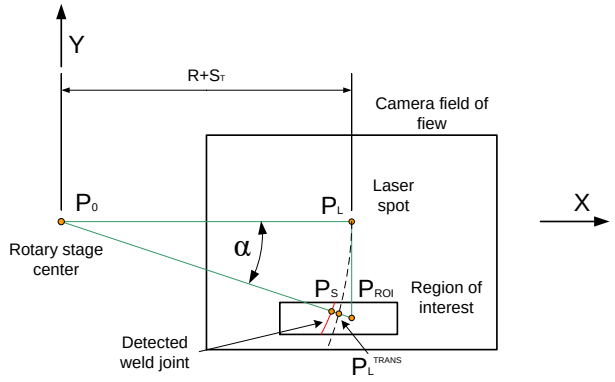

Fig. 7. The coordinate systems used in computations

A point P_L representing location of the laser beam has two coordinates assigned on the image. A P_{ROI} point is determined in the ROI window. Its X coordinate is equal to that of P_L while the Y coordinate equals a half of the *ROI* window height. The points P_0, P_L, P_{ROI} make a right triangle used for computations (Fig. 7).

Position of P_L and P_{ROI} in the image is determined manually in advance of the process and then, the adjustment signals change the X component of the distance between the P_L and P_0 as compared with the nominal value R.

$$|\overline{P_0 P_L}| = R + S_T \tag{1}$$

where: x – description, a – description, a^{n-k} – description, $\binom{n}{k}$ – description.

The points P_0 and P_{ROI} are positioned on the straight line along which the adjustment of the head position are computed. For each measurement cycle, the line representing the joint with the P_0, P_{ROI} line determine the point P_S of the assumed next position of the seam (Fig. 7).

The lasers' point of work P_L, is rotated around the P_0, and this way projected on the $|\overline{P_0 P_L}|$, axis, what provides for the next position of the point of laser P_L^{TRANS} relating to the current signal S_T. P_L^{TRANS} distance from P_{ROI} for a given angle of forwarding is determined as:

$$|\overline{P_L^{TRANS} P_{ROI}}| = (R + S_T) \cdot \left(\frac{1}{\cos(\alpha)} - 1\right) \tag{2}$$

where: x – description, a – description, a^{n-k} – description, $\binom{n}{k}$ – description.

The difference between the P_S and P_L^{TRANS} distances to the P_{ROI} determines the next value of the adjustment signal S_T:

$$S_{\Delta T} = \pm\left(|\overline{P_L^{TRANS} P_{ROI}}| - |\overline{P_S P_{ROI}}|\right) \tag{3}$$

An adjustment signal thus computed cannot be as yet sent to the CNC Controller. The adjustment signal shall provide the target position of the machine head at the given time, instead of the translation increments relating to the computed value of the adjustment signal $S_{\Delta T}$. Therefore, the base signal representing the position of the head at the time of measurement shall be added S_T

$$S_{T+\Delta T} = S_T + S_{\Delta T}\ [um] \tag{4}$$

The time of measurement ΔT pre-emption is computed from the values of the α angle and the table angular velocity ω assumed for the welding process.

$$\Delta T = \frac{\alpha}{\omega}[s] \tag{5}$$

6. SYSTEM OPERATION CHECK

The system operation has been assessed comparing the head trajectory with and without use of the positioning system. The processed item with a random imposed diversion from the base position was set up on the machine table.

Two job cycles with active laser beam were run:

- the first was an initial run with no positioning system, when the head travelled along the base trajectory, for the purpose of recording of the images used for computation of the head diversion from the joint edge;
- the second was a test run with an active positioning system. During the second run, the photo shots were taken which facilitate assessment of the accuracy of the laser beam with respect to the joint edge.

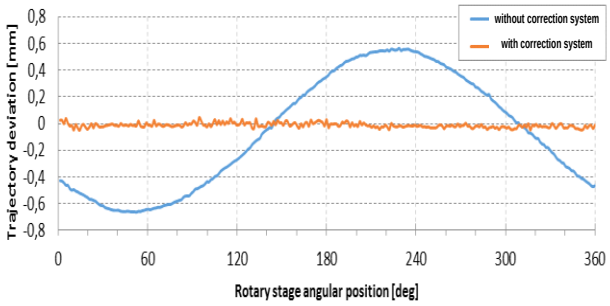

Fig. 8. Comparison of the head diversion from the position of the joint with active and inactive adjustment system (processing parameters: laser power 2kW, table rotation speed 45°/s)

The Fig. 8 chart shows the diversion of the head position with respect to the point of junction, recorded during the initial run without the adjustment system and then with active adjustment system. The diversion of the head position is computed as the distance between the junction point in the gap between the edges and the point of operation of the laser.

The test item showed diversions of 0.66 mm between the gap and the laser head position. The data gathered during the assessment run show that the adjustment system reduced the positioning error to 50 µm.

7. SUMMARY

The designed system of the real time laser head position adjustment provides for the more accurate welding process and elimination of the impact of the inaccurate assembly of the processed item on the seam accuracy.

The positioning accuracy of 50 µm achieved in the system assessment runs is several times better than the diameter of laser beam dots used for welding (about 600 µm). This provides for the proper adjustment of the laser position at about 10% with respect to the dot diameter. With this configuration, the accuracy of positioning of the kinematic system of the CNC machine becomes a leading factor in the overall accuracy.

Overall operation of the process monitoring system depend on types and shapes of the joints, the process parameters, the surface texture of the welded pieces, illumination, technology requirements and many other factors. This is why these systems are dedicated and further development may increase flexibility of their application.

The designed system strong points include detection of the joint traces where the gap between the pieces is narrower than accuracy of the triangulating sensors. Laser illumination allows for the process monitoring what is troublesome with traditional approach because of strong disturbances from plasma and process gases. This way the impact of the parametrisation on the process performance can be assessed, especially at the ends, where the seams are most prone to defects.

REFERENCES

1. **De Graaf M.** (2007), *Sensor-guided robotic laser welding*, University of Twente.
2. **De Graaf M., Aarts R., Meijer J., Jonker J.B.** (2005), Robot-sensor synchronization for real-time seam tracking in robotic laser welding, *Proceeding of the Third International WLT-Conference on Lasers in Manufacturing*, Munich.
3. **De Graaf M., Aarts R., Jonker J.B., Meijer J.** (2010), Real-time seam tracking for robotic laser welding using trajectory-based control, *Control Eng. Pract.*, Vol. 18, No. 8, 944-953.
4. **Dorsch F., Pfitzner D., Braun H.** (2013), Improved continous tube welding due to unique process sensor system and process control, *Phys. Procedia*, Vol. 41, 137-139.
5. **Fridenfalk M., Bolmsjö G.** (2003), Design and validation of a universal 6D seam tracking system in robotic welding based on laser scanning, *Industrial Robot: An International Journal*, Vol. 30, No. 5, 437-448.
6. **Gao X., Zhong X., You D.** (2013), Kalman Filtering Compensated by Radial Basis Function Neural Network for Seam Tracking of Laser Welding, *IEEE Trans. Control Syst. Technol.*, Vol. 21, No. 5, 1916-1923
7. **Huang W., Kovacevic R.** (2011), A Laser-Based Vision System for Weld Quality Inspection, *Sensors*, Vol. 11, 506-521.
8. **Huang W., Kovacevic R.** (2012), Development of a real-time laser-based machine vision system to monitor and control welding processes, *The International Journal of Advanced Manufacturing Technology*, Vol. 63(1), 235-248.
9. **Lee S.K., Na S. J.** (2012), A study on automatic seam tracking in pulsed laser edge welding by using a vision sensor without an auxiliary source, *Journal of Manufacturing Systems*, Vol. 21(4), 302-315
10. **Michalos G., Makris S., Eytan A., Matthaiakis S., Chryssolouris G.** (2012), Robot Path Correction Using Stereo Vision System, *Procedia CIRP*, Vol. 3, 352-357.
11. **Rafajłowicz E., Rafajłowicz W., Rusiecki A.** (2009), Image processing algorithms and an introduction to working with the OpenCV library *(in Polish)*, Wroclaw University of Technology Press.
12. **Regaard B., Kaierle S., Poprawe R.** (2009), Seam-tracking for high precision laser welding applications – Methods, restrictions and enhanced concepts, *Journal of Laser Applications*, Vol. 21 (4), 841–875.
13. **Siciliano B., Khatib O. (eds.)** (2008), *The Handbook of Robotics, Springer*, Berlin, Heidelberg.
14. **Siemens AG.** (2006), *SINUMERIK 840D Configuring the NCU*.

The project has been subsided by the European Union within the European Regional Development Fund Priority axis 1. Strengthening research, technological development and innovation; "Design of a new generation automobile seat in Sitech company (WND-POIG.01.04.00-02-067/12).